Iterative laser straightening of welded plates of varying thickness

Stefan M. Knupfer

Submitted for the degree of Doctor of Philosophy

Heriot-Watt University

School of Engineering and Physical Sciences

June/2010

Abstract

Laser forming uses a defocused laser beam which scans over the sample, generating high surface temperature and large thermal gradients, to produce bending and upsetting/shortening of the material. Laser forming is promising in a wide spectrum of industrial applications, for example flexible shaping of metallic components without mechanical contact, rapid prototyping, or creating complex 3D shapes and removing distortion. An iterative approach to laser forming has the advantage that unknown initial conditions can be accommodated, compared with single pass laser forming.

In this study iterative laser forming (ILF) was extended to plates of varying thickness, and the first ILF of pillow and saddle shapes of varying thickness plates is reported. This forming is done incorporating a finite element (FE) model into the process, which clearly requires the plate thickness to be known. Furthermore, a method is proposed which would adjust laser parameters, based on surface temperature measurements, when the plate thickness is not known.

An important factor for industrial application of ILF is the understanding of its effect on the material formed. Therefore, a systematic study for two common materials on mechanical properties, residual stress (RS) and process temperature of laser formed samples is conducted. Based on the through thickness temperature ranges identified, a method is proposed to determine the extent of affected material, independent of system parameters. For interpreting those results, an analogy between the microstructure in a laser formed heat affected zone and that observed in welding is proposed for the first time, which has proved extremely useful.

Transverse residual strain measurements were used to further validate an analytical-numerical model of laser forming, proposed previously. The through thickness transverse residual strain profile is predicted in a simplified way by the model, which shows its relation to characteristic line energy ranges and laser forming mechanisms.

Finally, ILF of varying thickness plates is demonstrated for the removal of welding induced distortion of industrial specimens, specifically plates with welded stringers. Laser parameters for those forming trials were chosen, based on previous investigations. Finally, the choice of laser parameters is validated through a study of the effect of the iterative laser straightening process on the material properties.

Acknowledgements

I would like to express my sincere appreciation to my supervisor, Professor Andrew Moore for his advice and encouragement throughout this project.

Many thanks are due to Dr. Sébastien Rouquette, especially for the help at the beginning of my PhD. I would like to thank Dr. Anna Maria Paradowska and Dr. Oliver Kirstein for their support in proposal writing and the experience during the residual stress measurements at their facilities. Many thanks to Dr. Jorge dos Santos and all members of the solid state joining group at GKSS and beamline scientists at HARWI II beamline at HASYLAB/DESY for their support during measurements and experiments. Furthermore, I would like to express my special thanks to Chris Mack and John Mason for machining test specimens and their company and support during laser forming experiments.

Many thanks go to my friends and especially family for help and company and of course my sister Birgit with Matthias and my wonderful parents Gise and Toni.

Part of this work was supported by the Engineering and Physical Sciences Research Council [grant number GR/S12395/01].

Declaration

ACADEMIC REGISTRY
Research Thesis Submission

Name:	Stefan M. Knupfer		
School/PGI:	School of Engineering and Physical Sciences		
Version: *(i.e. First, Resubmission, Final)*	First	Degree Sought (Award **and** Subject area)	Doctor of Philosophy

Declaration

In accordance with the appropriate regulations I hereby submit my thesis and I declare that:

1) the thesis embodies the results of my own work and has been composed by myself
2) where appropriate, I have made acknowledgement of the work of others and have made reference to work carried out in collaboration with other persons
3) the thesis is the correct version of the thesis for submission and is the same version as any electronic versions submitted*.
4) my thesis for the award referred to, deposited in the Heriot-Watt University Library, should be made available for loan or photocopying and be available via the Institutional Repository, subject to such conditions as the Librarian may require
5) I understand that as a student of the University I am required to abide by the Regulations of the University and to conform to its discipline.

* *Please note that it is the responsibility of the candidate to ensure that the correct version of the thesis is submitted.*

Signature of Candidate:	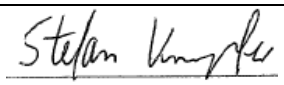	Date:	27/08/2010

Submission

Submitted By (name in capitals):	Stefan Michael KNUPFER
Signature of Individual Submitting:	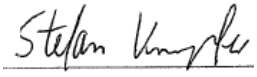
Date Submitted:	27/08/2010

For Completion in Academic Registry

Received in the Academic Registry by *(name in capitals)*:			
Method of Submission *(Handed in to Academic Registry; posted through internal/external mail)*:			
E-thesis Submitted ***(mandatory for final theses from January 2009)***			
Signature:		Date:	

Table of Contents

List of symbols

d^{hkl}	Lattice plane spacing [Å]
d_l	Laser beam diameter $[m]$
d_{paths}	Laser scan path distance $[m]$
f_d	Focal distance $[m]$
h	Surface height $[m]$
h	Planck constant $[J \cdot s]$
k	Thermal conductivity $\left[\frac{W}{m \cdot K}\right]$
l	Length of the heated area $[m]$
m	Mass [kg]
n	Strain hardening coefficient
q_0	Power per unit area $\left[\frac{J}{mm^2}\right]$
rms	Root means square shape error [mm]
s_0	Plate thickness $[m]$
s_1	Thickness of the upper heated layer/depth of the plastic zone $[m]$
s_2	Thickness of the lower layer $[m]$
t	Time $[s]$
u, u_0	Displacement in x $[m]$
v, v_0	Displacement in y $[m]$
v_l	Laser processing speed $\left[\frac{m}{s}\right]$
w, w_0	Displacement in z $[m]$
z	Coordinate through thickness $[m]$
A	Area $[m^2]$
A_l	Laser beam area $[m^2]$
AE	Area energy $\left[\frac{J}{mm^2}\right]$
CLE	Cumulative line energy $(N \cdot LE)$ $\left[\frac{J}{mm}\right]$
$CLED$	Cumulative area energy density $(N \cdot LE)$ $\left[\frac{J}{mm}\right]$
C_p	Specific heat $\left[\frac{J}{kg \cdot K}\right]$
D	Thermal diffusivity $\left[\frac{m^2}{s}\right]$
E	Modulus of elasticity $[MPa]$

E_a	Emissive power of the actual body $\left[\frac{W}{\mu m \cdot m^2}\right]$
E_b	Emissive power of a black body $\left[\frac{W}{\mu m \cdot m^2}\right]$
F_0	Fourier number
F_x	Net force $[N]$
H	Vickers hardness $\left[\frac{kg_f}{mm^2}\right]$
I_l	Laser intensity $\left[\frac{W}{m^2}\right]$
I_{ij}	Second moment of area cross section $[m^4]$
L	Distance $[m]$
LE	Line energy $\left[\frac{J}{mm}\right]$
M_B	Bending moment $[Nm]$
M_{ij}	Moment $[Nm]$
N	Number of laser scan passes
P_l	Laser power $[W]$
Q_l	Energy input $[W]$
SE	Specific energy $[W]$
T_a	Actual temperature [℃]
T_c	Colour temperature [℃]
T_m	Measured temperature [℃]
T_{max}	Maximum temperature [℃]
T_{pl}	Critical temperature where the yield stress is zero [℃]
T_{room}	Room temperature [℃]
T_s	Melting temperature [℃]
T_{sat}	Saturation temperature [℃]
T_{th}	Threshold temperature for the thermal induced plastic stress [℃]
UTS	Ultimate tensile strength $[MPa]$
YTS	Yield tensile strength (flow stress) $[MPa]$
α_B	Bend angle [deg]
α_{th}	Coefficient of thermal expansion $\left[\frac{1}{K}\right]$
γ_{ij}	Total strain
γ_{ij}^1	Bending strain
γ_{ij}^o	In-plane strain

ε	Emissivity
ε_1	Strain of the upper layer
ε_2	Strain of the lower layer
ε_2^i	Average principal minimal strain induced over the scan path spacing
ε_G	Emissivity of the graphite coating
ε_M	Radiation of the sample material
ε_{ij}	Total strain
ε_{ij}^0	In-plane strain
ε_{ij}^1	Bending strain
ε_{in}	Inherent strain
ε_l	Strain generated by laser forming
ε_t	Tangential strain
η	Absorption coefficient
η_{LE}	Line energy dilution factor
η_ε	Dilution factor for in-plane strain field
η_κ	Dilution factor for curvature field
θ_B	Diffraction angle [deg]
κ	Curvature $\left[\frac{1}{m}\right]$
λ	Wavelength $[\mu m]$
ν	Poisson's ratio
ξ	Convective heat exchange coefficient $\left[\frac{W}{m^2 \cdot K}\right]$
ρ	Mass density $\left[\frac{kg}{m^3}\right]$
σ	Boltzmann constant
σ_f	Yield/flow stress $[MPa]$
τ	Interaction time $[s]$
φ_l	Laser heat flux $\left[\frac{W}{m^2}\right]$
$\Delta T'$	Temperature rise of the upper layer s_1 $[K]$
Δh	Vertical shape residual $[m]$
ΔT	Temperature difference $[K]$
Δt	Heating time $[s]$
∇	Mathematical operator (partial derivative, vector)
∂	Mathematical operator (space derivative, vector)

List of publications

Journal publications:

Stefan Knupfer, Anna M. Paradowska, Oliver Kirstein and Andrew Moore, Investigation of Residual Stress in Laser Formed Mild Steel Plates Using Neutron Diffraction, Mater. Sci. Forum Vol. 652, pp. 123-128 (2010).

R. Ahmed, N.H. Faisal, S.M. Knupfer, A.M. Paradowska, M.E. Fitzpatrick, K.A. Khor and J. Cizek, Neutron Diffraction Residual Strain Measurements in Plasma Sprayed Nanostructured Hydroxyapatite Coatings for Orthopaedic Implants, Mater. Sci. Forum Vol. 652, pp. 309-314 (2010).

S.M. Knupfer, A.J. Moore, The effects of laser forming on the mechanical and metallurgical properties of low carbon steel and aluminium alloy samples, Mat. Sci. Eng. A 527, Issue 16-17, pp. 4347-4359 (2010).

S.M. Knupfer, A.M. Paradowska, O. Kirstein, A.J. Moore, Characterization of residual stress in laser forming, in preparation.

S.M. Knupfer, S. Rouquette, A.J. Moore, Iterative laser forming of varying thickness plates, in preparation.

Conference publications:

S. Rouquette, F. Bardin, S. Knupfer, D.P. Hand, J.D.C. Jones, A.J. Moore, Iterative Laser Straightening of Weld-Distorted Plates, Proc. of the LANE 2007, pp. 581-588.

S. Knupfer, S. Rouquette and A.J. Moore, Straightening of Distorted Welded Plates by Iterative Laser Forming, Proc. of the IWOTE 2008, pp. 205-213.

Chapter 1

Introduction

1.1 Background

Modern engineering requires metallic components or sheets to be formed into complex curvatures. Laser forming has industrial promise in a wide spectrum of applications, for example in rapid prototyping, creating complex 3D shapes and removing distortion. The process itself originates from flame bending or line heating, which was used mainly in the shipbuilding industry. In flame bending, the heat flux is dependent on the surface temperature, which cannot rise above the flame temperature, preventing high temperature gradients in materials with high thermal conductivity and thus restricting the type of forming that can be achieved. The heat flux applied through a laser beam is constant, giving potentially high surface temperature and large thermal gradients even for thin sheets and materials with high thermal conductivity. The laser forming process employs a defocused laser beam which scans over the sample, generating high surface temperature and large thermal gradients, between the irradiated surface and the surrounding material. The temperature distribution forces the material to expand non-uniformly, thus leading to non-uniform local stresses, which produce bending and shortening/shrinking of the material.

Nowadays, the many advantages of laser forming as a non-contact forming tool, including process flexibility or forming of complex surfaces like 3D shapes, have been recognized. Industry sectors, including aerospace, automotive, shipbuilding and micro electronics, have become aware of the technique for shaping, reconditioning and aligning applications of metallic components. However, for laser forming to be applied in an industrial process for the forming of general 3D shapes, including non-developable surfaces, further investigation and process understanding are needed. Although a considerable amount of work has already been done on 2D laser forming, only a few groups have tackled the problems, which have arisen during the laser forming of general 3D shapes. Those problems include the unknown initial stress state of the plate or the simultaneous contribution of in-plane and out-of-plane deformation induced during a single laser scan. An iterative approach is generally more tolerant to such unknown process parameters than single pass laser forming, which is commonly applied.

An iterative laser forming process has been developed at Heriot-Watt University in the past. It has been useful for the forming of non-developable 3D surfaces of uniform thickness plates. Therefore, the main objective of this thesis is to further develop the iterative laser forming for plates of varying thickness and industrial specimens. For this, a mechanical finite element simulation was incorporated in the process, and varying thickness plates were formed and welded plates were straightened. The effect of laser forming on the material was investigated through hardness measurements, tensile tests and optical microscopy, and related to the peak through thickness temperature. Further, the residual stress of laser-formed specimens was measured with neutron diffraction to further validate an analytical-numerical model of laser forming. This development and investigation aims to bring the process closer to a potential industrial application.

1.2 Organization of the thesis

In Chapter 2 the existing literature of laser forming is reviewed, with emphasis on the experimental work which has been carried out to date and work done on 3D laser forming regarding process design and industrial applicability. Other areas from the literature, such as laser forming mechanisms or analytical models of laser forming which form the background of this project and are relevant to the work, are also presented. Furthermore the iterative laser forming (ILF) process which was developed at Heriot-Watt University and applied to uniform thickness plates is described in the form inherited in this study.

Chapter 3 describes ILF process modifications made in this study to apply the process for the 3D forming of varying thickness plates. Those modifications included the implementation of a mechanical finite element (FE-) analysis for the computation of the in-plane strain field required, because the analytical solution applied on uniform thickness plates was no longer possible for more complex token geometries. The results of successfully formed pillow and saddle shapes of low carbon steel and an aluminium-copper alloy are presented, validating those modifications made. Based on surface temperature measurements with a pyrometer, an approach was sought which would use it as a supplementary control parameter and adjust the laser parameters required accordingly. Therefore, unknown process parameters, e.g. varying sample thickness or laser light absorption, could be accommodated for without *a priori* knowledge.

Chapter 4 provides background information and describes the experimental procedure and the application of three complementary techniques to record the temperature during a single line laser scan. Thermocouple measurements delivered an insight to the temperature distribution through thickness, while a pyrometer and infrared camera (IR) camera recorded the surface temperature. Those temperature measurements were fundamental and essential for process understanding and interpreting results throughout this study, and for adjusting a thermal FE-analysis, described later. This FE-analysis was developed with the same objective of understanding the forming process. It was applied in its validated form on the one hand to further understand and investigate the temperature field through depth and on the sample surface for the 3D forming of varying thickness plates; on the other hand, it was applied to estimate the local thermal histories of the material within a cross section of the HAZ produced during a single laser scan across a sample.

Chapter 5 presents a systematic study of the mechanical properties of laser formed low carbon steel and aluminium-copper alloy. Hardness measurements and tensile tests are presented for single- and multiple-pass laser forming (up to 12 passes) and for a wide laser line energy (LE) range that includes both the temperature gradient and the shortening laser forming mechanism. Before that, an analogy between the microstructure in a laser formed HAZ and that observed in welding is presented, which has proved extremely useful for interpreting the evolution of hardness and microstructure with increasing LE in laser forming.

Chapter 6 presents high resolution transverse through thickness residual strain measurements on thin low carbon steel and aluminium-copper alloy plates, which were compared with results of the analytical-numerical model of laser forming, proposed previously. Neutron diffraction at two different facilities was used to characterize the residual strain of laser scanned samples across the HAZ, which were treated in a broad laser parameter range with one and three laser passes. Multi-pass behaviour was of special interest to define process parameters for our approach to ILF. Finally, the effect of the ILF process on the residual stress is shown in one of its potential future industrial applications: the iterative laser straightening of a distorted friction stir welded (FSW) aluminium plate.

Chapter 7 shows the results of post process distortion correction on examples from various sources (BAE, Cranfield University, GKSS). Laser parameters chosen and adjustments made were a combination of the techniques presented in the previous chapters. Included in the study was the straightening of welded plates of varying thickness, such as stringers, and an investigation into the effect of the ILF process on the material after distortion correction, validating the laser parameters chosen.

Chapter 8 concludes the thesis with a summary of the findings and a discussion for future work on the iterative laser forming process itself. Then, a realistic prospective to the potential of (iterative) laser forming to be applied in an industrial process is given.

Chapter 2

Background and literature review

During the laser forming process, the surface of the material is heated by the laser beam which transverses the workpiece, as shown in Figure 2.1, and creates a thermal heat flux through the surface. The thermal expansion of the material near the surface introduces thermal stresses, which result in elastic-plastic strains because of the constraint of the surrounding cold material. After cooling, the plasticized material close to the surface is shorter than the material below, which results in a bending towards the laser beam.

In most laser forming applications, a defocused laser beam is used in order to prevent surface melting, which would be detrimental for the surface quality of the finished product. The laser scanning paths applied to the surface of the workpiece determine the shape and forming result. They can vary from only a point, through single lines to connected line patterns, based on stress computation, e.g. for 3D shapes. There are many parameters which are of importance for the control of laser forming. Those which have most influence on the process are identified in Figure 2.1. For example the laser power and the laser scan speed (and the absorption coefficient) define the heat input into the material and therefore the amount of forming that can be achieved. In the material, the extent of the heated zone and the peak temperature during laser forming are affected mainly by the thermal conductivity. Based on the peak temperature reached in the material and the coefficient of thermal expansion, plastification proceeds and with it a final bend angle develops on cooling. The large number of parameters indicates the complexity of the process. Through the good control of the laser beam, different types of temperature fields through the workpiece can be established, all yielding different forming mechanisms and results. Three main principles of laser forming mechanisms can be distinguished, namely Temperature Gradient Mechanism (TGM), Upsetting or Shortening Mechanism (SM) and Buckling Mechanism (BM). It should be noted that the term Shortening Mechanism is used hereafter, rather than Upsetting Mechanism, because it is more descriptive of the physical process. Those mechanisms are shown in Figure 2.2. TGM and SM, which are relevant for the iterative laser forming (ILF), are reviewed in the following section. The BM is not considered in this thesis and is described in more detail elsewhere [1,2].

2.1 Laser forming mechanisms

An outline of the three main forming mechanisms is given in Table 2.1 [3]. In particular TGM and SM, described in the following, are strongly related to each other and their interplay is of special importance regarding the process understanding of the 3D laser forming.

The TGM induces predominantly out-of-plane strain, which is also referred to as ‘curvature’ or ‘bending’. Similarly for the SM which induces predominantly in-plane strain, referred to as ‘shortening’ or ‘in-plane shrinkage’. These terms are used synonymously throughout this thesis.

2.1.1 Temperature gradient mechanism (TGM)

The temperature gradient mechanism proceeds in the following steps:

- Heating of the surface and thermal expansion against the cold bulk material
- Development of counter bending
- Further heating and plastic compression of the surface
- Cooling of the surface and thermal contraction
- Development of the bending angle

This mechanism is characterized by a steep temperature gradient through the sheet thickness. Typical temperature conditions required for the TGM are shown schematically in Figure 2.3. The beam diameter is typically the same as the sheet thickness or slightly less. Bending of the sheet occurs after cooling perpendicular to the laser scan path towards the laser beam (Figure 2.2). This bend angle varies along the laser scan line as a result of the non-uniform temperature distribution [4]. In the regime of the TGM an additional bending along the laser scan path can be noticed. This unwanted longitudinal distortion along the laser scan line is caused by the local shortening of near surface material [4,5]. Therefore, the thermal stress induced varies along the laser scan line and contributes to non-uniform bending (in both perpendicular and longitudinal direction with respect to the laser scan line).

A good way of thinking how the thermal stress develops in the regime of the TGM is shown schematically in Figure 2.4, which shows an example of a typical temperature stress cycle during TGM laser forming of low carbon steel. It should be noted that the exact shape of the temperature yield stress curve will vary significantly for different materials but the overall concept will be similar. As the material temperature T increases, the stress in the heated material follows the thermal-elastic stress curve (Figure 2.4, point [1]) until the local yield stress σ_f (Figure 2.4, point [2]) is reached.

The heating and expansion of the top surface layers causes a bending away from the laser beam; this is named ‘counter bending’ and shown in Figure 2.5. The induced thermal stress would be totally reversible if the heating was stopped at this stage (Figure 2.4, point [1]). Once the thermal stress exceeds the temperature dependent yield stress σ_f (Figure 2.4, point [2]) any further thermal expansion leads to an induced stress and thus permanent compressive plastic strain and deformation of the material (Figure 2.4, point [3]).

Cooling proceeds by heat conduction in the part to the colder, surrounding material where heat losses to the environment (radiation and conduction) can be neglected. On cooling, the workpiece shrinks laterally by the thermal contraction. Owing to the temperature gradient through thickness, layers closer to the top surface are shortened to a greater extent than layers further away. Therefore, the sheet bends towards the laser beam at ambient temperature (Figure 2.5). The magnitude of the bending angle observed for the TGM depends on the coupled energy, the geometry of the part and the thermal and mechanical properties of the material. It varies typically between 0.1 and 3 degrees per pass.

2.1.2 The upsetting or shortening mechanism (SM)

Laser forming conditions favouring the SM are typically as follows. The laser beam diameter is in the order of or greater than the sheet thickness and the energy input is high. Moreover, the geometry of the part does not allow buckling of the material, as is true for thick sheets, extrusions and stiff structures. If these conditions are fulfilled, the SM proceeds by the following steps (Figure 2.6):

- Heating of the cross section and thermal expansion
- Further thermal expansion that exceeds the elastic strain, resulting in a plastic compression of the cross section
- Cooling of the material with or without small out-of-plane strain and predominantly in-plane strain (in-plane shrinkage)

Through the low processing speed applied, a nearly isothermal through thickness temperature profile is reached. High temperature in the heated area decreases the yield stress. Thermal induced strains, exceeding yielding, result in plastic compression of the heated material, as it is hindered in free expansion by the surrounding colder bulk material. Therefore a large amount of thermal expansion is converted into plastic compression. Owing to the low temperature gradient, there is also a very small gradient in plastic strain across the thickness direction. On heating, the material expansion is

hindered locally, whereas contraction on cooling proceeds along the whole laser scan line. Therefore, on cooling, compressive plastic strains remain in the sheet, leading to a local shortening (in-plane shrinkage). Owing to the constancy of volume, there must be an increase in sheet thickness in the thermally plastified zone.

This mechanism can be applied in a wide range of forming applications. Plane sheets may be treated with conditions favouring the SM along radial paths, resulting in a spatially formed part, i.e. a 3D shape. The mechanism can also be used for shortening of small frames or aligning operations in micro parts production. Another possible application of this mechanism might be the forming of extrusions and pipes, in that the sections could be made to bend out of the plane by careful selection of the sequence of irradiations [6].

TGM and SM have been identified as two different laser forming mechanisms because of the characteristic phenomenon named above. However, both mechanisms link seamlessly into each other; i.e. if conditions favouring the TGM are applied, there will always be a certain amount of the SM (in-plane shrinkage) present. Shi *et al.* [5] proposed a mechanism called 'coupling mechanism' (CM), which is a combination of the TGM and the SM. For conditions of the CM, plastic deformation occurs on the top and bottom surfaces, but the plastic deformation at the top surface is greater than that on the bottom surface. Therefore, both bending (perpendicular to the laser scan line) and in-plane strain are induced. In addition, the bending deformation along the laser scan line is approximately equal to that of the TGM, because the contribution of the SM to this phenomenon is negligible [5,7]. Clearly, the bend angle observed in the CM varies strongly, dependent on heating conditions favouring either TGM or SM.
In complex laser forming, like laser straightening or 3D laser forming of non-developable surfaces, in-plain and bending strains are required. Therefore the understanding of the interplay between TGM and SM in the regime of the proposed CM [5] is of special interest.

2.2 Analytical models of laser forming

The two phenomenological mechanisms described in section 2.1 have been modelled analytically in the past. They are described in the literature and are reviewed in the following. For a complete analytical model of laser forming, four steps can be defined:

1) Calculation of the temperature field

2) Calculation of the plastic strains
3) Development of the out-of-plane strain
4) Calculation of the bend angle

2.2.1 Models for the temperature gradient mechanism (TGM)

Several models have been proposed for the TGM [8,9,10,11,12]. One of the earliest modelling attempts was made by Vollertsen [9,10] in his 'Trivial Model'. It calculated the bend angle from purely geometric considerations and an energy approach was made to calculate the temperature rise during laser interaction. Such an energy approach was used in flame bending to calculate the bending angle [13]. An assumption made in the model is that the thermal expansion of the material on heating is totally converted into plastic compression. Based on this 'Trivial Model', the 'Two Layer Model' was proposed [9,10]. The principle of the model is shown in Figure 2.7. Instead of only a geometrical approach, it takes moments and forces during bending into account, while the sheet cools down. Therefore, the bend angle (α_b) is given by the geometry and the difference in the strains of the upper (ε_1) and lower (ε_2) layer, divided by half the sheet thickness (s_0), where l is the length of the heated zone.

$$\frac{\alpha_b}{2} = \frac{l(\varepsilon_1 - \varepsilon_2)}{0.5 s_0} \qquad (2.1)$$

For the calculation of the strain (ε_1) in the upper layer, the assumption was made that all the thermal expansion (given by $\alpha_{th}\Delta T$) is converted into plastic compression. In reality, this is not the case, as some energy is used to strain the material elastically up to its temperature dependent yield point. However, an appreciable amount of elastic straining does not occur, because the free thermal expansion is greatly hindered by the cold and rigid surrounding material. In addition, the yield stress of the heated zone is reduced to almost zero during heating, since it is temperature dependent. It may be acceptable under conditions of high temperature to omit these parameters and assume that all the thermal expansion is converted into plastic compression. During cooling, as the heat flows into the surrounding regions, there may be a tensile plastic restraining of the previously compressed zone.

The thermal strain in the lower layer was not considered, based on the assumption made that the temperature profile there is perfectly flat. Therefore the strain (ε_2) was calculated by taking mechanical forces and moments only. This assumption may be acceptable as a simplification in an analytical model. However, as it was shown in experimental results of through thickness temperature measurements on low carbon

steel and aluminium alloy samples [14], a considerable temperature gradient can be present in the bottom half of the plate even if laser forming conditions are in the TGM regime.

The final expression of the bend angle was given by,

$$\alpha_b = \frac{12\alpha_{th}\Delta T' l s_1 (s_0 - s_1)}{s_0^3} \tag{2.2}$$

where α_{th} is the coefficient of thermal expansion. Calculating the bend angle with this formula requires the knowledge of the length of the heated zone l, the depth of the heating s_1, and the temperature rise of the upper layer $\Delta T'$. This requires the co-ordinates to be found as a function of the temperature. Since the expressions for the temperature contain transcendental or Bessel functions which cannot be inverted suitably [15], this is not possible analytically for laser processing.

Vollertsen adopted an energy approach to the solution of the temperature field instead. In this energy approach, all three factors l, s_1, and $\Delta T'$ are calculated simultaneously [8]. This assumption was made because the parameters l and s_1 determine the extent of the heated zone, which is governed by the thermal conductivity. The temperature increase $\Delta T'$ is controlled by the heated area, the heat capacity and the energy input from the laser beam. This approach was adopted, because as the thermal conductivity increases, the extent of the heated area increases, but the average temperature increase is lowered. From this, it was assumed that the thermal expansion remains constant. Using these assumptions the energy input Q_l is given by the time of heating t, the laser power P_l and the absorption η:

$$Q_l = 0.5\Delta t P_l \eta \tag{2.3}$$

0.5 is used as only one half of the heated area is considered for calculations. The heating time Δt is given by the fraction of the laser spot size d_l and the processing velocity v_l:

$$\Delta t = \frac{d_l}{v_l} \tag{2.4}$$

Introducing those assumptions, into equation (2.2) gives an expression for the bend angle in terms of known parameters only:

$$\alpha_b = 3\frac{\alpha_{th}}{\rho C_p}\frac{P_l \eta}{v_l}\frac{1}{s_0^2} \tag{2.5}$$

In this work by Vollertsen [10], experimental data from other authors was presented and compared with the analytical results, as shown in Figure 2.8. It can be seen that despite simplifications and assumptions having been made in the model, the bend angle is reasonably well predicted for high speed experiments. However, in the regime of the

SM, i.e. lower laser scan speed, it overestimated the bend angle because it did not take into account the heat flow to the lower layer (assumption of a perfectly flat temperature profile), which results in an energy loss and therefore significantly lower temperature and out-of-plane strain in the upper layer. Further, the strain of the lower layer increases with temperature and decreases the overall difference between the strain of the upper and the lower layer, and with it the final bend angle decreases.

In addition the model identified important material parameters such as the thermal conductivity, and showed their influence on the bend angle, as may be seen in the linear relationship between bend angle and thermal conductivity in Figure 2.9. Although substantial improvement in the agreement between this model and experimental work was achieved, compared with previous analytical models for the flame bending process [13], some of the basic concepts were still omitted. The model assumed that all of the energy was used for plastic deformation and this ignored the energy for the elastic straining.

In Yau's model [12] the 'Two Layer Model' approach was extended to include the counter-bending effect in order to account for some of the purely elastic straining. This modification resulted in two equations, one for the counter-bending angle and one for the bend angle at the end of the cooling cycle. The final equation for the bending angle (positive bend angle minus counter-bend angle) including the temperature field equation in Yau's model, was

$$\alpha_b = 3\frac{\alpha_{th}}{\rho C_p}\frac{P_l A}{v_l}\frac{1}{s_0^2}\left(\frac{7}{2}\right) - 36\frac{l}{s_0}\frac{\sigma_f}{E} \qquad (2.6)$$

where σ_f is the yield strength and E the modulus of elasticity. Comparing equation (2.5) and (2.6), Yau's solution includes some material and geometrical parameters which reduce the calculated bend angle, unlike Vollertsen's solution. Through the fact that the counter-bending is in the order of 10^{-5} to 10^{-6} degree under the TGM (for the material AA2024) [16], combined with the simplifying assumptions of the model both solutions differ only slightly for a single pass and less than expected originally. A comparison of the predicted bend angle from the models with experimental data shows that they overestimate the bend angle, especially with an increasing number of passes. This overestimation is the result of simplifications made in the models, for example regarding the temperature field or temperature constant material parameters. Another characteristic of these models is that they predict a constant bend angle increase with the increasing number of passes, which is not consistent with experimental results [17]. That is because the equations of those models did not take into account factors such as

coating degradation, section thickening, work hardening or microstructural changes of the material in the heat affected zone (HAZ).

Vollertsen extended his work on the TGM in another model, called the 'Residual Stress Model', to include the effects of a realistic temperature field (3D heat conduction) and a more realistic strain distribution analytically [18]. This model used the residual stress approach often applied in welding analysis. The strains in the y- and z-direction, Figure 2.10, were the only strains considered in the analysis for an infinitesimal strip in the direction in which the laser beam is scanning (x). Initially, it is assumed that there is a boundary temperature or isotherm T_{th}, defined as

$$T_{th} = \frac{\sigma_f}{\alpha_{th} E} \tag{2.7}$$

Above this boundary or threshold temperature, the thermal expansion, hindered by the surrounding material, leads to plastic compression.

As a result of the laser heating, an elliptical strain distribution was assumed, where plastic strain occurs if the strain caused by the thermal expansion exceeds the purely elastic strain. The elastic strain is governed by the temperature dependent properties, in that the flow or yield stress and Young's modulus decrease as the temperature increases. Therefore, elevated temperatures are beneficial to produce plastic compression and hence bend the material. If the depth of the plastic zone s_1 is less than the sheet thickness s_0, then integration of the local strains results in the local bending moment. The plate is said to bend about this depth s_1. The local bending moment can be determined from beam theory by integrating the local strains:

$$M_B = dxE \int_0^{s_1} \varepsilon(z) \left(\frac{s_0}{2} - z\right) dz \tag{2.8}$$

From geometrical conditions, it is known that the bending angle is given by the fraction of twice the length of the bent zone and the curvature. From beam theory, the fraction of the transverse bending moment and the elastic modulus times the moment of area yields the inverse of the curvature. The bending angle for the condition $s_1 < s_0$ can be calculated from

$$\alpha_b = \frac{\varepsilon_{in} l s_1}{s_0^3} (3\pi s_0 - 8 s_1) \tag{2.9}$$

where ε_{in} is the inherent strain which is the maximum plastic strain caused by thermal expansion less the purely elastic strain during heating. For the second condition, if the

plastified zone s_1 is greater than the sheet thickness s_0 the upper limit of the integral in equation (2.8) is s_0 instead of s_1 and yields

$$\alpha_B = \frac{\varepsilon_{in} l}{s_1 s_0^3}\left(6s_0^2\sqrt{s_1^2 - s_0^2} + 6s_0 s_1^2 \sin^{-1}\frac{s_0}{s_1} + 4(s_1^2 - s_0^2)^{\frac{3}{2}} - 4s_1^3\right) \qquad (2.10)$$

Calculating the bend angles with these formulas requires knowledge of the depth of the plastic zone s_1 and the length of the plastic zone l, which was one limitation of the approach. These parameters were calculated from the proposed temperature field calculations, which were an approximation of the Fourier equation (3D heat conduction) for a finite area source. However, the solution of these equations required the co-ordinates of length l and depth s_1 of the plastic zone as a function of temperature. As it was not possible to invert this form of the heat equation in a suitable fashion analytically (in particular to give the depth co-ordinate s_1) an approximate solution in the range relevant to laser bending was used. In this approximation the temperature increase as a result of the limited sheet thickness was described by a second symmetrical heat source and taken into account through lowering the boundary temperature T_{th} (equation (2.7)) above which plastic strain occurs [18]. Considering the whole sheet thickness for the calculation of the length l and width s_1 of the plastic zone was a significant improvement compared with the assumption made in the 'Two Layer Model' [9,10].

This model showed the importance of the thermal conductivity on the process. A slight change in the thermal conductivity changes the thermal expansion and the position of the elastic-plastic interface, as the average temperature in the irradiated zone is sensitive to slight changes in the thermal conductivity. Consequently, it is possible that the bend angle itself is sensitive to small changes in the thermal conductivity. As mentioned, both the yield stress and the elastic modulus are temperature dependent which required the knowledge of the function relating those parameters to temperature to calculate this contribution accurately. The model can predict the physical behaviour in the TGM regime, as shown in Figure 2.11, if provided with accurate information about the temperature dependent mechanical properties. However, the boundary temperature T_{th} above which thermal plastic stress is induced had to be chosen in the order of 600K to match the experimental data. It should be noted that this boundary temperature T_{th} is the temperature difference from ambient/room temperature. Using a realistic T_{th} around 100K (for the material St14) resulted in values of the bend angle which were more than an order of magnitude too high. Because of the many effects on this parameter (e.g.

finite stiffness of surrounding material), further work was proposed to investigate whether T_{th} can be evaluated in such a simple physical manner, as shown in equation (2.7).

In another modelling approach for the TGM, Mucha *et al*. [11] provided bend angle equations for rectangular, triangular, elliptical and circular shaped plastic zones. These shapes depend on the material, thermal properties and the laser processing parameters used. In this work [11], the temperature was calculated from the solution for a moving point source, taken from Duley [19]. The bend angle was found for the case of semi-circular isotherms. Dimensionless variables, laser power and transverse velocity allowed the calculation of the maximum depth of the isotherm. This model assists with determining the critical conditions which give rise to the TGM, Figure 2.12, but the knowledge of the isotherm makes it difficult to compare with/validate experimental data.

In later work by Mucha *et al*. [20], an analytical model for the TGM was presented, where the bend angle depended on four dimensionless parameters only. First, the Fourier number, defined as

$$F_0 = \frac{d_l D}{v_l s_0^2} \tag{2.11}$$

where D is the thermal diffusivity, s_0 is the plate thickness, d_l the surface heat diameter and v_l the heat source velocity. Further parameters were: the surface temperature related to the temperature at which the material loses its elastic properties, the beam diameter related to the thickness of the plate and the product of the coefficient of thermal expansion times the temperature where the material loses its elastic properties. For the calculation a quasi-stationary temperature field related to the heat source was assumed. Moreover, the temperature was assumed to be constant in the inherent strain zone, the final bend angle was assumed to be small and the material parameters were not dependent on temperature, with the exception of the yield limit which was assumed to drop to zero at the critical temperature T_{pl}. The conditions for the TGM were defined as $F_0 < 1$. An experimental verification of the bend angle dependence on the Fourier number was given, with satisfactory agreement between experimental and analytical results.

Both, Vollertsen's and Mucha's analytical modelling approaches significantly contributed to the understanding of laser forming in the form of mathematical descriptions of the process. However, the need of critical parameters, e.g. the boundary

temperature T_{th}, or the temperature where the material looses its elastic properties T_{pl}, and difficulties in the calculation of the extent of the plastic zone limited their accuracy and applicability.

In analytical work by Magee [16], it was argued that the above models for the TGM, although they have advanced the understanding of the process on a rudimentary level, are incomplete in terms of practical laser forming, owing to gross simplifications. The mechanics of the process were defined in terms of the engineering theory of bending and beam theory specifically. It was assumed that the stress distribution occurring during laser bending is similar to that around a hole in a plate because, as a result of heating, the mechanical properties (yield stress, elastic modulus) were reduced to almost zero in the laser irradiated zone. The laser spot itself was represented by a disk, subjecting a force around the edge [21]. The transverse bending moment was used to find the curvature, and the temperature field was approximated using an energy approach or by an approximation of the solution for the temperature field from a static laser beam impinging on a thin sheet. As a result of his proposed model, it was shown that in theory there should be two bend angles in laser forming under conditions of the TGM: the angle transverse to the direction of scanning and the angle parallel to the direction of scanning, which is of significant importance with regard to process accuracy in 2D and 3D laser forming. The unwanted distortion along the laser scan path was investigated later in more detail in a numerical study by Bao *et al.* [4].

In summary, all these analytical routes calculate the bend angle at the end of the process, but they do not describe the transient stages or physical behaviour between laser forming mechanisms such as TGM and SM. Knowledge of these transient stages is useful for successful process control [16], because both mechanisms link seamlessly into each other. Even if conditions favouring one mechanism are chosen, there will always be a certain contribution of the other mechanism to the final deformation. For future forming operations which will be concerned with forming an initially flat sheet into a final 3D geometry the understanding of these transient stages is of particular importance.

2.2.2 Models for the upsetting or shortening mechanism (SM)

Compared with the TGM, far fewer references of analytical modelling work on the SM were found. Krauss [22] modelled laser bending of extrusions with rectangular cross

sections using the SM. Box sections or extrusions can be made to bend out of plane by irradiating three sides of the rectangular cross section. Therefore, an assumption of the model was that three of four sides of the box section were heated simultaneously to initiate the bending. As this is not possible with a single laser beam, a sequence of irradiation paths was defined, which had an important influence on the bending result. The irradiation on the left and right side of the extrusion was applied to avoid the mechanical obstacle for the contraction of the front side of the extrusion and was not considered in the model, despite its influence on the deformation. The bend angle was determined from a geometrical consideration (amount of compression of the front surface of the extrusion) and the amount of shortening was obtained from an energy approach and the thermal data of the material. A similar approach was used in Vollertsen's models [8,10,18] where a geometry/strain relationship was drawn between the processing parameters and the bending angle. Compared with the experimental data the model showed good agreement with a deviation of less than a factor of 1.5 for most cases [23].

2.2.3 Analytical models combining bending and shortening

Analytical models, described earlier, helped to further understand laser forming mechanisms and to express characteristic behaviour with mathematical formulas. However, their application is limited to the distinct laser forming mechanism. Therefore more complete analytical models [24,25,26,27] were developed combining bending and shortening. They give a reasonable estimation of the bend angle and run within seconds, compared with complete FE-analysis, described in section 2.3. In the following, a brief outline of some analytical models combining bending and shortening is given.

Kyrsanidi *et al*. [24] developed a mathematical model which was valid only for conditions inducing a non-uniform temperature distribution through thickness. The plastic deformation, developed within the predefined laser path, was calculated, whereas each volume in the laser path was considered separately. An analytical thermal model calculated the thermal load, assuming that the temperature distribution within each layer is constant. In order to calculate the final angular distortion, an analytical elasto-plastic analysis was applied, where temperature dependent material parameters were taken into account. Plastic bending was considered only during heating. During cooling, it was assumed that no additional plastic strain develops in the element. Another analytical modelling approach [25] took plastic bending during both heating and cooling into

account. Since the heat conduction in the longitudinal direction was neglected, the prediction of this model was limited to high scanning speeds and therefore conditions in which it is most likely that the TGM will be dominant.

A more advanced analytical model for laser bending was presented by Shen *et al*. [26]. The plastic deformation was calculated, based on history-dependent incremental stress-strain relationship between both heating and cooling, and the elasto-plastic material behaviour was temperature dependent. In order to calculate the temperature field during and after laser interaction, a 3D analytical model was used which described the temperature field for a constant moving heat source [28]. The heat source was assumed to obey a normal Gaussian distribution for a laser beam. The model showed a reasonably good agreement with experimental results of 0.89mm thick low carbon steel plates, presented in [4], for conditions of the TGM and BM, as well as co-existing TGM and BM.

These more complete analytical models reviewed were able to predict the final bend angle in a broad laser parameter range. However, the characteristic physical behaviour of the bend angle evolution with increasing heat input, in the form of a lower threshold below which no deformation is induced and a saturation heat input where bending efficiency begins to decline (conditions favouring the SM), was described by neither of them. Before an analytical-numerical model which was able to predict those characteristic stages is reviewed in section 2.5.2, numerical solutions to the laser forming process are discussed.

Over the years, a further understanding of laser forming mechanisms has led to more accurate analytical models, as shown in Figure 2.13 (it should be noted that number in brackets represents the number of references). The error of the bend angle decreased, because thermal and mechanical parameters, such as yield stress, reduction factor of yield stress for elevated temperature and depth of plastic deformation were better described mathematically [29].

2.3 Numerical models for laser forming

Laser forming applied either in form of 2D bending through a straight line laser scan or 3D forming, which involves multiple and/or non-straight laser scan lines, is a very complex process, because variables such as temperature or geometry change in both

time and space (Figure 2.1). Therefore, the numerical approach is often more meaningful for modelling these situations than the analytical approach. In recent years, large scale numerical studies have become more viable consequent to the improvement in computational efficiency. With the release of more user friendly numerical software packages such as ABAQUS, ANSYS® or COMSOL® coupled with faster computers, the use of numerical models as a research tool for both academic and industrial sectors is becoming more prevalent. The investigation of complex processes, such as laser forming in a non-destructive manner in any situation, is extremely useful. However, as with any model, assumptions are made, and the quality of the output data is only as good as the quality of the input data. Several numerical models for laser bending, documented in the literature, are outlined next.

Vollertsen developed a finite difference model [30] for a two dimensional analysis of the process. The temperature dependent material parameters were included in the model by taking values at particular temperatures of interest and linearly interpolating between them. Then those functions were used to relate the temperature to the material properties. The laser beam was modelled as a rectangular shaped heat source, and the resultant 2D temperature field was used to calculate the thermal expansion, strains and stresses in each element. After accounting for the stiffness of the whole sheet, a calculation was made to asses in which elements the stress exceeded the temperature dependent yield stress. Then the elastic strain in those elements was reduced by the amount that exceeded the yield stress. The plastic strain was the amount of strain that exceeded yielding. A loop was initiated which continued with this calculation until there was equilibrium of forces and moments. After the thermal field was computed, the bending angle was calculated from the length of the upper and lower layers of an element in conjunction with the sheet thickness. This model provided a very fast means (seconds) of calculating the effects of various process parameters. However, accurate results (accuracy was not explicitly given) were obtained for the TGM only and materials with low thermal conductivity, such as low carbon steel, through simple boundary conditions chosen. The limitations of this approach led to the modelling with the finite element method (FEM) [31].

Shi *et al*. [7] performed a numerical model with ANSYS® which predicts the bending under the TGM not only transverse (x) but also parallel (y) to the laser scan line. In order to calculate the thermal load, a 3D heat equation was used, where the heat input

represented by the laser beam was assumed to have a Gaussian distribution. The numerical results were within a deviation of 12% of experimental results for both, bending in x- and y-direction. The discrepancy was assumed to have been caused by a varying coefficient of absorption for the laser energy with temperature and some initial residual stresses of the laser bent sample. The fact that the model predicted the distortion parallel to the laser scan line might be of interest in the application of high precision laser forming. The same group performed another FE-modelling approach [32] which again took bending in x- and y-direction into account. This numerical simulation showed the influence of laser power, spot diameter, scanning speed and geometrical parameters of the sample on the bending distortion. The simulation seemed to predict all characteristics resultant from varying input setting parameters, but since a comparison with suitable experimental data is not given, those results were questionable.

Yao's group at Columbia University, New York, developed the most complete numerical simulation of the laser forming process [33-42]. With years, their model was further developed and became more advanced. It allowed a vast variety of phenomena in laser forming to be investigated numerically. In the following, a brief overview of their numerical and experimental work is given in chronological order. The results of some studies are reviewed in more detail in the following sections.

In 2000 Li *et al*. [33] investigated the effect of the strain rate in laser forming on forming efficiency, residual stress and hardness numerically and experimentally. To isolate the effect of the strain rate, a 'constant peak temperature' method was developed. This method established the corresponding laser power for a constant peak surface temperature and laser scan velocity iteratively by numerical simulation. This method should ensure that the effect of temperature on the flow stress is relatively small so that the focus could be set solely on the effect of the strain rate.

In 2001, a further investigation of the laser forming process included the numerical and experimental studies of cooling effects in multi-scan laser forming [34], the deformation along the laser scan path referred to as 'edge effect' [4], laser forming at constant line energy [35] and laser bending of tubes [36]. The model showed good agreement ($< 10\%$) with experimental results in this broad range of applications, mainly because it took into account the temperature dependency of material properties and the strain rate dependency of the flow stress. The model was further developed in 2002 [37] in such a way that the change of microstructure on flow stress was considered for the low

carbon steel samples. This consideration is of special importance for multi-scan laser forming. In the model, the thermal history of the FE was coupled with a phase transformation kinetic model. The microstructural changes, which were taken into account, included the effects of strain hardening, dynamic recovery and recrystallization, superheating and phase transformation. Further studies, performed with this thermal-microstructural-mechanical model were the investigation of sheet metal anisotropy caused by rolling [38], clamping and size effects [39,40], microstructure evolution and mechanical behaviour [41] and the effect of phase transformation on the mechanical behaviour of AISI1010 [42] in laser forming.

The reduction of extensive computation time, while ensuring an accurate solution is a request in all numerical simulations. Yu *et al*. [43] presented a FE-model for a thermo-mechanical analysis of the laser forming process. A rezoning or re-meshing technique (redrawing the fine mesh around the laser beam as it moves) was employed to reduce greatly the simulation time yet still preserve the required accuracy. Two years later, the same group studied the effects of mesh size refinement on temperature distribution and final distortion [44]. In order to increase the accuracy of the simulation, the thermal boundary conditions were calculated by natural heat convection and radiation. All numerical results were within 15% compared with the experiment, which showed the effectiveness of the model.

An interesting study performed by Zhang *et al*. [45] aimed to investigate the minimum temporal and spatial discretization requirements of finite element modelling on the laser forming process. It was concluded that, to obtain an accurate solution for 3D finite element model, the temporal discretization requires at least four time increments per heat source radius and the spatial discretization requires two elements per radius and three elements through thickness.

Those FE-analyses, documented in the literature, were able to predict with good accuracy complex thermo-mechanical processes and deformation in laser forming. However, they are lengthy to set up and require extensive computation time (not stated explicitly). Even though attempts were made to reduce their runtime, this fact would limit their application for example in an iterative approach to laser forming, where fast computation between iterations would be required. Nevertheless, in single pass laser forming (‘single shot’ approach), as applied by Yao’s group, extensive and accurate

time resolved FE-analysis for calibration database and heating conditions are a useful tool, because they can be performed prior to laser forming.

2.4 Previous experimental work supporting analytical and numerical models of 2D laser forming

This section presents a summary of the experimental work done to date in laser forming. The focus was set on research of the effect of main forming process parameters (Figure 2.1) on the deformation induced, with particular interest in the parameters relevant to an iterative laser forming approach, e.g. multiple laser scan passes.

2.4.1 Laser parameters

One of the first experimental papers on laser forming was published by Namba [46] in 1985. The materials investigated were Ti, Al, AISI 304 stainless steel and carbon steel. A defocused CO_2 laser beam was used with travel speeds of 5-15m/min. The deformation obtained was attributed to the steep thermal gradient which results in thermal expansion, thermal stress and plastic deformation. In 1987, Scully [47] determined an empirical relation between the positive bend angle α_b, the power P_l, the transverse speed v_l and the plate thickness s_0, based on earlier work by Masubuchi [48] on flame forming.

$$\alpha_b = \frac{P_l}{s_0\sqrt{v_l}} \tag{2.12}$$

Scully [47] identified in his work an important parameter to analyze and estimate the amount of angular distortion of a plate; it was named ‘heat input’ and is later referred to as line energy (LE), defined as:

$$LE = \frac{P_l}{v_l} \left[\frac{J}{mm}\right] \tag{2.13}$$

It makes sense to consider laser forming process parameters in this way, because P_l represents the laser energy generation per unit time, while v_l affects the laser energy input to the workpiece per unit time. This relation, equation (2.13), was later used by Vollertsen and included in the mathematical expression for the bend angle, equation (2.5), of the ‘Two Layer Model’ [9,10]. Scully [47] showed in his work that the amount of out-of-plane strain increases with heat input (LE) until an optimum, which is different for each plate thickness.

The LE can be varied either by varying the laser power (P_l) and keeping the laser scan speed (v_l) constant or vice versa, equation (2.13). Vollertsen showed that there is a

strong linear dependence of the bend angle on LE [10]. In the experiments carried out, a power law was assumed between the bend angle and the processing speed. A linear dependence was obtained for a 3.5mm sheet with scanning speeds in the range 7-70mm/s. The gradient of the function was found to be -0.63. A negative slope was to be expected, because an increase in scanning speed decreases the process energy. As the bend angle is proportional to the coupled energy, it is expected that the bend angle should decrease linearly with increasing traverse speed. However, at low transverse speed, i.e. conditions favouring the SM, it was found that the bend angle continues to increase with increasing transverse speed until an optimum, where it decreases again. This behaviour may be attributed to the fact that the temperature gradient is increased with increasing velocity and the time for heat conduction in the depth direction of the sheet is reduced. Ultimately, this temperature gradient will result in the difference of the plastic strains between the upper and the lower layer of the sheet being more pronounced and a greater bend angle per unit time may be achieved. From the optimum, where forming is most efficient, the bend angle starts to decrease with higher velocities (lower LE). If the velocity is increased to a very high value, the temperature increase will be small and only an elastically reversible bending may occur. Also of note is the threshold energy of the process, referred to as threshold LE later on, below which no plastic deformation is induced. Therefore the boundary energy which will produce the onset of bending can be related to the temperature the material must reach at the limit of the thermal strain, at the yield point stress [10].

Although the LE as forming process parameter seems to be a useful measure, forming results can be different for identical material and geometry, if the LE is kept constant. Magee *et al*. [16,49] carried out experiments under the condition of constant LE, and showed that when the scanning velocity (v_l) as well as the laser power (P_l) increases proportionally, the bend angle initially increases and then it levels off. Li *et al*. [35] analyzed the physical phenomena taking place under the condition of constant LE and showed the effects of velocity change on temperature, net energy input, strain rate and material flow stress. They found that when the LE is held constant, the bend angle increases with scanning velocity, but the degree of increase reduces with velocity increase, as shown in Figure 2.14. This behaviour was attributed to two competing effects on the flow stress. The high strain rate at high velocity causes the flow stress to increase and at the same time the temperature rises, owing to less heat dissipation at high velocities which causes the flow stress to decrease. At high temperature, the effect

of strain rate on flow stress is more significant and slows the bend angle increase down (Figure 2.14). If the beam diameter decreases under the condition of constant LE, the slope of the bend angle curve was found to decrease in the higher velocity region. These explanations of the bend angle behaviour at constant LE given in the paper by Li *et al*. [35] are questionable. The behaviour shown in Figure 2.14 can be explained more straightforwardly as follows; first, if the laser power and the laser scan speed increase proportionally the temperature gradient through thickness increases and with it the bend angle. Second, if the beam diameter is small, the interaction time is lower, but the intensity (laser power per unit area) is higher which increases the thermal gradient through depth. Therefore the bend angle is larger for a smaller beam diameter (at constant LE).

The energy input by a laser beam to a sample per unit area is called area energy (AE). It extends the 2D description of the heat input through LE, equation (2.13), to three dimensions across the heat affected zone (HAZ) by including the laser beam diameter d_l. This average energy applied to the unit area along the scanning path is defined as

$$AE = \frac{P_l}{v_l d_l} = \frac{LE}{d_l} \quad \left[\frac{J}{mm^2}\right] \tag{2.14}$$

Li *et al*. [35] found for the condition of constant AE that the bend angle is large when the LE is higher and the beam diameter is large, because more energy is put in despite the area energy being the same.

It is evident from these observations that LE and AE as process parameters in laser forming are not ideal, because forming results can be different, despite LE and AE are kept constant and they do not characterize the energy input of the process in a general form. Therefore a more useful process parameter would be the specific energy (SE) of the process, which would include the laser intensity I_l, the interaction time τ and the laser beam area A_l, defined as

$$SE = I_l \cdot \tau \cdot A_l = \frac{P_l}{A_l} \cdot \frac{d_l}{v_l} \cdot A_l = \frac{P_l \cdot d_l}{v_l} \quad [J] \tag{2.15}$$

where P_l is the laser power, d_l the laser beam diameter and v_l the laser scan speed.

Both Masubuchi [48] and Scully [47] found in their fundamental work on laser forming a linear relationship between number of scan passes and the angular distortion. Knowledge of this behaviour is of special importance in multi-pass laser forming. Edwardson *et al*. [50,51] showed in a more detailed study that the bend angle rate decreases with number of laser scan passes. In comparison to the study of Masabuchi

and Scully, thinner plates were used and up to 60 passes per plate induced considerable distortion. The bend angle decrease was attributed to a number of influencing factors, already known from theory [52] as

1. Strain hardening as a result of increasing dislocation density within the lattice at a increasing deformation
2. Section thickening owing to the conservation of volume in the upper surface under the lateral compression
3. Variation in absorption because of coating degradation with increasing pass number
4. Thermal effects, attributed to the elevated temperature, left from the previous pass, which decreases the temperature gradient through the plate
5. Geometrical effects in the form of the transformation of the laser beam to an elliptical shape when incident on an inclined surface for one half of the beam.

Referring to point (4) Cheng *et al*. [34] investigated the effects of forced cooling in multi-scan laser forming under various conditions, i.e. different cooling air pressure, nozzle offset and laser scan speed and laser power. They found that forced cooling greatly reduces the waiting time between consecutive scans and has no undesirable effect on microstructure change and mechanical behaviour. The bend angle increased approximately linearly with laser scan passes (up to 10 passes applied), indicating that the work hardening effect was offset by the softening effect of the repeated laser scans on the 0.89mm thick AISI1010 specimens. Clearly, if multiple scans - as in a practical production process - are applied, substantial waiting time is normally necessary for the workpiece to cool down, so that a temperature gradient can be re-established in the next scan.

2.4.2 Workpiece geometry

The geometry of the laser formed sample affects deformation and thermally induced plastic strain, as has been shown in the past. Some of the studies are summarized next.

It was shown by Masubuchi and Scully [48,47] that the sheet thickness is one of the major variables in the development of the bend angle, equation (2.12). In the ‘Two Layer Model’ for the TGM from Vollertsen [10], the bend angle was related linearly to the inverse of the square of the sheet thickness, equation (2.5). The volume of material to be heated increases with the thickness of the sheet, and therefore the bend angle decreases with sheet thickness for constant heat input. In multi-pass laser forming, the

thickness of the sheet increases with each pass owing to compression of the uppermost layer, decreasing the bend angle rate per pass.

The bending leg, defined as the perpendicular distance from the laser scan line to a clamp or free plate boundary, was found to influence the bend angle because of significant changes in the thermal and mechanical field [49]. If the bending leg is short, cooling of the workpiece is restricted to one side [10] and the temperature gradient decreases and hence the bending decreases. For a long bending leg, gravitational forces act in the form of tensile surface stresses against the thermal induced compressive strain, and diminish the bend angle. For the case of one clamped plate edge, Birnbaum *et al*. [39] found a higher bend angle variation with increasing distance from a clamp than for an unclamped free edge, owing to the additional rigid constraint of the clamp.

Component size effects, such as variation of sheet width and sheet length, on laser induced deformation were investigated by Cheng *et al*. [40]. The results were interpreted in the form of heat sink effect and pre-/post-bending non-uniformity. The heat sink effect, which is the decrease in surface temperature with increasing sheet width (providing a larger heat sink), reduced the bend angle. The pre-bending of the sheet ahead of the laser beam, which was ~ 1/3 of the final bend angle magnitude, was found to be more pronounced in a shorter sheet (constant width), and the opposite was found for the post-bending effect. Generally the bend angle increased for a constant sheet width and increasing sheet length. When both the sheet length and width increase in even proportion, the bend angle increases before decreasing owing to both competing effects.

2.4.3 Material properties

This section names important material parameters in laser forming and their relation to the final bend angle. The understanding of those dependencies is of importance for the final forming result obtained.

The thermal conductivity of a material determines the temperature field and hence the development of thermal plastic strain. The effect of the thermal conductivity on the bend angle has been physically modelled by Vollertsen [1] (Figure 2.9). If the material is a good conductor, such as aluminium-copper alloy (thermal conductivity of $120 W \cdot (Km)^{-1}$), it is more difficult to establish a thermal gradient through thickness and

perform forming in the regime of the TGM. In general, it is better if the material is a relatively poor conductor for TGM laser forming, such as steel or titanium. The role of the thermal conductivity on the SM is slightly different. If the material has a high thermal conductivity, the size of the irradiated area will increase rapidly. Therefore, the average temperature of the material is lower than for a low thermal conductivity material and plastic strain and bend angle are also lower. However, the distinction is drawn as forming will still occur in the regime of the SM (in-plane shrinkage), but almost no bending (TGM) will occur if the temperature gradient is diminished to a large extent by a high thermal conductivity. The thermal conductivity itself is influenced by material strength and age hardening [1]. Clearly there are complex dependencies for the thermal conductivity.

Further work by Vollertsen [10] showed a linear influence of the fraction of the coefficient of thermal expansion and the specific heat times mass density when plotted against the bend angle, showing the influence of the material parameters on the bending deformation. This relation was useful, as the 'Two Layer Model' [1] assumed the same relationship between these parameters, equation (2.5). The amount of forming depends critically on the thermal expansion which was determined from the temperature increase and the coefficient of thermal expansion. It was found that the temperature increase of a volume is indirectly proportional to the volumetric heat capacity [10].

2.5 3D laser forming

The surfaces of many engineering structures are commonly fabricated as doubly curved shapes to fulfil functional requirements such as hydrodynamic, aesthetic or structural; e.g. a large portion of the shell plates of ship hulls or airplane fuselages are doubly curved. A considerable amount of research in laser forming has been aimed at forming those 'generic' complex 3D components and structures for possible application in industry, such as the aerospace, automotive and shipbuilding sectors. Laser forming has shown great potential for the manufacturing of metallic components using a 2D straight line or 3D spatial forming approach, as shown in the following outline. However, in order to advance the process further for realistic forming applications and for straightening and aligning operations in a manufacturing industry, it is still necessary to develop and improve systems for more accurate and repeatable part production.

2.5.1 Fundaments and process design

In engineering applications, surfaces are often classified as singly or doubly curved surfaces. A singly curved surface has zero Gaussian curvature at all points, like the cylinder (Figure 2.15). A doubly curved surface has non-zero Gaussian curvature, like the hyperboloid or the sphere (Figure 2.15). Each requires the application of different forming mechanisms, namely TGM and SM, to induce the required deformation and strain field.

Singly curved or developable surfaces are spherical ruled surfaces which can be unfolded or developed into a plane without stretching or tearing (or alternatively formed into a surface from a plane without stretching, tearing or compression) (Figure 2.16.) Doubly curved or non-developable surfaces require material to be removed, if formed from a flat sheet, as shown in Figure 2.17. The concept of these surfaces for laser forming is shown schematically in Figure 2.16 and Figure 2.17. Given is an example of a developable surface, a part-cylinder and a non-developable surface, a dome or a pillow shape. It can be seen from Figure 2.16 that, for a singly curved, developable surface, the TGM should be the dominant mechanism used to produce plastic bending strains and out-of-plane deformation. For a doubly curved non-developable surface (Figure 2.17) material needs to be removed or shortened (in-plane) in order to allow the deformation to take place. This suggests that the SM should be the dominant mechanism when forming this type of surface. The in-plane plastic shrinkage then accounts for the shortening of excess material, in particular near the edges (at the expense of section thickening). The relation between bending and in-plane strain in 3D laser forming of non-developable surfaces can be further emphasised by considering the mathematical analysis for thin plate theory available in literature [53,54]. For thin plate deformation, deflection $w(x,y)$ is assumed to be equal to the deflection of the mid-plane $w_0(x,y)$. The total strains of deflection can be expressed as follows:

$$\varepsilon_{xx} = \varepsilon_{xx}^0 + \varepsilon_{xx}^1 = \left[\frac{\partial u_0}{\partial x} + \frac{1}{2}\left(\frac{\partial w_0}{\partial x}\right)^2\right] + \left[-z\frac{\partial^2 w_0}{\partial x^2}\right]$$

$$\varepsilon_{yy} = \varepsilon_{yy}^0 + \varepsilon_{yy}^1 = \left[\frac{\partial v_0}{\partial y} + \frac{1}{2}\left(\frac{\partial w_0}{\partial y}\right)^2\right] + \left[-z\frac{\partial^2 w_0}{\partial y^2}\right] \qquad (2.16)$$

$$\gamma_{xy} = \gamma_{xy}^0 + \gamma_{xy}^1 = \left[\frac{\partial u_0}{\partial y} + \frac{\partial v_0}{\partial x} + \frac{\partial w_0}{\partial x}\frac{\partial w_0}{\partial y}\right] + \left[-2z\frac{\partial^2 w_0}{\partial x \partial y}\right]$$

where u_0, v_0, and w_0 are the displacement at the mid-plane, ε_{xx}, ε_{yy} and γ_{xy} are total strains, and ε_{xx}^0, ε_{yy}^0 and γ_{xy}^0 are in-plane strains, and ε_{xx}^1, ε_{yy}^1 and γ_{xy}^1 are bending strains for a given x and y and plate thickness z. Therefore, bending strain is a product

of curvature and distance from the middle surface (mid-pane) whereas in-plane strain is uniform through the thickness, equation (2.16). If the centre of bending is located at the middle surface, the bending strain is zero at the middle surface. The in-plane strain is uniform through the thickness; therefore the strain at the middle surface is the corresponding in-plane strain. When the deflection w_0 (the normal component to the displacement vector), of the mid-plane is small compared with the plate thickness s_0 ($w_0 \leq s_0$), Kirchhoff's linear plate bending theory gives sufficiently accurate results. The in-plane strain and the corresponding in-plane stress can then be neglected, equation (2.16). However, if the magnitude of deflection increases beyond a certain level ($w_0 > s_0$), these deflections are accompanied by stretching the mid-plane. As the ratio of w_0/s_0 further increases, the role of the in-plane strain becomes more pronounced [54].

Two convenient test shapes for ship hulls or aerospace structures are pillow and saddle, both characterized mathematically through a non-zero Gaussian curvature [55] (Figure 2.15). Both shapes are defined by the mathematical equation, given below:

1) Elliptic paraboloid (pillow), consisting of two curvatures with equal sign

$$Z = \left(\frac{x^2}{a^2} + \frac{y^2}{b^2}\right) \tag{2.17}$$

2) Hyperbolic paraboloid (saddle), consisting of two curvatures with opposite sign

$$Z = \left(\frac{y^2}{b^2} - \frac{x^2}{a^2}\right) \tag{2.18}$$

where a and b define the limits of the surface in x and y respectively.

To summarize, for the laser forming of pillow and saddle (non-developable) shapes and of possible industrial applications - for example on ship hulls or aircraft skins - the in-plane strain component is the largest factor in the calculation of the required strain field, equation (2.16), which suggests conditions to be chosen favouring the SM.

The process design of laser forming differs from other shaping processes, such as stamping, rolling or machining of free-form surfaces, in that the laser scanning path is not necessarily related with the desired shape, especially for 3D shapes. Certain regions of the desired shape need to be scanned (with one or multiple passes), but exact scanning paths and orientations, if linear or curved, are not obvious. Therefore, the inverse problem [56] needs to be addressed that is to design process parameters such as

laser scanning paths and heating conditions in terms of laser power and scanning velocity, given to form a desired shape.

Ueda *et al*. [57,58,59] showed in their study one of the first approaches in 3D laser forming, which was based heavily on the former process of flame bending in the shipyard industry. Fundamental problems of the process in this 'single shot' approach were defined as, first, what type and how much plastic strain should be applied on which location, and second, to determine the proper heating conditions in order to obtain the desired plastic strain. For the strain field calculation, an FE-model was used, which assumed the plate to be pressed to the desired form of a pillow shape by a spherical press. The 'spring-back' effect, known from the process of die forming, corresponded to the elastic deformation, induced during laser line heating. Based on the FE-model and experiment, Ueda *et al*. investigated the relation between in-plane strain and bending strain, and pointed out that bending strain is proportional to the product of thickness and curvature, and in-plane strain is proportional to the square of the curvature. Therefore the ratio of bending strain ε^1 to in-plane strain ε^0 can be expressed as

$$\frac{\varepsilon^1}{\varepsilon^0} \propto \frac{s_0}{\kappa} \tag{2.19}$$

where s_0 is the thickness and κ the curvature. Equation (2.19) shows that the relative effect of bending strain over in-plane strain increases with increasing thickness, and the relative effect of in-plane over bending strain increases with curvature, which corresponds with shell theory [54]. It is also visible from equation (2.19), that the contribution of in-plane strain becomes predominant as the thickness becomes small. Knowledge of the relation between bending strain and in-plane strain was necessary for subsequent steps, i.e. determination of scan path location and heating conditions along the scan line. They concluded that for successful and efficient plate forming by line heating, both bending and in-plane inherent strains have to be combined suitably and that scan paths should be applied in regions with *maximum* (absolute) compressive principal strain, normal to the direction of principal strain, because in laser forming highest (compressive) strains are induced normal to the scan path. Yao *et al*. [60,61] postulated that the scan paths should be perpendicular to vectors comprising *minimal* principal strain (smallest of either in-plane or bending strain). Both approaches have been experimentally validated.

Furthermore, Yao *et al*. [60,61] determined heating conditions along the scan path using a database, established by an FE-model, relating in-plane and bending strain to laser power and scanning velocity. The scan path spacing between two adjacent paths was found to be crucial because the FE-database was established for independent laser scans. Therefore, their HAZ should not affect each other. Generally, the smaller the spacing the larger the strains and the higher the forming accuracy which can be obtained. As a rough guideline, the spacing between two adjacent scan paths should not be smaller than d_{paths}, which is defined as

$$d_{paths} = \frac{\varepsilon_l d_l}{ave(\varepsilon_2^i)} \tag{2.20}$$

where ε_l is the strain generated by laser forming and ε_2^i is the average principal *minimal* strain over the spacing and d_l the laser beam diameter [60].

Hagenah *et al*. [62] investigated in their study solutions for the detection and closed loop controlled correction of bending angles and warpage. They derived some rules of thumb for the development of irradiation strategies for the removal of dents and the adjustment of angles: amongst others, that irradiation paths should follow the contour of the deformation, more energy should be introduced to the outer part of the deformation by smaller distances between irradiation paths, forming should take place from the outside towards the centre of the deformation. Higher laser beam power in combination with large beam diameters and cooling between intervals was found to be most successful.

Kim *et al*. used [63] in their study only geometrical information for process planning, which was based on the concept of planar development and angular defect [64] rather than complex stress-strain analysis, mentioned previously. The surface was decomposed into a combination of plane patches first. Then forming parameters such as scan paths, bend angles and shrinkage along the forming line, were calculated using an FE-established database which related bend angle and shrinkage to laser power and travel speed. This simplified approach was validated experimentally by the forming of pillow and saddle shapes (of coupon size 30x30x0.8mm^3) with relative success.

Several predictive techniques are available in 3D laser forming, ranging from simple empirical models that estimate angle of deflection from a single scan as a function of power and velocity to comprehensive physical based FE-models that provide

information about the internal stresses and strains [60,61] to database search algorithms [65] and neural networks [66,67,68] that provide a method of interpolating between empirically (or otherwise) determined processing results. All approaches applied a single pass strategy ('single shot approach') to form the desired shape, which brings along foreseeable disadvantages and problems, compared with an *iterative* approach, where the sample converges in multiple passes to the desired shape, explained in more detail in section 2.5.2. A single pass implementation using FE-simulation will produce accurate results but may run for hours or days. Despite the most accurate FE-analysis, laser forming is unable to duplicate exactly the strain field calculated. As shown in the preceding sections, it is not realistically possible to get exclusively in-plane or bending strain using a laser forming mechanism. A thermal gradient through the thickness can be established even if the beam diameter is large and the transverse speed low, in particular for materials with low thermal conductivity such as low carbon or mild steel. If a thermal gradient is present there will be an asymmetry in the in-plane plastic strains, generated through the thickness and hence net bending strains will develop, which may cause out of plane deformation. Similarly, in the regime favouring the TGM asymmetric in-plane strains will develop in the thermally plastified region through thickness (i.e. significantly larger plastic in-plane strains near the top surface compared to the bottom surface). Additional unforeseeable non-uniformities in the process include the reduction of bending deformation on curved scan lines [69,70], unknown residual stresses, originating from manufacturing, transport and storage, and material non-uniformities, such as anisotropy caused by preferential texturing generated during the rolling process [38].

2.5.2 Iterative laser forming

As mentioned in section 2.5.1, all predictive methods will yield in some inaccuracy, owing to the inability to control and fully predict factors influencing the laser forming process. An *iterative* approach to laser forming is more tolerant to 'unknown' process parameters - amongst others bend angle degradation with multiple passes [6,50,51] or material non-uniformities - and offers the possibility of compensating modelling inaccuracies through employing plate shape measurement (feedback control) between iterations. Subsequent processing conditions can then be adjusted to converge to the desired shape, which enhances process accuracy and repeatability.

Reutzel *et al*. [71,72,73] showed in their studies for the first time an iterative process design that incorporated sensing and control techniques in the form of a shape measurement between subsequent iterations, to converge to the desired shape. The input for the scan path planning algorithm was the difference or error between the desired and actual shape (shape residual). To determine laser parameters along the heating line, a simple linear relation between scanning velocity and bend angle (constant laser power) was used, based on Vollertsen's 'Two Layer Model' [9]. The proportionality constant for material and laser settings over the chosen parameter space was determined from a series of line path experiments. Primarily forming results on 20mm thick A36 steel specimens, based on line heating by superposition, showed reasonably good accuracy for the shapes chosen (twisted and tapered valley), considering assumptions made in this first approach to iterative laser forming.

The idea of the iterative process design for 3D laser forming was applied and further developed by the group at Heriot-Watt University in Edinburgh. A short historical review about their laser forming project is given next.

The activity in the area of laser forming started at Heriot-Watt University with a dynamic in-process distortion measurement of a 2D laser scan [74], to further understand laser forming during a single laser scan. The shape measurement system at Heriot-Watt University was able to monitor transient distortions of continuous surfaces using coherent fringe protection. Results of the measurement (locations at the start, middle and end of the laser scan line of the Ti-6Al-4V specimen) in terms of the transient evolution of the surface shape during and after laser forming were predicted by an FE-model, which was developed in ABAQUS. This project was carried out in collaboration with the Materials Science Department of Rolls-Royce (University of Cambridge) and the Department of Engineering at the University of Liverpool.
First 3D iterative forming attempts were carried out in collaboration between Heriot-Watt University and the Laser Group at the University of Liverpool. It was an incremental adaptive approach for subsequent passes utilizing the error between the current and desired geometry to give a new scan strategy [75,76]. In the adaptive system created, the use of sensors, i.e. shape measurement between each iteration, provided controlled feedback and allowed the adjustment of process parameters accordingly. Measured and target (pillow shape) surfaces were defined with a Bezier curve and lines of constant gradient were determined. From different scan strategies investigated to

form a pillow shape, such as scanning either perpendicular to the contour plots of resultant gradient vector or along the contour lines of constant height of the shape (90° rotated to lines of constant gradient), the latter was found to give the most promising forming result. The energy distribution was chosen based on the sum of bending and in-plane strains resolved in the direction of the principal gradient; after the first pass, a scaling factor between measured and predicted deformation was determined for subsequent iterations. However, between bending and in-plane strain was not specifically distinguished and laser parameters (scanning velocity) were determined with an experimental database for the TGM only. The accuracy of the results obtained suggested that a distinction has to be made between the two mechanisms (TGM and SM), which means using the TGM for accurate shape definition and the SM to account selectively for the additional material.

The iterative approach to 3D laser forming was continued at Heriot-Watt University. McBride *et al*. [77,78] developed an analytical-numerical model of the generation of bending strains in laser forming. The model was extremely useful to understand key elements of bending behaviour, i.e. the interplay between TGM and SM, and gave a clear insight into the parameters most important in the practical control of laser forming, which fed into the development of our iterative process design [78,79] for 3D laser forming, explained in more detail in section 2.5.3. The analytical-numerical model is briefly described next.

Key elements of behaviour in laser forming were modelled in four decoupled stages; first, the gradient of maximum temperature through thickness caused by a CW laser spot is calculated analytically with a 1D heat flow model [80]

$$T_{step}(z,t) = \frac{2q_0}{k}\sum_{n=0}^{\infty}\left[ierfc\left(\frac{2ns_0 + z}{2\sqrt{Dt}}\right) + ierfc\left(\frac{2(n+1)s_0 - z}{2\sqrt{Dt}}\right)\right] \qquad (2.21)$$

where z is the depth, t is the time, q_0 is the power per unit area, s_0 is the plate thickness, k is the thermal conductivity and D the thermal diffusivity. The temperature after the laser beam has passed $[t > \tau]$ is

$$T_{pulse}(z,t) = T_{step}(z,t) - T_{step}(z,t-\tau) \qquad (2.22)$$

The maximum through thickness temperature profile calculated for a top hat and Gaussian heat source is shown in Figure 2.18. The upper half of the material has a gradient in T_{max} while the maximum temperature profile in the lower half is perfectly flat. This T_{max} profile possibly justifies Vollertsen's choice of two layers in the 'Two

Layer Model' approach [10], and the conclusion made that all the thermal expansion of the upper layer is converted into plastic compression.

The use of the peak temperature rather than the temperature at an instant removed the need for an assumption regarding the extent of the plasticized zone. Based on the peak temperature profile through depth, the induced stress profile on rigidly constraint cooling is calculated. Figure 2.4 shows the principle of thermally induced stress in laser forming applied in the model. As the material temperature increases, the stress in the heated area follows the thermal-elastic stress curve until the local yield stress σ_f is reached (Figure 2.4, point [2]). If the temperature increases, further stress is maintained at $-\sigma_f$, leading to an induced stress on cooling (Figure 2.4, point [3]) which causes the deformation of the material. This induced stress, which saturates at the material yielding in tension (Figure 2.4, point [5]), is applied to the cold material to obtain localized bending and in-plane shrinkage, whereas the net force F_x gives the shrinkage $\bar{\varepsilon}_x^0$

$$F_x = b\int_{-\frac{s_0}{2}}^{\frac{s_0}{2}} \sigma_x(z)\,dz \qquad \bar{\varepsilon}_x^0 = \frac{F_x}{EA} \tag{2.23}$$

and the net bending moment M_B the curvature κ

$$M_B = b\int_{-\frac{s_0}{2}}^{\frac{s_0}{2}} \sigma_x(z) z\,dz \qquad \kappa = \frac{M_B(x)}{EI} \tag{2.24}$$

where A is the area and I the second moment of area cross section (with width b). By integrating the curvature κ across the heating line, the resultant bend angle is obtained (the limits $\pm d$ must be chosen to include the entire region of induced curvature) [77].

$$\alpha_b = \int_{-d}^{d} \kappa_y(x)\,dx \tag{2.25}$$

The calculated plate bending, equation (2.25), contributes a linearly varying stress distribution through depth. Adding the thermally induced stress (based on the maximum through thickness temperature T_{max}), to the linearly varying bending stress (calculated from the final bend angle in equation (2.25)) allowed a prediction of the transverse residual strain profile through thickness, which is compared with measured data and discussed in more detail in Chapter 6.

Figure 2.19 shows that the model was able to predict both curvature or bend angle (TGM) and in-plane strain or shrinkage (SM) in terms of area energy or line energy simultaneously. The bend angle curves (Figure 2.19[c]), show characteristic behaviour such as threshold LE, near linear operating region and saturation LE (where the bend angle drops off). For line energies above saturation LE the SM becomes predominant

and shrinkage more efficient (gradient of the shrinkage graph increases) (Figure 2.19[d]) at the expense of a decrease in bend angle (TGM). Modelling both effects (bending and shrinkage) simultaneously enhanced the understanding of this interplay between TGM and SM in such a way that higher LE favours in-plane strain while lower LE favours curvature.

Compared with the experimental results, the model underestimated the bend angle and shrinkage, and threshold and saturation LE. This underestimate originates from its assumptions and simplifications, such as 1D temperature field, no spatial heat diffusion, fully-constrained heating and cooling and temperature independent material parameters. However, the evolution of the bend angle and shrinkage profiles with LE (Figure 2.19[c-d]), and the physical behaviour were predicted well.

The main advantage of this analytical-numerical model, compared with other analytical or FE-models reviewed in section 2.2.3 and section 2.3 is that it delivered an insight into the laser forming process itself through the description of transient stages between the two mechanisms (TGM and SM), rather than calculating the bend angle only at the end of the process. This insight contributed significantly to the understanding of the influence of important process parameters on laser forming and the interpretation of calibration experiments (section 2.5.3). This analytical-numerical model was the basis on which the iterative laser forming (ILF) process for uniform thickness plates at Heriot-Watt University was built. The next section describes this process in the form inherited in this study. It is the main objective of this study to modify and develop this ILF process further to the forming of plates of varying thickness (section 3.1).

2.5.3 Iterative laser forming process at Heriot-Watt University

The ILF process at Heriot-Watt University was developed by McBride *et al*. [78,79] and applied to uniform thickness plates. The overall strategy of this ILF process is shown in Figure 2.20. The process aims to produce the required strain field in terms of curvature and in-plane strain to form the desired shape. Both are determined independently from each other. At the start of the process, the measured and target shapes are defined in terms of gradient and curvature by using an n^{th} order Legendre polynomial to approximate the sample surface. After that, the shape residual in terms of Δh (which is the difference in surface heights) is calculated by subtracting target and measured shape. Further, changes in curvature ($\Delta\kappa$) and in-plane strain ($\Delta\varepsilon$) are determined, which are

required to transform the current shape into the target shape. If the shape residual Δh meets the required accuracy, the iterative process is stopped. The typical accuracy is ~ 0.2mm *rms* as a result of shape measurement error or assumptions and nature of the ILF process design. However, because of the sample history prior to laser forming, this maximum achievable accuracy may vary to a greater or lesser extent. The curvature change $\Delta\kappa = \kappa_0 - \kappa$ is calculated by taking numerical second derivatives of surface heights of measured and target shapes over a pre-defined x-y grid and subtracting. The change in in-plane strain $\Delta\varepsilon$ is determined independently with a differential geometry analysis [79], because it varies quadratically with deflection, equation (2.16), and therefore cannot be obtained with Δh alone. The resultant in-plane strain field was corrected by adding a radially-varying, compatible strain field to remove all tensile strains, because only compressive in-plane strains can be induced by laser forming. For uniform thickness plates, this analytical method of the in-plane strain computation was chosen for its computational and experimental efficiency.

The required curvature κ and in-plane strain ε are then projected onto a predefined scan grid (Figure 2.20). Instead of forming along the lines of principal curvature and strain, curvatures and in-plane strains with arbitrary principal axes were generated from transverse strains and curvatures, developed on predefined scan lines. This transformation was achieved by noting that an arbitrary in-plane strain has three degrees of freedom $(\varepsilon_{px}, \varepsilon_{py}, \gamma_{pxy})$. Hence an arbitrary strain field can be produced by adding three or more unidirectional strains, each with a different principal axis [81]. Exactly the same process was used for bending, which has a set of equivalent relationships. The transformation matrix is shown in more detail in the Appendix A 1. Thus the scan lattice chosen comprises four fixed scan directions at 0˚, 45˚, 90˚ and 135˚ to the x-axis in order to simplify scan line geometry and strain history between subsequent iterations. This fixed scan path approach also allows the calibration for the effect of repeated passes on the bend angle. The approximation of principal strains by superposition of the four independent strains is shown in Figure 2.21.

Heating conditions (fixed laser power, fixed laser beam diameter and variable laser scan speed) are obtained from an experimental calibration database for bending and in-plane strain [77]. To relate curvature (out-of-plane strain) to LE, a single laser scan was applied in the middle of a clamped square token (Figure 2.22) and the bend angle was measured before and after the laser scan. This procedure was repeated five times and the

mean of all bend angles measured was taken. For the in-plane strain calibration experiments, circular tokens were clamped in their centre with a bolt and radial laser scans were applied (Figure 2.23[a]). To minimise the intrinsic asymmetry of the process, a path strategy, shown in Figure 2.23(a), was applied. Starting at the outer edge of the disc in (1), a linear path was heated at the forming feed rate until it reached the selected radius length. Then, because no laser power control variation is allowed during a scan without introducing a dwell in the laser power, a 180° circular path and a straight radial scan was performed at feed rate fast enough to ensure a LE below the threshold (~ 5J/mm) until (2). The same procedure was then repeated until (1) was reached again. This sequence was repeated for all 16 radially varying scan lines to complete one sequence (Figure 2.23[b]), followed by a shape scan. In order to avoid any interference with previous laser scans, each sequence was performed with a shift of the starting point of a few degrees. From the height of the dome shape, the shrinkage per sequence and finally the shrinkage per pass were calculated. Figure 2.24 shows the experimental calibration graphs for low carbon steel (Figure 2.24[a-b]), and aluminium-copper alloy (Figure 2.24[c-d]), for tokens of different thickness, which were done for the 3D forming trials presented in section 3.3. These calibration graphs are already shown here to clarify the description of the ILF process. The graphs in Figure 2.24 show material specific characteristic behaviour for the bend angle (threshold LE, near linear region and saturation LE), as it was physically predicted by the analytical-numerical model (Figure 2.19[c]). For the in-plane shrinkage an almost constant linear increase over the whole LE-range applied would have been expected (Figure 2.19[d]). This behaviour is visible in Figure 2.24(b) and (d) for thicker tokens, but not as clear for thinner tokens as shown in Figure 2.24(a) and (c).

The heating conditions in terms of LE were calculated using a linear approximation to the working region of the measured bending and shrinkage calibration curves in Figure 2.24. The laser scan speed (for constant laser power and beam diameter) as a final control parameter was generated as a G-code file to drive the CNC (Computed Numerically Controlled) bed automatically along the fixed laser scan lattice.

A ‘bending’ scan was applied first on the top surface of the plate, followed by a ‘shrinkage’ scan on the bottom surface of the plate, which provided an accurate and stable solution [78,79]. After each iteration, the process restarted (Figure 2.20), by adding the feedback loop until the required accuracy is met.

The principle of the iterative process design is based on sequentially calculating the shape residual between the measured (current) shape of the plate, and the target shape. The mathematical description of relevant target shapes, such as pillow and saddle shape (section 2.5.1) was experimentally implemented here. Figure 2.25 shows an example of a pillow shape with uniform thickness, which converges towards the target shape as the number of iterations increases. The left-hand column in Figure 2.25 shows the measured shape in the initial state, after 2 iterations and in the final state. The residual error, which decreases as more iterations were applied, can be seen in the right-hand column. At the final stage, after 4 iterations, the shape residual is ideally close to the maximum forming accuracy of the process.

2.5.4 3D Laser forming applications

Laser forming has great promise to become an inexpensive and flexible mainstream manufacturing process for both rapid prototyping and manufacturing applications. A typical application might call for small secondary deformations, i.e. shape tuning or distortion correction of formed, machined or welded components [82]. In the following section, a brief survey of laser forming applications and their potential to be applied in an industrial process is given, with the focus on forming varying thickness plates and distortion correction, which are relevant to this study. A more specific overview of the industrial potential of laser forming can be found in [6].

In the past, attempts were made to analyze varying thickness plates [83,84] in particular, but analytical solutions have been sparse and *ad hoc*, owing to inherent difficulties in mathematical treatment. For instance, Zenkonur [85] gave an exact solution for the bending of thin rectangular plates with uniform, linear and quadratic thickness variation based on classical thin plate theory [54]. However, for the bending of varying thickness plate caused by laser irradiation few references have been found, owing to the complicated thermo-elastoplastic process mechanism.

With the aim of implementing laser forming in the shape tuning of compressor air foils and complex 3D geometries with large thickness and curvature change, Cheng *et al*. [86,87,88] performed an analysis and process synthesis of tapered-thickness plates. In the same context, laser metal forming was discussed as a reconditioning and modification tool for advanced gas turbine components in an overview of Alstom's reconditioning capabilities [89]. Cheng *et al*. [86-88] showed in their experimental,

numerical and analytical study that, with increasing plate thickness, peak temperature decreases while the temperature gradient and bending rigidity increase. The interaction between those three competing effects causes the final bend angle trend. It is indicated by the Fourier number, equation (2.11), that there may be a transition between TGM ($F_0 < 1$), favouring thicker sections and SM ($F_0 \geq 1$), favouring thinner sections. Heating conditions were obtained from a thickness-dependent FE-database and laser scan paths were determined by vector averaging the in-plane and bending strain. After those extensive FE-analyses prior to laser forming, tapered plates were formed in a single pass to pillow and saddle shape with reasonable accuracy [86,87] (~ 0.8mm error for pillow shape with 3.5mm target deflection, and ~ 1.4mm error for saddle shape with 5mm target deflection). Furthermore, Cheng *et al*. [88] applied their process to correct the shape of an extruded and formed compressor airfoil (nickel-based alloy). The experimental result presented was promising, although there were still many practical issues to be solved, like the complexity of the varying airfoil cross section in combination with the airfoil bow, including bending, shrinkage, wrapping and twisting, or the challenge to find lasing parameters which may not degrade microstructure and properties critical to performance.

Within the EU-founded EcoShape (Economic Advanced Shaping for Integral Structure) project, a laser forming process for the laser beam bending of complex fuselage aluminium panels in the aircraft industry has been proposed [90,91]. The project's consortium consisted of ten partners with both academic and industrial backgrounds, such as Airbus, EADS or the Technical University of Munich. The aim was to build up the fundamental expertise for an industrial manufacturing process performing most of the production steps in flat condition due to a minimum of machining costs, technological complexity and a maximum of robustness and reliability. The influences of single structural elements of the fuselage panels, such as stringers and pockets, and the metallurgy and mechanical behaviour after laser forming were studied. For an industrial upgrade, the process was integrated into a discrete control loop, which used the forming result of the previous laser scan path to determine the laser parameters for the following. The conclusion after first 2D forming attempts with a prototype system (Figure 2.26[a]) of test specimens with different geometrical complexity, ranging from uniform thickness plates to plates with welded stringers and pockets (Figure 2.26[b], it should be noted that the red regions are welds) was as follows: (a) concerning the material properties, laser forming showed high potential for the implementation into the

production of the aviation industry (the material used was representative of an aluminium-alloy of the 6xxx group); (b) the efficiency of laser forming in comparison to conventional production processes, e.g. stretch forming, indicated its economical potential for the future; (c) but the influence of the non-uniform plate thickness and residual stresses around the weld seams in particular (Figure 2.26[b]) caused substantial twisting of the specimen. Further work to address these uncontrolled distortions was not undertaken, because in 2008 this project was stopped owing to the emphasis and increasing application of composite materials in the aircraft industry.

Distortion induced during welding operations is a common problem in industry. The fundamental cause of the welding induced distortion is the non-uniform heating of the material during the welding process, which in turn produce plastic strains and residual stress caused by the mismatch of thermal expansion in the weld and surrounding material. The correction of distortion, for example in the shipbuilding industry, remains a significant issue and requires up to 25 man hours' straightening rework per tonne. During the last few years, several reduced-distortion welding techniques have been proposed. These methods can be classified into pre-process, in-process and post-process methods. Pre-process approaches attempt to optimize welding conditions to balance residual stress. In-process approaches aim to minimize residual stress during the welding process, for example through thermal tensioning with torches. Most of these methods provide pre-tensioning through mechanical or thermal means to compensate for the welding induced mismatch of thermal expansion. They have been investigated in more detail in the SEALS (Stress Engineering Applied to Large Structures) programme [92,93,94], which aimed to develop stress engineering techniques, i.e. global and local mechanical tensioning and thermal processes, to control and/or manipulate the welding stress and therefore distortion. Another possible way to remove welding induced distortion is through thermal or mechanical straightening after the welding process. Compared with mechanical straightening, thermal straightening is the preferred method because the material is handled much more gently while shape is being altered. Laser forming, as shown in this study, could provide a promising and repeatable approach to reduce welding induced distortion. Only a few investigations have been taken to date to make use of laser forming as a post-process tool to remove welding induced distortion. Cheng *et al*. [95] showed in his study on three different bead-on-plate laser weld paths (straight, curved and circular) that the forming strategy proposed can reduce not only distortion, but also the tensile longitudinal residual stress on the welded surface. Scan

paths were determined based on the magnitude and direction of the bend angle and the longitudinal residual stress, measured for each specimen separately with X-ray diffraction ($\sin^2\psi$-method). They proposed to apply laser scan paths along the weld on the bottom surface to remove angular distortion (TGM). Scans to remove longitudinal distortion with BM laser forming should be applied on the top surface with scanning paths perpendicular to the weld path. However, the feasibility to remove distortion by laser forming was shown, even though the complexity and effort for each specimen was immense (residual stress measurement). This approach was again single pass laser forming, but through the residual stress measurement the initial state of the samples was known and thus accommodated for.

Kim *et al*. applied laser forming to flatten an intentionally induced protrusion of a sample [96]. The protrusion was produced by pressing a steel ball into the sheet. Therefore, thermally induced, complex residual stress fields, as they can be found in a distorted plate after welding, were not present, which question the capability of their strategy and approach for laser straightening.

2.6 Metallurgy

This section presents an overview of the studies done to investigate the mechanical properties and microstructure of low carbon steel and aluminium alloy after laser forming. If laser forming is to be used in an industrial manufacturing process, it is extremely important to characterize fully its effect on material performance and adjust the process parameter envelope appropriately.

Some experimental studies have been carried out on the effects of laser forming on the material and in particular on low carbon steel and aluminium alloy specimens [97-106]. Generally, rapid heating and cooling cycles can cause severe microstructural changes such as phase transformation or dynamic recrystallization in the heat affected zone (HAZ). These effects can accumulate if multiple laser scan passes are applied. A summary of the more relevant publications to this study are presented next.

Ramos *et al*. [97] studied the microstructure and through-thickness microhardness of aluminium alloy alcad-AA2024-T3 specimens of thickness 0.9 mm. They observed a variety of microstructural changes, such as recrystallization of finer grains in the upper region of the sheet, dispersoid precipitation at grain boundaries, hot tearing and partial melting around the recrystallized grain boundaries and melting and resolidification of

the material below the alclad layer for cumulative area energy densities (CAED) in the range 25 to 133 J/mm^2, where

$$CAED = N \cdot \frac{LE}{d_l} \tag{2.26}$$

and N is the number of laser scan passes and d_l is the laser beam diameter (mm). Merklein *et al*. [98] investigated the effect of laser forming on the microstructure of 1 mm thick sheets of aluminium alloys AA1050 and AA6082 (-T41 and -T61) for just two specific laser forming conditions. The formation of dislocation structures was observed in the microstructure at one and 30 laser passes. The through thickness hardness was measured after 30 laser passes, and was found to be reduced most significantly for the artificial aging (-T61) heat treatment.

Fan *et al*. [41,42] showed in his numerical and experimental study on AISI1010 samples grain refinement in the HAZ, adjacent to the laser scanned surface. Owing to the high temperature and deformation there, recrystallization takes place and carbide particles are dissolved from the pearlite. In forming conditions favouring the TGM, no grain refinement was found on the bottom surface. Recrystallization can reduce work hardening and dislocation of particles, and therefore decreases the strength and hardness of the material. An extended HAZ was visible under conditions of higher power and scanning speed. Li *et al*. [35] noticed an increase in hardness with increasing plastic strain, owing to work hardening from the high bending deformation in multi-pass laser forming. The non-homogeneous microstructure around the boundary of the HAZ was found to be the location of significant stress concentration when experiencing impact loads [99].

Thomson and Pridham [100] performed tensile tests on 1 mm thick low carbon steel specimens laser formed with single passes in an unspecified LE range. Shen and Yao [101] performed tensile tests on 2mm thick low carbon steel components in a restricted LE range from 20-33 J/mm with one, two and three passes. Both observed an increase in yield stress and a decrease in ductility with increasing laser energy input. An increase in fatigue life was also observed [101,102,103]. Edwardson [6] observed changes in the microstructure texture and the presence of carbon dissolution for 1.5 mm thick low carbon steel formed with LE 14, 25 and 38 J/mm at one, 10 and 20 passes. Again, the hardness was observed to increase with heat input, including at the bottom surface owing to cold work.

Cheng *et al*. [38,104] presented research on the effect of material anisotropy on the laser forming process. Cold rolled sheet metal exhibit anisotropic properties, which are mostly caused by preferred orientations of grains, developed during rolling reductions. The anisotropic index or R-value of a material in a particular orientation, i.e. the ratio between the strain in width and thickness direction of the sheet, was determined using an ASTM standard tensile test. It was found that there was a significant difference in the laser forming characteristics of the cold rolled AISI1010 mild steel, depending on the orientation of the scan line to the rolling direction. The anisotropic effects increased with increased rolling reduction, i.e. thinner materials, and it was shown that, at higher temperature, the anisotropic effect decreased relative to deformation.

Microstructural changes caused by laser forming significantly affect the corrosion performance, as shown in the study of Liu [105,106] on aluminium-alloys and ferritic and austenitic stainless steel. Through the laser induced sensitisation, various precipitates formed at the grain boundaries in the HAZ and laser-bent zones, which decreased the corrosion performance in the form of severe inter-granular corrosion.

The input CAED and LE ranges quoted above are specific to the laser wavelength and surface coating used in each study and cannot be generalized to other laser forming systems. The variation observed in tensile properties and hardness were not related to specific LE ranges nor related to overall material suitability in service. Further, the tensile tests were restricted to three laser passes (or less) due to the difficulty of increased specimen deformation with higher number of passes, and the applied LE ranges did not cover both the TGM and SM forming regimes: an understanding of both is required for iterative laser forming of general 3D shapes, including non-developable surfaces.

2.7 Residual stress

The forming of the sheet material in laser forming arises from the setting up of complex residual stress (RS) fields associated with the induced thermal gradient. It is well known that microstructure together with achieved residual stresses, critically control the mechanical properties, especially fracture, fatigue behaviour and corrosion resistance of the material [107]. If laser forming is to be used in an industrial process, it is of critical importance to characterize these residual stresses as a function of process parameters,

such as LE, and to gain an insight into the mechanism of the formation of the final geometries.

Some studies have already been carried out to map the RS after laser forming around the heat affected zone (HAZ) [108,109,110]. Topić *et al*. [108] measured near-surface RS with lab X-rays ($\sin^2\psi$-method). They found higher compressive stress along the laser scan path than in transverse direction. One sample where multiple laser scan passes were applied (5 scans at three locations with no overlapping) showed relaxation of the near-surface RS compared with samples scanned only once. The RS of the multi-pass sample was not significantly different compared with that of rolled steel plates (parent material).

Studies performed with high energy synchrotron radiation or neutrons showed that directly below the laser scan path longitudinal strains are tensile and dominant, while normal strains are compressive and transverse strains tensile [109,110]. The residual strain is most significant in the longitudinal direction, because the shrinkage as a consequence of inhomogeneous temperature distribution is impeded to a much larger extent than, for example, in the transverse direction. However, deformation in laser forming arises from the gradient of thermally induced transverse plastic strain through the material. Therefore, the distribution and understanding of the transverse residual strain through thickness is of particular interest.

Topić *et al*. [109] performed through depth synchrotron strain mapping on a section, cut from a 8mm thick WA300 steel sample which was laser formed with 3 passes at LE = 133.3J/mm. The measurement showed a maximum transverse strain of about -310μstrain on the laser scanned surface and +190μstrain on the bottom surface. The strain through thickness varied between tension and compression with a maximum of about +450μstrain at a depth of ~ 1.9mm from the top surface. However, the measurement setup (white polychromatic synchrotron beam and small Bragg scattering angle 2θ) accompanied by the elongated gauge volume (GV) did not allow through thickness strain scanning of thinner samples.

Later, Venter *et al*. [110] measured the RS with neutron diffraction of a small section cut across the HAZ of the sample measured previously [109] (LE = 133.3J/mm, 3 passes). It was shown, that the residual strain relaxed to about 50% through this

sectioning. The neutron measurement was done across the heat affected zone (HAZ) at five different positions through the depth of the 8mm thick samples. It included specimens scanned with one, two and three laser passes at the same LE (133.3J/mm). It was shown that the RS decreases in magnitude with the number of laser scan passes, and for the single laser power investigated, a correlation between RS state and microstructural evolution, determined with optical microscopy, was found in both studies [110,108]. The residual strain of d_0 cubes, which were EDM wire cut from the HAZ of a sample scanned at LE = 133.3J/mm, 3 passes, showed no significant changes in lattice-plane spacings compared with parent d_0, owing to the heat input applied (strain variation measured was within 100μstrain).

2.8 Summary

The literature survey showed that a considerable amount of work has been done on 3D laser forming of uniform thickness plates. Nearly all those studies were based on single pass laser forming, requiring extensive FE-analysis prior to laser forming. An iterative laser forming approach, which did not require FE-analysis because it was restricted to uniform thickness plates, was developed at Heriot-Watt University. The effect of laser forming on the metallurgy of low carbon steel and aluminium-copper alloy specimens has also been reported, but the heat input in the form of CAED and LE ranges was specific to the laser wavelength and surface coating used in each study and cannot be generalized to other laser forming systems.

Therefore, this work will extend the iterative laser forming approach to plates of varying thickness. The effect on mechanical properties, metallurgy and residual stress after laser forming will be investigated, with the emphasis on single and multiple laser scan passes for a wide laser line energy range. Those investigations are brought together in Chapter 7, where the industrial potential of this iterative laser forming approach will be demonstrated by the removal of welding induced distortion.

2.9 Figures

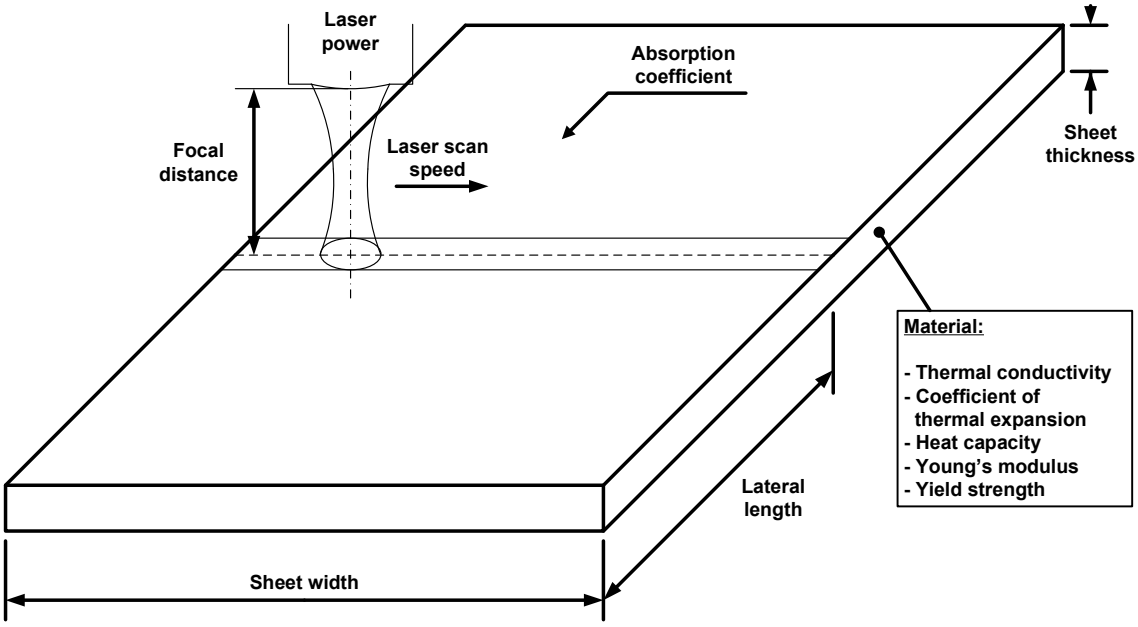

Figure 2.1: Parameters influencing the laser forming process, after [1].

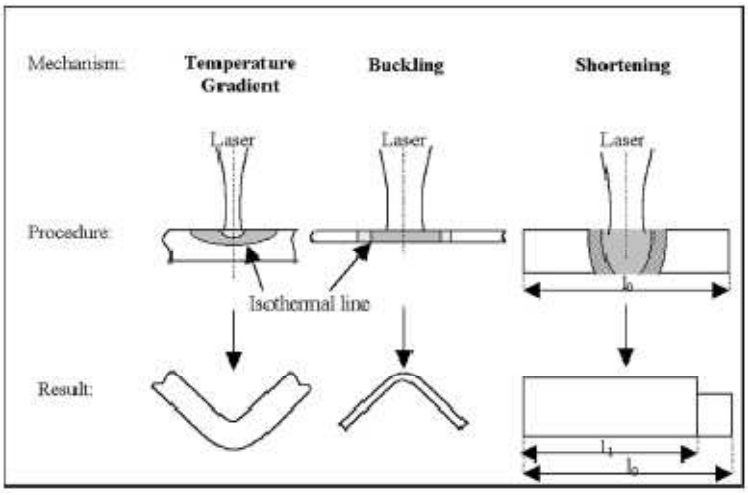

Figure 2.2: Laser forming mechanisms [6].

Mechanism	Procedure	Forming efficiency	Results
Temperature Gradient Mechanism (TGM)	Spot diameter ≈ thickness Higher traverse speeds Applicable to thin sections	~ 1-3˚ bending per pass	High control Low efficiency
Shortening Mechanism (SM)	Spot diameter ≥ thickness Applicable to stiff/geometrical restricted geometries	μm shrinkage per pass	Shortening thickening
Buckling Mechanism (BM)	Spot diameter > thickness Lower traverse speeds Applicable to thin sections	~ 15˚ bending per pass	High efficiency Reduced control

Table 2.1: Outline of the three main laser forming mechanisms [3]

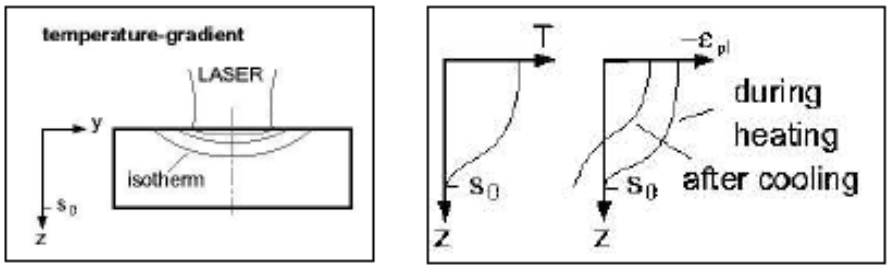

Figure 2.3: Energy conditions required for the TGM [1].

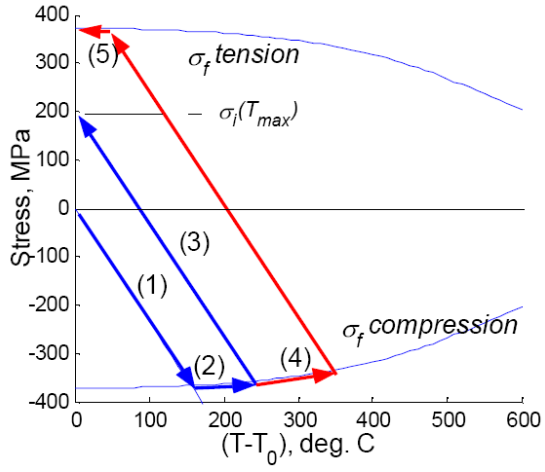

Figure 2.4: Thermally induced stress for steel SAE1513 [77]. The blue and red lines indicate a typical temperature stress cycle during TGM laser forming.

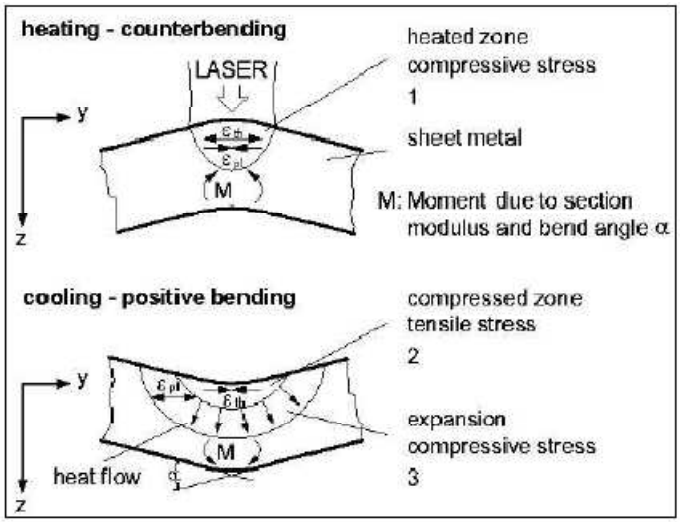

Figure 2.5: Principle of the Temperature Gradient Mechanism (TGM) [1].

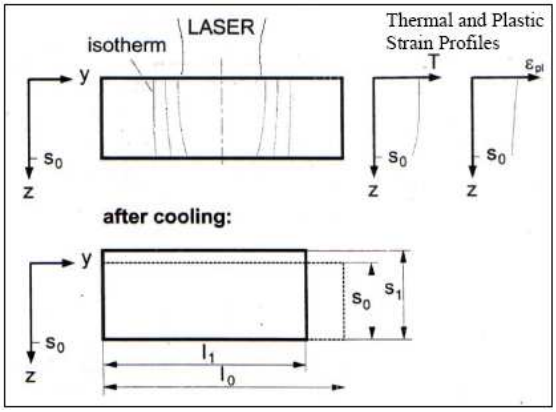

Figure 2.6: Principle of the upsetting or shortening mechanism (SM) [1].

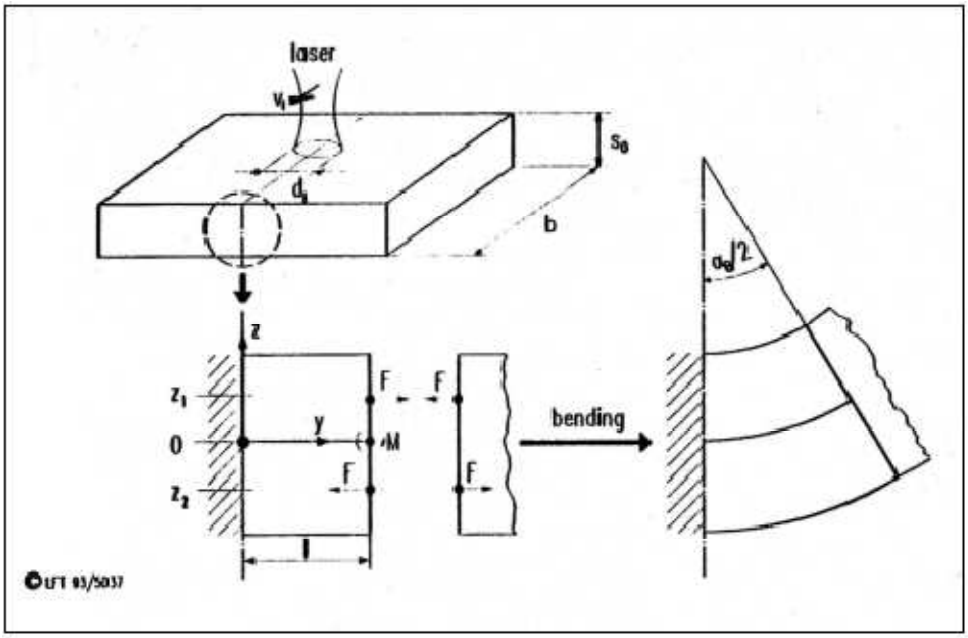

Figure 2.7: Forces and moments acting in the 'Two Layer Model' [9].

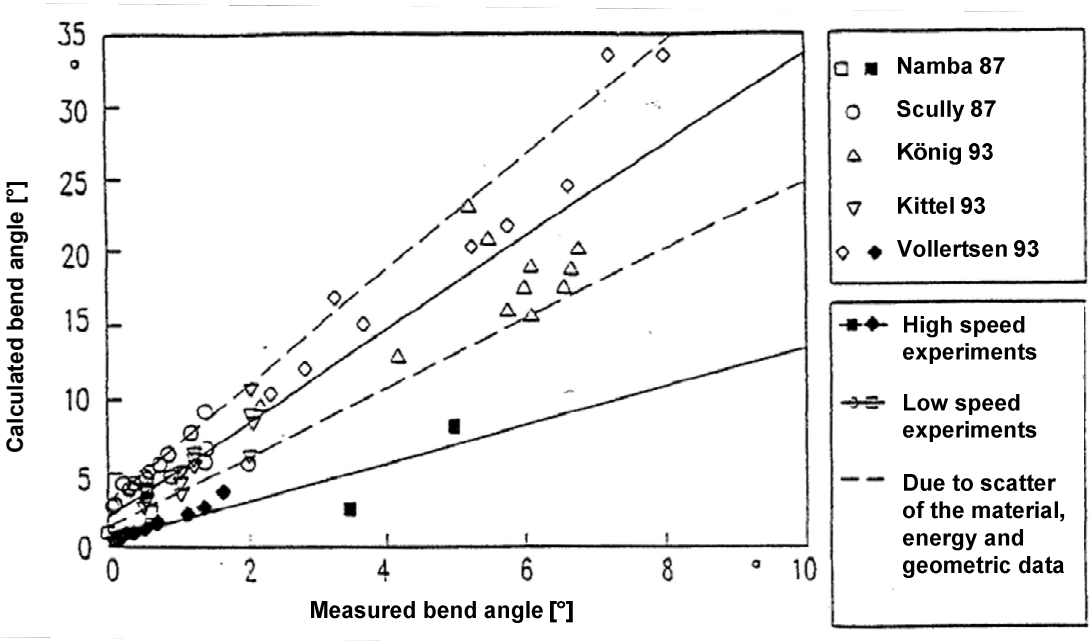

Figure 2.8: Results of the TGM model after Vollertsen compared with existing experimental results [10].

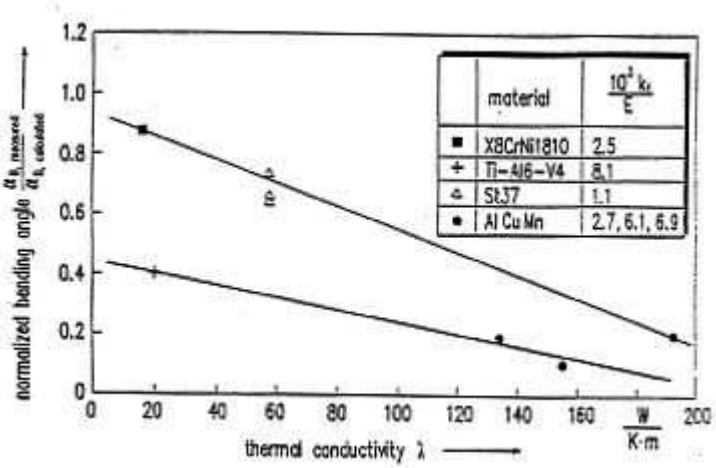

Figure 2.9: Influence of the thermal conductivity on the bend angle [1].

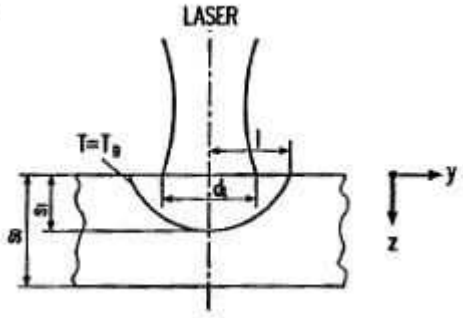

Figure 2.10: Partially plastified cross section of the sheet in the 'Residual Stress' modelling approach after Vollertsen [18].

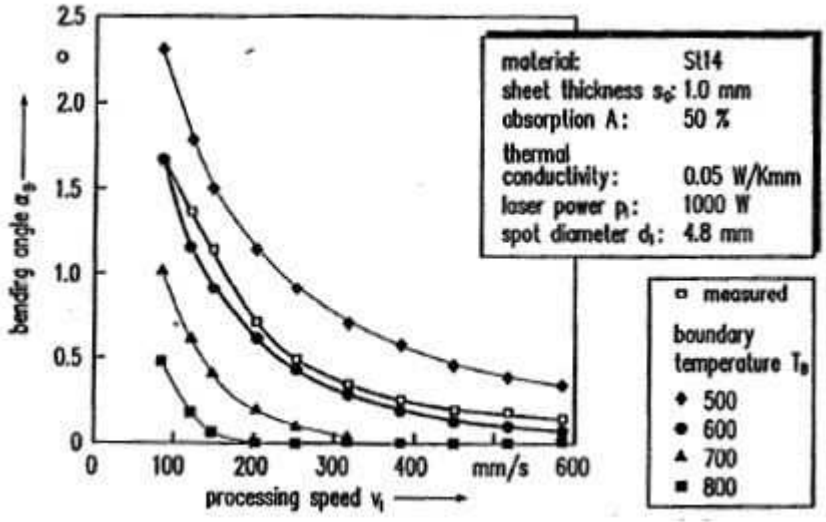

Figure 2.11: Comparison of the calculated and measured influence of the processing speed on the bend angle [18].

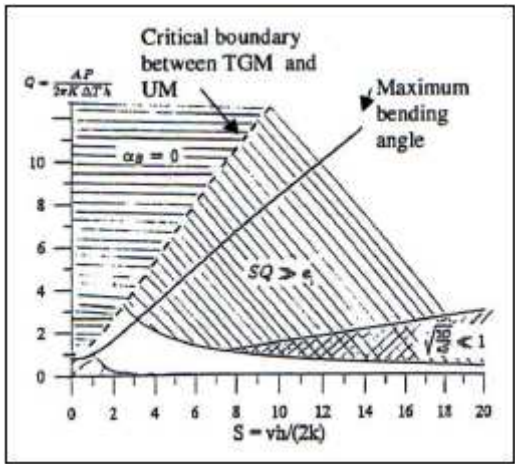

Figure 2.12: Critical operating region for the TGM [11].

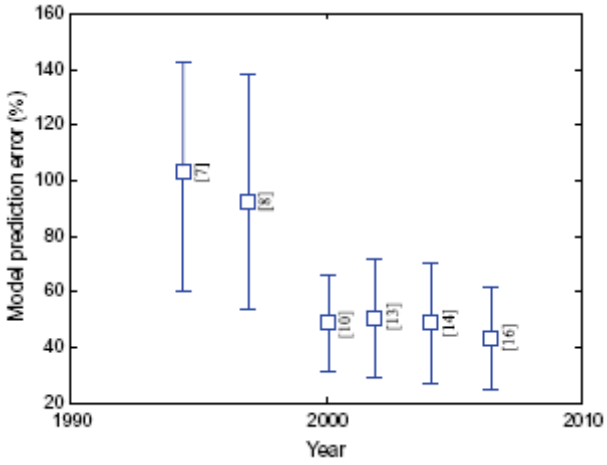

Figure 2.13: Prediction accuracy of analytical models; number in brackets represents the number of references [29].

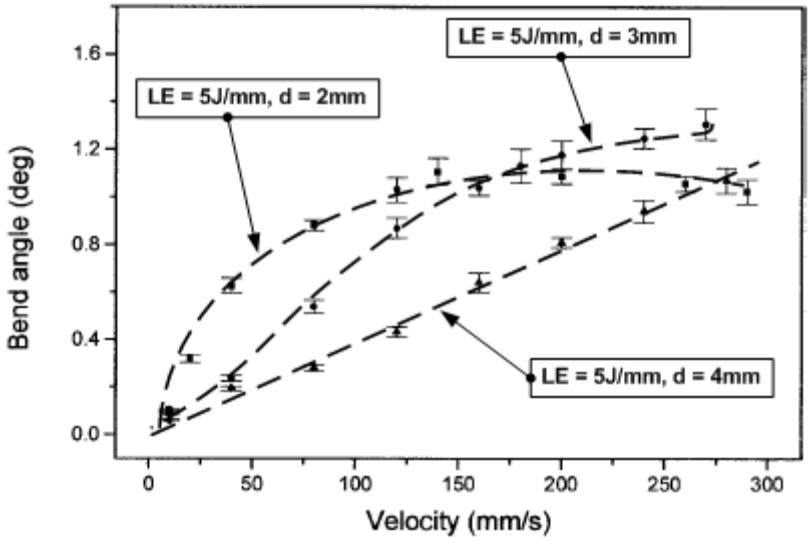

Figure 2.14: Bend angle vs. scanning velocity for constant LE and different beam diameters d [35].

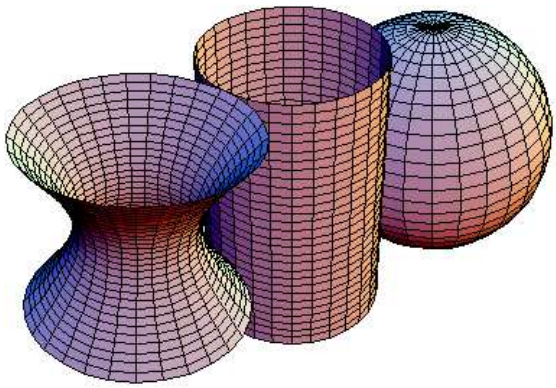

Figure 2.15: Examples of Gaussian curvature [111]; (left) Negative Gaussian curvature (hyperboloid); (middle) Zero Gaussian curvature (cylinder); (right) Positive Gaussian curvature (sphere).

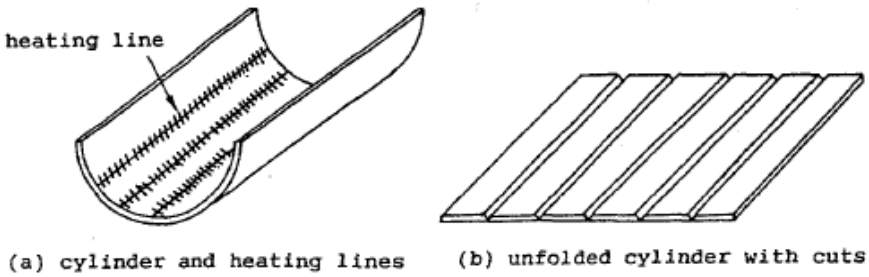

Figure 2.16: Developable surface (singly curved), requiring bending strain only (TGM) [57].

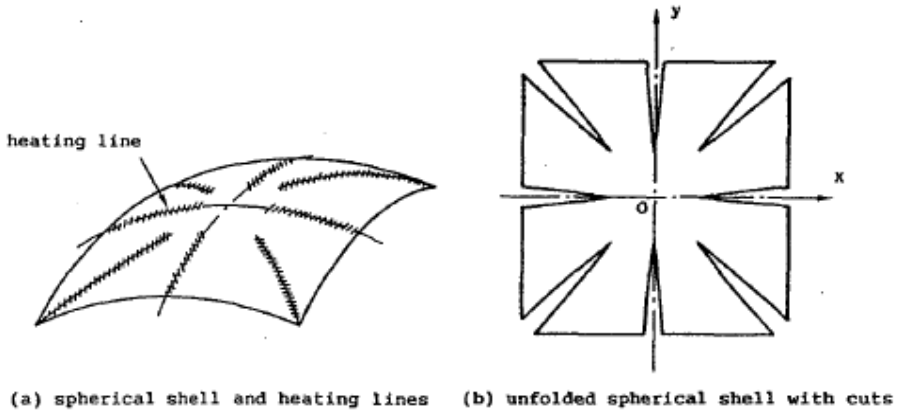

Figure 2.17: Non-developable surface (doubly curved), requiring both in-plane (SM) and bending (TGM) strain [57].

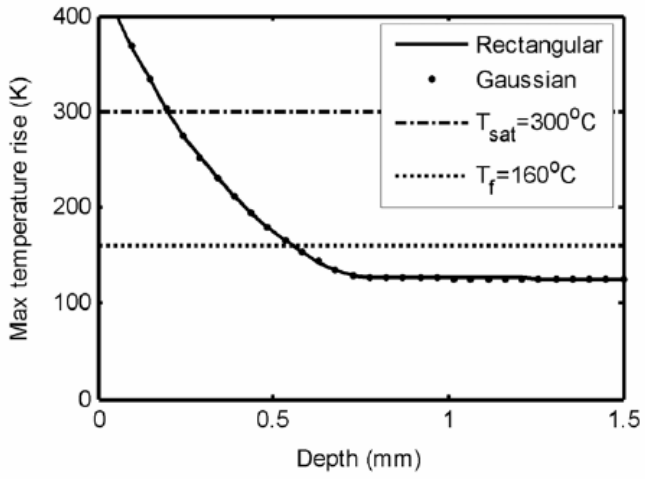

Figure 2.18: Depth profile of maximum temperature T_{max} for Top Hat and Gaussian heat profile (interaction time $\tau = 30ms$) [77].

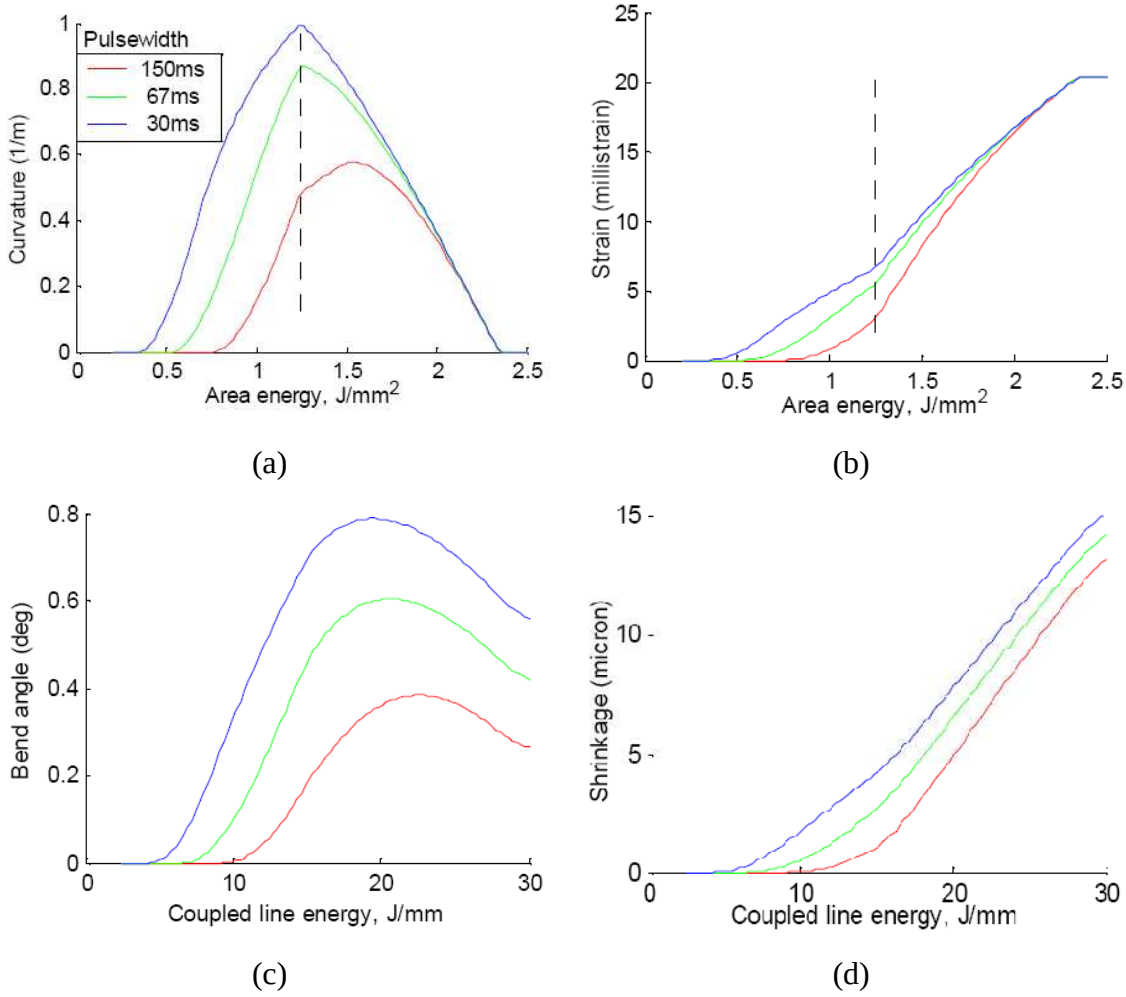

Figure 2.19: Results of the analytical-numerical laser forming model [78] showing (a) Curvature vs. area energy; (b) In-plane strain vs. area energy; (c) Bend angle vs. LE; (d) In-plane shrinkage vs. LE.

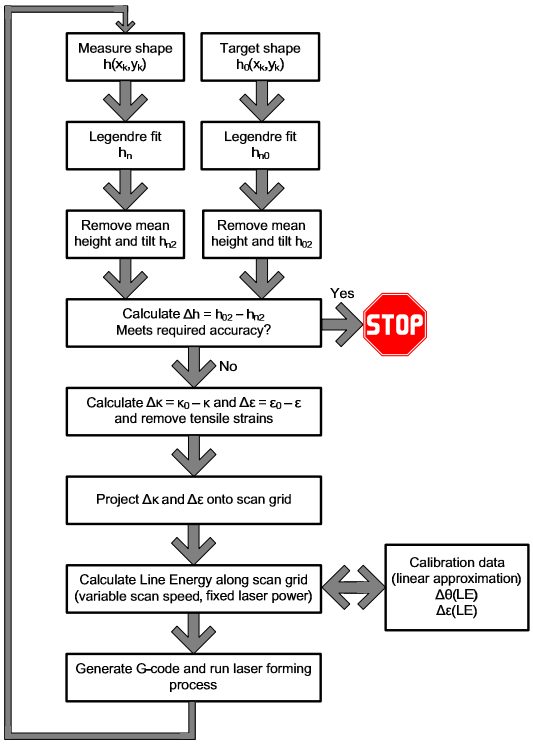

Figure 2.20: Process design of the iterative laser forming (ILF) [77,78] as it was inherited in this study.

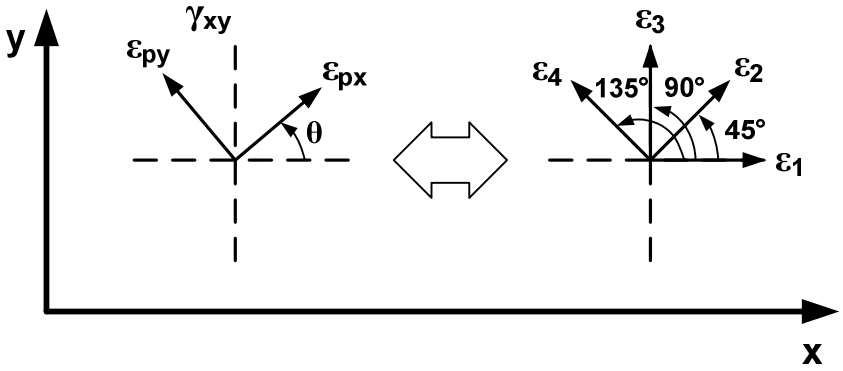

Figure 2.21: Approximation of principal strains by superposition of four independent strains.

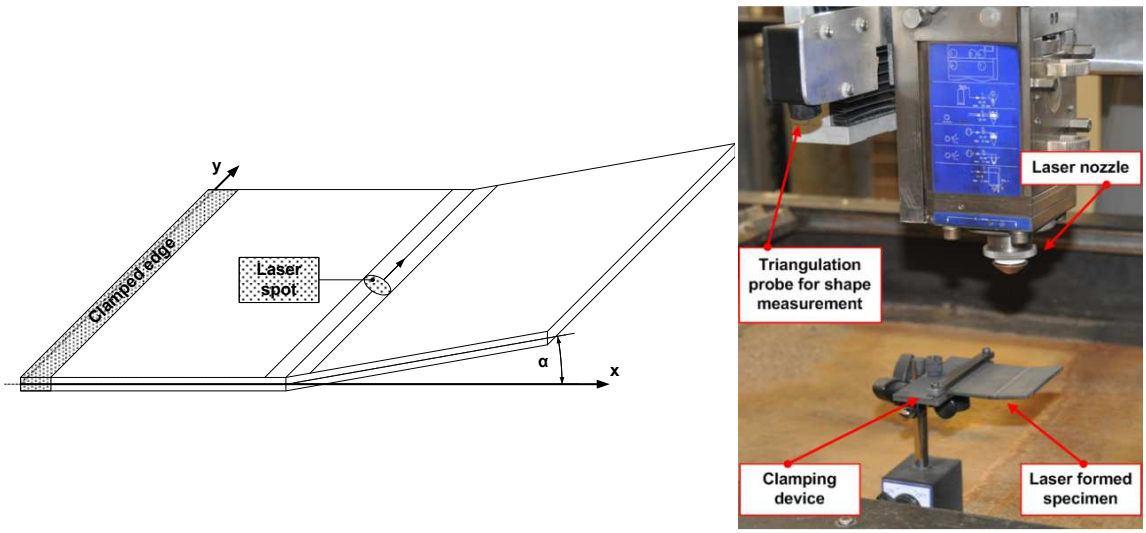

(a) (b)

Figure 2.22: Bend angle calibration experiments; (a) Experimental setup (schematically); (b) Picture of the experimental setup.

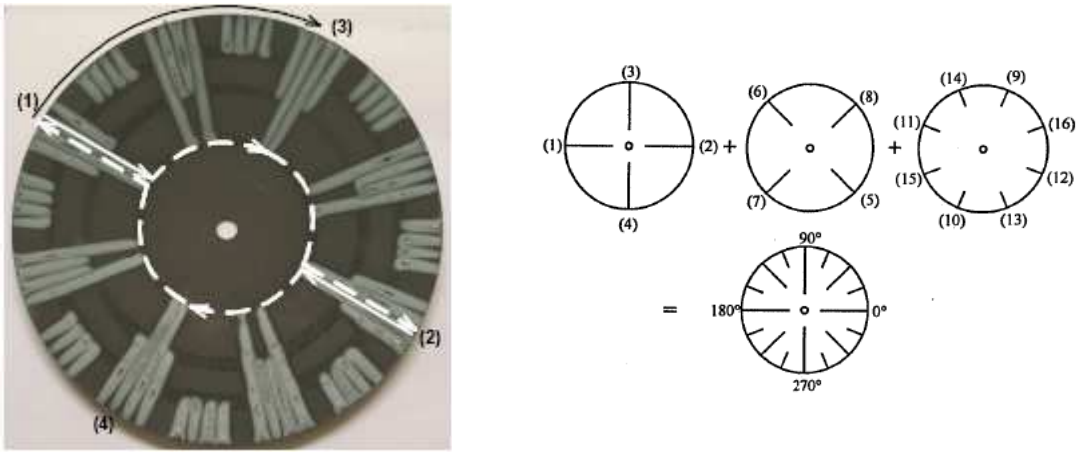

(a) (b)

Figure 2.23: Schema of the radial scan line pattern for experimental database relating in-plane strain to LE.

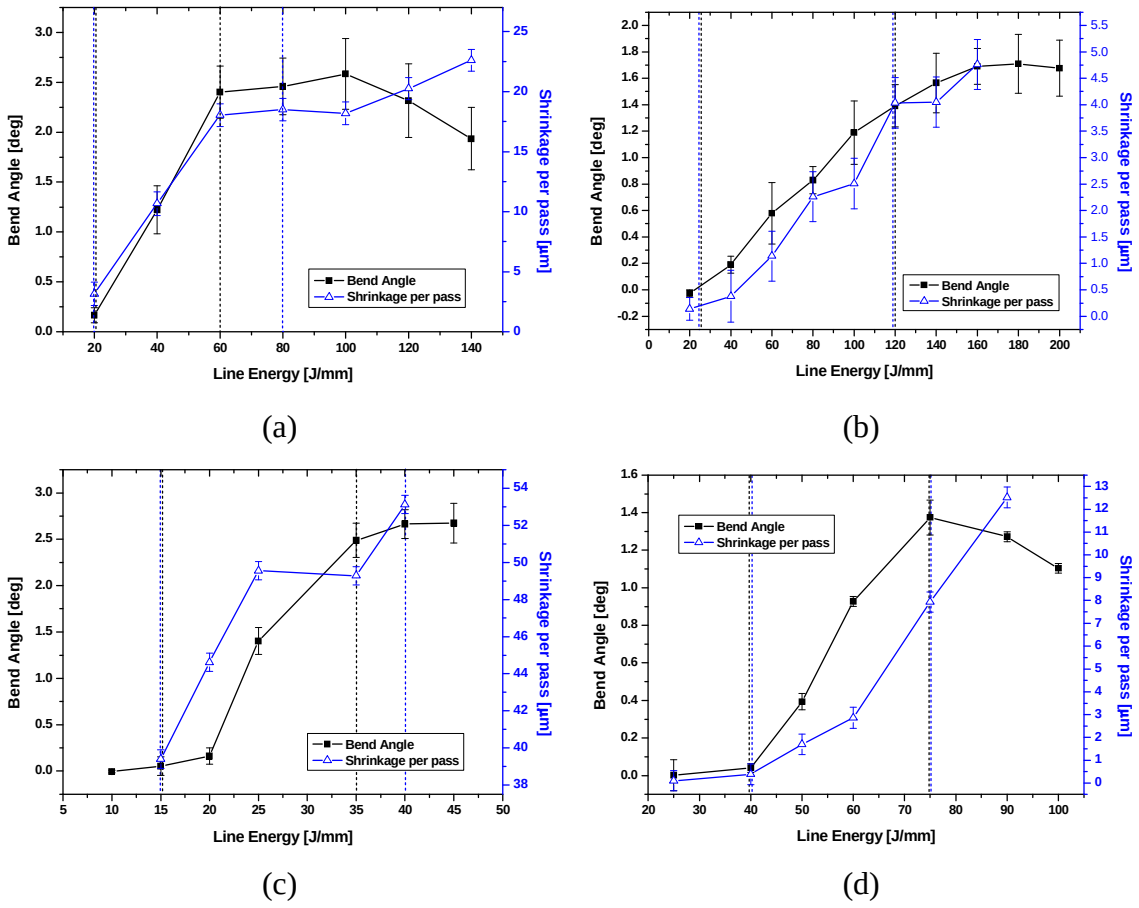

Figure 2.24: Experimental calibration database, relating bend angle and shrinkage to LE; (a) 1.5mm AISI1010; (b) 2.8mm AISI1010; (c) 1.5mm A2024-T3; (d) 3.2mm AA2024-T3; Vertical lines show minimum and maximum threshold LE applied for iterative laser forming.

Iteration	Measured shape	Residual error
0	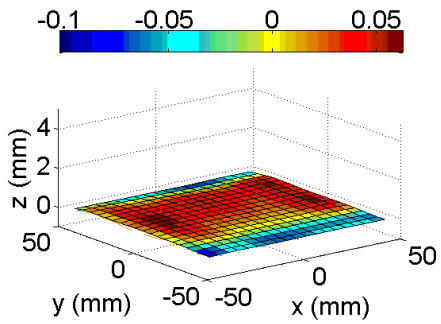	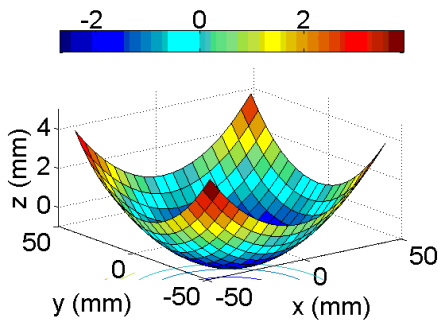
2	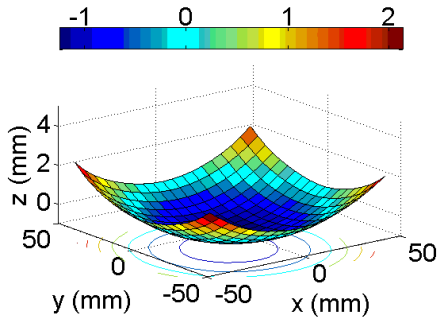	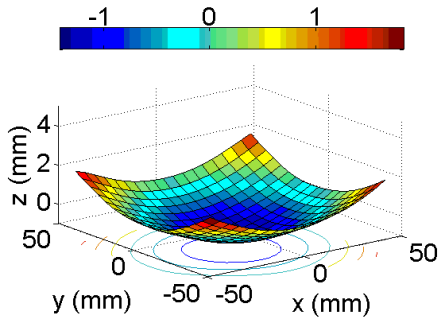
4	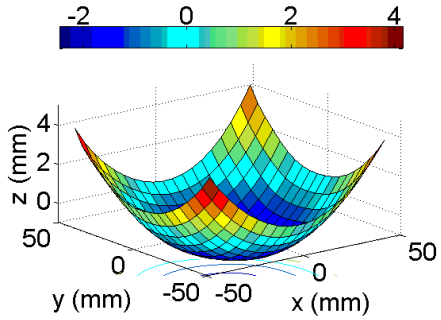	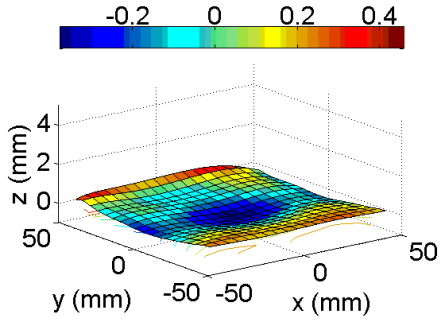

Figure 2.25: Sample converging towards the target shape in the ILF process. Comparison between measured shape and residual error (pillow shape with 8mm target deflection after 4 iterations, final *rms* = 0.201mm, sample: AISI1010, 2.8mm thick). The colour scale of the vertical *z*-deflection is in [mm].

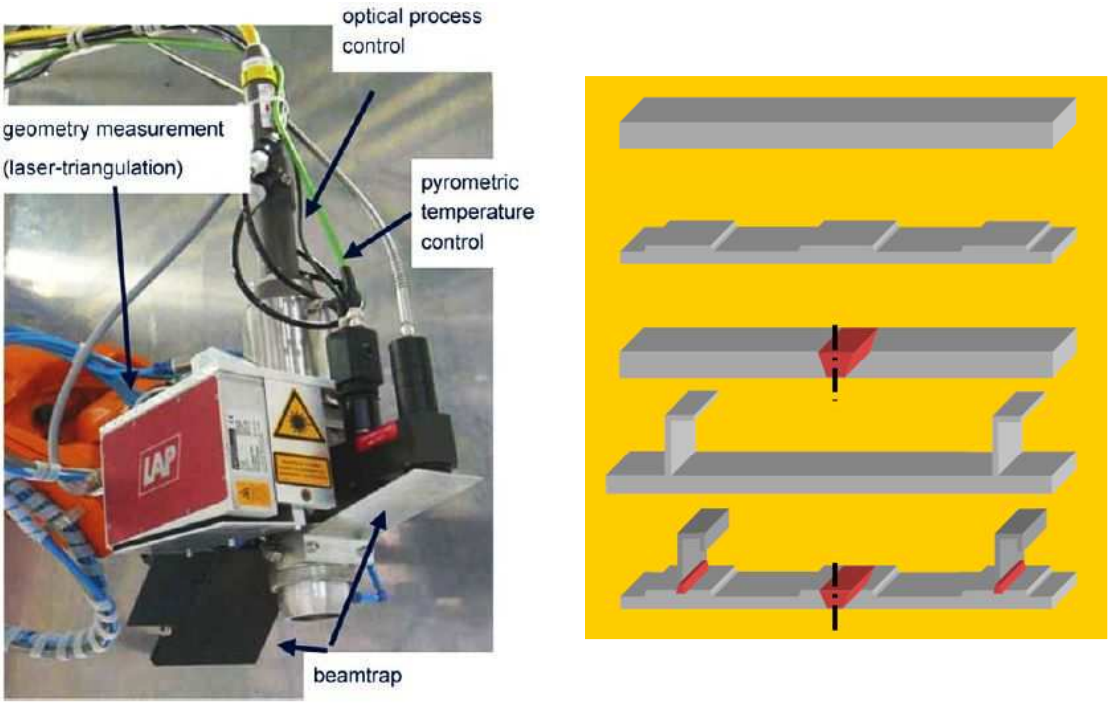

(a) (b)

Figure 2.26: (a) Prototype system for laser beam forming [90]; (b) Test specimens with different geometrical complexity investigated in first forming trials; it should be noted that the red regions are welds.

Chapter 3

Iterative laser forming of plates of varying thickness

The iterative laser forming (ILF) process, described in section 2.5.3 was applied in the form inherited in this study to uniform thickness plates. The aim of this chapter is to develop this process further to plates of varying thickness, through modifications such as the implementation of a finite element (FE-) analysis for the strain field computation; these were necessary to extend the ILF process to varying thickness plates and the straightening of welded distorted plates (Chapter 7). The modifications were validated through the forming of pillow and saddle shapes with plates of uniform and varying thickness.

3.1 ILF process modifications for the forming of varying thickness plates

For the forming of more complex geometries like plates of varying thickness or further straightening applications, the analytical method to calculate the required in-plane strain could not be applied straightforward. Instead, a mechanical FE-analysis, described in section 3.1.1, was implemented in the ILF process. Modifications made specifically in the main ILF program to incorporate the varying thickness geometries chosen are given in section 3.1.2.

3.1.1 Mechanical FE-analysis

The FE-analysis and modifications made in the main ILF program assume knowledge of the plate thickness and geometry. Their explanation is more straightforward if the shape is assured. Therefore, the specific varying thickness plate geometries used here will be described first in the following.

Figure 3.1 shows the two geometries of varying thickness plates chosen. The AISI1010 plates were laser cut from the parent sheet and either slots (Figure 3.1[a]), or wedge shape (Figure 3.1[b]) were machined with a CNC-mill. The simplified shapes were chosen to clarify and study the effect of the ILF process on varying thickness without inducing other complexities, such as welds or stringers, and without loss of generality. The intention and step in the development of the ILF process towards forming/straightening of more complex monolithic structures by choosing those shapes is shown in Figure 2.26(b), where the slots of the second geometry are recognizable (see

Figure 3.1[a]). Moreover, the geometries allowed the study and clear identification of the surface temperature varying with thickness, which is discussed further in section 3.4.

For the computation of the required in-plane strain field a FE-analysis [112,113] was carried out with the software Comsol® because of its compatibility with Matlab, where the main ILF program code was written. The input for the purely mechanical simulation (module: '3D structural mechanics') was the vertical displacement or shape residual Δh, defined as the difference between current shape and target shape after each iteration.

If a flat plate with moments along all four edges is considered, as it is the initial state in the ILF process, then, considering plate theory [21,54], the displacements u_0, v_0, w_0 in x, y, z direction (Figure 3.2) are

$$u_0 = -(1-\nu)\cdot\frac{M_B}{EI}\cdot x\cdot z$$
$$v_0 = -(1-\nu)\cdot\frac{M_B}{EI}\cdot y\cdot z \qquad (3.1)$$
$$w_0 = (1-\nu)\cdot\frac{M_B}{2EI}\cdot(x^2+y^2)+\frac{\nu M_B}{EI}\cdot z^2$$

where M_B is the bending moment in x and y direction, E is the bulk elastic modulus, I the second moment of area $\left(I=\frac{bs_0^3}{12}\right)$ and ν Poisson's ratio. If only the mid-plane of a sample plate $(z=0)$ for a given deflection is considered, those equations reduce to

$$w_0 = (1-\nu)\cdot\frac{M_B}{2EI}\cdot(x^2+y^2) \qquad (3.2)$$

and

$$M_x = \frac{2wEI_x}{(1-\nu)\cdot(x^2+y^2)}$$
$$M_y = \frac{2wEI_y}{(1-\nu)(x^2+y^2)} \qquad (3.3)$$

With the moments in x and y direction, the displacement u and v for this condition $(z=0)$ was calculated to

$$u = \frac{M_x-\nu M_y}{EI_x}$$
$$v = \frac{M_y-\nu M_x}{EI_y} \qquad (3.4)$$

The displacement w in z direction was the shape residual (Δh) as input in the FE-analysis from the main ILF program (it should be noted that it was assumed that on the element considered, shear forces/stresses vanish as is the case for pure bending).
The output from the FE-analysis to the main ILF program was the required strain field ε_{ij} in x- and y-direction $(\varepsilon_{xx}, \varepsilon_{yy}, \varepsilon_{xy}, \varepsilon_{yx})$ over the pre-defined grid.

$$\varepsilon_{ij}^{0} = \frac{1}{h}\int_{-\frac{s_0}{2}}^{\frac{s_0}{2}} \varepsilon_{ij}\, dz \tag{3.5}$$

$$\varepsilon_{ij}^{1} = \frac{2}{s_0}\int_{-\frac{s_0}{2}}^{\frac{s_0}{2}} \left(\varepsilon_{ij} - \varepsilon_{ij}^{0}\right) dz \tag{3.6}$$

The in-plane strain ε_{ij}^{0} was calculated from the total strain field ε_{ij} after equation (3.5) since it comprised both out-of-plane (ε_{ij}^{1}) and in-plane (ε_{ij}^{0}) strain components. As seen from equation (3.5), the in-plane strain arises from the integration of the total strain along the thickness s_0. It should be noted that the bending strain ε_{ij}^{1} was already accounted for through the curvature $\Delta\kappa$ and equation (3.6) is only shown for completeness.
The following strain correction to remove all tensile strains was modified in such a way that the 'opposite' in-plane strain field, $\varepsilon_{applied} = -\varepsilon_{FEM}$, was used, proposed in [57,60]. This modification provided a more accurate solution to the strain correction for varying thickness plates than adding a uniform, compressive isotropic in-plane strain with the magnitude of the maximum tangential strain ε_t applied in the 'original' analytical approach for plates of uniform thickness [79]. The corrected strain field was then related to heating conditions (LE) using the experimental database.

In the mechanical FE-analysis, the plate was fixed at a single point, its geometric centre. Material parameters used in the FE-analysis were $E = 207GPa$, $\nu = 0.3$ and $\rho = 7871kgm^{-3}$ for AISI1010 [138], and $E = 72.4GPa$, $\nu = 0.33$ and $\rho = 2780kgm^{-3}$ for AA2024-T3 [144]. In all 3D forming applications presented, the z-deflection (normal to the sample surface) was large relative to the sample thickness and therefore in-plane strain became more pronounced over bending strain [54]. It was assumed that the material of the plate is elastic, homogeneous, and isotropic; elements initially normal to the middle surface before bending, remained straight and normal to the middle surface during the deformation, and the length of such elements was not altered. For simplicity the simulations were run without residual stresses. Those simplifications

assured a fast computation of ~ 20 seconds between subsequent iterations. Figure 3.2 shows an example of the first principal strain for a given displacement of both types of varying thickness geometries chosen.

3.1.2 Main ILF program

Beside the FE-analysis, the varying thickness geometry was incorporated in the main ILF program to determine the heating conditions in terms of LE from the calibration databases shown in Figure 2.24. For the plates with slotted recesses, either the database for 2.8mm or 1.5mm was entered; for the plates with uniformly varying thickness, a linear interpolation between both databases was performed. Figure 3.3 shows the linearly interpolated bending and shrinkage calibration databases.

The basic structure of the program is such that it generates a grid on the plate with the four scan path directions (Figure 2.21) in 0˚, 45˚, 90˚ and 135˚ to the x-axis. After the calculation of residual curvature $\Delta\kappa$ and in-plane strain $\Delta\varepsilon$ the following information for each point on the pre-defined grid over the token is present:

1. Coordinate in x- and y-direction on the sample surface
2. Required strain and curvature vector in all four directions of the scan lattice

With the information in (2), the experimental database is entered in order to determine the LE required to impose the desired curvature and shrinkage for each scan path along the four directions in the fixed scan lattice. To implement the varying thickness geometry, the corresponding thickness of each point in the pre-defined grid was added to the main ILF program in the form of a matrix. From this information heating conditions from the database were adjusted accordingly.

This implementation of the geometry in the ILF process, described here, assumed the knowledge of the plate thickness. A potential approach for unknown plate thickness, based on surface temperature, is considered in section 3.4.

3.2 Experimental details

Square tokens were laser cut from parent sheet material with a hole in the centre where they were fixed with a screw during laser forming. A picture of the experimental setup for the 3D laser forming experiments is shown in Figure 3.4. The dimensions for uniform thickness plates of both materials are shown in Table 3.1. Prior to laser forming, each token was degreased with acetone and then hand coated with a thin layer of graphite to improve the coupling efficiency of the laser energy into the sample

surface. The effect of the graphite coating layer on the laser forming process is discussed in section 3.5.

Laser forming experiments were carried out with a TRUMPF TLF 2700 Turbo 2.7kW CO_2 laser with standard metal-cutting laser optics and nozzle [77]. The beam was used beyond its focus, providing a constant diameter of 9mm. To adjust the line energy, the transverse speed of the sample relative to the laser was varied and the laser power was held constant at 600W for AISI1010 and 1000W for AA2024-T3. This laser spot size and power for each material were previously found to produce an acceptable range of LE inputs for iterative forming [77]. During the ILF process, each scan path in the scan lattice was repeated with a fast feed rate (~ 2500mm/min), shutter closed (no laser power) and a nozzle airstream of ~ 1.5bar to allow the plate to cool down and deformation to develop fully before the next laser scan pass was induced.

Calibration experiments relating bend angle and in-plane shrinkage to LE for low carbon steel (1.5mm and 2.8mm thickness) and aluminium-copper alloy (1.5mm and 3.2mm thickness) were done, following the procedure described in section 2.5.3. The minimum and maximum threshold LE applied in the ILF on uniform thickness tokens are shown in the final calibration graphs in Figure 2.24 through dashed vertical lines for both materials. The calibration graphs of 1.5mm and 2.8mm thickness of low carbon steel (Figure 2.24[a-b]) corresponded approximately to the thick and thin end of the wedge shape and to the thick and thin section of the plates with slotted recesses (Figure 3.1). Thus, for forming of varying thickness plates, either the one or the other database (slot) was entered, or a linear interpolation (wedge) between both was done.

Generally, the choice of heating conditions is designed to avoid overshoot, to tolerate errors in induced bend angle and shrinkage (for example caused by calibration errors, scan line history, geometry and coupling), to tolerate interdependence between induced bend angle and shrinkage and also interdependence between transverse and axial bending and shrinkage. Therefore, the main ILF program allowed the LE determined to be multiplied by a factor η_{LE}, which was set to $\eta_{LE} = 0.8$ for all laser forming experiments, presented in this thesis. Two other factors, η_κ and η_ε were chosen, because in the ILF approach, predicted line bends are applied to generate a fraction η_κ of the required curvature field and similar apply line shrinkages targeting η_ε of the required in-

plane strain field. Those factors are given separately for each forming application shown.

The shape measurement was performed with a single point triangulation probe connected to a National Instrument data acquisition card (type: NI-USB-6221 M series). The acquisition rate was 200 samples per second. After each forming iteration, the probe scanned the top surface of the sample, referred to as the surface where the first iteration was done, in lines parallel to the x-axis (Figure 3.5), in 5mm intervals along the y-direction. The shape data was recorded continuously to determine the deflection of the plate from which the shape residual Δh was calculated. The accuracy of the shape measurement was within ± 0.1mm.

For the surface temperature measurement a double wavelength pyrometer was used. A description of the device together with the experimental setup is described in section 4.2.

3.3 Forming results

In the following section, the forming results of pillow and saddle shapes for uniform and varying thickness tokens are presented. The pillow shape, equation (2.17), which comprises two curvatures with equal sign, was chosen for simplicity, because it required laser scans on only one surface. The forming of a saddle shape, equation (2.18), which consists of two curvatures with opposite sign, was chosen, because this shape required laser scans on both top and bottom surfaces.

The scan path distance for these forming trials was set to 10mm between parallel vertical and horizontal scans in the fixed scan lattice applied ($\sqrt{2} \cdot 10$mm for scans in 45° and 135°). The influence of the scan path distance in the scan lattice is discussed later in this study. During the forming trials, it proved to be more accurate to begin with the target shape set to a fraction of the intended deformation, and then to increase the target deformation after the first forming passes. In particular, initially forming a low-profile version of the final/target shape avoided early asymmetry errors which were difficult to correct with further iterations.

3.3.1 Uniform thickness plates

The forming experiments with uniform thickness plates of low carbon steel and aluminium-copper alloy aimed to validate the implementation of the FE-analysis for the strain field computation [112,113] and the modified strain correction. Furthermore, parameters such as η_κ and η_ε in the ILF process were adjusted accordingly to obtain the most accurate forming results for plates of different thickness for AISI1010 (1.5mm and 2.8mm thickness) and AA2024-T3 (1.5mm and 3.2mm thickness).

Table 3.2 shows the final symmetry in the form of measured curvature in y-direction (κ_y) over measured curvature in x-direction (κ_x) and final *rms* error (root mean square shape error between measured and target shape) of the most successful forming trials of pillow and saddle on AA2024-T3 tokens. For the pillow shape, a bending and shrinkage scan was applied alternately on the top surface. The saddle shape was formed with alternating bending scans on the top and bottom surfaces. Only bending scans were applied here, because the deflection was small and of the order of the plate thickness.
The results of forming trials of pillow and saddle shapes of AISI1010 are shown in Figure 3.6 and Table 3.3. Although the deflection for the case of the saddle shape was large, i.e. greater than the plate thickness, the same forming strategy was applied (bending scans on the top and bottom surfaces) and accurate saddle shapes were formed. This result implies that, during a bending scan, sufficient in-plane shrinkage was induced for the target deflection chosen. Therefore, those forming strategies were kept consistent throughout this thesis.

The forming dilution factors η_κ and η_ε shown in Table 3.2 are equal for AA2024-T3, and for AISI1010, Table 3.3, the strain had to be diluted significantly $\left(\eta_\varepsilon = \frac{1}{10}\eta_\kappa\right)$. This dilution originates from the high thermal conductivity of AA2024-T3 compared with AISI1010, making it more difficult to establish a temperature gradient through the thickness. From the calibration databases (Figure 2.24), it can be seen that, for the same bend angle, considerably more in-plane shrinkage is induced and, conversely, for a given shrinkage, less bending is induced for AA2024-T3 than for AISI1010. However, the symmetry and final accuracy of pillow and saddle shapes formed validated modifications made in the forming process, and showed its controllability. The trials were fundamental to adjust parameters for the forming of varying thickness plates (section 3.3.2), and for straightening applications (Chapter 7).

3.3.2 Varying thickness plates

Modifications made in the ILF process (section 3.1) were validated through forming of pillow and saddle shapes of the two specific varying thickness geometries chosen. Figure 3.7 shows successful approaches of pillow and saddle for plates with slotted recesses, and the corresponding target deflection, symmetry and final *rms* error is shown in Table 3.4. The shape measurement was applied on the flat surface, referred to as top surface later, because a continuous surface was required to calculate the shape residual Δh.

Forming results of uniformly varying thickness plates are shown in Figure 3.8, and the accuracy of the final pillow and saddle shapes is shown in Table 3.5. It was necessary to anneal [114] the plates prior to laser forming to release residual stresses from machining, discussed in section 3.5. For shape scan and laser forming, the plate surface was adjusted so that it was levelled horizontally and perpendicular to the incident laser beam. The first iteration (bending scan) was applied on the non-machined surface, which is referred to as top surface.

The accuracy of pillow and saddle shapes formed on uniform thickness plates was about in the same order as shown in Table 3.2 and Table 3.3. However, for varying thickness plates, the *rms* error was larger, in particular for the saddle shapes which required scans on the top and bottom surface. The least accurate saddle shape formed was on plates with uniformly varying thickness (Table 3.5). This lower accuracy was caused by the increased scan path distance chosen and the change in the pre-dominant forming mechanism with varying thickness, discussed in section 3.5.

3.4 Surface temperature measurements

The mechanical FE-model (section 3.1.1) requires knowledge of the plate thickness and time to set up, although it runs quickly. This section investigates a method of adjusting the LE in process without the FE-model and knowledge of the plate thickness. An approach is proposed and its feasibility demonstrated which would adjust the LE, based on monitoring the surface temperature.

For the 2D laser forming experiments, presented in this section, the bend angle was calculated by measuring the shape of the tokens before and after forming, following the procedure, described in section 3.2 and shown in Figure 3.5. The bend angle at each y-

value was then calculated from the shape change, and the mean bend angle calculated over all intervals for the final bend angle of the token.

To investigate the effect of plate thickness on surface temperature, measurements with a double wavelength pyrometer were carried out during a single line scan on plates with uniform and varying thickness. Figure 3.9(a) shows the surface temperature, measured along the laser scan line of low carbon steel plates ($80x80mm^2$) with a uniform thickness of 2.8mm and 1.5mm. Figure 3.9(b) relates the surface temperature measured to LE for both thicknesses. Each point in Figure 3.9(b) consists of four individual measurements, as shown in Figure 3.9(a), with 90 seconds' cooling time between consecutive scans in order to minimise the increase in bulk temperature. The error bars in Figure 3.9(b) indicate the standard deviation from the mean over all four measurements per LE. The relatively large error is the result of fluctuations in the absorption and emission of the laser light caused by the particles of the graphite coating, which is further discussed in section 3.5. As is visible from Figure 3.9(b), the error is larger at lower coupled energy (LE) and temperature. The surface temperature measured for both thicknesses shows similar behaviour. For a low LE, the temperature is low because of the fast scanning speed and low coupled energy. As LE increases, the surface temperature increases and at ~ LE = 80J/mm both graphs start to flatten off, owing to the heat sink effect (with increasing interaction time) of the surrounding cold material. The thinner samples show a higher surface temperature compared with that of the thicker samples, because of the reduced heat dissipation through thickness.

The surface temperature along the laser scan line at LE = 100J/mm is shown in Figure 3.10(a) for a plate with slotted recesses and in Figure 3.10(c) for a plate with uniformly varying thickness. A LE of 100J/mm was chosen, because it provided enough heat input to show the temperature variation with thickness, and the error of the recorded temperature was relatively small (Figure 3.9[b]). Based on the surface temperature measurement of uniform thickness plates (Figure 3.9[b]), the LE was adjusted to the sample thickness for a constant surface temperature of 1200℃. The LE applied for plates with slotted recesses was LE = 62.6J/mm in the thin sections and LE = 95.7J/mm in the thick sections. For the wedge shape, the LE was adjusted uniformly in 5mm steps along the scan line from 62.6J/mm at the thin end to 95.7J/mm at the thick end, because the CNC control did not allow a uniform linear variation of the scan speed. The surface temperature recorded is shown in Figure 3.10(b) for a sample with slotted recesses, and

in Figure 3.10(d) for a sample with uniformly varying thickness. It can be seen that the temperature along the scan line is fairly constant, but too high in magnitude compared with that (1200℃) of uniform thickness plates, possibly caused by the reduced heat flow originating from the varying thickness geometry.

These experiments showed that, despite the varying surface temperature with plate thickness, laser forming parameters (here the laser scan speed) can be adjusted to the plate thickness for a constant surface temperature (Figure 3.10[b] and Figure 3.10[d]). Therefore an approach was sought to use the surface temperature as an additional control parameter in laser forming. Figure 3.11(a) shows the relation of bend angle to plate thickness with LE, obtained from linear interpolating between both bend angle graphs of the calibration experiment (Figure 2.24[a-b]). Figure 3.11(b) relates the surface temperature recorded at a distinct LE to plate thickness, based on the measurement given in Figure 3.9. For the approach, the surface temperature profile of a constant LE scan at 100J/mm across tokens of both varying thickness geometries was recorded with the pyrometer (Figure 3.12[a-b]). These two surface temperature profiles were then used to adjust the LE for a bend angle of one degree, applying the relation of surface temperature and bend angle to LE and plate thickness (Figure 3.11[a-b]). The LE profile based on the surface temperature measured is shown in the form of a blue line in Figure 3.12(c)-(d) for both varying thickness geometries. It should be noted that the data from the pyrometer measurement at LE = 100J/mm were filtered (‘average’ filter with resolution of 15 samples), owing to the high pyrometer sampling frequency of 50Hz which would have been too high for inertia and control resolution of the CNC table. The effect of the filtering is indicated with the red dotted line, shown in Figure 3.12(a)-(b).

To study the effect of this surface temperature control approach on the bend angle rate and accuracy of a single line scan, experiments with the following three laser settings were done on tokens of both varying thickness geometries:

1. LE = 100J/mm = constant.
2. LE adjusted for a constant surface temperature of 1200℃ (Figure 3.11[b]).
3. LE adjusted based on previously measured surface temperature of a constant LE scan at LE = 100J/mm (Figure 3.12[a-b]), as described above.

The line energy profiles of case (1)-(3) are shown in particular in Figure 3.12(c)-(d). Conditions (1) and (2) were chosen because the bend angle of a uniform thickness plate with 2.8mm thickness is about one degree (1.18°) at LE = 100J/mm (Figure 2.24[b]),

case (1), and its surface temperature at LE = 100J/mm was recorded to be ~1200℃ (Figure 3.9[b]), case (2). Those LE profiles (Figure 3.12[c-d]) were applied five consecutive times in alternating directions across the tokens and the initial shape, and the bend angle after each laser scan pass was measured. Figure 3.13(a) shows the bend angle rate per pass for plates with slotted recesses and Figure 3.13(b) the bend angle rate per pass for plates with uniformly varying thickness. Error bars are not included in the graphs for clarity. Instead, the bend angle uniformity along the scan path is shown in the form of the *rms* error of the bend angle measured over all 20 individual intervals of a shape scan (Figure 3.5). It can be seen for both varying thickness geometries that the use of the surface temperature to control the LE along the laser scan path significantly reduced the variation in bend angle rate over consecutive passes (Figure 3.13[a-b]), and the *rms* error along the laser scan path (Figure 3.13[c-d]). Clearly, the lower LE and heat input applied in cases (2) and (3) decreased the bend angle rate per pass. The effect of annealing on the bend angle rate of samples with uniformly varying thickness is visible from Figure 3.13(b), showing less variation in bend rate per pass for an annealed sample compared with that of a non-annealed sample, both treated under conditions of case (2). Interestingly, the sample scanned at the LE profile based on the surface temperature measured (case [3]), showed the lowest bend rate variation with passes even though it was not annealed (Figure 3.13[b]). The effect of annealing on the final shape formed is discussed further in section 3.5.

For case (3), the LE was adjusted for a bend angle rate of one degree per pass, but, as shown in Figure 3.13(a)-(b), it was lower in magnitude. The LE profile for case (3) was based on the relationship between bending, surface temperature, thickness and LE obtained from uniform thickness plates. As shown in Figure 3.10, the surface temperature of varying thickness plates was higher compared with that of the uniform thickness plates. Therefore the calculated thickness based on the surface temperature measurement is thinner and the resultant LE profile is lower. However, an iterative process design would accommodate this underestimation. A more ‘conservative’ approach would be desired in ILF to avoid ‘overshooting’ of the target shape. The implementation of this approach in the ILF process is described in the following section.

3.5 Discussion

When the thickness of the plate varies along the laser scan line, two competing mechanisms affect the bend angle along the plate: in thicker sections the peak (surface) temperature decreases (Figure 3.9[b]), while the temperature gradient and bending rigidity increases. The increasing temperature gradient with thickness favours bending, but at the same time reduced peak temperature and higher bending rigidity decrease the bend angle. Therefore, in thinner sections, the SM may dominate, inducing predominantly in-plane shrinkage, and in thicker sections the TGM favours bending, which is apparent from the comparison of both (1.5mm and 2.8mm thickness) experimental calibration graphs (Figure 2.24[a-b]). To accommodate this change in pre-dominant forming mechanism in the forming trials, a more 'conservative' forming approach was required, i.e. a gradual increase of the target deflection with subsequent iterations and/or a dilution of the shrinkage (η_ε) scan.

Forming of uniformly varying thickness tokens was successful only if the samples were annealed prior to forming (650℃ - 700℃ for ~ 1h10min [114]) and if the first iteration was applied on the non-machined sample surface. Through the annealing process, residual stress (RS) was released, particularly in the thin section where material removal and thus process temperature was highest. For plates with slotted recesses, the iterative process design accommodated the RS induced during milling, and annealing was not necessary. The effect of annealing on the shape of both geometries is shown in Figure 3.14 which compares the measured shape before and after the annealing. The characteristic RS induced during the corresponding milling process [115,116] of both shapes is shown in Figure 3.15, in the form of a steep near surface RS gradient, which is balanced further through thickness of the bulk material. The effect of annealing and relaxation of those RS on the shape was negligible for plates with slotted recesses, as shown in Figure 3.14(a) and Figure 3.14(c). Either the RS induced as a result of milling was insignificant, or the constraint of thicker sections was strong enough to accommodate/balance those residual stresses. The initial positive bending around the y-axis (Figure 3.14[a]) is a result of the reduction of rigidity (i.e. broken surface) in the slots on the bottom surface. The residual stresses and RS gradient induced during milling of the wedge are higher in magnitude in the near-surface region and have an opposite sign (Figure 3.15[b]) compared with that of plates with slotted recesses (Figure 3.15[a]). They are particularly high in the thin (less rigid) section where most of the material was removed. Therefore, after annealing, buckling is visible in this section as

shown in the comparison of Figure 3.14(b) and Figure 3.14(d). The relaxation of tensile near-surface RS on the machined bottom surface is visible in the form of a negative bending around the y-axis after annealing. Deformation is largest in the middle of the sample, ($x = 0$, $y = \pm 50$, Figure 3.14[d]), where the large rotating milling tool ($d >$ sample width) entered and left the plate while the wedge was machined.

The scan path distance for the forming trials on both varying thickness token geometries was 14mm between two vertical or horizontal parallel lines in the fixed scan lattice. This distance was found experimentally and was chosen on the one hand, to prevent scan lines at locations with significant thickness change, such as along the edges of the slots; on the other hand it was chosen, to reduce the energy input per area compared with uniform thickness plates, where a scan path distance of 10mm was applied. Inducing fewer scan lines per area was crucial in the thin section of the wedged plates to dilute the pre-dominance of the in-plane shrinkage. However, the wider scan path distance chosen reduced the accuracy of the final shape formed, in particular for the saddle shape, as shown in section 3.3.2.

Figure 3.16 shows an example of buckling/non-uniform bending of a sample with slotted recesses, which was formed with a scan path distance of 10mm. This scan path distance applied laser scans along the edges of the slots resulting in non-uniform temperature distribution and deformation.
One of the first forming trials to form the pillow shape of a wedged shaped token is shown in Figure 3.17. The sample in Figure 3.17(a) was not annealed after machining and the sample in Figure 3.17(b) was annealed [114] prior to laser forming. It can be seen, that the stress relief annealing significantly improved the shape formed, in particular in the thinner section, where the largest residual stresses after machining were present. Despite the annealing, the accuracy of the forming result shown in Figure 3.17(b) was not yet sufficient, because the shrinkage scans applied were not diluted ($\eta_\varepsilon = 0.7$).

Crucial for both non-contact surface temperature measurements and the laser forming process in general is the absorption of the incident laser radiation and thus the coupled energy into the work piece. Figure 3.18(a) shows that the reflectivity of iron and aluminium is very high at the wavelength of $10.6\mu m$, which is emitted by a CO_2 laser. Therefore, thin layers of absorptive coatings are commonly used in laser forming to

enhance the coupling efficiency between the defocused low intensity laser beam and sample surface. In these thin layers, the laser power is absorbed and transferred to the substrate. The absorption may then be increased to rates of 70-80%, depending on coating and surface quality (Figure 3.18[b]). Generally, those coatings are sprayed or painted manually onto the surface to be processed, because an automatic application is difficult to perform. As a consequence, their thickness may vary. Apart from absorbing the laser energy, coatings have to transport the released heat to the sample surface; hence the thermal conductivity of the substrate will influence the overall absorption.
Coating of the sample could be avoided by the use of Nd:YAG or diode lasers, which have a shorter wavelength, which is absorbed more efficiently by metallic surfaces. For example a Nd:YAG laser emits laser light at a wavelength of $\lambda = 1.06\mu m$, which is absorbed to about 20% by aluminium and to about 50% by steel (Figure 3.18[a]). Therefore, those lasers would not require any additional coatings for efficient laser forming. In addition, compared with a CO_2 laser, glass fibres and light optics for the beam management could be used for flexible handling and guidance of the Nd:YAG and diode laser light. However, the CO_2 laser was the source available for the laser forming experiments presented in this thesis. Even though coating was required, the process was consistent enough that conclusions could be drawn.

For all experiments presented in this study graphite coating ('Graphit 33' spray lubricant from AGAR Scientific Ltd.) was used to enhance coupling. The thermal properties of pure graphite can vary in a broad range dependent on the lattice orientation and therefore the thermal vibartional amplitude of the crystal in the corresponding direction; for example, the thermal conductivity of Pyrolytic graphite (at $25℃$), which is typically used in coating sprays, is $390\frac{W}{mK}$ in ab-direction and $2\frac{W}{mK}$ in c-direction [117]. In addition to that, it was previously shown by Vollertsen [9] that a graphite coating exceeding $20\mu m$ in thickness can dissipate energy from the laser, rather than enhancing coupling efficiency. Because the graphite was sprayed by hand, there was no way of standardizing the thickness of coating layer applied; it is probable that its thickness varied from sample to sample and on the sample itself. Clearly, those effects, together with the sample surface condition (cold rolled steel), laser wavelength ($\lambda = 10.6\mu m$) and 'signature' of the laser (natural given variation in laser power output) result in measurement 'noise' of a surface temperature measurement (Figure 3.9), and generally in non-uniformities of the laser forming process. The method proposed in

section 3.4 to use the surface temperature as additional control parameter in laser forming would accommodate any of those variations in laser light absorption.
However, coating degradation with the number of laser scan passes applied, variation of absorption and heat transmission to the work piece might reduce the process reliability. Nevertheless, as shown in the forming results presented, the iterative process design accommodated those unforeseeable non-uniformities.

Based on the method presented in section 3.4, an overall approach for the implementation of a surface temperature control in the ILF process would require material-specific databases for minimum and maximum sample thickness, relating bend angle to LE and surface temperature to LE. The information about the plate thickness along the laser scan paths in the scan lattice could originate from the surface temperature, recorded during a pre-scan at constant LE, as shown in section 3.4. Therefore the LE for the required deformation could be adjusted, based on the surface temperature of this pre-scan. This approach would account for temperature rise caused by plate boundaries and surface temperature fluctuations owing to varying thickness or non-uniform laser light absorption without *a priori* knowledge. A more sophisticated approach may be to monitor the temperature on the top and bottom surfaces, or even in-process and adjust the LE accordingly. Eventually this real time control proposed was not implemented here because it was not necessary for the specimen geometries studied. The in-plane strain was not considered in this approach, because the establishment of a mechanical FE-model would require detailed knowledge of the plate thickness. However, for a class of objects with shallow bending (deformation $\leq$ plate thickness) in-plane shrinkage scans would not be necessary. Even for reasonably large deflections, sufficient in-plane strain is induced during a bending scan, as shown in section 3.3, where saddle shapes were formed with top and bottom bending scans only.

3.6 Conclusion

The implementation of a mechanical FE-analysis for the in-plane strain computation was validated through the forming of pillow and saddle shapes with low carbon steel and aluminium-copper alloy tokens. The FE-analysis was necessary for the forming of more complex geometries for example plates of varying thickness, because this was not possible with the analytical method used previously.

The ILF process was further developed to form plates of varying thickness. The modifications made were validated through 3D forming experiments of two varying thickness geometries chosen, plates with slotted recesses and plates with uniformly varying thickness. It was found that the scan path distance in the fixed scan lattice is crucial, and must be chosen suitably with respect to token thickness, and that annealing prior to forming was necessary for plates with uniformly varying thickness, because in this specific case the significant residual stress from machining adds to the thermally induced stress, which justified the annealing. Owing to these residual stresses, non-annealed samples showed buckling in the thin section of the wedge shape after laser forming. To prevent annealing, the sample thickness and thus the rigidity of the plate would have to be increased. It was also shown in the experiments that shrinkage or the SM is predominant in thinner sections and bending or the TGM is favoured in thicker sections. Therefore, a more 'conservative' forming approach, i.e. gradually increasing the target deflection with subsequent iterations and/or a dilution of the shrinkage scan (η_ε), was required to form the pillow and saddle of both geometries.

From the surface temperature, recorded with a pyrometer at a single line laser scan on plates of uniform and varying thickness, an ILF approach was sought which would choose the LE required based on the surface temperature without *a priori* knowledge of the sample thickness and without FE-model. Furthermore, any surface temperature fluctuations, for example an approaching plate boundary or non-uniform laser light absorption, could be accommodated through this supplementary control parameter. Single laser scan experiments where the LE was adjusted to the surface temperature measured at a pre-scan, showed an increase in forming accuracy compared with that of constant LE scans, which indicates that the proposed approach is feasible.

3.7 Figures

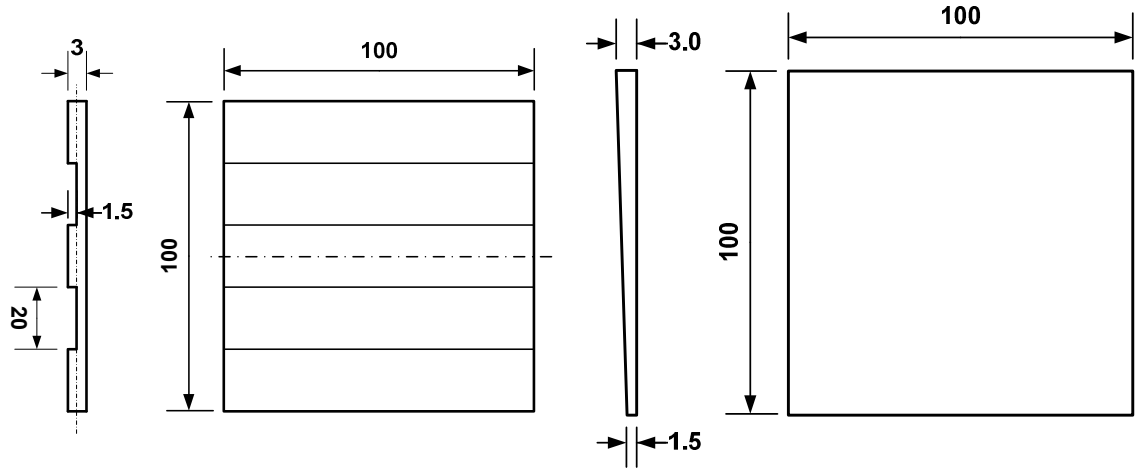

(a) (b)

Figure 3.1: Varying thickness geometries chosen; (a) Plate with slotted recesses; (b) Plate with uniformly varying thickness; (AISI1010).

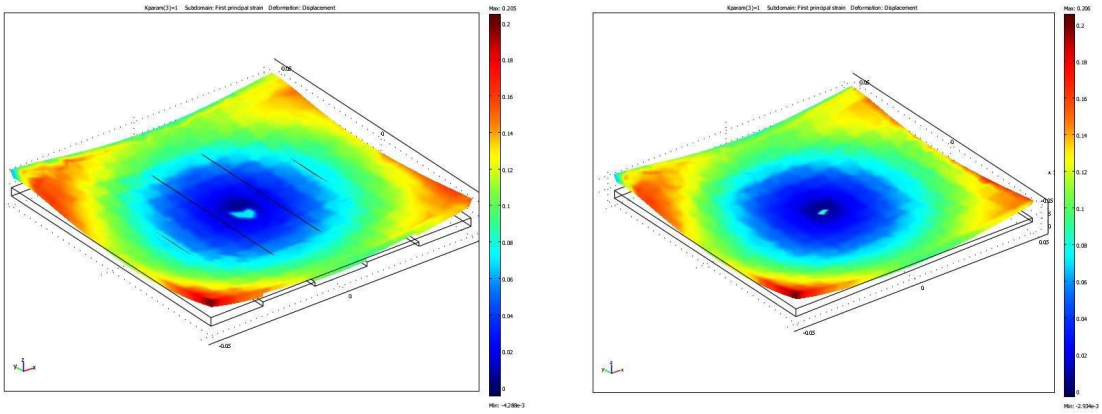

(a) (b)

Figure 3.2: First principal strain for a given displacement as output of the FE-analysis; (a) Plate with slotted recesses; (b) Plate with uniformly varying thickness; (it should be noted that the displacement as input in the model was the same in both simulations).

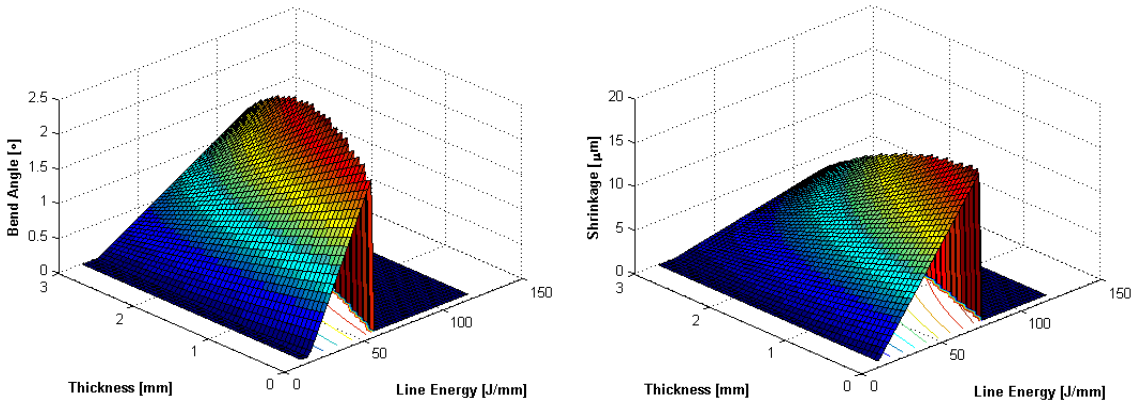

(a) (b)

Figure 3.3: Interpolation of the experimental calibration database between 1.5 and 2.8mm thickness (AISI1010); (a) Bend angle with thickness and LE; (b) Shrinkage with thickness and LE. Obtained through linear interpolation between the calibration databases in Figure 2.24(a)-(b).

Material	**Thickness [mm]**	**width x length [mm^2]**
AISI1010	1.5	80 x 80
AISI1010	2.8	100 x 100
AA2024-T3	1.5	80 x 80
AA2024-T3	3.2	120 x 120

Table 3.1: Dimensions of square plates with uniform thickness used for 3D iterative laser forming.

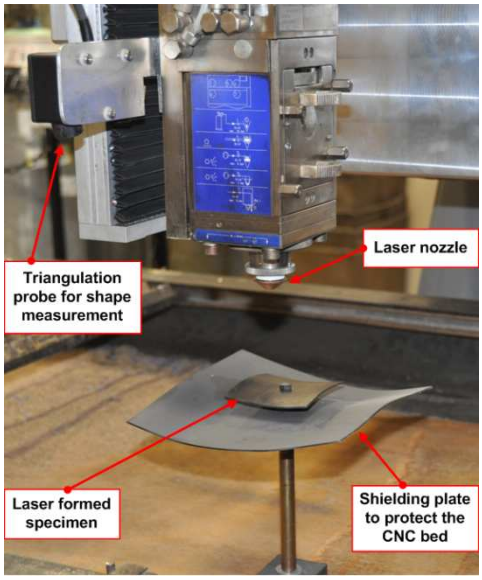

Figure 3.4: Experimental setup for 3D laser forming.

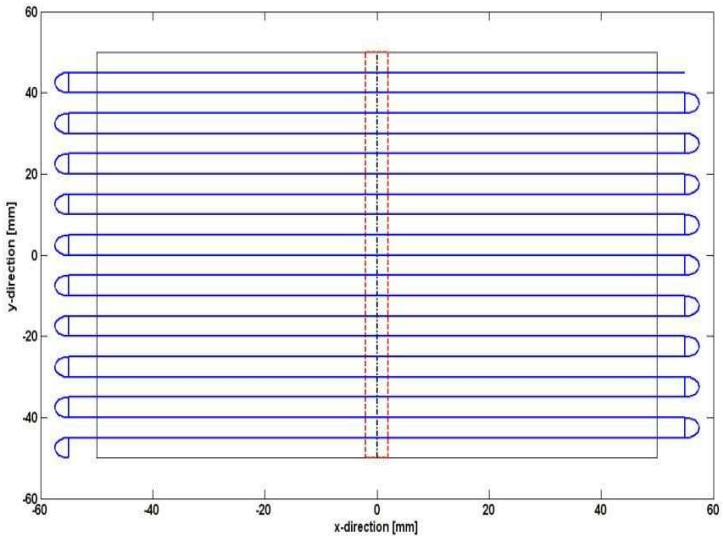

Figure 3.5: Shape scan pattern showing the individual scan lines of a shape scan (blue) for a 100x100mm^2 token.

	Target deflection [mm]	**Number of iterations**	$\left\|\frac{\kappa_y}{\kappa_x}\right\|$	***rms* error [mm]**
a) 1.5mm thickness **(η_κ = 0.3, η_ε = 0.3)**				
Pillow	6	6	0.967	0.254
Saddle	2	9	1.139	0.356
b) 3.2mm thickness **(η_κ = 0.6, η_ε = 0.6)**				
Pillow	8	4	0.981	0.325
Saddle	4	12	0.875	0.479

Table 3.2: Target deflection, final symmetry and final *rms* error of the most accurate forming approaches for AA2024-T3 tokens; (a) Thickness 1.5mm; (b) Thickness 3.2mm.

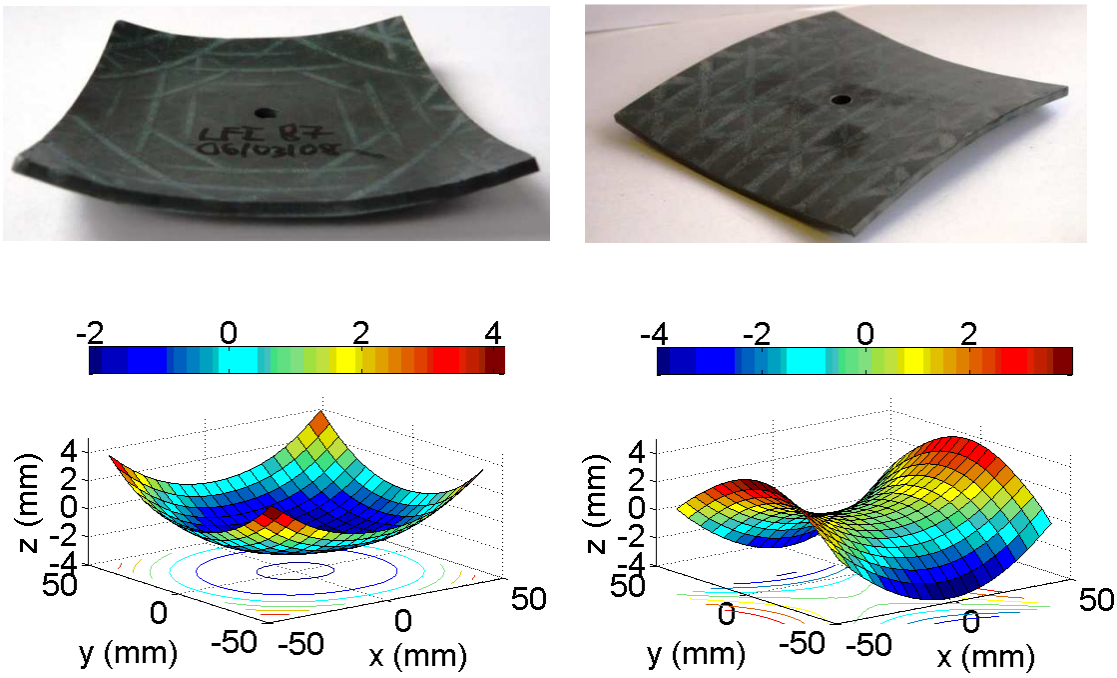

(a) (b)

Figure 3.6: Example of (a) pillow and (b) saddle shape; (sample: AISI1010, thickness 2.8mm).

	Target deflection [mm]	**Number of iterations**	$\left\|\frac{\kappa_y}{\kappa_x}\right\|$	***rms* error [mm]**
a) 1.5mm thickness **(η_κ = 0.2, η_ε = 0.02)**				
Pillow	6	10	0.936	0.235
Saddle	6	8	0.843	0.453
b) 2.8mm thickness **(η_κ = 0.7, η_ε = 0.07)**				
Pillow	8	4	0.941	0.201
Saddle	6	8	0.961	0.457

Table 3.3: Target deflection, final symmetry and final *rms* error of the most accurate forming approaches for AISI1010 tokens; (a) Thickness 1.5mm; (b) Thickness 2.8mm.

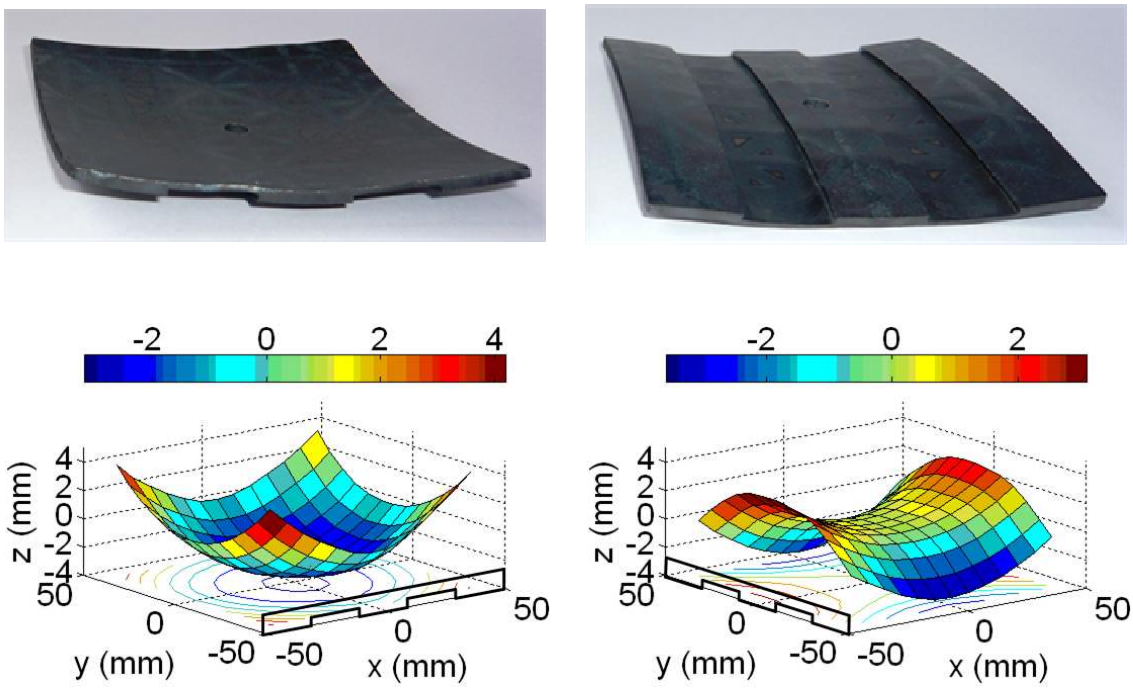

(a) (b)

Figure 3.7: Example of (a) pillow and (b) saddle shape for tokens with slotted recesses (AISI1010). The colour scale of the vertical z-deflection is in [mm].

	Target deflection [mm]	**Number of iterations**	$\left\|\frac{\kappa_y}{\kappa_x}\right\|$	***rms* error [mm]**
Pillow	8	7	0.998	0.214
Saddle	6	10	0.874	0.842

Table 3.4: Target deflection, final symmetry and final *rms* error of the most accurate forming approaches on plates with slotted recesses ($\eta_\kappa = 0.7$ and $\eta_\varepsilon = 0.07$).

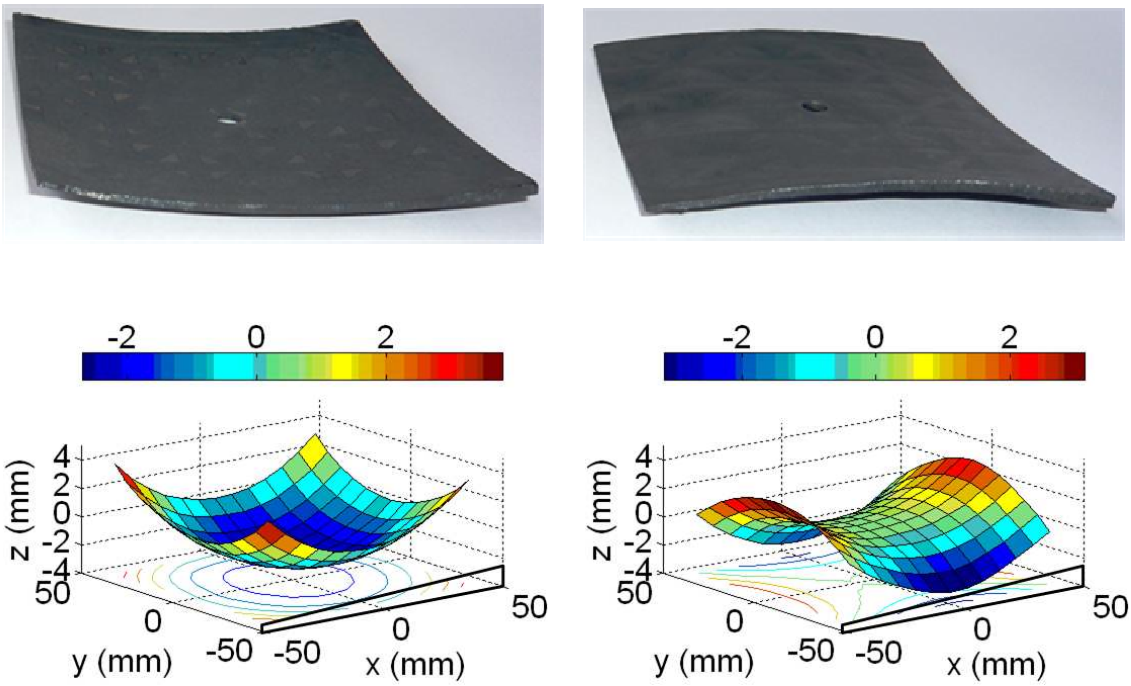

(a) (b)

Figure 3.8: Example of (a) pillow and (b) saddle shape for tokens with uniformly varying thickness (AISI1010). The colour scale of the vertical z-deflection is in [mm].

	Target deflection [mm]	**Number of iterations**	$\left\|\frac{\kappa_y}{\kappa_x}\right\|$	***rms* error [mm]**
Pillow	8	6	1.172	0.330
Saddle	6	8	1.005	1.010

Table 3.5: Target deflection, final symmetry and final *rms* error of the most accurate forming approaches on uniformly varying thickness plates ($\eta_\kappa = 0.7$ and $\eta_\varepsilon = 0.02$); (tokens were annealed prior to laser forming [114]).

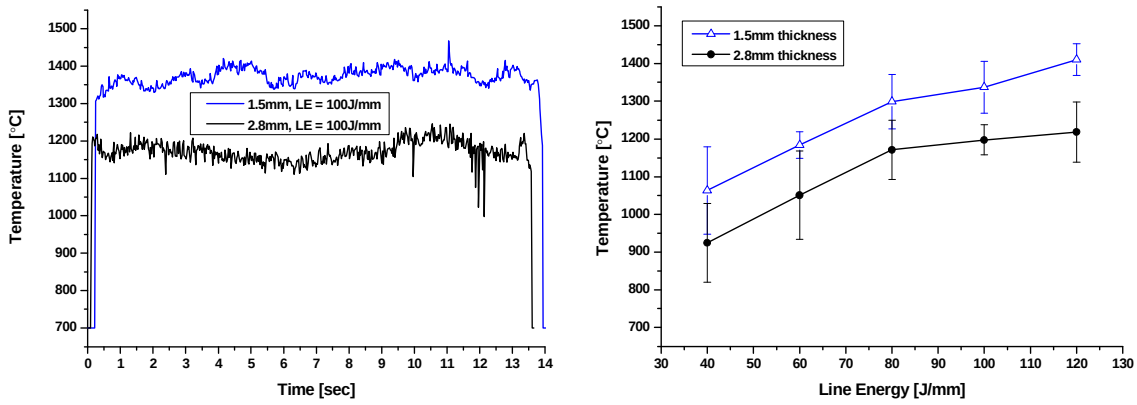

(a) (b)

Figure 3.9: Surface measurement with the pyrometer; (a) Uniform thickness plates; (b) Surface temperature variation with LE at 1.5mm and 2.8mm thickness (AISI1010).

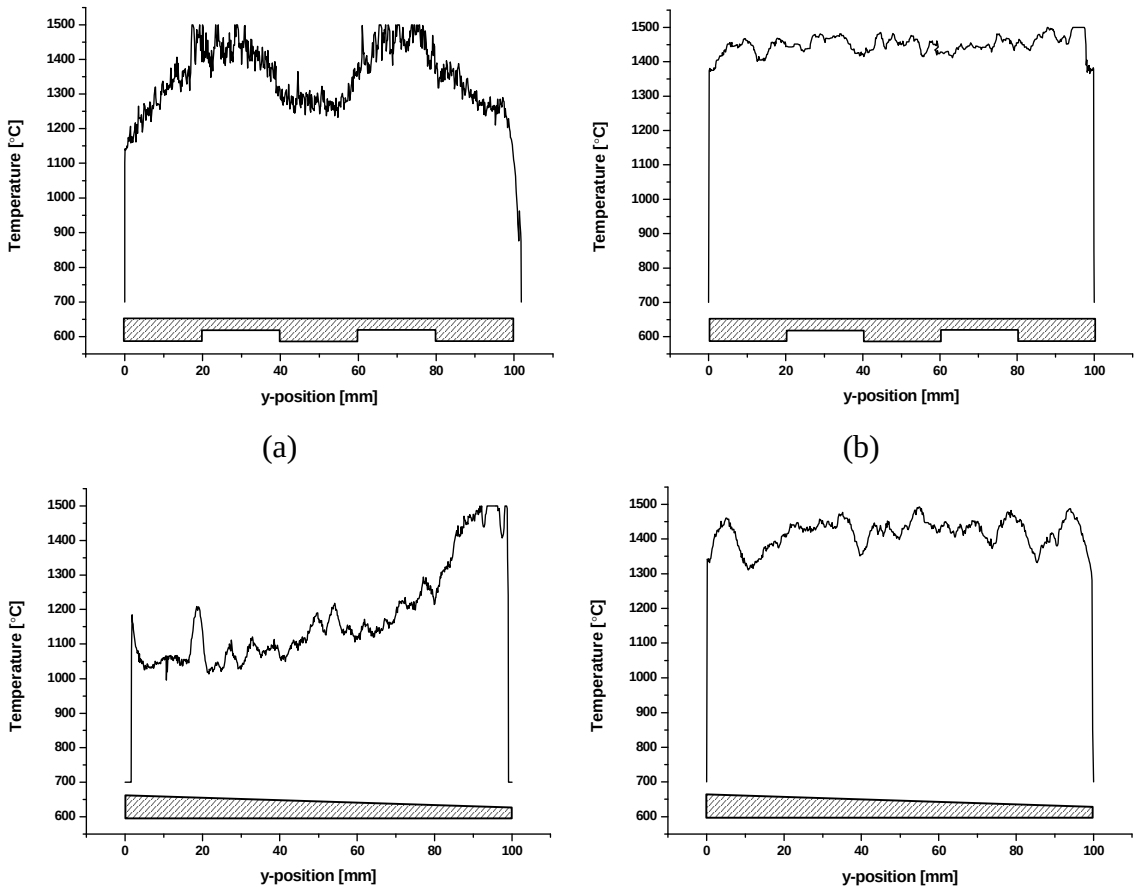

Figure 3.10: Surface temperature, measured with the pyrometer along the laser scan line; (a) Plate with slotted recesses LE = 100J/mm; (b) Plate with slotted recesses and adjusted LE for constant surface temperature $T_{surface} = 1200℃$; (c) Plate with uniformly varying thickness LE = 100J/mm; (d) Plate with uniformly varying thickness and adjusted LE for constant surface temperature $T_{surface} = 1200℃$; (AISI1010).

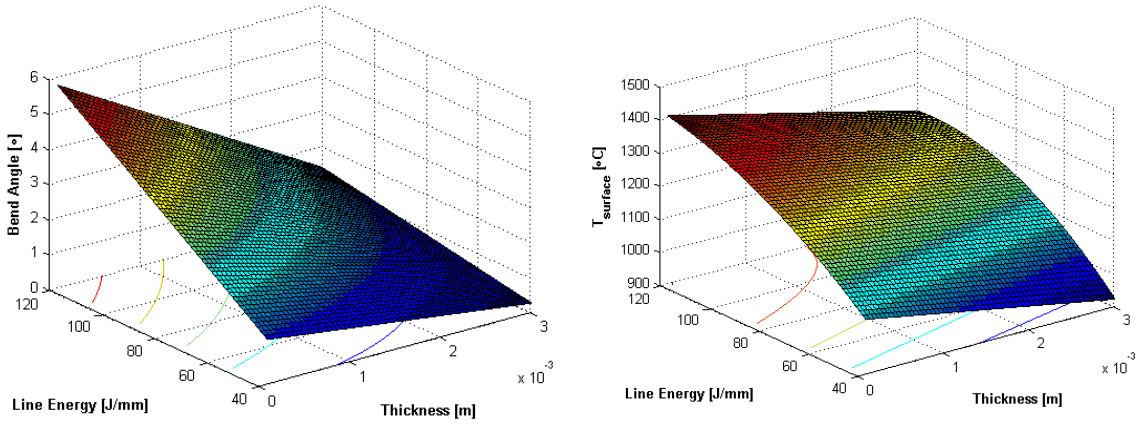

(a) (b)

Figure 3.11: (a) Bend angle related to plate thickness and LE (linear interpolation between Figure 2.24[a] & [b]); (b) Surface temperature related to plate thickness and LE (linear interpolation between both graphs in Figure 3.9[b]).

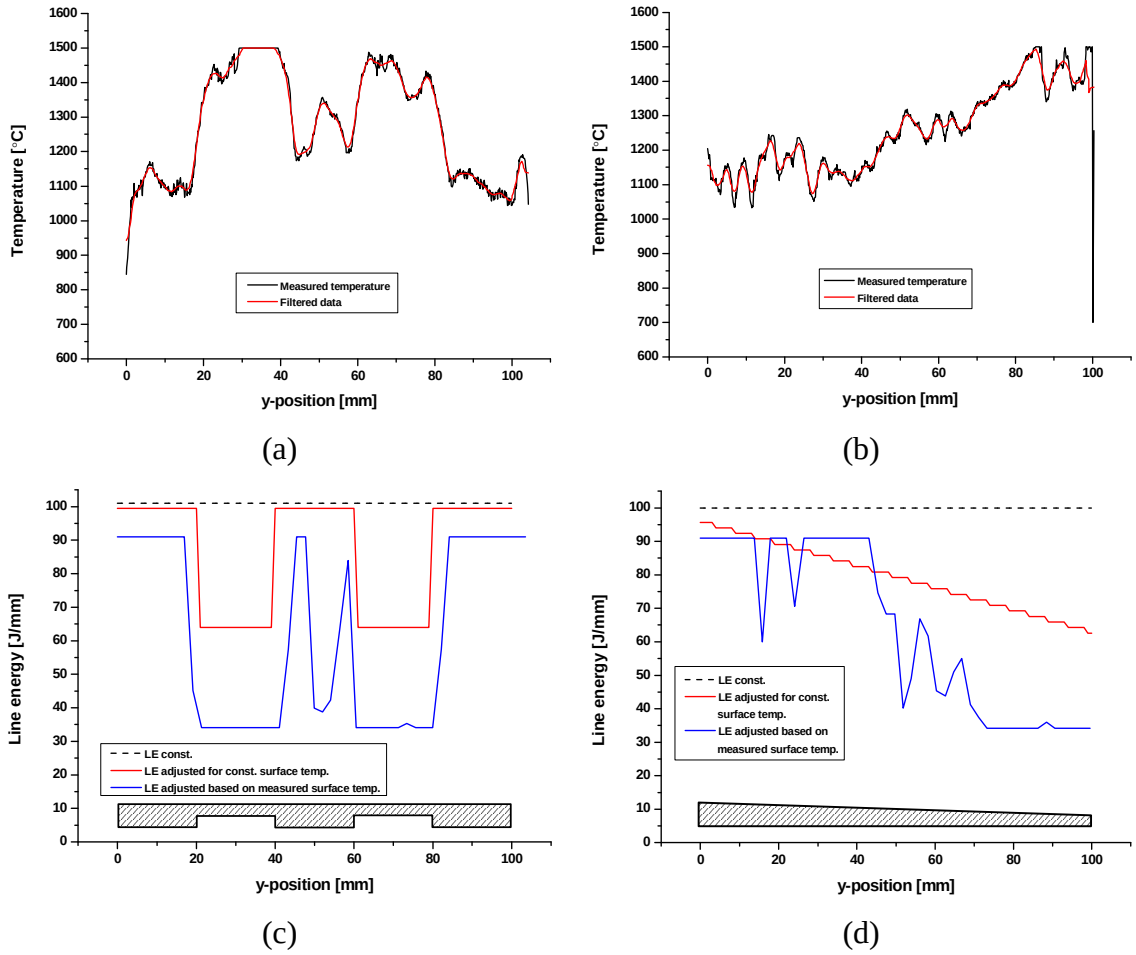

Figure 3.12: Surface temperature measurement at LE = 100J/mm and the effect of filtering; (a) Plate with slotted recesses; (b) Plate with uniformly varying thickness. The three cases of LE profiles applied; (c) Plate with slotted recesses; (d) plate with uniformly varying thickness. LE = constant (black dashed); LE adjusted for constant surface temperature of 1200℃ (red); LE adjusted based on previously measured surface temperature at LE = 100J/mm shown in (a)-(b) (blue).

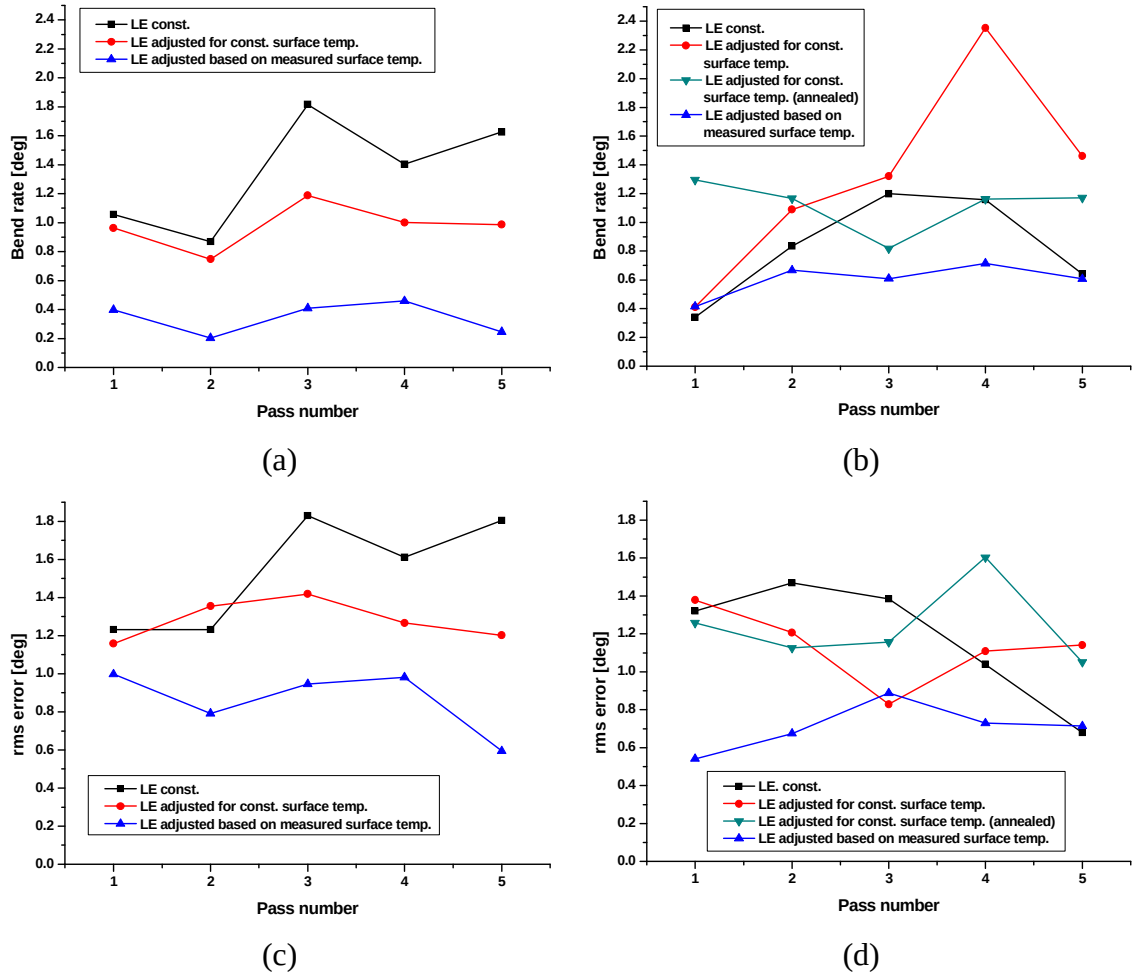

Figure 3.13: Bend rate per pass and *rms* error along the scan path; (a) & (c) Token with slotted recesses; (b) & (d) Token with uniformly varying thickness.

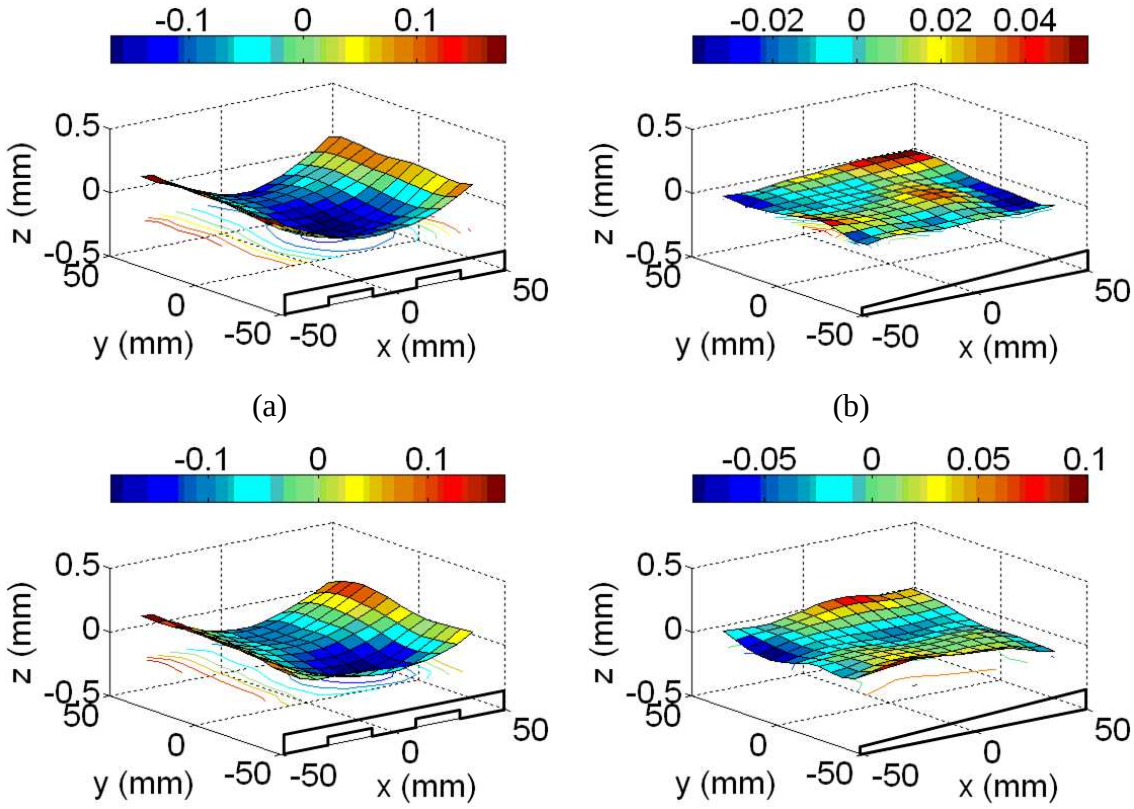

Figure 3.14: Measured shape of the initial state after milling; (a) Plate with slotted recesses; (b) Plate with uniformly varying thickness. Measured shape of the same samples after annealing (at 650℃ - 700℃ for ~ 1h10min. [114]); (c) Plate with slotted recesses; (d) Plate with uniformly varying thickness (machined surface is bottom surface). The colour scale of the vertical z-deflection is in [mm].

Figure 3.15: Characteristic residual stress (RS) distribution (longitudinal RS solid line, transverse RS dashed line) in steels as a result of face-milling with perpendicular cutting axis [115,116]; (a) Milling to produce slotted recesses; (b) Milling of the wedge shape.

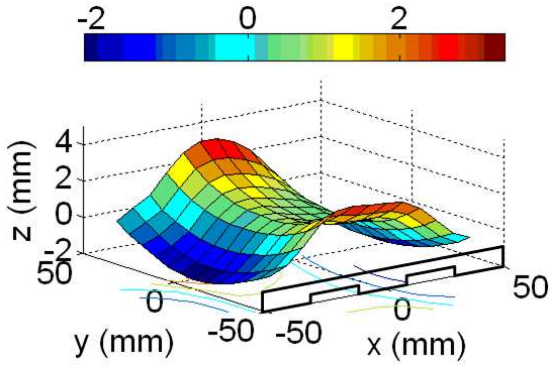

Figure 3.16: Buckling/non-uniform bending of a token with slotted recesses, scan path distance applied was 10mm. The colour scale of the vertical *z*-deflection is in [mm].

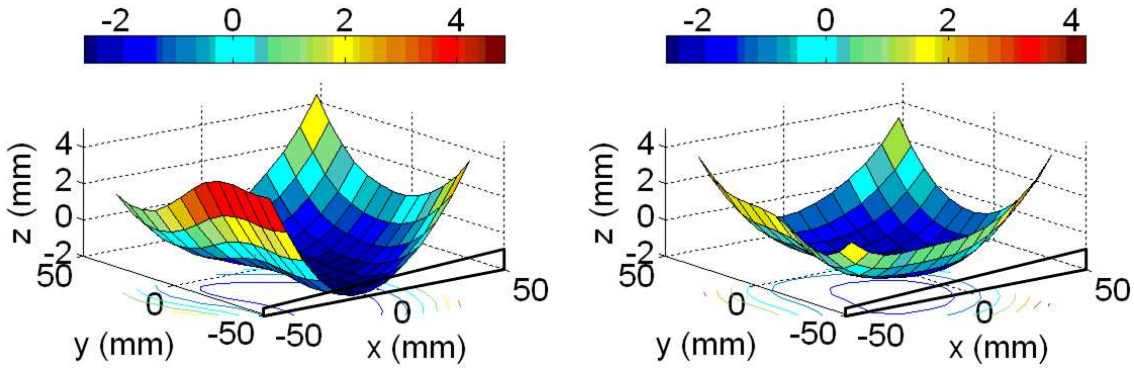

(a) (b)

Figure 3.17: Unsuccessful trials to form a pillow shape with uniformly varying thickness tokens; (a) Sample not annealed; (b) Sample annealed at 650℃ - 700℃ for ~ 1h10min [114]. The colour scale of the vertical *z*-deflection is in [mm].

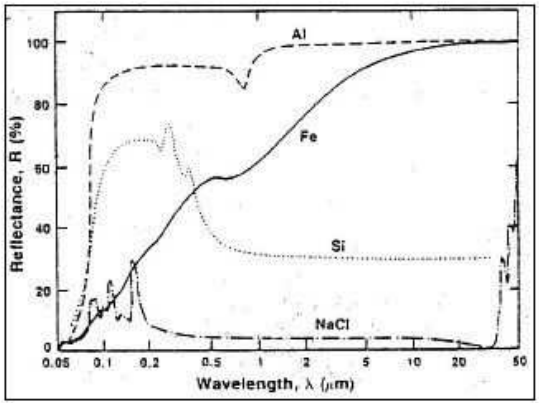

(a)

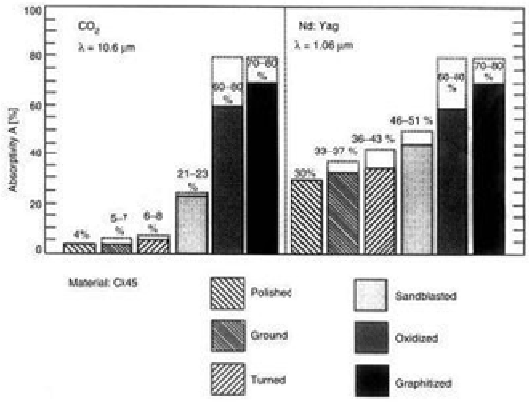

(b)

Figure 3.18: (a) Reflectivity of various metals as a function of wavelength [9]; (b) Influence of various steel treatments on the absorption of CO_2 ($\lambda = 10.6\mu m$) or Nd:YAG ($\lambda = 1.06\mu m$) laser light [118].

Chapter 4

Thermal analysis

This chapter presents the application and experimental procedure of three complementary techniques to record the temperature during a single line laser scan. The thermocouple technique was used for low carbon steel and aluminium-copper alloy tokens to measure the temporal temperature cycle at different points through sample thickness. Non-contact temperature measurements with pyrometer and infrared (IR) camera recorded the surface temperature during a single line laser scan. Because of the lower temperature range applied during laser forming of an aluminium-copper alloy (AA2024-T3) compared with that of low carbon steel (AISI1010) non-contact surface temperature measurement techniques could not be applied. Thereafter, the development of a thermal FE-analysis is shown, which was calibrated through temperature measurements with the thermocouples and applied to investigate further the temperature field through depth and on the sample surface, produced during a single line laser scan.
The surface temperature measurement with the pyrometer was used in the previous Chapter for adjusting the LE. The through thickness temperature measurement with thermocouples will be used in Chapter 5.

4.1 Thermocouple temperature measurement

During a single line laser scan the temperature was recorded with thermocouples at different positions through depth of low carbon steel and aluminium-copper alloy tokens. The thermocouples used in this measurement were beaded-welded unsheathed ‘K Type’ thermocouples. ‘Type K’ thermocouples comprise a welded chromel-alumel junction, where cromel (Nickel-10% Chromium) is positive relative to alumel (Nickel-5% Aluminium). This welded junction has a reliable linear temperature range of $-200℃$ - $1250℃$. The thermocouple wire was 0.25mm thick which provided a fast response time (sampling frequency during the experiment was 100Hz). The thermocouples were supplied with calibration certificate (supplier OMEGA®) and the measurement uncertainty was given with $2.0℃$ or 2%, dependent on which is greater.

For the through thickness temperature measurement, the unsheathed thermocouple wires were run in a round, two hole ceramic insulator to suppress measurement noise and spurious temperature readings resulting from the wires touching the sample. Holes

were drilled into the rear surface along the centreline of each token in the middle of the laser scan line, using a milling machine to ensure maximum accuracy in hole depth and position (Figure 4.1). Per token, four thermocouples for AISI1010 (plate size 100x100x2.8mm^3) and five thermocouples for AA2024-T3 (plate size 120x120x3.2mm^3) were glued on the bottom surface with the beaded-welded tip touching the top surface of the drilled blind hole (Figure 4.1). Because of the high temperature expected, although glued on the bottom sample surface, a high temperature chemical set cement (OB-600 OMEGABOND^{TM}, supplier OMEGA$^{®}$) was used.
During laser forming the tokens were clamped on one side, as shown in Figure 2.22. Between subsequent laser scans, 60 seconds were allowed for the token to cool down in order to minimise the increase in bulk temperature. The laser settings applied were a constant beam diameter of 9mm and a constant laser power of 600W for low carbon steel and 1000W for AA2024-T3 respectively. The tokens were coated with graphite following the standard procedure (section 3.2). Each specimen was then scanned with a particular laser line energy and the temperature distribution during the scan recorded with a data logger.

Figure 4.2 shows typical temporal thermal cycles experienced at different depths through low carbon steel (Figure 4.2[a-b]) and aluminium-copper alloy (Figure 4.2[c-d]) tokens, recorded during a laser scan at LE = 60J/mm and LE = 100J/mm. Because of the lower thermal conductivity of low carbon steel $\left(k = 41.5\frac{W}{Km}\right)$ compared with that of aluminium-copper alloy $\left(k = 120\frac{W}{Km}\right)$, peak temperatures reached are higher despite the LE applied being the same. The slight increase in cooling rate, most clearly shown for example in Figure 4.2(b) after ~15 seconds and in Figure 4.2(d) after ~ 12.5 seconds is caused by an airstream (~ 1bar) blowing from the laser nozzle. After finishing the laser scan and closing the shutter, the CNC table positioned itself, so that the laser nozzle with the airstream was over the centre of the sample. As cooling of the sample at that stage has already proceeded to $\leq 150℃$, the increase in cooling rate through the airstream has no effect on the laser forming process itself.
The peak through thickness temperature of low carbon steel and aluminium-copper alloy are shown in Figure 4.3(a) and Figure 4.3(b) respectively. Each point of the through thickness temperature profiles is the average peak temperature of two individual tests undertaken for each particular LE, as shown in Figure 4.2. The difference between both separate readings was within ± 10% for all measurements.

4.2 Experimental procedure for pyrometer measurement

To record the surface temperature along the laser scan path in the laser spot, a two-colour pyrometer was used (Figure 4.4). This measurement device makes use of IR radiation emitted in the wavelength range of $\lambda_{IR} = 0.75 - 14\mu m$ by a surface, based upon individual temperature, which can be explained according to the black body radiation laws [119,120]. The IR energy received from a target is then focused onto a detector which produces an electric output directly related to the radiant energy received.

A two-colour pyrometer applies the concept of colour or ratio temperature which is used if the target emissivity is uncertain or may vary, such as for graphite-coated low carbon steel samples, used in the laser forming experiments. By definition the colour temperature T_C of a target is given by the equality of ratios at two different wavelengths, λ_1 and λ_2 close to each other (later referred to as 'wide band' and 'short band').

$$\frac{E_{a\lambda_1}(T_a)}{E_{a\lambda_2}(T_a)} = \frac{E_{b\lambda_1}(T_c)}{E_{b\lambda_2}(T_c)} \tag{4.1}$$

As shown in equation (4.1), the ratio of spectral emissive powers at two wavelengths λ_1 and λ_2 of the actual body E_a (at the actual temperature T_a) is the same as that of the corresponding one of the black body E_b. A double wavelength pyrometer (like the one used for the surface temperature measurements in this study) measures the ratio of the actual emissive powers $\frac{E_{a\lambda_1}(T_a)}{E_{a\lambda_2(T_a)}}$, shown in the left hand side of equation (4.1). The actual temperature T_a finally depends on this ratio of emissive powers and the ratio of the emissivities $\frac{\varepsilon_2(\lambda_2)}{\varepsilon_1(\lambda_1)}$ in the two spectral bands. For the surface temperature measurements during laser forming of low carbon steel plates in this study, the ratio of emissivities (or slope) was equal to one, as depicted in the pyrometer manual [121] for metals with oxidized, non-polished surfaces (they behave as grey bodies).

The surface temperature of low carbon steel samples was recorded during laser forming with a two-colour pyrometer (type: RAYTEK FR1BCF2). It measured the emissive power or radiance in two different wavebands: the wideband ($0.75\mu m \leq \lambda \leq 1.1\mu m$) and the narrowband ($0.95\mu m \leq \lambda \leq 1.1\mu m$). This measurement device was chosen because the errors caused by obstructions in the field or intensity variations in the pyrometer spot, as they could potentially occur during a laser scan, were suppressed

owing to the proportional ratio of detected energy in the two wavebands, chosen close to each other. Figure 4.4 shows the experimental setup for the surface temperature measurement. The focal distance f_d from pyrometer to sample surface was 340mm at an angle $\alpha \approx 30°$ to the vertical. This focal distance gave a pyrometer spot diameter of ~ 9mm, which was equal to the laser beam diameter applied. For the measurement, the pyrometer spot was adjusted to be coincident with the laser spot (Figure 4.4). The uncertainty of the measurement recorded was given with ± 0.75% [121].

4.3 Experimental procedure and calibration for the infrared (IR) camera

During laser forming experiments, the IR camera monitored the surface temperature of a whole plate section comprising the scan path (Figure 4.5), to show the lateral temperature field and how it was affected, for example, through a varying sample thickness. The Electrophysics camera (type: PV 320 – L2E) used in these experiments was highly versatile in that manual control was given to the gain and levels at which the camera was operated. However, no direct temperature reading could be taken from the sensor, thus creating an un-calibrated system. For the calibration of this system, readings of known temperatures across the thermal gradient would need to be obtained in order to match the output counts from the camera to the intensity of light emitted from the sample plate. The camera's maximum frame rate was 25 frames per second with a full frame, 320x240 pixels of which are 48.5 microns in pitch.

When using the IR camera with a CO_2 laser, an additional filter had to be used to suppress the characteristic CO_2 laser wavelength of $10.6\mu m$. The transmission profile [122] of the 2mm thick sapphire filter, which was placed in front of the optics, is shown in Figure 4.6. Combining the spectral response of the camera, which was between $2\mu m$ and $14\mu m$, and the filter transmittance, a range from $2\mu m$ - $5\mu m$, where the intensity of light across a wavelength would remain at a relatively constant level was selected to account for the filter transmittance,

$$transmittance = -0.06 \cdot \lambda \left[\frac{1}{\mu m}\right] + 0.96 \quad [2\mu m \leq \lambda \leq 5\mu m] \qquad (4.2)$$

This transmittance, equation (4.2), was obtained through linear interpolating between a wavelength of $2\mu m$ and $5\mu m$ (Figure 4.6). Therefore the system (camera and filter) only yields a spectral response between the wavelengths of $2\mu m$ - $5\mu m$. The lower limit is due to the camera specifications and the upper limit is due to the filter transmittance. Based on Planck's radiation law [119,120], the camera can detect temperatures starting

at $\sim 600℃$ - $700℃$. At lower temperatures, the maximum of emissive power is reached at wavelengths greater than $5\mu m$ and is therefore suppressed by the filter.

The output of the IR camera in the form of an intensity number, referred to as #counts, was related to a material specific temperature through calibration experiments, employing a Carbolite tube furnace to heat the low carbon steel samples to a temperature ranging from $600℃$ to $1300℃$. It should be noted that the calibration samples were not coated with graphite, because of the long term exposure to high temperatures ($T \geq 600℃$), which would have 'burnt-off' and degraded the graphite coating.

The experimental setup of the calibration experiment is shown in Figure 4.7. Temperature readings were taken in increments of $50K$, by removing the alumina bung and recording five exposures with an exposure time of 0.04 seconds per exposure. The bung was then replaced again and the temperature was reset for the next reading. To ensure correlation between sample surface temperature and oven temperature, an additional temperature reading with a handheld pyrometer was taken during exposures. The camera generated a greyscale image from which the individual sensor pixel counts were extracted using LabView^{TM}. By taking these data from a line drawn across the AISI1010 sample, each pixel across the 5 exposure images was then averaged to give a mean pixel count along that line. The average along this line gave the mean pixel count for the specified temperatures, as shown in the final calibration graph (Figure 4.8) for IR camera settings of level 8, gain 4 and a focal distance of 350mm. The error bars in the experimental calibration graph in Figure 4.8 indicate the standard deviation from the mean over five repeated calibration measurements per temperature. All calibration settings were carefully kept constant for any further temperature measurements during laser forming.

The experimental calibration graph relating #counts to temperature is shown in Figure 4.8. The remarkable flattening off seen at a temperature of $\sim 950℃$ could be owing to different reasons. First, if steel is exposed to temperatures in the range from $600℃$ - $1200℃$ it changes its temper colour from 'brown red' to 'white' respectively [123]. The temper colour transition between red and yellow takes place between $900℃$ - $1000℃$ and might decrease the emitted power to such an extent that a proportionally lower number of counts would be detected by the IR camera. Another additional effect could be the phase change from α-ferrite to γ-austenite, which takes place at $\sim 900℃$ for low

carbon steel [128]. Further, the experimental calibration graph (Figure 4.8) was matched with theory for an emissivity of $\varepsilon_1 = 0.75$ between $600℃ \leq T_1 \leq 948℃$ and $\varepsilon_2 = 0.5$ between $948℃ < T_2 \leq 1300℃$. Evidence of this decrease in emissivity of cold rolled steel with temperature was found in the literature [124], where the emissivity at 93℃ was given between 0.75 - 0.85 and at 938℃ - 1099℃ between 0.55 - 0.61. These effects explained the shape of the calibration graph and validate the calibration for use in the further experiments. Therefore, in the following measurements, the intensity (#counts) was related to temperature with equation (4.3) and equation (4.4), obtained through fitting the calibration graph in each of the two temperature intervals identified.

$$\#counts = 0.0091 \cdot T^2 - 11.022 \cdot T + 5036.3 \quad for\ 600℃ \leq T \leq 948℃ \tag{4.3}$$

and

$$\#counts = 0.0027 \cdot T^2 - 2.6302 \cdot T + 2.833.2 \quad for\ 948℃ < T \leq 1300℃ \tag{4.4}$$

An example of a calibration image taken at 1100℃ in false colour is shown in Figure 4.9. The 'raw' image with the intensity (#counts) is shown in Figure 4.9(a) and the corresponding conversion to a temperature using equation (4.3) and (4.4) from the calibration curve is shown in Figure 4.9(b).

4.4 Application of temperature measurements

The three complementary temperature measurement techniques described in the previous sections were fundamental for process understanding and interpreting results throughout this study. Where those temperature measurements were used is briefly described in the following section.

The surface temperature was monitored with a pyrometer and IR camera during single line laser scans to further investigate and understand the temperature field for the forming of uniform, and in particular varying thickness plates. The results of the pyrometer measurement fed into the proposed ILF approach, section 3.4 and 3.5, which would use the surface temperature monitored to adjust the LE in-process to the plate thickness and unforeseeable process non-uniformities. For this method, the pyrometer would be essential to enhance forming accuracy.

Temperature cycles at different depths were recorded with thermocouples. This measurement allowed the identification of the through thickness temperature profile in the HAZ and bulk material, produced during a single laser scan across a sample. Through the temperature profile, zones were identified which provided the basis and validation of the microstructural evolution that occurred in the material during laser processing, as shown in Chapter 5. Furthermore, those thermocouple measurements were used to validate a thermal FE-analysis, described in the following section, and to adjust through thickness temperature profiles, predicted by the analytical-numerical model (section 6.2.).

4.5 Thermal FE-analysis

In this section, the background and development of a thermal FE-analysis are described. Hereafter, the calibrated model (section 4.6) was applied to laser formed cross sections of 2.8mm thick low carbon steel tokens and compared with surface temperature measurements from pyrometer and IR camera (section 4.8).

Figure 4.10 shows the token geometry, which is the domain Ω investigated in this thermal FE-analysis, and the relevant subdomains, i.e. top surface, Γ_{Top}, and bottom and side surfaces, $\Gamma_{Bottom/Sides}$. The space coordinates are denoted by $\{x, y, z\} \in \Omega^3$, where $\Omega \in R$ and R is the space of real numbers. The time is denoted with $t \in I$, where I is the time interval of investigation. Then $T(x, y, z, t)$ is the temperature calculated at a point $[x, y, z]$ at time t and $T_m(x, y, z, t)$ is the temperature measured with a thermal sensor at point $[x, y, z]$ at time t. The classic transient heat conduction for an immobile body with no internal heat production $(q = 0)$ is considered in the token geometry Ω,

$$\rho C_p \frac{\partial T}{\partial t} - \nabla \cdot (\mathrm{k}\nabla \mathrm{T}) = \mathrm{q} \qquad \Omega \times I \qquad (4.5)$$

where ρ is the density, C_p the specific heat and k the thermal conductivity of the sample material; ∂ and ∇ are mathematical operators which denote the partial derivative (scalar) and space derivative (vector) respectively. On its top surface, Γ_{Top}, the sample is exposed to the laser heat flux φ_l and heat losses through convection and radiation,

$$-k \frac{\partial T}{\partial n_{Top}} = \xi (T - T_{room}) + \varepsilon_G \sigma (T^4 - T_{room}^4) + \varphi_l(x, y, t) \qquad \Gamma_{Top} \times I \qquad (4.6)$$

where n_{Top} is the exterior normal to the surface Γ_{Top}, ξ the convective heat exchange coefficient, T_{room} the room temperature, ε_G the emissivity of the graphite coating and σ the Boltzmann constant $[5.67 \cdot 10^{-8}\, W \cdot (m^2 K^4)^{-1}]$. Bottom and side surfaces are not exposed to the laser heat flux. Therefore the boundary conditions for $\Gamma_{Bottom/Sides}$ consider only convective and radiation losses,

$$-k\frac{\partial T}{\partial n_{Bottom/Sides}} = h(T - T_{room}) + \varepsilon_M \sigma (T^4 - T_{room}^4) \qquad \Gamma_{Bottom/Sides} \times I \qquad (4.7)$$

where ε_M is the radiation of the sample material (here low carbon steel).

The thermal FE-analysis was developed using the software Comsol® Multiphysics, in the application mode '3D General Heat Transfer'. The geometry investigated was divided into three subdomains, as shown in Figure 4.11(a), where the red coloured subdomain is coincident with the laser scan path applied. In this subdomain, the coarse mesh was discretized more finely (element size of 0.0012) compared with that of the subdomains on either side of the laser scan path (element size 0.05). The computation time was thereby reduced but the requirements for the spatial discretization in the area of particular interest were still met, as stated in [45] (two elements per radius and three elements through thickness). Temporal discretization of all simulations was set to 0.1 seconds in a time interval between 0 and 40 seconds [45], which took about six minutes' runtime on a 2.5GHz processor with 4GB memory.

The laser material interaction was modelled with a Gaussian function [125], after Goldak,

$$\varphi_l(x, y, t) = 2\eta \frac{P_l}{\pi R_l^x R_l^y} \cdot exp\left[-2 \cdot \left(\frac{\left(x - x_l(t)\right)^2}{R_l^{x2}} + \frac{(y - y_0)^2}{R_l^{y2}}\right)\right] \qquad (4.8)$$

where η is the absorption coefficient, P_l the laser power, R_l^x and R_l^y the laser beam radii and $x_l(t)$ and y_0 the position in x- and y-direction respectively (Figure 4.10). For a laser scan, y_0 was kept constant and $x_l(t) = v_l \cdot t = \frac{P_l}{LE} \cdot t$. Another possible way of describing the laser material interaction in laser forming is the top hat function [126]

$$\varphi_l = \eta \frac{P_l}{\pi R_l^x R_l^y} \text{ if } (x, y) \in \left[\left(\frac{x - x_l(t)}{R_l^x}\right)^2 + \left(\frac{y - y_0}{R_l^y}\right)^2\right] \leq 1, 0 \text{ else} \qquad (4.9)$$

In section 4.8, the modelling results with top hat, equation (4.9), and Gaussian function, equation (4.8), are compared. However, if not mentioned explicitly, all thermal

simulations apply a Gaussian heat flux distribution, equation (4.8), to describe the laser material interaction. The temperature dependent thermophysical material properties of AISI1010 are shown in Figure 4.12. All other material parameters applied [127] were assumed to be constant with temperature. They are shown in Table 4.1 together with the laser settings, chosen for modelling.

4.6 Validation of the thermal FE-analysis

The calibration of the thermal model was done by comparing temperatures simulated with experimental thermocouple measurements, and adjusting the absorption coefficient or coupling efficiency between laser and workpiece η in equation (4.8). Figure 4.13(a) shows a comparison between the thermal histories, measured with thermocouples at three depth positions in the sheet and the corresponding modelled thermal cycles at LE = 100J/mm. The absorption coefficient, adjusted to these thermocouple temperatures was $\eta = 0.51$. Sensor positions and LE were chosen to ensure the most stable and repeatable forming conditions for this validation. It can be seen from Figure 4.13(a) that the thermocouple measurement shows good agreement with temperatures calculated. Minor discrepancies $(< 25℃)$, are caused by uncertainties in both experiment, e.g. positional error, and model, e.g. material specific thermal conductivity at elevated temperature. The heating and cooling rates predicted show excellent agreement with experimental results. A time offset was applied in Figure 4.13, to shift the two graphs which belong together along the time scale, for clarity.

Figure 4.13(b)-(c) shows a further comparison between experimental and simulated temperatures at LE = 130J/mm (Figure 4.13[b]) and LE = 70J/mm (Figure 4.13[c]), using the absorption coefficient of $\eta = 0.51$. It can be seen that the temperature at a depth of 1.3mm is predicted less well by the model, and closer to the laser scanned surface good agreement between measured and modelled temperature is observed. Therefore, through the well-predicted thermal histories at two different line energies, the absorption coefficient was kept constant at $\eta = 0.51$ for all thermal FE-simulations presented in this study.

4.7 Application of the model

The thermal FE-analysis developed, helped to further understand the temperature field during laser forming of varying thickness plates and to adjust process parameters accordingly. For the forming of tokens with slotted recesses (section 3.3.2), the insight

on the non-uniform surface and through thickness temperature distribution when scanning across or along edges of the slots was extremely useful. Figure 4.14 shows the simulation results at different time steps t, which were chosen to show the surface temperature (in ℃) when the laser beam was scanning on a thick or a thin section (Figure 4.14[a] and [c]), or approaching an edge of the slots (Figure 4.14[b] and [d]). Similar locations were chosen for the IR-images, shown in Figure 4.15(a)-(d). As can be seen from both Figures, the more or less restricted through thickness heat dissipation affects the width and temperature of the laser heated surface spot. When scanning across an edge of a slot, the spot becomes elliptical, and its peak temperature either decreases or increases dependent on whether the edge was approached from a thick or a thin section. Clearly, these non-uniformities, seen in the surface, temperature affect the through thickness temperature gradient, as shown in Figure 4.16, and with it the bending and shrinkage induced during laser forming.

Through the thermal FE-analysis it was possible to estimate and compare the local thermal histories of the material within a cross section of the HAZ produced during a single laser scan across a sample. Such an estimation could provide the basis and validation of the microstructural evolution that occurs in the material during laser processing (Chapter 5). Therefore important physical temperature boundaries such as recrystallization, or the heating and cooling cycles induced within the material could be identified.

4.8 Discussion and conclusion

In the following paragraph the surface temperature predicted by the FE-analysis is compared with the experimental results of IR camera and pyrometer. Hereafter, potential sources of inaccuracies occurring in thermocouple and non-contact temperature measurement are identified. Finally, the influence of material and laser forming specific process parameters on the temperature, calculated with the model are discussed.

A comparison between the pyrometer surface temperature measurements on plates with slotted recesses (Figure 3.10[a]) and IR camera images (Figure 4.15) shows that both measurement results are within ~ 10% of each other. Confidence in these temperatures recorded was provided through the agreement between the two independent measurements. The surface temperature predicted by the FE-model (Figure 4.14) was

somewhat (~ 20%) lower than that of the IR camera (Figure 4.15). This lower temperature predicted could be due to the choice of coupling efficiency, which was adjusted to the through thickness temperature. Or it could be that the experimental measurements are too high because they are representative of the coating rather than the temperature of the plate surface underneath. However, the exact value of the surface temperature was not required to inform the forming strategies for plates of varying thickness.

The modelled and experimental through thickness temperature distributions are presented in Chapter 6. As shown there, the temperature predicted by the model in the upper part of the plate matches well with the experimental results, but was somewhat (~ 50%) higher in the bottom part of the plate. This effect was seen already in the comparison with the thermocouple measurements in Figure 4.13. But as shown in Chapter 6, the temperature predicted by the FE-model was a considerable improvement on the analytically-calculated through thickness temperature distribution, particularly in the upper part of the plate with the laser-formed HAZ, the region of main interest.

The following paragraph discusses a number of potential sources of inaccuracies occurring during the thermocouple and non-contact temperature measurements applied. Inaccuracies in the thermocouple measurement could originate from an error in the drilled holes, i.e. depth or lateral position, or from the poor thermal contact of the beaded-welded thermocouple junction on the bottom surface of the blind hole. The use of a milling machine for drilling the blind hole minimized the positional error to ± 0.1mm in depth and ± 0.01mm in lateral direction. The induced bending towards the laser beam during a scan, could lead to the thermocouples touching the surface of the drilled hole at the measurement start not touching the surface after the laser beam had passed their position, and thus showing a too low or sudden drop in the temperature reading. Nevertheless, the validation of the thermal FE-analysis with a realistic absorption coefficient, consistent over the LE-range applied, provided confidence for the accuracy of the through thickness temperature profiles recorded.

For surface temperature measurements with the IR camera, potential sources of errors include inaccuracies during calibration of the device, which were minimized through matching and explaining the experimental calibration graph with theory (section 4.3). Other sources include the experimental setup and camera adjustment, e.g. focal distance or aperture, which were carefully kept the same during laser forming experiments as for calibrating the device. Finally, both non-contact measurement devices, pyrometer and

IR camera, are sensitive to variation in coupled energy, owing to non-uniformities in the hand-sprayed graphite coating layer, discussed in section 3.5. Therefore, the discrepancy between simulation and surface temperature recorded may vary to a greater or lesser extent although all these effects were kept to a minimum during the calibration and laser forming experiments.

The influence of material and laser forming parameters on the temperature field simulated with the thermal FE-analysis is shown in Table 4.2. For this numerical sensitivity analysis, the thermophysical material properties were kept constant first, and one property at a time was varied ± 10%. This approach should isolate the effect on the temperature field of the single parameter varied. The LE chosen in the simulation was 100J/mm, and the effect on the temperature calculated at four through thickness positions (top surface, 0.3mm, 0.8mm and 1.3mm depth) in the centre of the sample and middle of the scan line is shown in Table 4.2 in the form of the deviation from the reference temperature in %. Finally, two simulations with temperature constant and temperature dependent thermophysical properties are compared.

The absorption coefficient η influences the temperature most significantly, evident from equations (4.8) and (4.9). With it, the coupling efficiency and thus the heat input into the material varies linearly. As expected, thermal conductivity and specific heat affect the temperature calculated to a reasonable extent, whereas the effect of the laser beam diameter is negligible in the range investigated. The choice of the heat flux distribution function for the laser beam was found to have significant influence on the temperature field. As seen from Table 4.2, a Gaussian heat flux distribution function, equation (4.8), results in a considerably higher peak temperature through depth, compared with that of a top hat function, equation (4.9). The high, short pulse peak intensity of a Gaussian heat flux distribution affects in particular the temperature field close to the top surface (Table 4.2). Temperature dependent thermophysical properties affect the temperature to a greater extent in the bottom part of the sample, mainly because temperature constant properties were chosen to be representative of low carbon steel at $\sim 500℃$. This temperature is approximately the average temperature to be expected for a scan at LE = 100J/mm in the upper half of the plate, the region of main interest in this study. Therefore, the discrepancy is smaller for near surface positions than further towards the bottom surface. Nevertheless, the overall discrepancy between both simulations was distinct, which can be seen in Table 4.2. Therefore, as shown in this numerical sensitivity analysis, absorption coefficient, thermal conductivity, specific heat and the

heat flux distribution should be considered carefully in any laser forming modelling approaches. Other parameters in the simulation, such as density, heat exchange coefficient or the emissivity of the plate surfaces were varied in the same manner, but their effect on the temperature was found to be less than 1%.

4.9 Figures

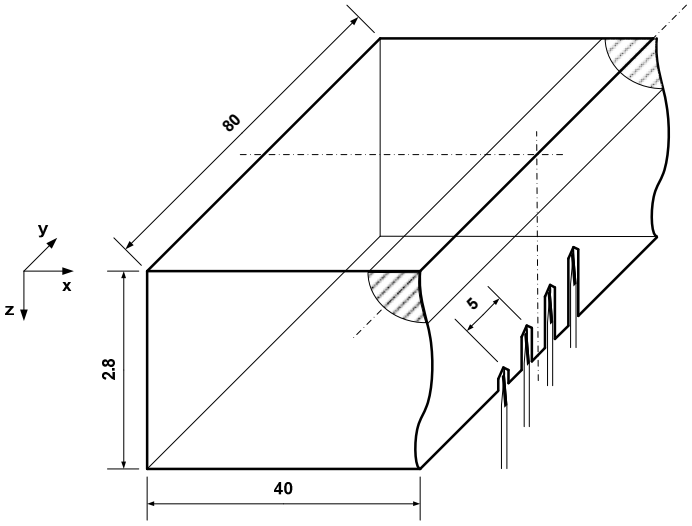

Figure 4.1: Thermocouple positions (schematically) along the scan path in the centre region of the plate (example: AISI1010 token).

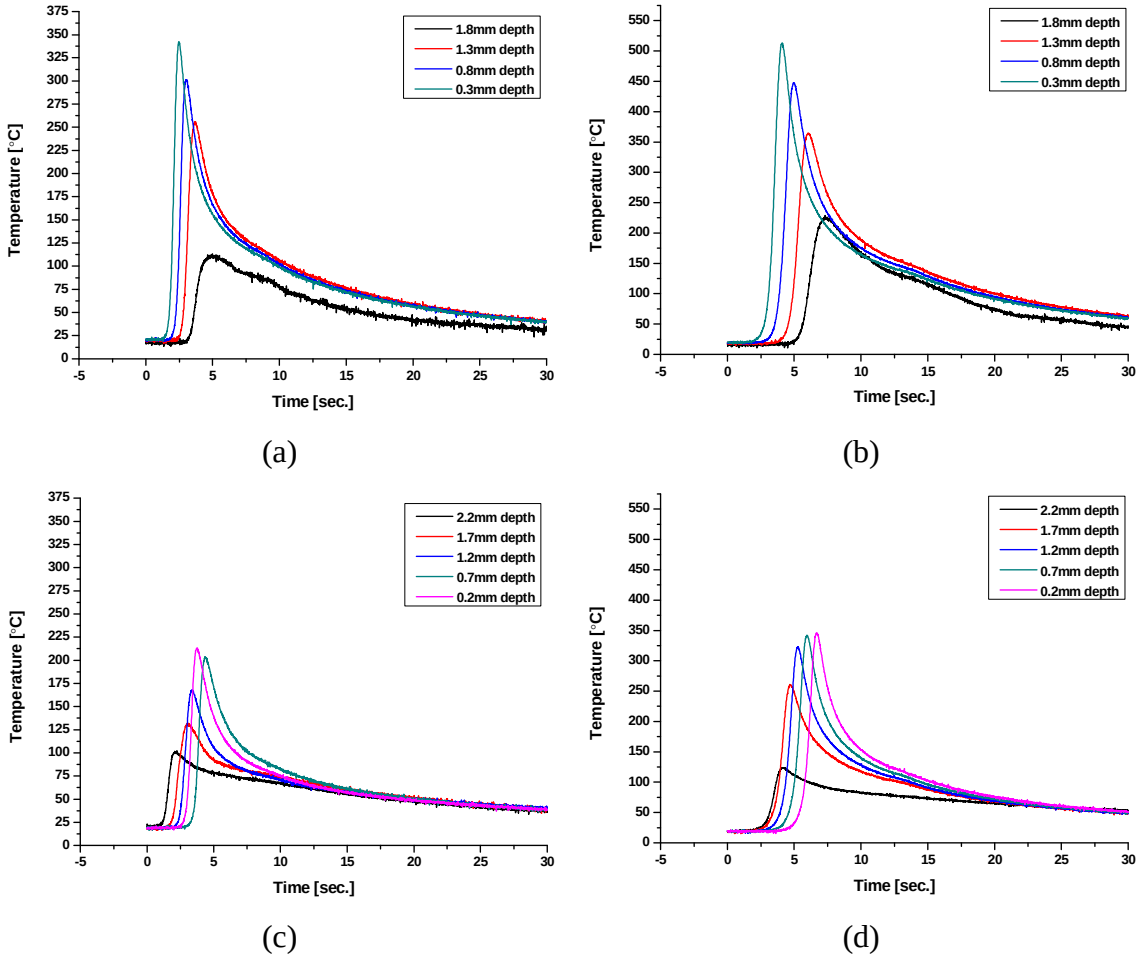

Figure 4.2: Thermocouple measurements at different depth through thickness; (a) LE = 60J/mm (AISI1010); (b) LE = 100J/mm (AISI1010); (c) LE = 60J/mm (AA2024-T3); (d) LE = 100J/mm (AA2024-T3); Laser scanned surface is reference for depth positions.

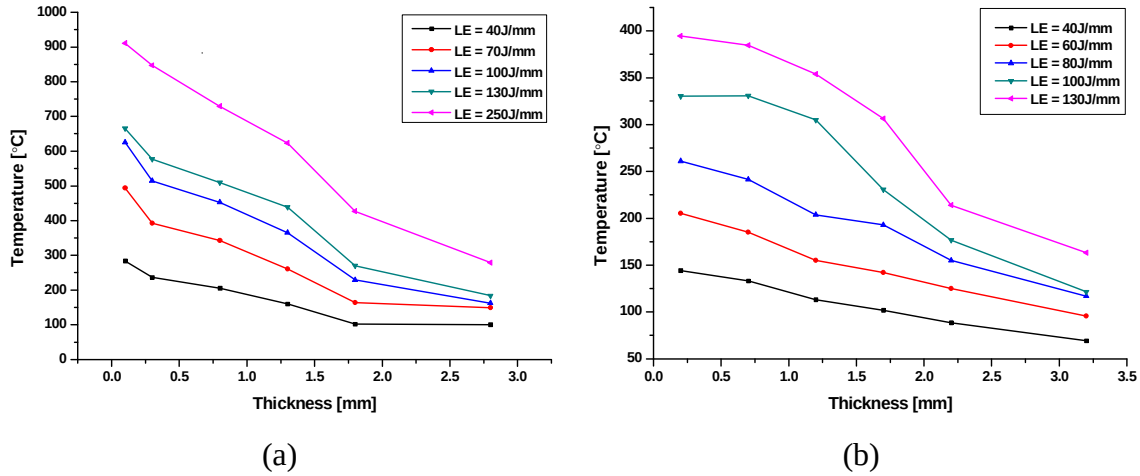

Figure 4.3: Through thickness peak temperature profiles at different line energies; (a) AISI1010; (b) AA2024-T3.

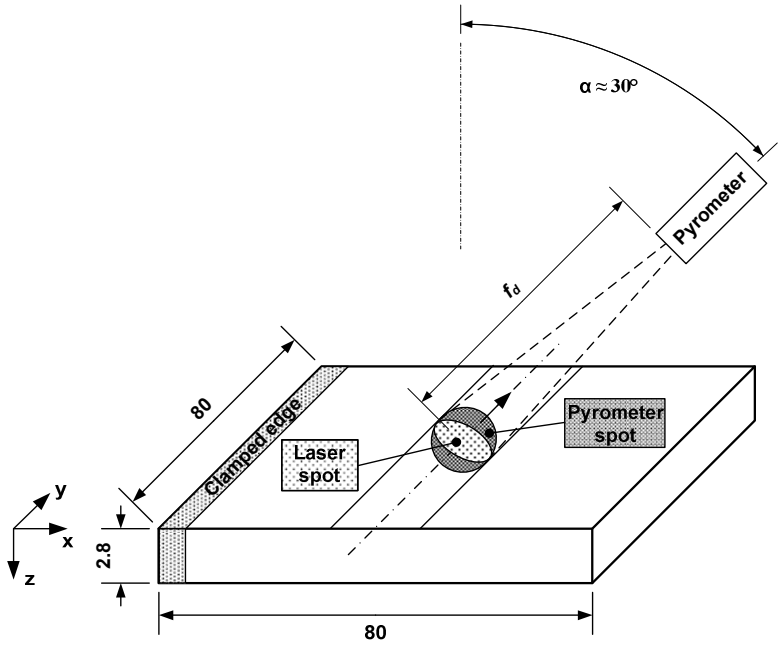

Figure 4.4: Experimental setup (schematically) for the surface temperature measurement of low carbon steel samples with the two-colour pyrometer.

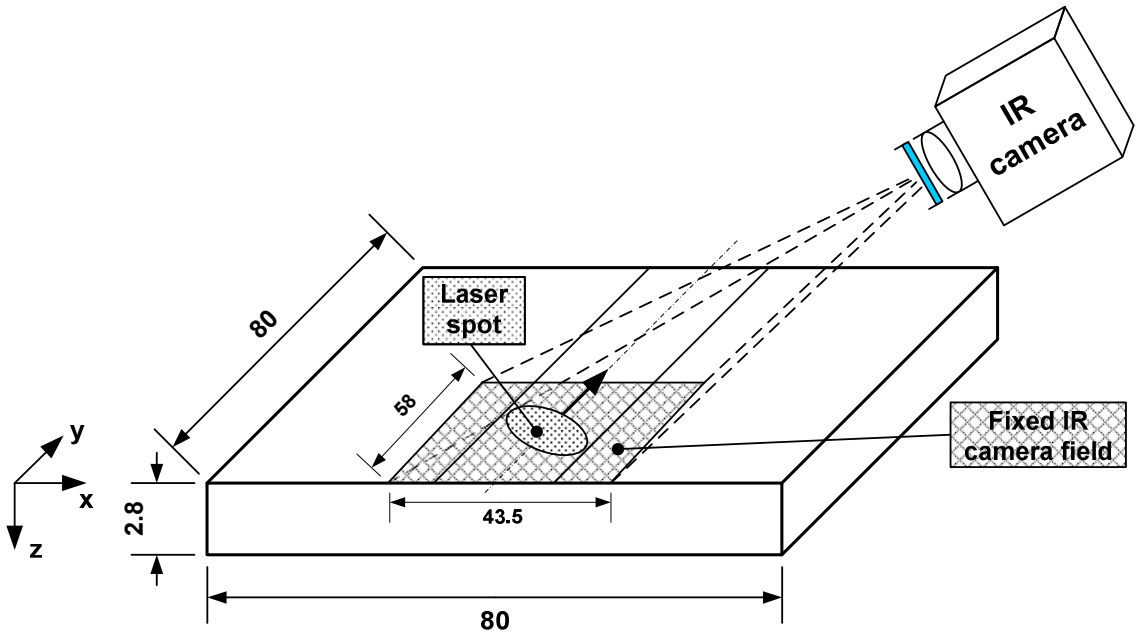

Figure 4.5: Experimental setup (schematically) for the surface temperature measurement with the IR camera.

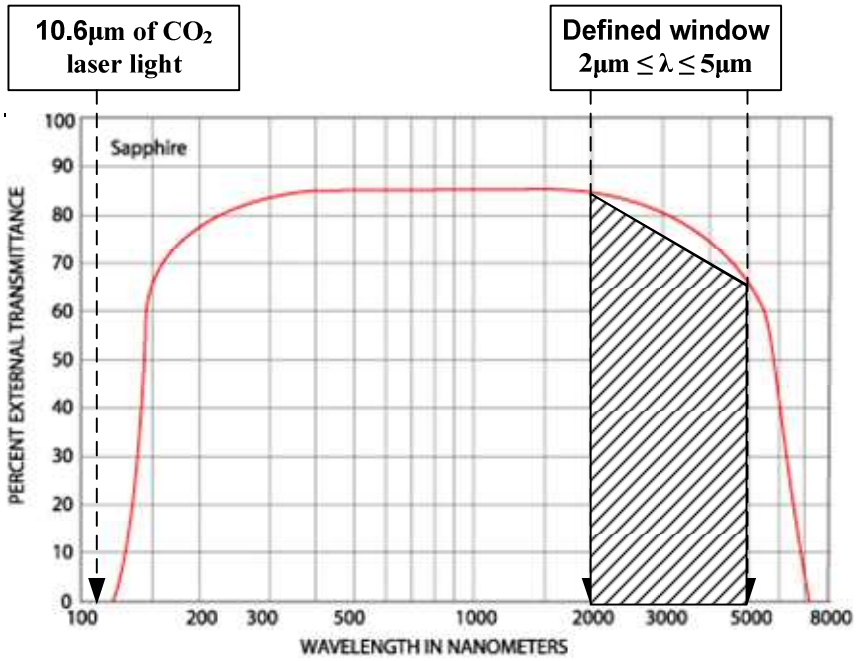

Figure 4.6: Transmission profile of the sapphire filter and defined window of wavelengths, detected by the system comprising IR camera and filter [122].

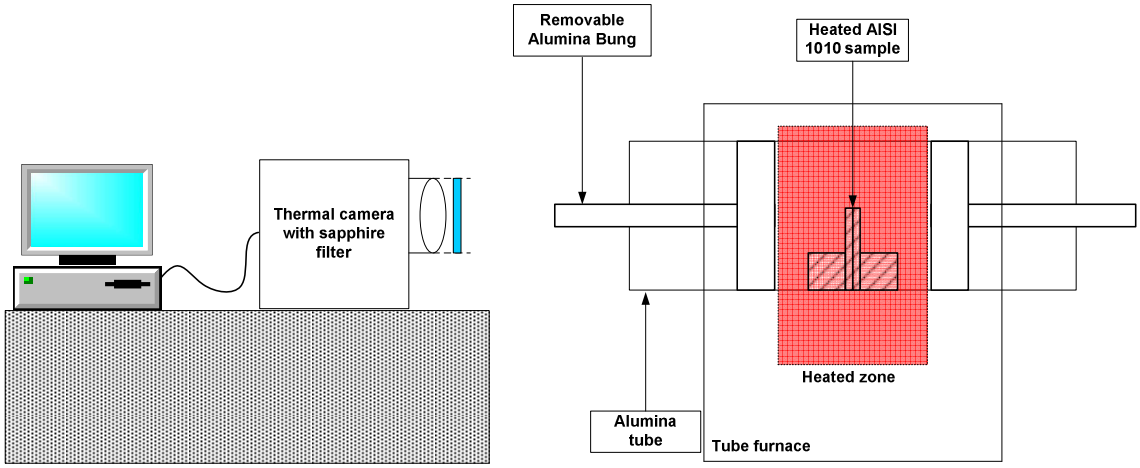

Figure 4.7: Experimental setup (schematically) of the IR camera calibration experiment.

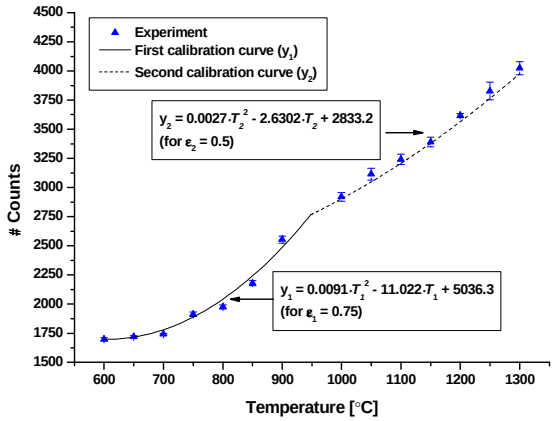

Figure 4.8: Experimental calibration curve of the mean pixel counts for specified temperatures.

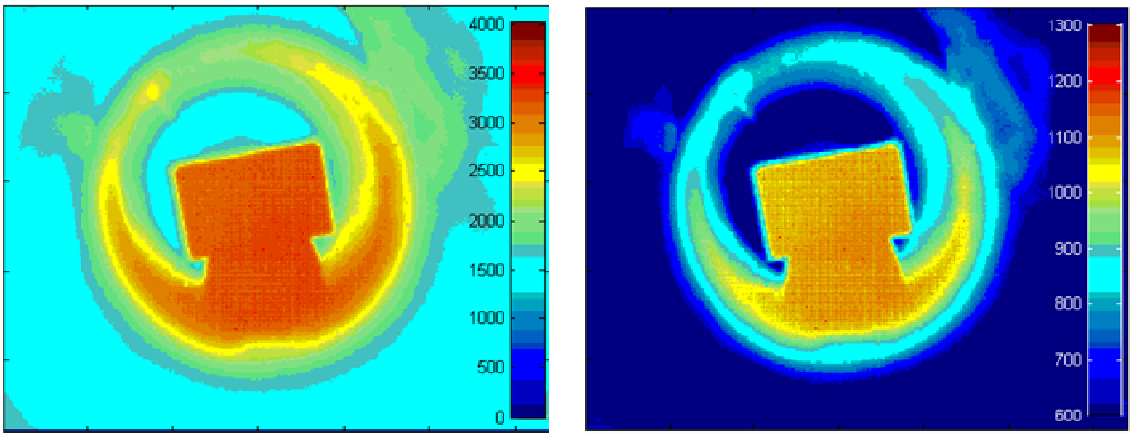

(a) (b)

Figure 4.9: Calibration images at 1100℃ applied through LabView^{TM}; (a) False colour in #counts; (b) Converted into temperature [℃] with equations (4.3) and (4.4).

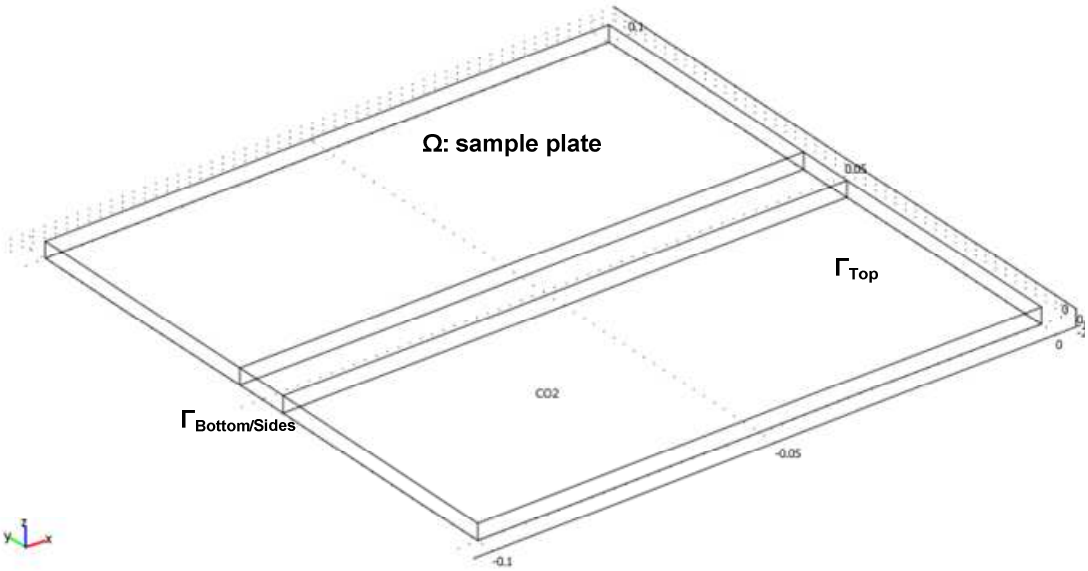

Figure 4.10: Global domain Ω of the token and relevant subdomains of top surface, Γ_{Top}, and bottom and side surfaces, $\Gamma_{Bottom/Sides}$, in the FE-analysis.

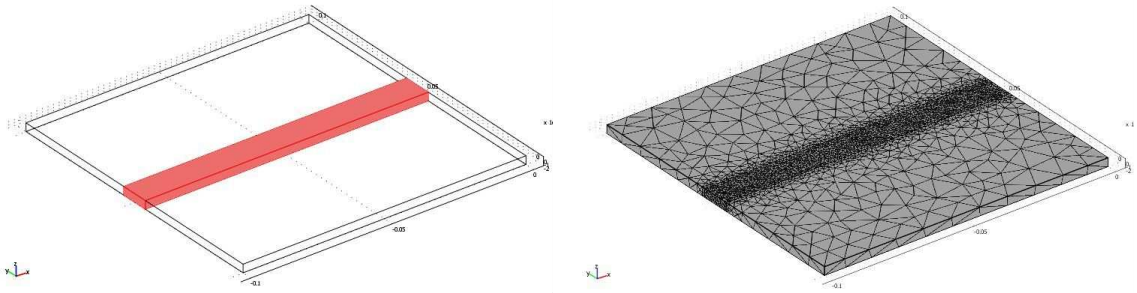

(a) (b)

Figure 4.11: (a) Token geometry and highlighted (red) subdomain of the laser scan path; (b) Coarse mesh grid showing the refined mesh in the laser scan path subdomain.

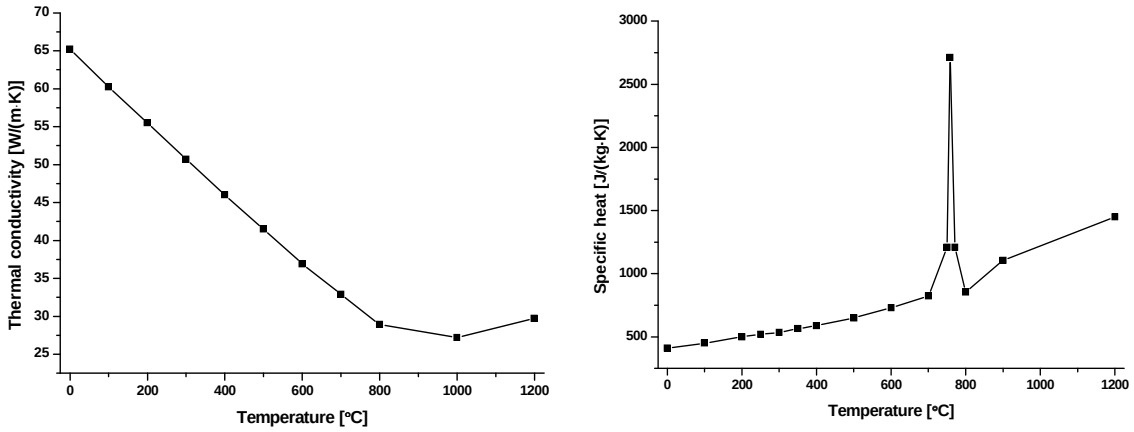

(a) (b)

Figure 4.12: Temperature dependent thermophysical properties of AISI1010; (a) Thermal conductivity; (b) Specific heat [138].

Expression	**Value**
Density ϱ	7871 [kg·m^{-3}]
Heat exchange coefficient (convection)	15 [W·(m^2·K)$^{-1}$]
Emissivity of Γ_{Top}	0.9
Emissivity of $\Gamma_{Bottom/Sides}$	0.2
Ambient temperature	293K
Laser power	600W
R_{laser}^{x}	0.00435m
R_{laser}^{y}	0.00435m

Table 4.1: Temperature constant material parameters of AISI1010 [127] and laser settings chosen for the thermal FE-analysis.

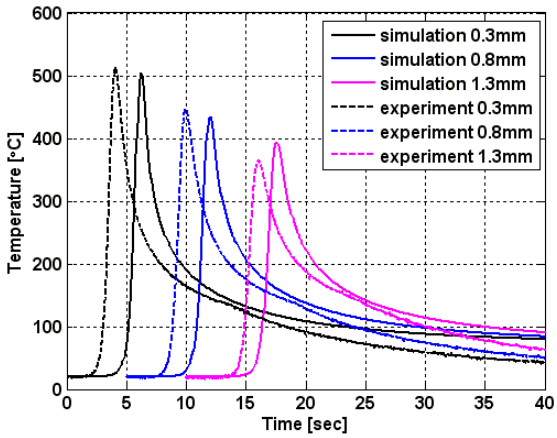

(a)

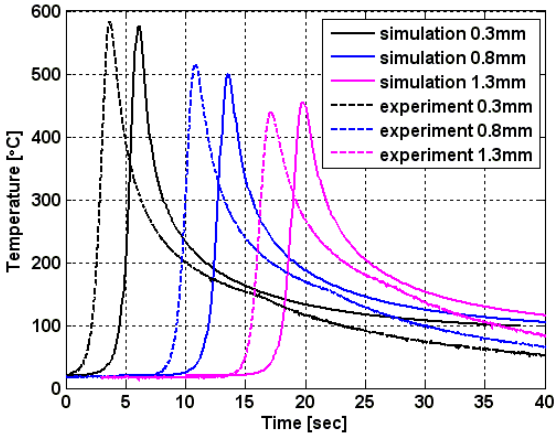

(b)

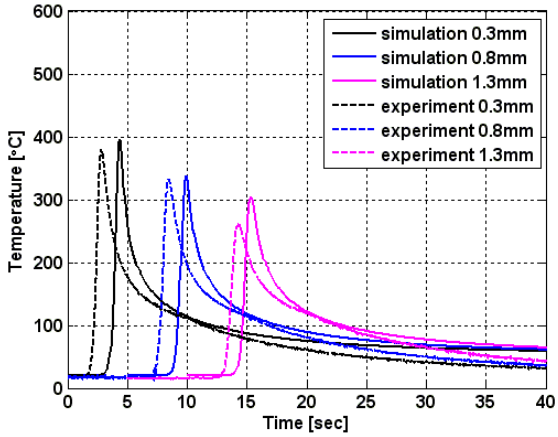

(c)

Figure 4.13: Graph comparing calculated and measured (thermocouple) temperature at a depth of 0.3mm, 0.8mm and 1.3mm from the top (laser scanned) surface during a laser scan using an absorption coefficient of $\eta = 0.51$; (a) LE = 100J/mm; (b) LE = 130J/mm; (c) LE = 70J/mm; To keep the graph clear for comparison, a time offset has been applied to shift the two graphs which belong together along the time scale.

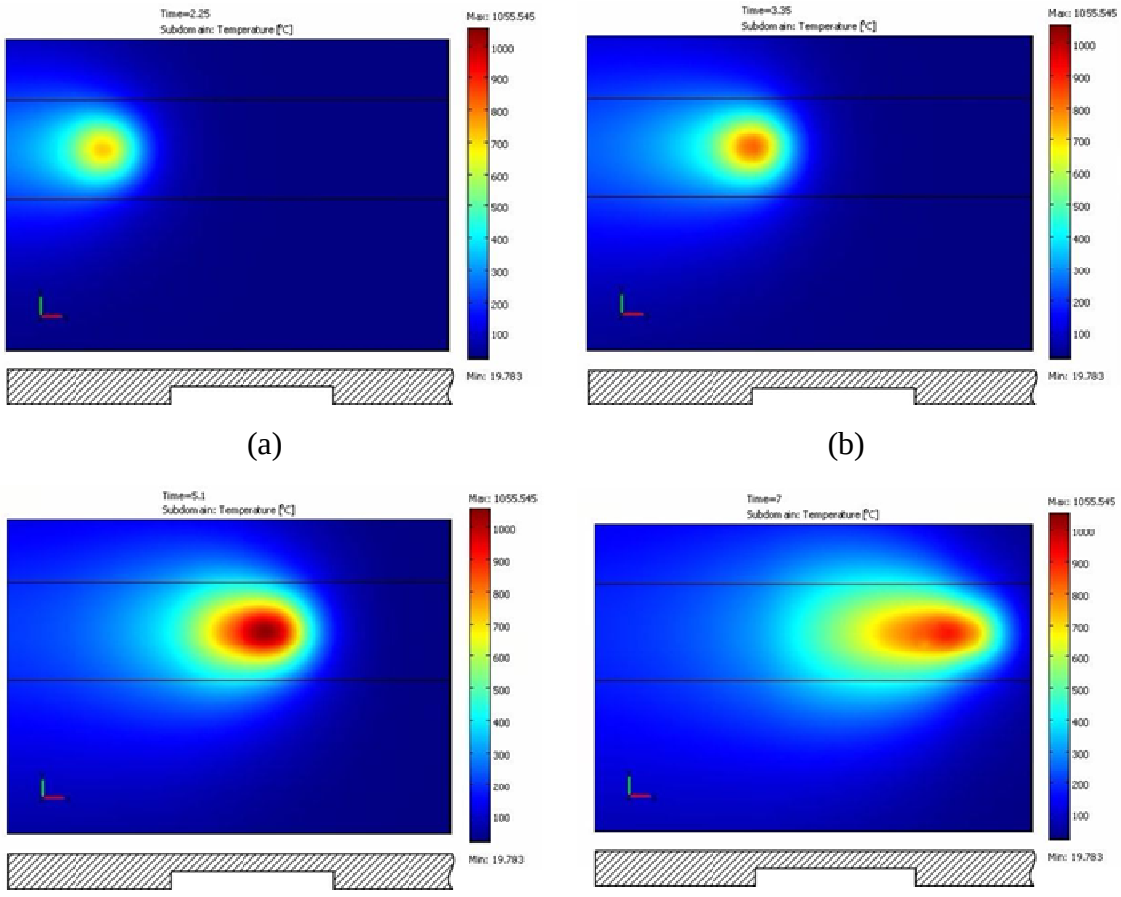

Figure 4.14: Simulation results of the surface temperature of a plate with slotted recesses, scanned at LE = 100J/mm, at different time steps t; (a) t = 2.25 sec.; (b) t = 3.35 sec.; (c) t = 5.1 sec.; (d) t = 7 sec..

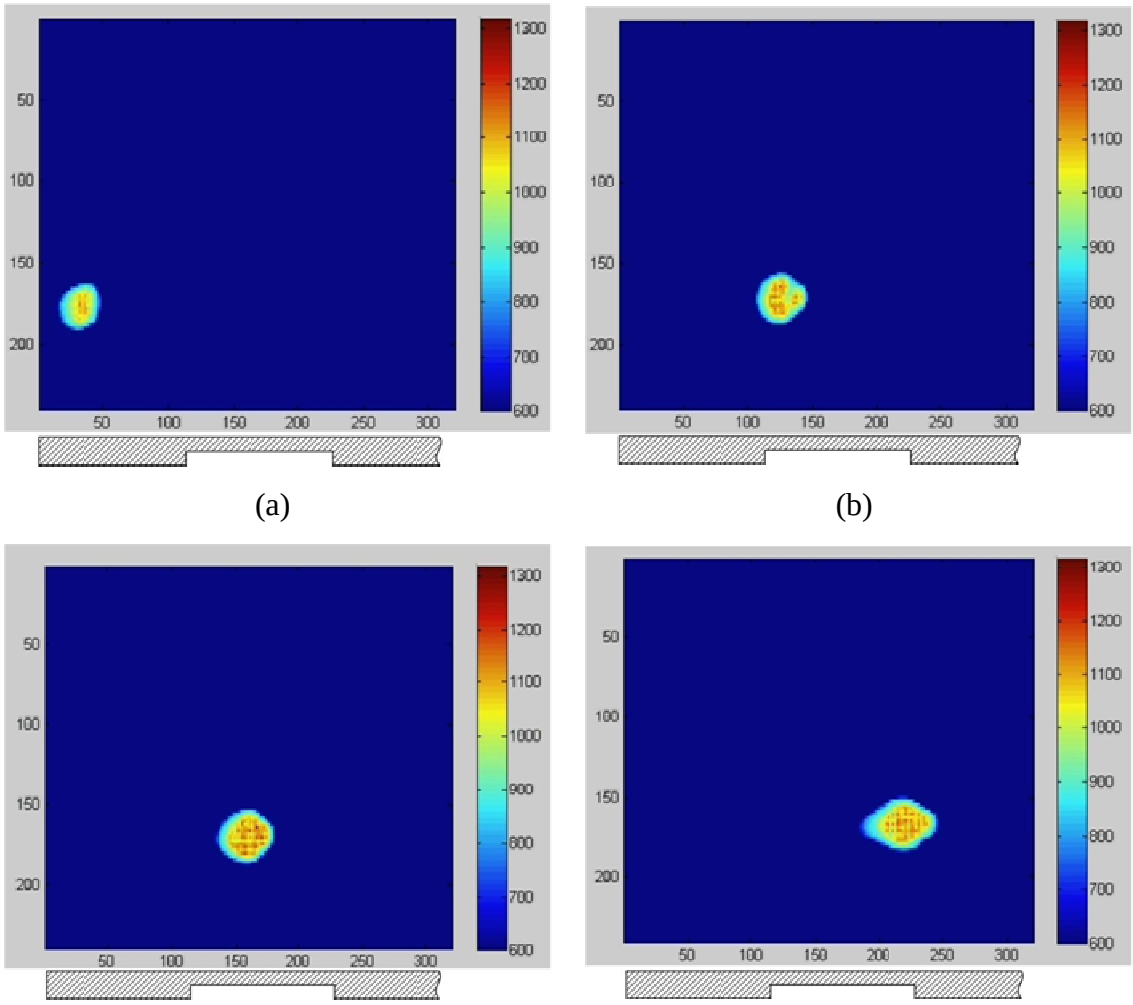

(a) (b)

(c) (d)

Figure 4.15: IR-camera images from a laser scan at LE = 100J/mm on a plate with slotted recesses; (a) On a 2.8mm thick section; (b) At an edge approached from a thick section; (c) On a 1.5mm thick section; (d) At an edge approached from a thin section; (The temperature scale is in [°C]).

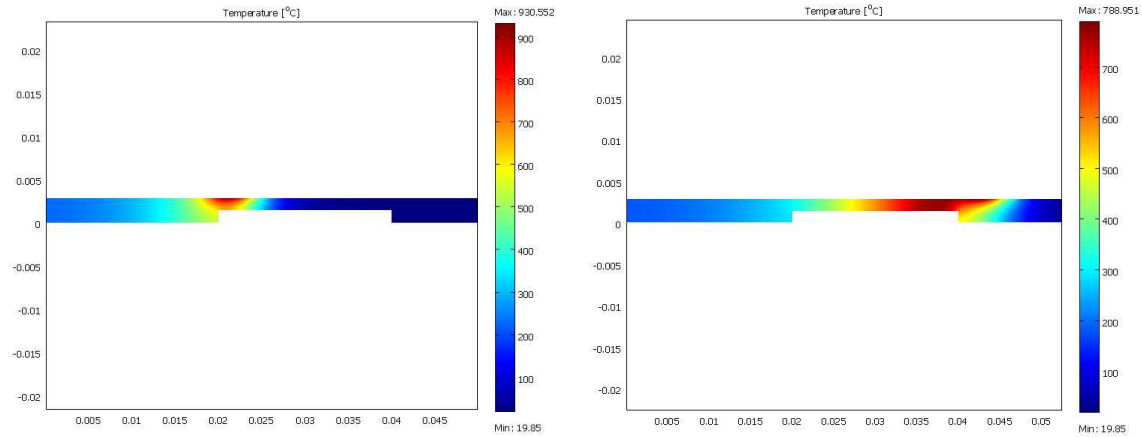

(a) (b)

Figure 4.16: Simulation results showing the non-uniform through thickness temperature field; (a) At an edge approached from a thick section (t = 3.7 sec.); (b) At an edge approached from a thin section (t = 7.3 sec.); It should be noted that the temperature scale in both cross section plots is different; (LE = 100J/mm, scan direction in the images from left to right).

Parameter	**Variation of data**	**Top surface**	**$0.3mm$ depth**	**$0.8mm$ depth**	**$1.3mm$ depth**
Reference temperature		530.7℃	476.3℃	403.5℃	359.2℃
Absorption coefficient η	$\pm$10%	$\pm$9.6%	$\pm$9.6%	$\pm$9.5%	$\pm$9.4%
Thermal conductivity k	$\pm$10%	$\pm$4.8%	$\pm$4.4%	$\pm$3.8%	$\pm$3.4%
Specific heat C_p	$\pm$10%	$\pm$4.3%	$\pm$4.7%	$\pm$5.5%	$\pm$6.2%
Laser beam diameter	$\pm$10%	$\pm$1.1%	$\pm$1.0%	$\pm$0.8%	$\pm$0.7%
Top hat function, equation (4.9)		23.6%	20.6%	14.8%	11.0%
Temperature dependent thermophysical properties		$-$8.1%	$-$9.9%	$-$13.0%	$-$16.0%

Table 4.2: Numerical sensitivity analysis about the influence of thermophysical and process specific laser forming parameters on the temperature at four positions (at LE = 100J/mm) in the middle of the scan path and at the centre of the plate; The reference temperature was calculated with temperature constant thermophysical parameters, representative of a low carbon steel at elevated temperature (~ 500℃) [119]: $k = 41.5\ \frac{W}{mK}$, $C_p = 650.1\ \frac{J}{kgK}$.

Chapter 5

Metallurgy and mechanical investigation

As shown in Chapter 3, the ILF process was well established through 3D forming of uniform and varying thickness plates. However, for any further industrial application, the effect of laser forming on the mechanical properties of a material must be understood to manufacture serviceable components. The variation in mechanical properties for different applied laser powers and scan speeds has been reported, but these are specific to the system used because absorption of the laser energy depends on, for example, its wavelength and if a coating is applied to specimen surface.

This chapter explores the possibility of defining acceptable processing regimes based on conditions in the material, rather than parameters of the applied laser. Therefore a systematic study of the mechanical properties of laser formed AISI1010 and AA2024-T3 is presented. Hardness measurements and tensile tests are presented for single- and multiple-pass laser forming (up to 12 passes) and for a wide LE-range that includes both the TGM and SM laser forming mechanism. Before that, an analogy between the microstructure in a laser-formed HAZ and that observed in welding is presented, which has proved extremely useful for interpreting the evolution of hardness and microstructure with increasing LE in laser forming.

5.1 Microstructure in the HAZ of welded specimens

In this section, an analogy is drawn between the microstructure of the material in a laser-formed HAZ and that observed in welding. Clearly there are differences between the two processes: for example in iterative laser forming, multiple laser passes over the same area are possible, and melting and subsequent solidification of the material surface should be avoided. The analogy between the microstructure of welding and laser-formed HAZs has not been proposed before, and has proved an extremely useful tool to interpret the results presented in sections 5.3 and 5.4.

Figure 5.1(a) shows schematically the typical microstructure in a weld HAZ for low carbon steel [128]. We have sub-divided the HAZ into two characteristic regions, namely HAZ I adjacent to the liquid metal and HAZ II further away and merging in to the bulk material. Equivalent regions are proposed for laser forming (Figure 5.1[b]). It is understood that these regions may be present after a single pass of the forming laser,

or more likely evolve during several passes, depending on the energy input from the laser. Changes in microstructure may progress to an intermediate stage and stall after a single pass, but then be initiated again and progress further on subsequent laser passes. Similarly, it is understood that there is a gradual transition in microstructure between the identified zones.

The material in HAZ I experiences the highest temperature and steepest thermal cycles, allowing carbon dissolution and phase transformation to take place. Martensitic and bainitic (ferrite with embedded carbides) structures as well as grain growth are characteristic in HAZ I (Figure 5.1[a]). The concentration of martensite is highest close to the heat source, but bainitic structures with a low percentage of martensite are most likely to occur for low carbon steel because a very fast cooling rate is required to form massive martensite [128]. The material in HAZ II is plastified (cold worked) as a result of the thermal expansion of the material in HAZ I. The additional cold work causes the dislocation density to increase and produces grain refinement caused by recrystallization. Adjacent to the recrystallized material, HAZ II is characterized by carbon dissolution from the pearlite of the parent material to form carbon particles particularly at the grain boundaries. The amount of carbon dissolution decreases as the peak temperature reached decreases and HAZ II merges gradually into the parent material. At a sufficient distance from the HAZ microstructural changes do not occur and the initial structure of the parent material is unchanged; i.e. ferrite grains with pearlite grains are evenly distributed between them.

The microstructural changes depend on the temperature reached, cooling rate and work done on the material. Typical temperatures for the changes discussed above can be taken from the iron-carbon phase diagram for a low carbon steel (< 0.1% carbon) such as AISI1010: HAZ I martensite and bainite formation starts at temperatures $> 900℃$ and HAZ II carbon dissolution from the pearlite starts at $723℃$ [128]. However, microstructural changes would be expected to occur at somewhat lower temperatures during laser forming as a result of the additional work done on the material caused by bending.

For an aluminium-copper alloy, the characteristic microstructure seen in a weld HAZ is shown in Figure 5.1(c) [128] and the HAZ produced by laser forming is drawn by a similar analogy (Figure 5.1[d]). Owing to its higher thermal conductivity, the HAZ

extends less far into the aluminium alloy than for the low carbon steel. In HAZ I (Figure 5.1[c]), the temperature reaches or exceeds the solvus, causing precipitates to coagulate within grains and at grain boundaries. The material is then ‘over-aged’ and its strength decreases significantly [129]. In HAZ II, the change in size and distribution of precipitates cannot be resolved with an optical microscope. Recrystallization of the precipitates into a microscopically resolvable grain structure can take place in HAZ II, if the material is exposed for sufficient time to the required temperature combined with sudden cooling to preserve the sub-grain structure. Dynamic recrystallization occurs if plastic deformation (and therefore an increase in dislocation density) occurs simultaneously with the temperature change, but rapid quenching is still required to observe sub-grain structures within grains [130]. Dynamic recrystallization might occur in laser forming, but without quenching no recrystallization region is expected.

Typical temperatures for the microstructural changes can be taken from the aluminium-copper equilibrium phase diagram for AA2024 (4.4% copper): the solvus temperature is 630˚C, annealing occurs in the range 250℃ - 410℃ and precipitation heat treatment occurs in the range 170℃ - 250℃ [129,139]. Again, these microstructural changes would be expected to occur at somewhat lower temperatures during laser forming as a result of the additional work done on the material caused by bending.

Figure 5.2 shows macrographs of AISI1010 and AA2024-T3 samples scanned with 5 passes at a LE of 130J/mm. The HAZ in each sample is clearly visible, although the regions HAZ I and HAZ II cannot be distinguished because of the low magnification. Higher magnification micrographs are shown in section 5.3 in which these regions are observed. For the same energy input, the HAZ penetrates more deeply into the material, and the increase in section thickness is less, for the low carbon steel than for the aluminium alloy owing to their different thermo-mechanical material properties. It should be noted that the discoloration that extends to the bottom surface of the aluminium alloy specimen (Figure 5.2[b]) is believed to be caused by the etching process used for the optical micrographs and is not the HAZ extending to the bottom surface. Energy dispersive X-ray (EDX) measurements in the discoloured region revealed no difference in the material composition compared with the parent material, excluding copper dissolution as a possible reason for the discolouration. The results of an EDX analysis from a sample scanned at LE = 100J/mm, 5 passes, with a similar discoloration and parent material are shown in the Appendix A 2.

5.2 Experimental procedure

The chemical composition of the two materials investigated in this study, namely a low carbon steel (AISI1010) and an aluminium-copper alloy (AA2024-T3 condition, i.e. solution heat treated, cold worked and naturally aged to a substantially stable condition), can be found in Table 5.1 and Table 5.2 respectively. Square tokens of $165\times165mm^2$ were laser cut from the parent sheet material of thickness 2.8mm for low carbon steel and 3.2mm for aluminium alloy. Each token was degreased with acetone and then coated with a thin layer of graphite to improve the coupling efficiency of the laser energy into the sample surface. Laser forming experiments were carried out following the procedure described in section 3.2.

The token geometry and laser scan line are shown in Figure 5.3. During laser forming, laser scans were applied perpendicular to the rolling direction of the parent sheet. For multiple laser scans, a period 60 seconds was allowed between scans for the token to cool down in order to minimise the increase in bulk temperature. Multiple laser scans were applied in alternating directions along the same line to minimise distortion of the tokens along the y-direction. The tokens were clamped on both sides during forming in order to restrict the overall bend around the y-axis to approximately 50% of that compared with an unclamped specimen. The bending constraint was necessary in order to machine tensile test specimens from the deformed plate and subsequently to perform the tensile tests. The effect of clamping is discussed in section 5.4.

The induced bend angle was calculated by measuring the shape of the tokens before and after forming (with edge clamping released) using a single point triangulation probe [77]. The probe was scanned in lines perpendicular to the laser forming scan direction (i.e. parallel to the x-axis in Figure 5.3) in 10mm intervals along the y-direction. The bend angle at each y-value was calculated from the shape change, and the mean bend angle calculated over all 17 intervals for the final bend angle of the token.

Following laser forming, samples for tensile tests, hardness tests and optical microscopy were cut from each laser formed token, as shown in Figure 5.3. Tensile test specimens were machined from the laser formed tokens to the dimensions specified in DIN50125 type H [131] for a test section width of 10mm. Two specimens were cut from each token in case the tensile test failed for any reason and a second specimen was required. The laser scan path was perpendicular to the tensile axis in the centre of the specimen

gauge length (Figure 5.3). Uniaxial tensile testing of as-received and laser formed samples was performed on an Instron 3367 tensile testing machine fitted with a 100kN load cell and wedged grips. In order to accommodate the laser-formed samples, clevis tension couplings were used. The samples were fixed into the centre of the grips, using 5mm spacers, to ensure balanced loading. The crosshead speed was 2mm/min and the elongation was measured using a calibrated extensometer (10mm ± 50% travel) covering the region of the laser beam footprint. The extensometer was removed after a strain of 3% to prevent damage of the device. Each specimen was then tested to failure.

Samples for Vickers microhardness tests and optical microscopy were cut from the middle of the laser formed token, using a diamond wafer blade on a Buehler IsoMet low-speed cutting saw. The section was cut perpendicular to the laser scan direction and included the HAZ in order to investigate the cross section through the thickness. The specimens were cold mounted with an epoxy resin (Buehler EpoxiCure) for grinding and polishing with 15 micron, 6 micron and 1 micron paste. AISI1010 samples were etched with 2% nital for 30 seconds and AA2024-T3 samples were etched with a 'Kroll' etchant for 15-25 seconds [132]. Section images were recorded with an Olympus GX51 (AISI1010) and a Reichert-Jung MeF3 (AA2024-T3) optical microscopes. Vickers mircohardness tests were performed on a Mitutoyo MVK-H1 hardness testing machine in steps of $100\mu m$ through the specimen thickness in the centre of the HAZ, with a load of 200g and a dwell time of 10sec [133].

A final set of experiments was conducted to measure the temperature distribution through the plate thickness during laser forming. Square tokens were again cut from the parent material and six thermocouples (Type K, 0.25mm diameter, sampling frequency 100Hz) were placed in holes drilled into the rear surface of each token in the centre of the laser scan line. The front surface was coated with graphite, following the standard procedure. Each specimen was then tested for a particular laser scan LE and the temperature distribution during the scan recorded with a data logger. Two tests were undertaken for each LE. During the laser scan, the top surface temperature was measured for low carbon steel at the centre of the plate and in the middle of the laser scan line with a double wavelength pyrometer (Raytek, model FR1BCF, section 4.2). The surface temperature for the aluminium alloy specimens was below the measurement range of the pyrometer.

5.3 Results

The following section presents the results of the tensile tests and the hardness measurement separately for each material. Table 5.3 shows the forming parameters (LE, number of laser scans and cumulative line energy CLE, i.e. number of passes multiplied by the LE) for the low carbon steel (AISI1010) specimens. The measured parameters shown are the bend angle of the sample (after release of the clamping used in laser forming) and the results of the tensile tests, namely ultimate tensile strength (UTS), yield strength (YTS) and failure strain. These values can be compared with typical minimum required service values for low carbon steel of UTS 365MPa, YTS 305MPa and failure strain 20% [138]. Table 5.4 shows the same parameters measured for the aluminium alloy (AA2024-T3) specimens. These values can be compared with typical minimum required service values of UTS 435MPa, YTS 290MPa and failure strain 10-15% [139].

The measured bend angles are included in Table 5.3 and Table 5.4, primarily to demonstrate the geometry of the tensile test specimens. However, it can be seen that the bend rate (i.e. the change in bend angle per laser pass) decreases with number of passes at each line energy. This effect is the result of a combination of graphite coating degradation, work hardening of the material and section thickening, and is accounted for in our iterative laser forming approach [77]. Both the TGM and SM laser forming mechanisms are present simultaneously, and, as the LE increases, conditions favour the latter over the former mechanism. For low carbon steel, the LE = 250J/mm is significantly higher than usually used for laser forming, but was included to be representative of conditions where the TGM efficiency has declined and the SM efficiency has increased. This effect is shown in Table 5.3, where the bend angle has reduced for LE = 250J/mm compared with LE = 130J/mm.

5.3.1 Low carbon steel (AISI1010)

Tensile test:

Figure 5.4 shows two example stress-strain graphs for low carbon steel from which the UTS, YTS and failure strain were determined, in this case for the parent material and one laser formed sample (LE = 100J/mm, 3 passes). The measured UTS, YTS and failure strain for all specimens are shown in Table 5.3. All specimens were tested to failure and none failed in the laser HAZ. Generally, YTS and UTS were found to increase, and the failure strain to decrease, with increasing LE. It should be noted that

the variation of the YTS is more significant than for the UTS in Table 5.3, because the laser HAZ (approximately 9mm) is a significant fraction of the extensometer gauge length (10mm) used to calculate the YTS. The UTS was calculated from the specimen gauge length (50mm) after the extensometer had been removed to prevent it being damaged in the test to failure. The YTS and UTS of all tested samples met the typical minimum service requirements (Table 5.3). Four samples, shaded in the table, failed to meet typical minimum service strain requirements, because the elongation was below 20%.

The observed trend of an increase in YTS and decrease in failure strain with increasing LE is consistent with the published literature [100,101], and was significant for LE $\geq$ 100 J/mm. Therefore one tensile test was performed at each LE. The evolution of material properties and microstructure in relation to conditions within the material (specifically the through-thickness temperature) has not been reported previously and are the subject of the next section.

Vickers microhardness:

The through-thickness microhardness of the low carbon steel sheet as-supplied (parent material) is shown in Figure 5.5. The hardness is reasonably constant through the sheet thickness, with an average of 136.9 ± 3.9 Hv0.2. Figure 5.6 shows an example of the through-thickness hardness evolution as the number of scans is increased at a particular LE (i.e. increasing CLE). The through-thickness hardness distributions for each LE have been plotted on one graph in Figure 5.7. Clearly Figure 5.7(c) shows the results recorded at LE = 100J/mm presented in Figure 5.6. All hardness profiles presented are the average of two independent measurements from the same indent. Figure 5.6(b)-(d) shows both hardness measurements at each point as an error bar around their mean. Error bars are omitted from subsequent plots of through-thickness hardness variation for clarity. Following the increase in specimen thickness at the HAZ (Figure 5.2), all thicknesses are shown relative to the top surface, and the thickness increases with number of passes in the hardness profiles.

From Figure 5.7(a)-(e), three characteristic profiles of the through-thickness hardness were identified at increasing LE. These characteristic profiles are described and related to the through-thickness temperature and microstructure in the following paragraphs. Figure 5.7(f) shows the peak through-thickness and surface temperatures recorded with

the thermocouples and pyrometer, respectively. The temperatures shown are the average of two independent experiments at each LE.

The first characteristic through-thickness hardness profile at lower LEs shows an increase in hardness towards the top surface, whilst the rear surface is not significantly different from the parent material (Figure 5.7[a], Figure 5.7[b] and Figure 5.7[c]) for 1 to 5 passes. The increase in hardness is the result of cold work of the material induced by the bending strain caused by laser forming. For higher line energies, the increase in hardness at the surface is even more pronounced because, in addition to the cold work, small particles of carbon dissolve from the pearlite and form around the ferrite grain boundaries. Figure 5.8(a) shows a micrograph taken from the parent material in which white ferrite grains and dark pearlite grains are evenly distributed in the microstructure. Figure 5.8(b) shows a micrograph taken from adjacent to the top surface for a sample scanned at LE = 70J/mm, 3 passes. Despite the increase in hardness to approximately 185 Hv0.2, no optically resolvable effect on the microstructure was visible.

The second characteristic through-thickness hardness profile is seen in Figure 5.7(c) for 8 passes and Figure 5.7(d) for 3 to 12 passes. The typical profile can also be seen individually (and so more clearly) in Figure 5.6(d), which is the same as Figure 5.7(c) for 8 passes. The increased hardness at the surface falls steeply to a distinctive local minimum, followed by a local maximum as the hardness profile rises and falls in the remaining depth. The increased surface hardness is caused by the continued carbon dissolution from the pearlite and the local minimum is associated with recrystallization, both characteristics of HAZ II. The local maximum in hardness is a result of cold work of the material induced by the bending strain from laser forming becoming more pronounced. Figure 5.8(c) shows an optical micrograph for LE = 100J/mm 8 passes from the depth associated with the characteristic local minimum hardness in which small recrystallized ferrite grains are visible in the central region. Towards the top surface of Figure 5.8(c), the progressed carbon dissolution is now visible in broadened pearlite. Figure 5.8(d) shows an optical micrograph for LE = 130J/mm 1 pass in HAZ I adjacent to the laser scanned surface. The carbon dissolution from the pearlite has progressed further and the grains are evenly distributed and visibly refined. Lower bainite [128] has formed owing to the high heat input, high temperature and rapid cooling, which is reflected in a hardness of ~200 Hv0.2.

The depth range corresponding to the local hardness minimum for 8 laser scan passes is marked in Figure 5.7(c). This depth range corresponds to the extent of recrysallization in HAZ II, from which the corresponding peak temperature range (480℃ to 520℃) was determined from Figure 5.7(f). This temperature range is marked on Figure 5.7(f) and the corresponding depths for each LE were then transferred to the other through-thickness hardness profiles in Figure 5.7(a)-(b) and (d)-(e). It was found to give a good estimate of the extent of HAZ II recrystallization, as judged from the position of the local hardness minimum over the broad range of laser line energies studied.

The third characteristic through-thickness hardness profile at higher LEs is seen in Figure 5.7(e). The hardness at the surface is further increased as a result of bainite formation, characteristic of HAZ I. The hardness decreases through the thickness of the specimen without forming a local maximum. Cold work of the material induced by the bending strain is still present, but its contribution is less evident because the laser parameters promote the shortening mechanism, as discussed above. Further, the temperature deeper into the material exceeds approximately 450℃ or ~ 0.3 times the melting point (Figure 5.7[f]), enabling recovery to take place on cooling [134]. A micrograph for LE of 250J/mm 1 pass is shown in Figure 5.8(e). The microstructure consists of upper and lower bainite and shows an increase in grain size, characteristic of HAZ I. Carbide fingers growing into the grain and triangular regions indicating the formation of martensite (hexagonal phase) are visible (although images with higher resolution would be required to see the martensite directly). Figure 5.8(f) shows the HAZ from the same specimen but at a lower magnification. The two proposed regions of the HAZ based on the microstructure with their transition zone are clearly visible, comprising at increasing depths into the material the microstructure of the type shown in the micrographs (Figure 5.8[e-a]).

5.3.2 Aluminium-copper alloy (AA2024-T3)

Tensile test:

Figure 5.9 shows two example stress-strain graphs for aluminium alloy from which the UTS, YTS and failure strain were determined, in this case for the parent material and one laser formed sample (LE = 80 J/mm, 5 passes). The measured UTS, YTS and strain for all specimens are shown in Table 5.4. All specimens were tested to failure, which generally occurred in or close to the HAZ. With increasing specimen thickness after multiple laser passes, the specimens failed further away from the HAZ. Only one

thickened sample, P17, failed in the HAZ. The thickened cross section effectively lowered the engineering stress in the HAZ, cancelling out the decrease in material strength.

Generally, YTS, UTS and the failure strain were found to decrease compared to the parent material with increasing LE. Six samples, shaded in Table 5.4, failed to meet the typical minimum service UTS requirements of 435MPa. A further two samples were below the specified YTS and one sample below the specified failure strain. The observed trend of a decrease in UTS and failure strain with increasing LE is consistent with other measurements from the published literature [98] and was significant for LE ≥ 100 J/mm. Therefore one tensile test was performed at each LE.

Vickers microhardness:

Figure 5.10 shows the through-thickness hardness of the aluminium alloy sheet as supplied (parent material). The hardness is reasonably constant through the sheet thickness, with an average of 122.0 ± 1.2 Hv0.2. The through-thickness hardness distributions for each LE are shown in Figure 5.11(a)-(e). Figure 5.11(f) shows the peak through-thickness temperatures recorded with the thermocouples. The temperature range of 200℃ to 380℃ is marked in Figure 5.11(f). The depth at which this temperature range occurred for each line energy was transposed from Figure 5.11(f) to the through thickness hardness graphs (Figure 5.11[a-e]), corresponding to regions of reduced hardness over the broad range of laser line energies studied. The reduction in hardness is most likely to have been caused by precipitations present in the parent material being dissolved. Precipitated particles cannot be resolved at the optical magnification used for the micrographs, for example in the parent material (Figure 5.12[a]). Grain boundary precipitation is characteristic of HAZ II, as seen from the dark grain boundaries in the micrograph of the specimen formed with LE = 60J/mm for 8 passes (Figure 5.12[b]). However, these primary precipitates are not responsible for any significant change in hardness.

Figure 5.11(c) and (d) clearly show reduced through-thickness hardness with increased heat input for the temperature range 200℃ to 380℃. Even though the bend angle of these samples was quite significant (Table 5.4), cold work affects the hardness profile to a minor extent only in the bottom part of the plate. The micrograph for LE = 130J/mm for 5 passes (Figure 5.12[c]) shows dark lines around the grain boundaries caused by

partial melting and hot tearing between grain boundaries. Further away from the laser irradiated surface grain growth is visible in the form of large ($> 100\mu m$) non-elongated grains.

5.4 Discussion

The mechanical properties of laser-formed material must meet typical minimum service specifications. The tensile tests showed that the reduction in failure strain with increasing LE limits the performance for low carbon steel (Table 5.3). The failure strain measured from the tensile tests is plotted against CLE in Figure 5.13(a). It was found for aluminium alloy that the reduction in UTS limits material performance (Table 5.4). The UTS measured from the tensile tests is plotted against CLE in Figure 5.13(b). From these graphs, it might be estimated that the CLE should not exceed approximately 600J/mm for AISI1010 and 480J/mm for AA2024-T3. However, these graphs show that similar CLEs produce quite different failure strain and UTS values. Similar CLEs can also produce different hardness profiles, e.g. for low carbon steel at LE = 40J/mm for 5 scans compared with LE = 70J/mm for 3 scans. Furthermore, a processing range expressed in CLE is system specific.

As an alternative criterion, it was shown for both materials that the characteristic through thickness hardness of the HAZ over a significant LE range can be related to the through thickness peak temperature. For the low carbon steel, a 'recrystallization' temperature range ($480℃$ to $520℃$) was identified over the broad range of LEs studied (Figure 5.7), suggesting that variations in heating and cooling rate (e.g. caused by the variation in laser scan speeds) or differences in the dynamic cold work caused by bending (e.g. owing to specimen geometry) are of secondary importance. The depth of the recystallization zone in the material determines the extent of HAZ I. If HAZ I is a significant fraction of the material section, carbon dissolution and ultimately bainite formation increase hardness and reduce the section strain unacceptably (Figure 5.7[d] and [e]). Therefore, if the peak through thickness temperature can be measured or modelled, the laser energy input can be chosen to restrict the depth of HAZ I. For our system, the recrystallization temperature range can be translated into a LE per pass that should not exceed 100J/mm for AISI1010.

With the thermal FE-analysis (section 4.5) it was possible to compare modelled thermal through thickness profiles with the width and depth of the optical resolvable HAZ

(corresponding to the extent of HAZ I) produced during laser forming. Figure 5.14 and Figure 5.15 show the modelled temperature cross sections of low carbon steel from the FE-analysis at LE = 70J/mm and LE = 100J/mm (Figure 5.14[a-b]), and at LE = 130J/mm and LE = 250J/mm (Figure 5.15[a-b]). The white dashed line in the cross section plots corresponds approximately to an estimated temperature isotherm at the recrystallization temperature of $T \approx 550℃$, which shows the extent of HAZ I for low carbon steel. The points, marked in the temperature plots and macrographs, correspond to the extent of the optical visible HAZ (coincident with HAZ I), estimated within $50\mu m$ from the prepared cross sections and shown in Table 5.5. It should be noted that although multiple laser scan passes at the same LE were applied, the width and depth of the visible HAZ remained about constant. As it can be seen from Figure 5.14 and Figure 5.15, the modelled recrystallization temperature shows good agreement with the extent of HAZ I, measured experimentally with an optical microscope.

For the aluminium alloy, a 'reduced hardness' temperature range of $200℃$ to $380℃$ was identified over the range of LEs studied (Figure 5.11). The depth of this range determines the extent of HAZ I. If HAZ I represents a significant fraction of the material section, the hardness and section UTS are reduced unacceptably (Figure 5.11[d] and [e]). Therefore, the laser energy should again be chosen to restrict the depth of HAZ I by considering the peak through thickness temperature. For our system, the temperature range can be translated into a LE per pass that should not exceed 80J/mm for AA2024-T3.

As expected, the recrystallization temperature range ($480℃$ to $520℃$) identified experimentally for low carbon steel is lower than inferred from the iron-carbon equilibrium phase diagram, because the rapid heating and cooling and dynamic cold work present in laser forming increase the dislocation density and so reduce the temperature range required for recrystallization [42]. Interestingly, the observed recrystallization temperature range is similar to that observed in the welding of low carbon steels, of approximately 0.4 times the melting point or $\sim 600℃$ [134]. Hence the identified recrystallization temperature range should be applicable generally to laser forming experiments and geometries.

The low carbon steel and aluminium alloy tokens were clamped during laser forming in order to restrict the bend angle of the tensile test specimens, which enabled tensile

testing for specimens with more than 3 laser scans for the first time. Clamping of the plate reduces the dynamic cold work and could therefore lead to an overestimate of the identified temperature ranges compared with laser forming of free plates. However, by the arguments of the previous paragraphs, the temperature profile and the localized rapid heating and cooling within the HAZ are of primary importance and the cold work resulting from bending is secondary. Therefore the temperature ranges are not expected to be significantly different in the bending of free plates or specimens of different geometry.

The reduction in failure strain determined the acceptable processing range for low carbon steel (Table 5.3). The values of failure strain and YTS in Table 5.3 were determined with the extensometer fitted over the HAZ on the tensile test specimens. The UTS values were estimated for the entire gauge length (50 mm), because the extensometer was removed when the strain reached 3% to prevent it from being damaged. Therefore an additional estimate of the UTS in the HAZ was made to ensure that it did not represent the acceptable processing limit, rather than the reduction in failure strain. The YTS and UTS (MPa) can be related to the Vickers hardness [135,136,137] by:

$$UTS = \left(\frac{H}{2.9}\right) \cdot \left(\frac{n}{0.217}\right)^{n}$$
$$YTS = \left(\frac{H}{3}\right) \cdot (0.1)^{n} \qquad (5.1)$$

where n is the strain hardening coefficient and H is the Vickers hardness in kg_f/mm^2 (1 kg_f/mm^2 = 9.80665MPa). The strain hardening coefficient n was determined for each sample from the experimental tensile test with extensometer, so that it was representative of the properties primarily of the HAZ. The mean through-thickness hardness H was calculated for each sample from the profiles presented in Figure 5.7 and Figure 5.11. Figure 5.16 shows the graphs of experimental YTS and UTS plotted against the values calculated from equation (5.1). The calculated YTS is only slightly larger than the measured YTS (the slope of the linear regression is 0.72) owing to the small effect of the parent material in the extensometer gauge length. However, measured UTS is significantly smaller than the calculated UTS (the slope of the linear regression is 0.09) owing to significant parent material in the gauge length of the test specimen. Therefore the higher values of UTS calculated in the HAZ confirmed that reduced failure strain is most significant for low carbon steel.

5.5 Conclusions

Representative low carbon steel (AISI1010) and aluminium-copper alloy (AA2024-T3) were studied. Laser forming of low carbon steel generally produces a decrease in failure strain, whilst laser forming of aluminium alloys produces a decrease in ultimate tensile strength (UTS). An approximate processing range in terms of cumulative line energy (CLE) of the applied laser beam was determined for both materials (Figure 5.13). For the low carbon steel, the CLE should not exceed 600J/mm for the failure strain to remain above the service threshold, and for the aluminium alloy the CLE should not exceed 480J/mm for the UTS to remain above the service threshold. However, these CLE values are specific to the system used because absorption varies with, for example, laser wavelength and surface coating. Furthermore, similar CLEs can produce quite different values of UTS and failure strain. An alternative criterion was sought.

The through-thickness hardness distribution was related to the peak through-thickness temperature reached during forming for a range of laser line energies (LE) and number of laser passes. Regions within the HAZ were identified from the hardness distributions and related to the peak temperature reached at corresponding depths. Specifically, for low carbon steel the region closest to the surface, HAZ I, was characterised by increased hardness caused by carbon dissolution and ultimately bainite formation. The depth of HAZ I was determined by the position of the recrystallization temperature range (peak temperatures of approximately 480℃ to 520℃). If HAZ I was a significant fraction of the material section, the failure strain was reduced unacceptably. Similarly for the aluminium alloy, HAZ I was characterised by the ‘reduced hardness’ temperature range (peak temperatures of approximately 200℃ to 380℃), and if it was a significant fraction of the material section the UTS was reduced unacceptably.

It is concluded that for both materials, the extent of HAZ I can be restricted to an acceptable depth for the geometry under consideration by controlling the peak through-thickness temperature. The use of temperature enables processing regimes to be defined independently of system parameters such as laser wavelength and surface preparation. These temperature ranges were valid for a broad range of laser forming line energies for the two materials studied. The approach proposed could be extended to other materials if similarly significant temperature ranges are identified.

5.6 Figures

Low carbon steel

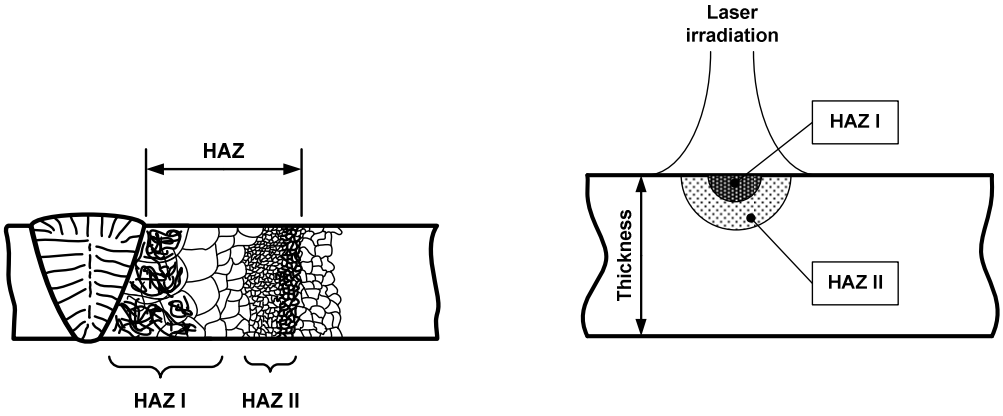

(a) (b)

Aluminium alloy

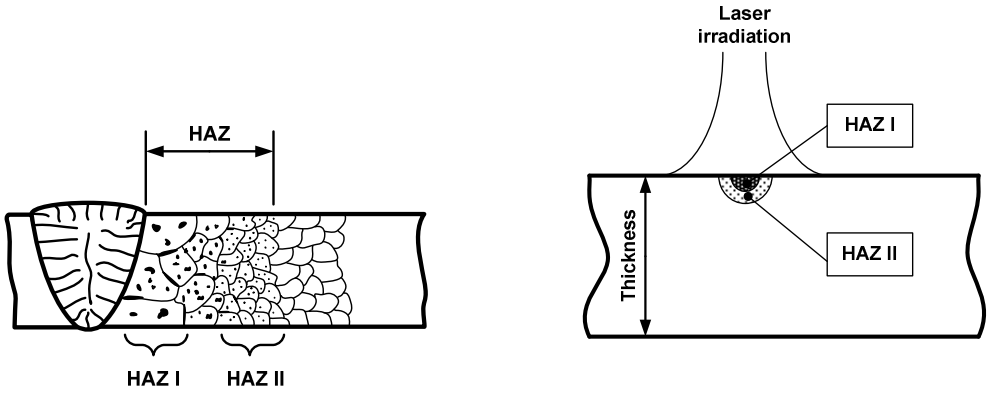

(c) (d)

Figure 5.1: Schematic of the proposed microstructure zones in a laser-formed HAZ based on an analogy with welding [128]. Low carbon steel: (a) butt-weld; (b) laser forming. Aluminium alloy: (c) butt-weld; (d) laser forming.

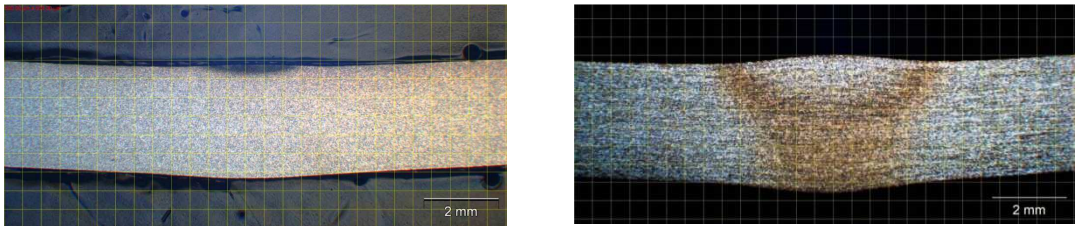

(a) (b)

Figure 5.2: Macrographs showing increase in thickness of the HAZ, LE = 130J/mm, 5 passes; (a) AISI1010; (b) AA2024-T3.

	%C	%Mn	%P	%S	%Si	%Cr	%Ni	%Mo	%Al	%As
AISI1010	0.08	0.31	0.029	0.05	0.08	0.04	0.07	0.02	0.002	0.032

Table 5.1: Chemical composition of AISI1010 [138].

	%Al	%Cu	%Mn	%Mg
AA2024	93.50	4.4	0.6	1.5

Table 5.2: Chemical composition of AA2024 [139].

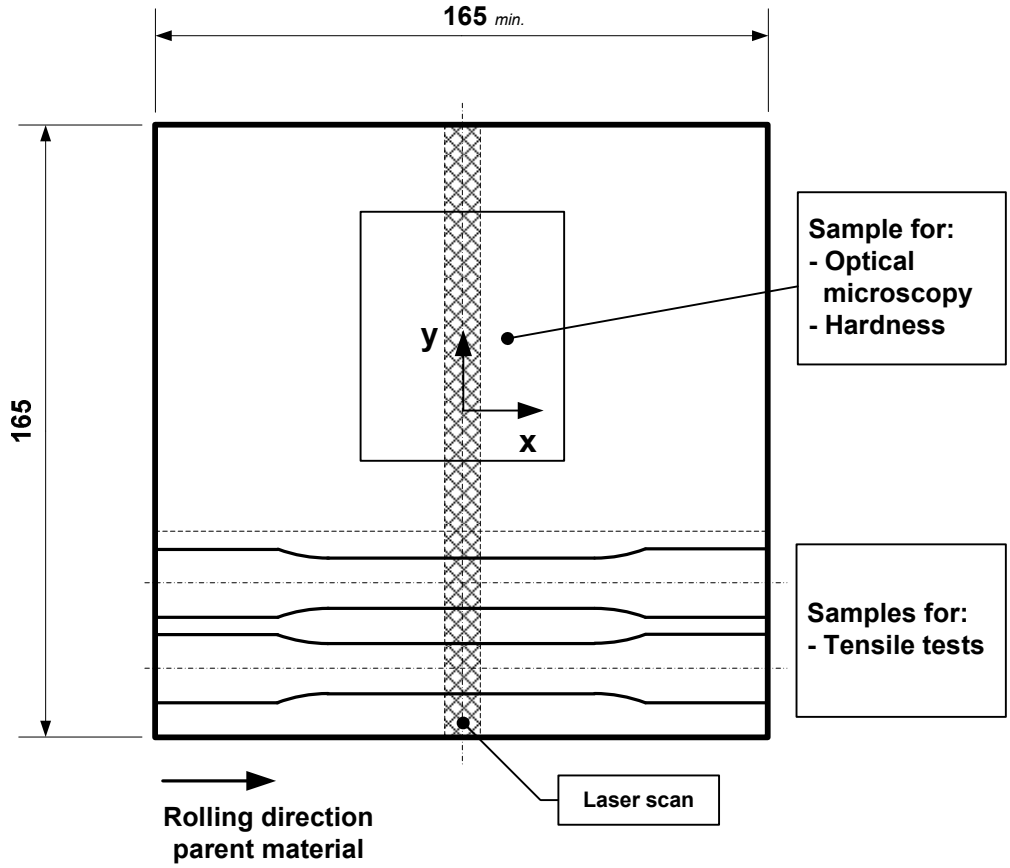

Figure 5.3: Test specimen locations in the laser-formed tokens.

Sample No.	No. of passes	Line Energy [J/mm]	CLE [J/mm]	Bend angle [°]	UTS [MPa]	YTS [MPa]	Failure strain [%]
P01	1	40	40	0.28	469.1	331.8	28.9
P02	3	40	120	0.50	464.2	318.2	30.6
P03	5	40	200	0.51	454.9	313.5	35.3
P04	8	40	320	0.91	458.9	323.6	34.1
P05	1	70	70	0.59	466.3	316.7	29.9
P06	3	70	210	1.81	453.2	325.3	29.3
P07	5	70	350	2.55	465.0	321.4	28.8
P08	8	70	560	3.40	471.9	354.6	27.5
P09	1	100	100	0.72	463.4	327.1	29.1
P10	3	100	300	2.06	480.8	351.3	20.2
P11	5	100	500	3.37	472.3	353.1	25.2
P12	8	100	800	4.65	472.2	367.8	18.2
P13	1	130	130	1.20	468.6	345.7	28.8
P14	3	130	390	3.02	462.5	352.4	22.0
P15	5	130	650	4.32	475.9	367.8	20.2
P16	8	130	1040	5.83	468.8	379.9	13.9
P17	12	130	1560	7.56	477.4	406.9	13.8
P18	1	250	250	0.84	465.9	363.5	25.3
P19	3	250	750	2.84	458.7	369.3	24.9
P20	5	250	1250	4.15	465.2	377.0	12.8
P21	Parent material				463.4	322.1	33.1

Table 5.3: Laser processing parameters for low carbon steel AISI1010 including cumulative line energy (CLE) and experimental results including ultimate tensile strength (UTS) and yield strength (YTS). Typical minimum required service values [138]: UTS = 365MPa, YTS = 305MPa and failure strain 20%. Highlighted values indicate where these minimum values have not been maintained.

Sample No.	No. of passes	Line Energy [J/mm]	CLE [J/mm]	Bend angle [˚]	UTS [MPa]	YTS [MPa]	Failure strain [%]
P01	1	40	40	2.35	486.8	314.6	26.8
P02	3	40	120	0.31	484.4	315.4	25.4
P03	5	40	200	0.34	482.7	316.7	24.8
P04	8	40	320	0.96	478.4	318.1	23.5
P05	1	60	60	0.87	481.4	302.0	24.9
P06	3	60	180	1.09	476.8	313.8	28.5
P07	5	60	300	1.76	477.1	314.7	25.7
P08	8	60	480	3.27	485.8	318.0	26.6
P09	1	80	80	0.90	483.2	313.0	27.4
P10	3	80	240	3.21	483.2	316.2	24.4
P11	5	80	400	5.83	443.0	310.0	23.1
P12	8	80	640	7.80	430.5	299.2	23.3
P13	1	100	100	1.54	480.2	318.5	24.1
P14	3	100	300	4.89	443.1	311.4	24.0
P15	5	100	500	5.90	420.1	303.2	20.0
P16	8	100	800	8.50	416.5	286.3	19.4
P17	12	100	1200	10.88	363.0	272.2	9.9
P18	1	130	130	1.71	479.9	315.2	24.8
P19	3	130	390	3.77	422.0	304.8	21.3
P20	5	130	650	5.45	400.0	290.3	21.1
P21	Parent material				484.1	322.8	26.7

Table 5.4: Laser processing parameters for aluminium alloy AA2024-T3 including cumulative line energy (CLE) and experimental results including ultimate tensile strength (UTS) and yield strength (YTS). Typical minimum required service values [139]: UTS = 435MPa, YTS = 290MPa and failure strain 10-15%. Highlighted values indicate where these minimum values have not been maintained.

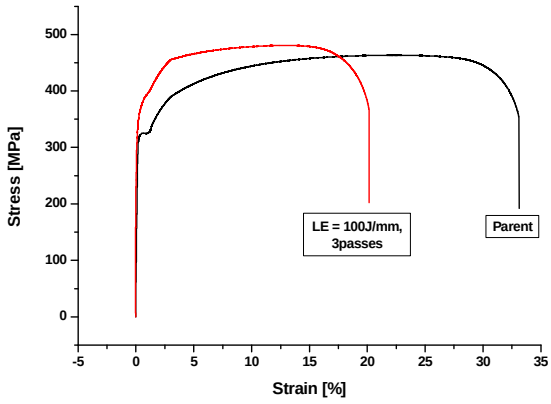

Figure 5.4: Example stress-strain graph for AISI1010 of the parent material and laser formed material, LE = 100J/mm, 3 passes.

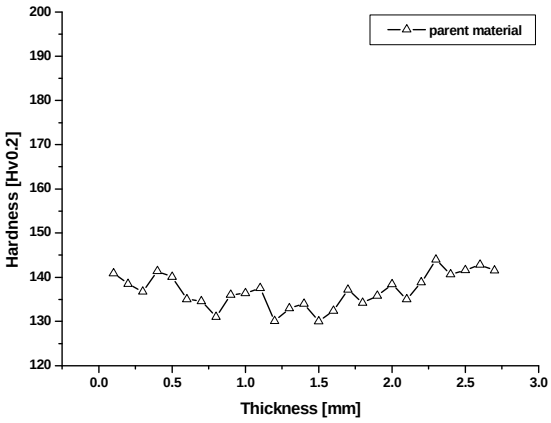

Figure 5.5: Hardness measured through thickness for AISI1010 parent material.

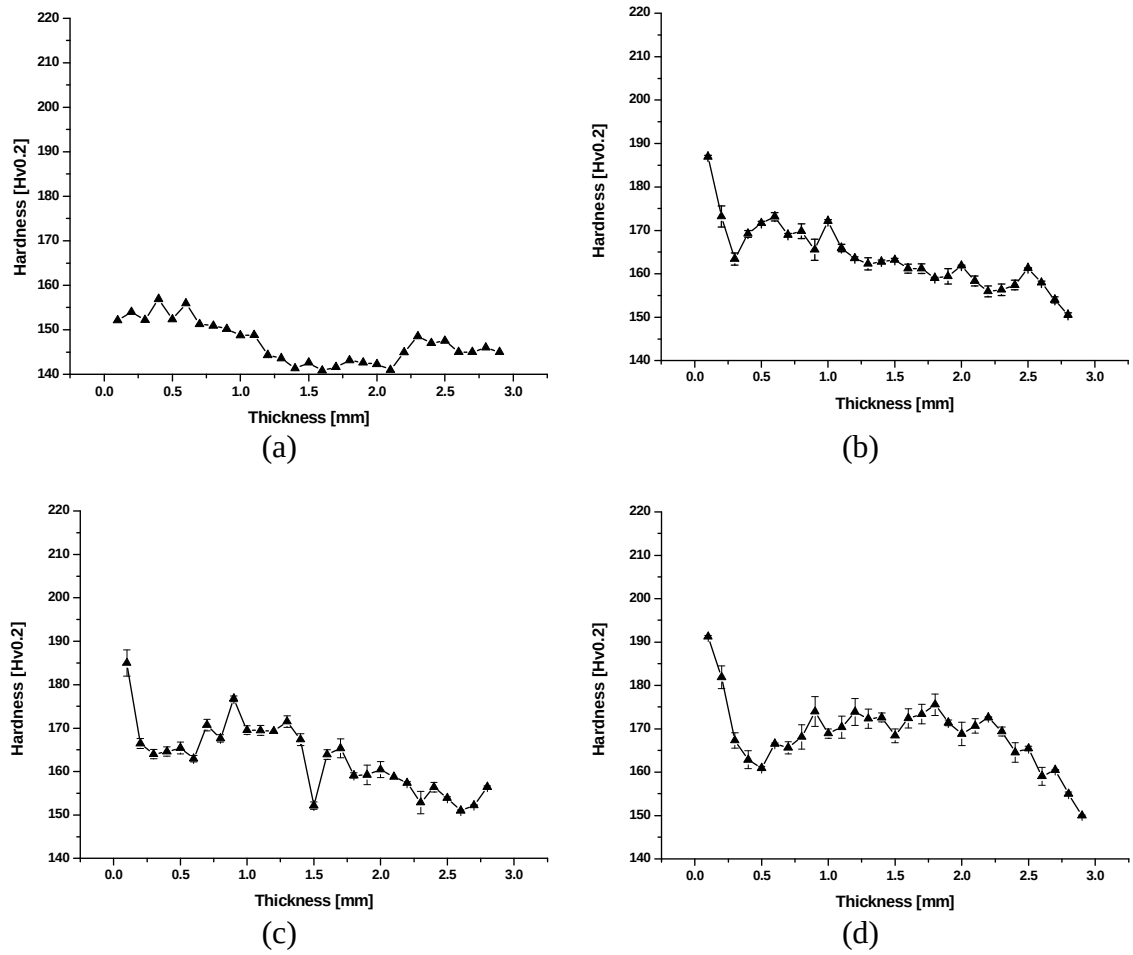

Figure 5.6: Error and repeatability of hardness measured through thickness for AISI1010 LE = 100J/mm; (a) 1 pass; (b) 3 passes; (c) 5 passes; (d) 8 passes.

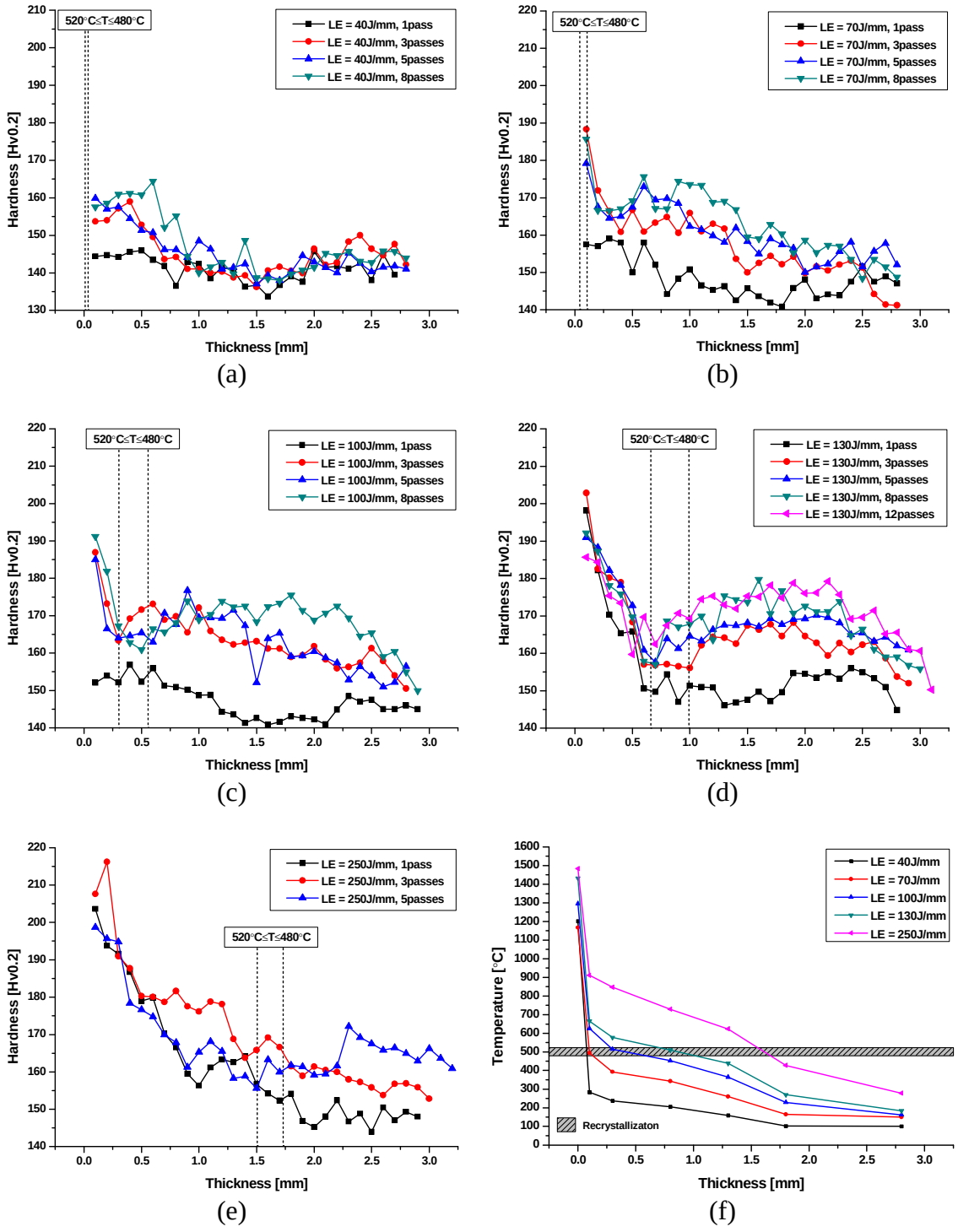

Figure 5.7: Hardness measured through thickness for AISI1010; (a) LE = 40J/mm; (b) LE = 70J/mm; (c) LE = 100J/mm; (d) LE = 130J/mm; (e) LE = 250J/mm; (f) Peak temperature measured through thickness.

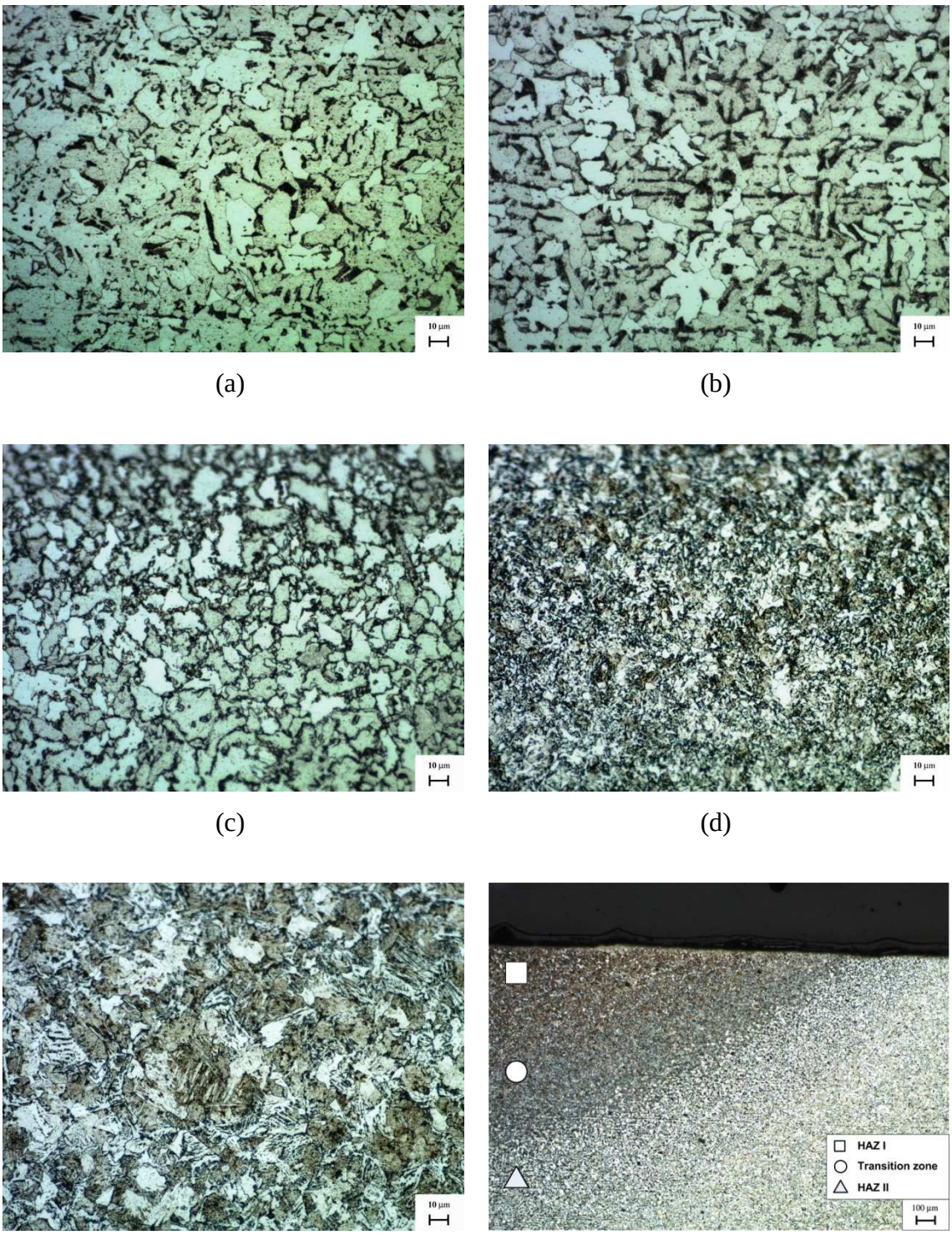

Figure 5.8: Optical micrographs (mag. ×500) of AISI1010; (a) Parent material; (b) LE = 70J/mm, 3 passes; (c) HAZ II, initiated carbon dissolution and recrystallization for LE = 100J/mm, 8 passes; (d) HAZ I lower bainite for LE = 130J/mm, 1pass; (e) HAZ I grain growth, upper and lower bainite for LE = 250J/mm, 1pass; (f) Optical macrograph (mag. ×50) for LE = 250J/mm, 1pass; HAZ regions comprising microstructures of type shown in parts (e)-(a).

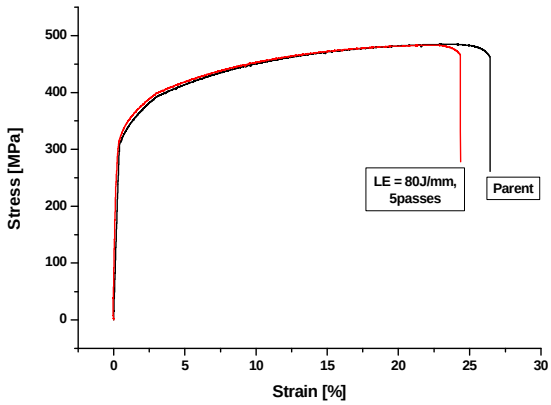

Figure 5.9: Example stress-strain graph for AA2024-T3 of the parent material and a laser formed sample, LE = 80J/mm, 5 passes.

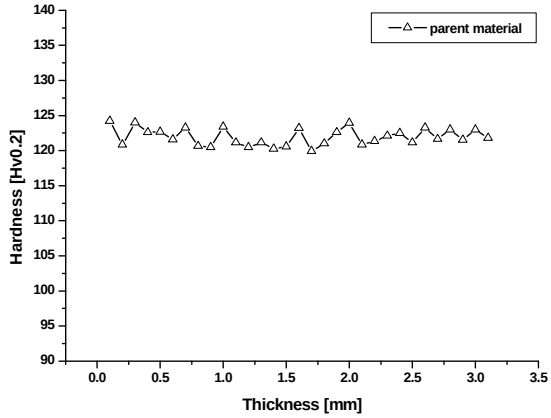

Figure 5.10: Hardness measured through thickness for AA2024-T3 parent material.

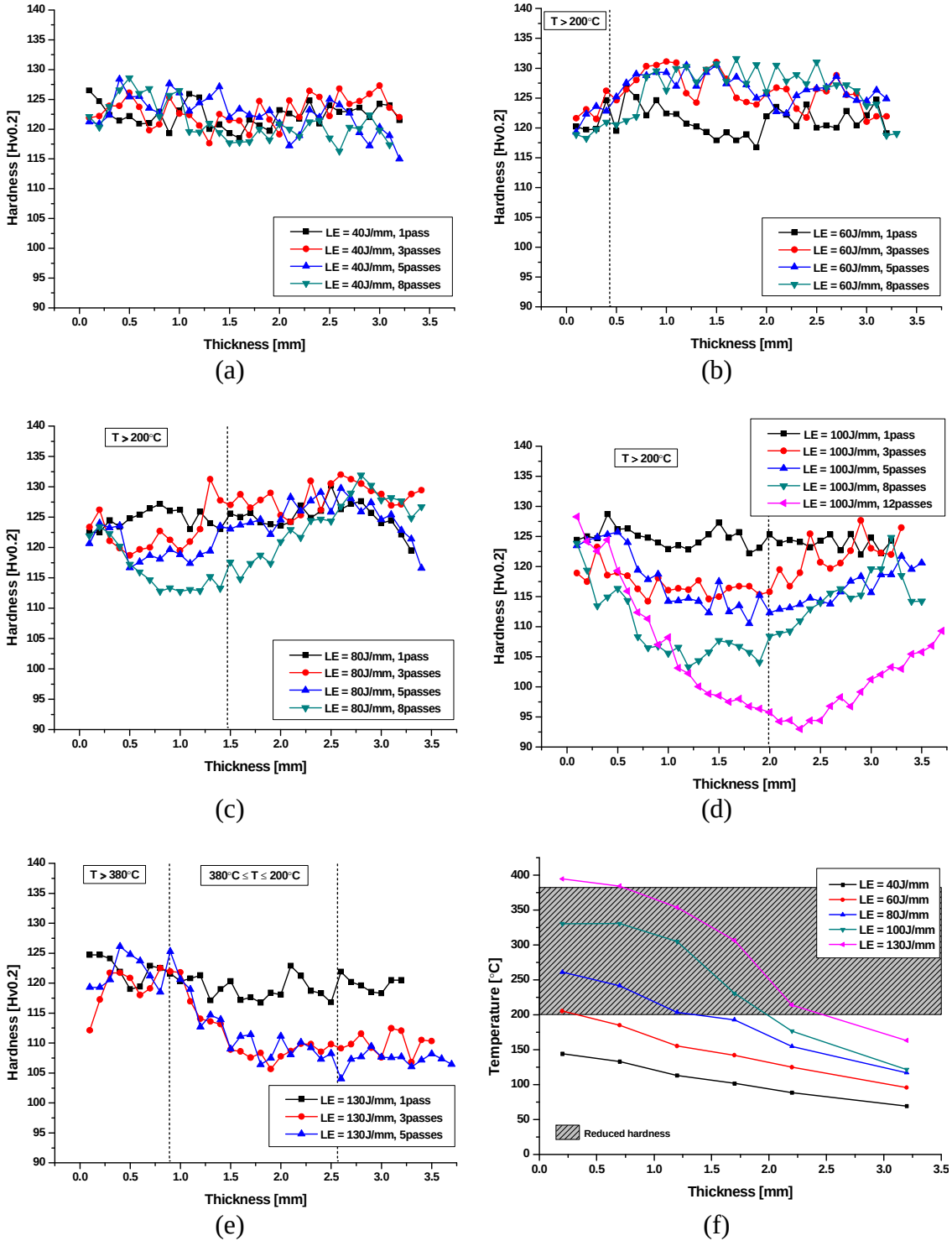

Figure 5.11: Hardness measured through thickness for AA2024-T3; (a) LE = 40J/mm; (b) LE = 60J/mm; (c) LE = 80J/mm; (d) LE = 100J/mm; (e) LE = 130J/mm; (f) Peak temperature measured through thickness.

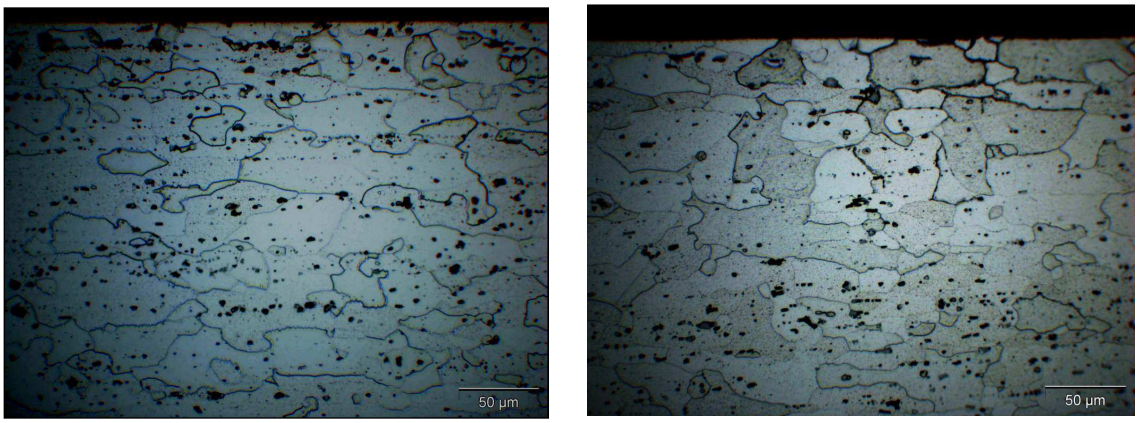

(a) (b)

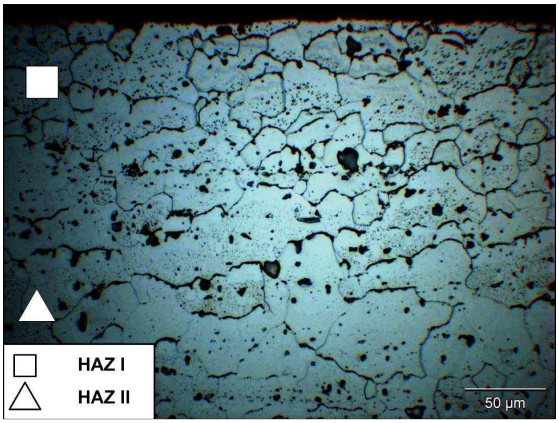

(c)

Figure 5.12: Optical micrographs (mag. ×500) of AA2024-T3; (a) Parent material; (b) HAZ II grain boundary precipitation, i.e. dark boundaries surrounding the grains for LE = 60J/mm, 8 passes; (c) HAZ I partial melting and hot tearing at grain boundaries for LE = 130 J/mm, 5 passes.

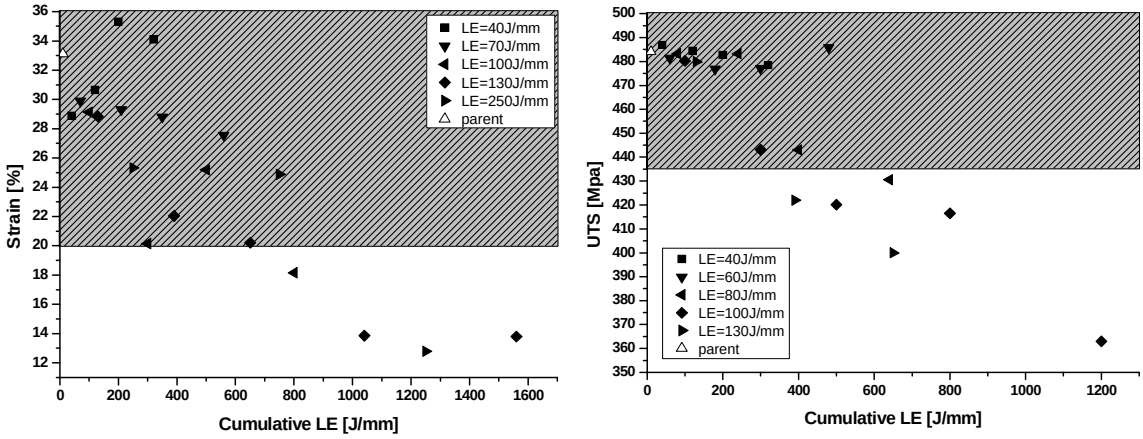

(a) (b)

Figure 5.13: (a) Failure strain plotted against CLE for AISI1010; (b) UTS plotted against CLE for AA2024-T3.

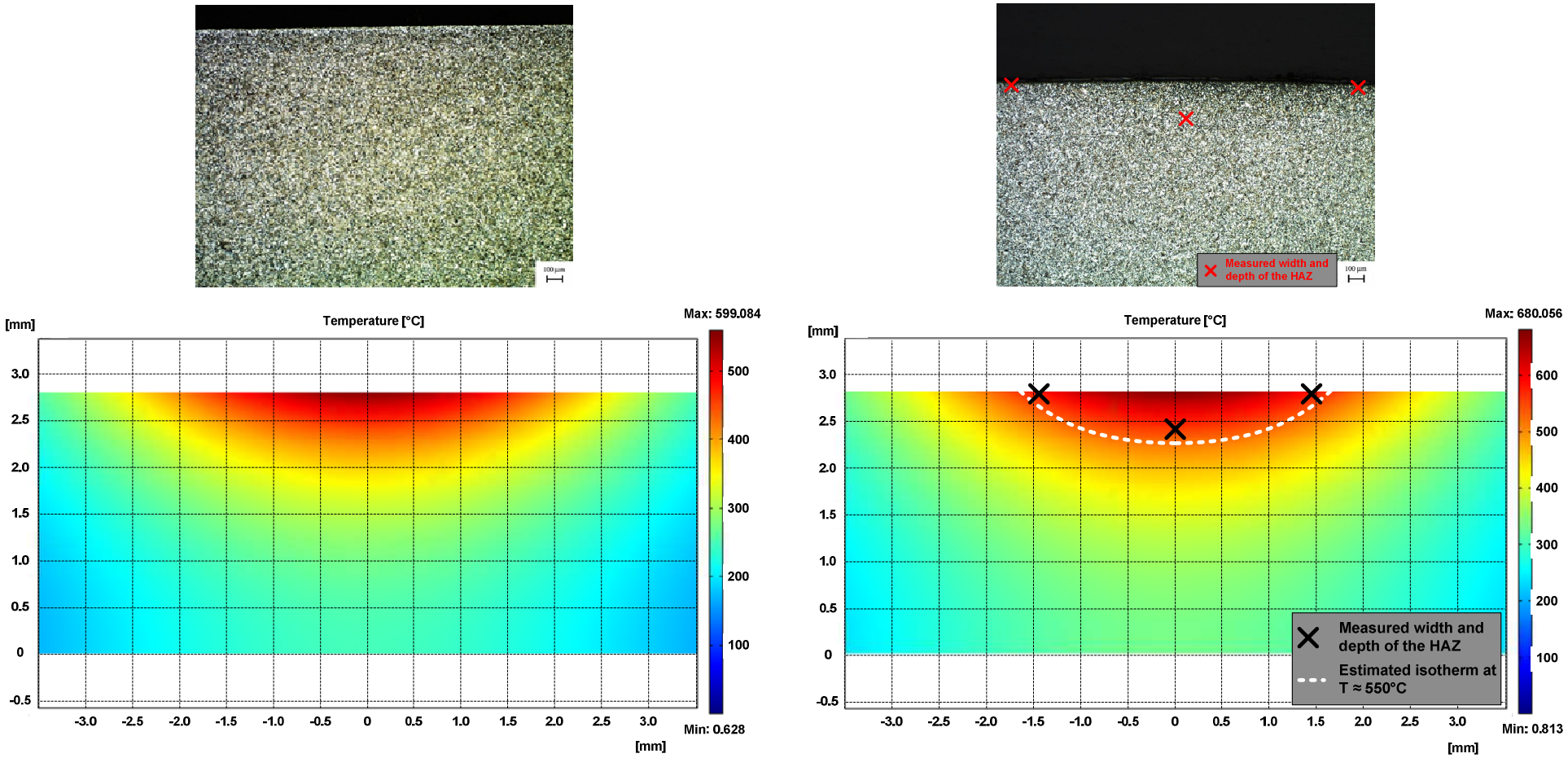

(a) (b)

Figure 5.14: Optical macrograph of low carbon steel (mag. x50) and modelled through thickness temperature; (a) LE = 70J/mm; (b) LE = 100J/mm (please note that the sample was scanned 8 times to show an optical resolvable effect).

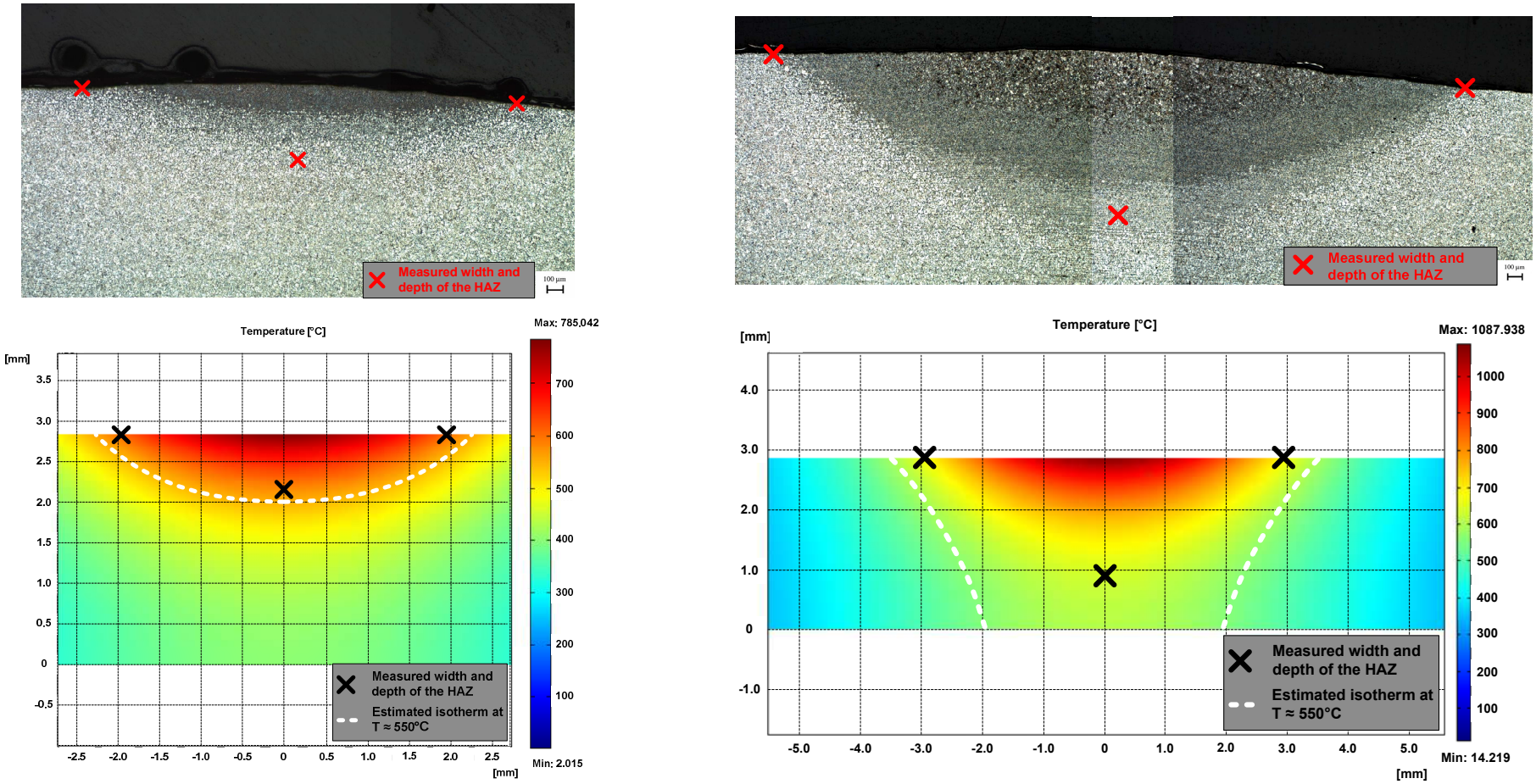

(a) (b)

Figure 5.15: Optical macrograph of low carbon steel (mag. x50) and modelled through thickness temperature; (a) LE = 100J/mm; (b) LE = 250J/mm (Please note that the optical macrograph was put together from 3 separate images, because the HAZ was too large to be captured in one image).

Sample No.	No. of passes	Line Energy [J/mm]	CLE [J/mm]	HAZ depth* [µm]	HAZ width* [µm]
P01	1	40	40	-------	-------
P02	3	40	120	-------	-------
P03	5	40	200	-------	-------
P04	8	40	320	-------	-------
P05	1	70	70	-------	-------
P06	3	70	210	-------	-------
P07	5	70	350	-------	-------
P08	8	70	560	-------	-------
P09	1	100	100	-------	-------
P10	3	100	300	-------	-------
P11	5	100	500	-------	-------
P12	8	100	800	336	2793
P13	1	130	130	594	3525
P14	3	130	390	622	3551
P15	5	130	650	610	3551
P16	8	130	1040	662	3457
P17	12	130	1560	717	3473
P18	1	250	250	1861	5741
P19	3	250	750	1808	5477
P20	5	250	1250	1923	5562

Table 5.5: Width and depth of the optical resolvable HAZ of laser formed AISI1010 tokens; (*Each value shown is the average of two independent measurements).

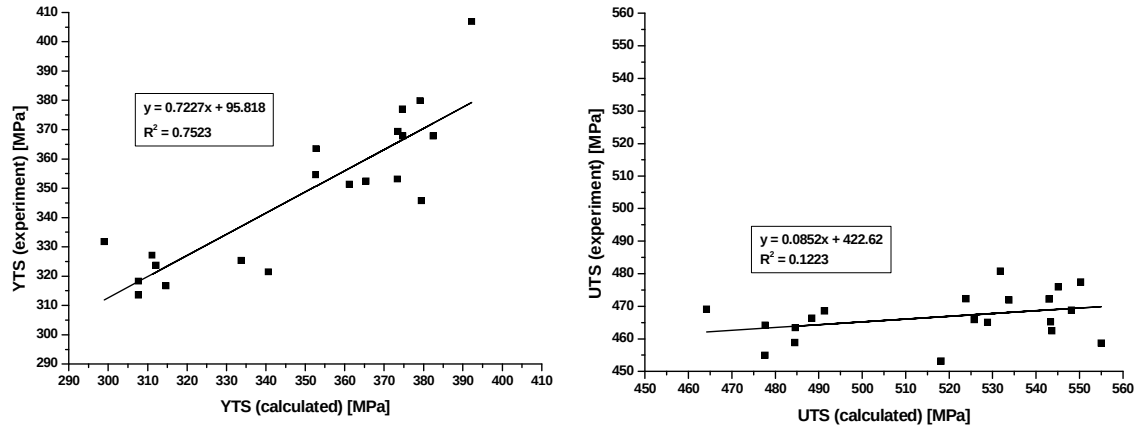

(a) (b)

Figure 5.16: Comparison of measured tensile properties against tensile properties calculated from the hardness measurement for AISI1010; (a) YTS; (b) UTS.

Chapter 6

Residual stress measurement

In laser forming, the thermally induced transverse plastic stress varies with depth and contributes most significantly to the sample deformation. Therefore the understanding of the stress distribution in this direction is of particular interest. This chapter presents high resolution transverse through thickness residual strain measurements on thin low carbon steel and aluminium-copper alloy tokens, which were further compared with the results of the analytical-numerical model of laser forming, proposed previously [77]. Neutron diffraction at two different facilities was used to characterize the residual strain of laser scanned samples across the HAZ, which were treated in a broad laser line energy range with one and three passes. Multi-pass behaviour was of special interest to define process parameters for our approach to iterative laser forming (ILF). Following measurements at a third facility, the effect of the ILF process on the residual stress (RS) is shown in one of its potential future industrial applications: the iterative laser straightening of distorted friction stir welded (FSW) aluminium plates.

6.1 Theory and background

This section gives a brief introduction to the definition of residual stresses. Then, the principle of diffraction measurement with X-rays or neutrons is reviewed, which allows the determination of those residual stresses non-destructively.

Residual stress is the stress which remains in a body that is stationary and at equilibrium with its surroundings [140]. Therefore, residual stresses are mechanical stresses present in a work piece or component which is not subject to external forces, a momentum or temperature gradient. Residual stresses arise as a result of a misfit between two or more distinct regions of a sample. This misfit may be plastic, thermal, chemical, or caused by the interaction of parts in an assembly, e.g. a rivet, joining two plates. By definition, residual stresses are self-equilibrating stresses [134]. They are categorized most commonly when dealing with diffraction methods, based on their length scale over which they equilibrate [141], as shown in Figure 6.1. Type I, or σ^I, residual stresses result from long range strain incompatibilities introduced e.g. by temperature gradients across a weld, causing misfits in thermal expansion and strength. Those residual macrostresses can often be controlled for example through thermal or mechanical

tensioning during welding [92]. Type II, or σ^{II}, and Type III, or σ^{III}, residual stresses are microstresses which arise for instance as a result of deformation misfits between neighbouring grains (Type II), or are caused by voids, solute atoms or dislocations in the crystal lattice [142] (Type III), (Figure 6.1). The RS measurements, presented in this chapter focus on residual macrostresses (Type I, σ^{I}), arising in the HAZ of tokens after single and multiple laser scan passes.

The underlying physical principle of diffraction measurements is the constructive interference of radiation waves, such as those of X-rays or neutrons. This interference under the glancing angle θ^{hkl} occurs only, if radiation of the wavelength λ strikes a lattice plane with the Miller indices (hkl) and the interplanar lattice spacing (or lattice constant) d^{hkl}. The diffraction condition on crystalline materials can be described by the Laue or Bragg equation [143],

$$n\lambda = 2d^{hkl} \sin\theta^{hkl} \qquad (6.1)$$

where n is an integer which fulfils the condition. The Bragg condition is shown schematically in Figure 6.2, where the dots represent atoms within the lattice planes (hkl) and the arrows represent rays of incident and diffracted radiation (either X-rays or neutrons). If one considers ray 1 and 2 which are in phase at X-X', the distance travelled by ray 2 to reach Y-Y' is greater than that of ray 1. To remain in phase, the difference in distance travelled must be an integer number of wavelengths $n\lambda$. From Bragg's law, equation (6.1), it can be seen that the diffraction angle for a given wavelength is proportional to the lattice spacing d^{hkl}.

For the analysis of internal stresses, the crystallites forming the polycrystalline solid aggregate act as strain gauges. The presence of internal stresses may therefore shift the reflection position $2\theta^{hkl}$. Monochromatic diffraction measurements, as they are made for example at reactor sources, record the diffraction angle $2\theta^{hkl}$ with suitable detector equipment. From the knowledge of the incident constant wavelength λ the lattice spacing d^{hkl} can be calculated with equation (6.1). Figure 6.3 shows the diffraction peak of the Fe(211) Bragg reflection, measured at the Australian research reactor OPAL with a monochromatic thermal neutron beam of $\lambda = 1.66$Å on the KOWARI strain scanner. Pulsed neutron sources, such as ISIS (Didcot, UK), use neutrons created over a wide energy range for energy dispersive diffraction measurements, applying the time of

flight technique (TOF). The speed of a neutron v is related to its wavelength λ through the de Broglie relation,

$$h\lambda = mv \tag{6.2}$$

where h is the Planck constant $[6.626 \cdot 10^{-34} Js]$ and m is the mass of the neutron $[1.674 \cdot 10^{-27} kg]$. Because all neutrons leave the source at the same time, the wavelength of a neutron travelling a known distance L_1 from source to sample and L_2 from sample to detector, is readily defined from its TOF t.

$$\lambda = \frac{h}{mv} = \frac{h}{m} \cdot \frac{t}{(L_1 + L_2)} \tag{6.3}$$

A typical diffraction spectrum from an aluminium-copper alloy (AA2024-T3) sample, measured at ENGIN-X instrument at ISIS, is shown in Figure 6.4. The spectrum is typical of a polycrystalline sample, showing several diffraction peaks corresponding to different (hkl) families of lattice planes, as given by Bragg's law, equation (6.1), obtained with a fixed diffraction angle θ_B, defined by the detector position (for ENGIN-X the detector position is $2\theta_B = \pm 90°$). If a strain free lattice parameter d_0 is known, the strain ε in the direction normal to the reflecting lattice plane (direction of the scattering vector $\vec{q}$, [Figure 6.2]) is calculated as the change in lattice spacing over the unstressed spacing,

$$\varepsilon^{hkl} = \frac{d^{hkl} - d_0^{hkl}}{d_0^{hkl}} \tag{6.4}$$

6.2 Analytical-numerical model of laser forming [77]

This section supplies background information to the analytical-numerical laser forming model [77], described in detail in section 2.5.2. It reviews briefly key elements of the understanding gained, and gives material parameters used for the simulation results presented.

The model gave an insight into the laser forming process and helped to understand it in such a way, that on the one hand TGM and SM are two distinct mechanisms, but on the other hand, one mechanism links seamlessly into the other. The regions where one mechanism outbalances the other were predicted by the model, as shown in Figure 6.5. In the near linear region between threshold and saturation LE, the TGM is predominant, and if the LE increases beyond the saturation LE, TGM efficiency has begun to decline and conditions favour the SM (in-plane shrinkage). Clearly, if conditions of one

mechanism are chosen in a forming approach, there will always be a certain amount of the other one present. The model underestimated the bend angle, as shown in the comparison in Figure 6.5, between bend angle predicted and experimental calibration data, which is the same as the calibration data in Figure 2.24(b) and (d). This underestimation of the bend angle and thus induced bending stress arises from the assumptions and simplifications made, for example the 1D temperature field, no spatial heat diffusion and fully-constrained heating and cooling. Because of those assumptions, a slight offset in threshold and saturation LE predicted is visible in Figure 6.5, which is more pronounced for the aluminium-copper alloy (Figure 6.5[b]), compared with low carbon steel (Figure 6.5[a]).

The calculated plate bending from the model (Figure 6.5) contributes a linearly varying stress distribution through depth. Adding this stress to the thermally induced stress, which was based on the peak through thickness temperature profile (Figure 6.7[a]), allowed a prediction of the transverse residual strain profile after deformation. This through thickness transverse residual strain profile is shown in Figure 6.6(a)-(b) for both materials respectively. It is the purpose of this Chapter to validate the simplified model with residual stress measurements.

The temperature constant material parameters chosen for the modelling of low carbon steel (AISI1010) [138] and aluminium-copper alloy (AA2024-T3) [144] are shown in the caption of Figure 6.5. The through thickness temperature profiles calculated by the model for both materials after equations (2.21) and (2.22) were matched with through thickness thermocouple measurements (Figure 5.7[f] and Figure 5.11[f] respectively). Those calculated and measured temperature profiles of low carbon steel are compared with the ones of the thermal FE-analysis (section 4.5) in the following paragraph. Furthermore, the flow or threshold temperature, required in the analytical-numerical model was calculated for each material from the yield (flow) stress with $T_{th} = T_0 + \sigma_f/(\alpha E)$, based on the assumption of perfectly constrained heating and cooling. The saturation temperature T_{sat} was one third of the material melting temperature T_s [145], limiting the maximum thermal induced stress to σ_f [77].

Figure 6.7 compares the through thickness temperature distribution for low carbon steel samples at different line energies of the analytical-numerical model (Figure 6.7[a]), with that of the thermal FE-analysis (section 4.5), (Figure 6.7[b]). It can be seen that the analytically calculated temperature profiles in the upper half of the plate are almost

twice the magnitude of those predicted by the FE-model. Furthermore, the analytical temperature profiles show a steeper temperature gradient in the top half of the plate and are perfectly uniform in the bottom half, whereas the profiles from the FE-analysis have a more parabolic shape. If both are compared with through thickness thermocouple measurements (Figure 5.7[f]), the temperature magnitude is predicted well by the FE-analysis in the upper part of the plate, but over estimated in the lower part of the sample, which diminishes the total though thickness temperature gradient. The temperature gradient and shape of the analytically calculated through thickness temperature profiles match that of the experimentally found (Figure 5.7[f]) well, even though the temperature predicted is about double the magnitude, owing to the model not taking into account the heat sink effect of cold surrounding material (only 2D).

6.3 Experimental procedure

The chemical composition of the two materials investigated in this study, as representative of low carbon steel (AISI1010) and aluminium-copper alloy (AA2024-T3 condition, i.e. solution heat treated, cold worked and naturally aged to a substantially stable condition) is shown in Table 5.1 and Table 5.2 respectively. Square test tokens were laser cut from parent sheet material for laser forming of dimensions 80x80x2.8mm^3 for low carbon steel and 120x120x3.2mm^3 for aluminium alloy. The plates were not annealed, because the RS measured in a non-formed laser cut specimen (parent material) was negligible compared with that induced by laser forming. Each token was degreased with acetone and then coated with a thin layer of graphite to improve the coupling efficiency of the laser energy into the sample surface.

Laser forming experiments were carried out following the procedure described in section 3.2. The forming process was applied by either one or three laser scan passes along the centreline, as shown in Figure 2.22. For multiple laser scans, 60 seconds were allowed between scans for the token to cool down in order to minimise the increase in bulk temperature. Multiple laser scans were applied in alternating directions along the same line to minimise distortion of the tokens along the ‘longitudinal’ direction (Figure 6.8).

The bend angle was calculated by measuring the shape of the tokens before and after forming using a single point triangulation probe [77]. The probe was scanned in lines perpendicular to the laser forming scan direction (i.e. parallel to the ‘transverse’ direction, Figure 6.8) in 5mm intervals along the ‘longitudinal’ direction. The bend

angle at each shape scan line was calculated from the shape change, and the mean bend angle calculated over all intervals for the final bend angle of the token (Table 6.1 and Table 6.2).

RS measurements were made at two neutron facilities using two different strain scanning modes, namely monochromatic (constant wavelength) on the KOWARI strain scanner at the Australian research reactor OPAL and time-of-flight on ENGIN-X neutron scattering diffractometer at ISIS, Rutherford Appleton Laboratory, UK.
The strain measurements on KOWARI were done using the Fe(211) Bragg reflection observed at a scattering angle 2θ of $\sim 90°$ with a monochromatic thermal neutron beam of 1.66Å, which was extracted from a double focusing Si (400) monochromator at a take-off angle of $\sim 75°$. Accurate sample alignment and surface finding were performed on each sample separately using the neutron beam. For this, the sample was shifted through the beam and the integral intensity of the desired reflection was recorded, where the intensity was half of the maximum intensity relative to the true sample surface.
ENGIN-X is the dedicated time-of-flight engineering diffractometer at ISIS pulsed neutron source. The instrument has two detector banks centred on horizontal scattering angles of $\pm 90°$, enabling simultaneous measurement of two orthogonal strain components. Measurements were made following the guidelines present in [146,147]. As ENGIN-X utilises a spallation neutron source, it is a time-of-flight facility and multiple diffraction peaks were acquired simultaneously. This enables lattice spacings to be obtained directly by performing Pawley-Rietveld refinement using the general structure analysis system (GSAS) [148], after time focussing the raw data from each detector bank. Accurate alignment of the thin specimens was achieved using the software SScanSS [149]. The laser-formed samples, mounted on the specimen holder with their Fiducial points for accurate alignment in the experimental hutch, are shown in Figure 6.9(a). Figure 6.9(b) shows the samples from Figure 6.9(a) in the 'virtual' measurement during the simulation in SScanSS.

For the measurement at both facilities, the specimens were positioned to permit determination of stresses in the three primary working orthogonal directions of the deformed plates. Stress free d_0 measurements were performed on a small cube sample (2x2x2.8mm^3 for AISI1010 and 2x2x3.2mm^3 forAA2024-T3) carefully cut from the parent material and the HAZ (Table 6.1 and Table 6.2), using a diamond wafer blade on

a low speed cutting saw. For the measurement itself, four of those cubes were glued together.

The sample conditions, induced distortion and measurement facility for both materials investigated are shown in Table 6.1 and Table 6.2. The coordinates of the RS measurement across the HAZ are shown in Figure 6.8(a) for AISI1010 and Figure 6.8(b) for AA2024-T3. The measurement of AA2024-T3 tokens were not made closer to the HAZ because of the sample setup on the specimen holder. As shown in the simulation in SScanSS prior to the measurement, there would have been the potential risk of a collision with the collimators, placed in front of the detector, if measurements would have been made closer to the HAZ and sample surface.
The depth of 0.9mm from the laser scanned surface was chosen for the measurement of AISI1010 tokens to ensure that the sample gauge volume (GV) was completely submerged in the deformed specimen, because the samples were distorted not only along the 'transverse' direction (Figure 6.8), but also in 'longitudinal' direction. This unwanted distortion in longitudinal direction is well known in laser forming and explained in more detail in section 2.1.1. Even though the samples were carefully aligned, as described above, this depth minimised the risk of spurious strains owing to an only partially filled GV. The GV of the measurement across the HAZ was 1x1x20mm^3 at ISIS and 1x1x10mm^3 at ANSTO, which allowed all measurements to be made in an acceptable time. (It should be noted that the discrepancy in the GV length between both facilities was owing to the higher neutron flux at reactor sources compared with pulsed neutron sources. Over this GV length, strains were relatively constant in 'longitudinal' direction [Figure 6.8]).

The coordinates of the transverse residual strain measurement through thickness are shown in Figure 6.10(a) for AISI1010 and Figure 6.10(b) for AA2024-T3. The through thickness measurement of AISI1010 was performed with a GV of 0.5x0.5x15mm^3. Because of the larger grain size of AA2024-T3 ($\geq 50\mu m$) compared with that of low carbon steel ($\leq 10\mu m$), the through thickness measurement was performed with an instrument GV of 1x1x20mm^3 to ensure that enough representative grains were within the sample GV for a reasonable statistic. Moreover, through this GV, an acceptable counting time was ensured to make efficient use of the beamtime allocated. Therefore, measurement points as close to the surface as for AISI1010 (Figure 6.10[a]), where the instrument GV was 0.5x0.5x15mm^3, were not possible for AA2024-T3 (Figure 6.10[b]).

6.4 Results

The following section presents a back-to-back measurement from a stress-free reference sample, carried out at both facilities first and further compares the d_0 cut from the HAZ of samples, scanned with the highest and lowest LE considered in this study. Then the results of the RS measurement across the HAZ and through thickness of both materials are presented. For low carbon steel (AISI1010), one and three laser passes are considered in the corresponding LE range. Owing to limited allocated beam time, only the results of single laser scans are shown for the aluminium-copper alloy (AA2024-T3).

6.4.1 Unstressed lattice parameter

Table 6.1 shows a comparison of the d-spacing in in-plane and normal direction of a d_0 cube sample, which was cut from a parent AISI1010 plate (no heat input, LE = 0J/mm) and measured at both facilities. The negligible discrepancy of this back-to-back measurement (~ 85μstrain) justifies the direct comparison of residual strain measurements made at the different institutes.

The d-spacing of stress-free d_0 cut from the HAZ of low carbon steel samples, scanned once with the highest and lowest LE, which was considered in this study (LE = 40J/mm and LE = 130J/mm), are shown in Table 6.1. The observable discrepancy of 10^{-4}Å is equivalent to ~ 85μstrain, which is an order of magnitude smaller than the strain, measured in the bulk samples. For samples, scanned three times at constant LE, it was assumed that material properties would not be altered to such an extent that the d-spacing of a stress-free d_0 would be affected. This assumption was based on the literature [108], where it was shown that the d-spacing discrepancy of stress-free mild steel d_0 cubes cut from a laser-formed HAZ, scanned three times at LE = 133.3J/mm, was equivalent to ~ 100μstrain, compared with parent material. The minor discrepancy observed in this study follows the trend shown in Table 6.1. Owing to the fact that there were no significant changes in d_0 with LE, lattice spacings were converted into engineering strain using equation (6.4) and the d_0 of parent material (LE = 0J/mm, Table 6.1) in the corresponding direction.

The d-spacing variation with heat input of AA2024-T3 cube samples is shown in Table 6.2. Compared with parent material (LE = 0J/mm), the d_0 in the in-plane direction does not change significantly with LE applied (equivalent to ~ 120μstrain), but it is slightly

larger in the normal direction (equivalent to ~ 240μstrain). In the following analysis the d_0 was treated as constant and as shown in section 6.5, the results with a d_0, varying with LE, differ negligible. This larger variation of unstressed lattice parameter, observed for the aluminium-copper alloy, is most likely caused by the dissolution or coarsening of precipitates, which will lead to changes in the local solute concentration and hence the unstressed lattice spacing [150]. This behaviour was found more distinctively in the thermal affected zone of friction stir welds [154].

6.4.2 Residual stress measurement across the HAZ

In the following section, the results of the RS measurement across the HAZ of both materials investigated are presented separately.

Low carbon steel (AISI1010)

Figure 6.11 shows an example of residual strain and RS in all three perpendicular directions across the HAZ, measured at a sample scanned at LE = 70J/mm, 1 pass. Lattice spacing was converted to residual strains with equation (6.4). To determine the RS tensor components the generalized three dimensional Hooke's law [151] was used. The expression for one of the three orthogonal principal stress components σ_{xx} has the form

$$\sigma_{xx} = \frac{E}{1+\nu} \cdot \varepsilon_{xx} + \frac{E \cdot \nu}{(1+\nu)(1-2\nu)} \cdot \left(\varepsilon_{xx} + \varepsilon_{yy} + \varepsilon_{zz}\right) \tag{6.5}$$

where ε_{xx}, ε_{yy}, ε_{zz} are the orthogonal normal strain components, and E and ν are the bulk elastic modulus and Poisson's ratio, which was 190GPa and 0.3 for AISI1010 respectively. The errors in the assessment of stress tensors are obtained by differentiating equation (6.5) with respect to all principal strain components ε, since each of them contributes to the resulting stress tensors. Since these errors are statistically independent, and also the measurements are governed by normal distribution, then the uncertainty for each of the principal stress tensors is written as the quadratic sum of the original strain uncertainties $\Delta\varepsilon_{ij}$ [152], which are itself the d-spacing error from the peak fit of the diffraction peak(s).

$$\Delta\sigma_{xx} = \frac{E}{(1+\nu)} \sqrt{\left(1 + \frac{\nu}{(1-2\nu)}\right)^2 \Delta\varepsilon_{xx}^2 + \left(\frac{\nu}{(1-2\nu)}\Delta\varepsilon_{yy}\right)^2 + \left(\frac{\nu}{(1-2\nu)}\Delta\varepsilon_{zz}\right)^2} \tag{6.6}$$

The uncertainties for the other two principal stress components $\left(\Delta\sigma_{yy}, \Delta\sigma_{zz}\right)$ can be easily calculated by permutation of xx, yy, zz indices in equation (6.6).

From Figure 6.11, it can be seen that in the centre of the HAZ, residual stresses and strains in longitudinal direction are tensile and dominant and the normal ones are compressive. In the transverse direction, residual strains are compressive and residual stresses are close to zero or slightly tensile. Outside the laser beam footprint, the RS in all three perpendicular directions is close to zero. The normal RS at the plate boundary 35mm away from the HAZ (Figure 6.11[b]) should be zero under the assumption that there is no out-of-plane component to the stress tensor over the GV (biaxial stress state), because of the thin token. Possible sources for the minor discrepancy of about -33MPa include residual stresses from the previous laser cutting of the token from the parent sheet, or stresses equilibrating the stress peak in the HAZ.

Figure 6.12 shows the evolution of the dominant longitudinal residual strain across the HAZ with increasing LE at one and three passes. The residual strain peak is most significant in the longitudinal direction, because the shrinkage as a consequence of inhomogeneous temperature distribution is impeded to a much larger extent than, for example, in the transverse direction. It can be seen in Figure 6.12 that, with the increasing heat input associated with higher LE and/or multiple passes, the longitudinal residual strain increases until a threshold is reached. For samples scanned at LE = 130J/mm (Figure 6.12[d]), the magnitude of the strain cusp slightly decreased, but its total height was found to remain constant. Generally, if the heat input in the form of LE induced per pass is higher, the difference in longitudinal residual strain becomes more distinct between samples treated with one and three laser scans, caused by the steeper through thickness peak temperature gradient reached (Figure 5.7[f]).

Aluminium-copper alloy (AA2024-T3)

The residual strains and stresses of an AA2024-T3 sample scanned once at LE = 80J/mm are shown in Figure 6.13. The RS was calculated using equation (6.5) with a bulk elastic modulus E of 73GPa and Poisson's ratio ν of 0.33. Stresses and strains in longitudinal direction are tensile and dominant. Normal and transverse stresses and strains are compressive. Outside the laser affected region the RS in all three perpendicular directions converges to zero. As shown in Figure 6.14 and already observed for AISI1010, the dominant longitudinal strain peak increased with heat input (LE) until it reached a threshold at LE = 80J/mm. Higher heat input (LE = 100J/mm) increased its width, but not its strain magnitude, in the depth of the measurement

(Figure 6.8[b]). Generally, the shape of all strain peaks measured from AA2024-T3 samples is sharper and not as broad as those observed at low carbon steel (Figure 6.11), owing to the three times higher thermal conductivity of the aluminium-copper alloy compared with low carbon steel, which reduces the peak temperature and width of the thermal affected region.

6.4.3 Transverse residual strain measurement through thickness

In this section, the results of the transverse residual strain, measured through thickness of AISI1010 and AA2024T3 specimens are presented. Afterwards, they are compared with the strain profiles predicted by the analytical-numerical laser forming model [77].

Low carbon steel (AISI1010)

Figure 6.15(a) shows the transverse residual strain through plate thickness of single pass laser formed low carbon steel samples with LE. From the laser scanned surface the compressive strain decreases in magnitude to a local maximum at a sample depth of ~ 0.75 - 1.0mm as the residual strain profile falls and rises again in the remaining depth and finishes in tension at the bottom near-surface region. Figure 6.15(b) shows the transverse residual strain profile at one and three passes of samples scanned at LE = 130J/mm. It can be seen that repetitive laser treatment shifts the strain profile further towards the tensile region, whereas its shape remains similar. Generally, the effect with heat input associated with higher LE and/or multiple laser passes on the transverse through thickness residual strain profile of AISI1010 samples is not significant, as can be seen from Figure 6.15.

Aluminium-copper alloy (AA2024-T3)

Figure 6.16 shows the transverse residual strain profiles through thickness of AA2024-T3 samples scanned with a single pass at different line energies. The profiles from Figure 6.16 are similar to those previously observed for low carbon steel (Figure 6.15[a]). Owing to the use of a GV of 1x1x20mm^3 during the measurement, it was not possible to measure the strain closer to the sample surface in the thermally plastified heat-affected region. The residual strain profiles in the LE range of 60-100J/mm, shown in Figure 6.16, are characteristic to inhomogeneous plastic sheet bending [153]. They become less compressive with increasing heat input. At LE = 40J/mm, which is just above the threshold LE seen in the experiment (Figure 6.5[b]), almost no residual strain through thickness is induced. This relation between threshold LE, forming mechanism and transverse residual strain is discussed further in section 6.5.

Comparison with the analytical model

It can be seen in the comparison between the model (Figure 6.6) and experiment (Figure 6.15[a] and Figure 6.16) that the transverse residual strain profile is predicted qualitatively by the model in a greatly simplified way for both materials investigated. Through assumptions made in the model (section 6.2), the residual strain profiles predicted did not match with the ones from the measurement in the heat affected plastified zone and the strain magnitude predicted was too low, as it was already observed for the bend angle. The compressive near-surface residual strain (Figure 6.15[a] and Figure 6.16) in the heat affected region is a result of the spatial thermal plasification and the induced bending strain. If the microstructure in this near surface region is visibly affected through the heat input, e.g. as it was found in the form of a bainitic microstructure for low carbon steel samples scanned at LE = 130J/mm (section 5.3.1), additional residual microstresses become more distinct and superimpose residual macrostresses which arise as a result of plastification and bending deformation. Layers in the bottom part of the plate experience plastification only if the induced bending strain there exceeds yielding. Therefore, the transverse residual strain profile in the remaining non-plastified material through depth shows characteristic evolution brought about by inhomogeneous plastic sheet bending, explained in more detail in [153]. Clearly, superposition of complex processes in the thermally plastified near-surface region would necessitate a FE-analysis for more accurate residual strain prediction.

6.5 Discussion

In all the results presented, the d_0 of parent material was used to calculate the residual strain with equation (6.4). For low carbon steel, the change in d_0 with LE was negligible. A slightly larger change in d_0 was observed for the aluminium-copper alloy in the normal direction. The discrepancy made through this assumption of a constant parent d_0 was $\ll 10\%$ strain in the HAZ, where the d_0 was known (Table 6.2). Generally, the d_0 should have been measured at each point of the RS measurement across the HAZ and further into the bulk material. Owing to the time constraint of allocated beam time this was not possible. However, the discrepancy made through this assumption was acceptable compared with the strain measured in the bulk samples.

Figure 6.6 shows the transverse residual strain profile through thickness predicted by the analytical-numerical model [77] for low carbon steel (Figure 6.6[a]) and aluminium-copper alloy (Figure 6.6[b]). If those profiles are related to the bend angle predicted

(Figure 6.5), it can be seen that the transverse residual strain around the centre region through the token thickness increases in magnitude with LE under conditions favouring the TGM, which is between threshold LE and saturation LE. In the regime of the SM, at line energies above saturation LE, the residual strain predicted decreases in magnitude, because the through thickness peak temperature profile becomes more uniform, decreasing thermal misfit and bend angle efficiency. This physical behaviour is visible in the through thickness residual strain profiles measured for AA2024-T3, shown in Figure 6.16, where the strain is highest in magnitude at LE = 60J/mm, which is just before saturation LE is reached (Figure 6.5[b]). Furthermore, it decreases for line energies in the regime of the SM, i.e. LE = 80J/mm and LE = 100J/mm. The through thickness strain profiles of AISI1010 tokens (Figure 6.15[a]) are all very close together and no distinct trend is visible. However, as shown in Figure 6.5(a), the line energies chosen for AISI1010 make only a small section of the TGM regime. Therefore, a large difference between them would not have been expected.

The RS measured across the HAZ of low carbon steel (Figure 6.11[b]) and aluminium-copper alloy tokens (Figure 6.13[b]) showed that in the centre of the HAZ longitudinal stresses are tensile and dominant, normal stresses are compressive and transverse stresses are predominantly tensile for AISI1010 and compressive for AA2024-T3. Clearly, these trends across the HAZ identified here are representative only for the specific depth of the measurement. Their magnitude may vary as a function of depth through the sample thickness. The longitudinal residual strain was found to increase with heat input, associated with higher LE and/or multiple passes, until a threshold was reached. For low carbon steel (Figure 6.12), this threshold was caused by material yielding in tension, shown at the longitudinal RS of the sample scanned at LE = 100J/mm, 3 passes (Figure 6.12[c]), which was calculated with equation (6.5) to 326.3MPa. However, for AA2024-T3 (Figure 6.14), material yielding in tension had not yet been reached, because the dominant longitudinal RS for samples scanned at LE = 80J/mm and LE = 100J/mm was 111.6MPa and 87.1MPa respectively, which is below the specified yield strength of 290MPa [144]. The threshold seen here is the result of the minor temperature difference of $\Delta T \approx 35K$ (Figure 5.11[f]) at the measurement depth $(s_0/2)$. Through this minor temperature difference, the impeded shrinkage after thermal expansion for both samples is about the same and with it the residual strain induced.

The dominant longitudinal strain measured across the HAZ at the start (10mm), middle (60mm) and end (110mm) of an AA024-T3 sample scanned at LE = 80J/mm, 1 pass, is shown in Figure 6.17(a). The measurement was done at a depth of 1.6mm from the laser scanned surface.

It can be seen that the dominant longitudinal strain across the HAZ is significantly lower at the start and the end of the laser scan line than in the middle, because the RS drops to zero at the edge of the plate for equilibrium reasons, as is seen in welds [153]. Although the measurement locations at the start and end of the laser scan path have identical geometrical constraints, the longitudinal strain at the end is twice as high as the one induced at the start (Figure 6.17[a]). The temperature profile in Figure 6.17(b) shows that the temperature at the end of the laser scan is notably higher than that at the start, which increases the thermal misfit and thus induces higher residual strain (Figure 6.17[a]). It is also noticeable that the slope of the temperature profile becomes significantly steeper in the second half of the laser scan, because the heat wave travelling ahead of the laser beam is reflected from the approaching border and contributes to the temperature increase towards the end of the laser scan.

The temperature was recorded with five thermocouples, placed at different positions in the centre and along the laser scan line (LE = 80J/mm, 1pass) at 1.6mm depth, where the RS was measured previously. This temperature profile affects the bend angle in form of an increasing bending deformation towards the end of the laser scan line (Figure 6.17[c]). The sudden bend angle ‘drop off’ ~ 20mm away from the plate border (position 100mm, Figure 6.17[c]) is caused by a vanishing temperature gradient through thickness and therefore conditions favouring the SM. This characteristic bend angle non-uniformity was described in more detail in section 2.1.1.

The residual strain profiles along the laser scan line are explicitly shown in Figure 6.17(d). Clearly, the points in the HAZ centre (pos. 0mm) of Figure 6.17(a) are the same as at 10mm, 60mm and 110mm of the longitudinal strain profile in Figure 6.17(d). If the transverse residual strain profile (Figure 6.17[d]) and the bend angle (Figure 6.17[c]) along the laser scan path are compared, the physical behaviour predicted by the analytical-numerical model is visible. From the start of the laser scan, the bend angle increases and with it the transverse residual strain becomes more compressive until it reaches a maximum, as was seen with increasing LE in the regime of the TGM. With the approaching plate border the temperature increase (Figure 6.17[b]) shifts laser forming conditions in the regime of the SM. Therefore bend angle and transverse residual strain decrease in magnitude.

Residual stress measurements on FSW and laser straightened FSW plates were done with synchrotron radiation at the HARWI II beamline at HASYLAB/DESY. The thin plates (2mm thick) necessitated high energy X-rays for the measurement of longitudinal and transverse RS (assumption of biaxial stress state), which was done in transmission mode, integrating over the sample thickness and using the Al(311) Bragg reflection. During the synchrotron measurement an image with the diffraction rings (of the different hkl lattice planes) was recorded at each measurement point. From this image the diffraction angle θ^{hkl} of a 10° segment of the whole diffraction ring was calculated in the longitudinal and the transverse direction respectively. Figure 6.18 shows an example of such a 10° segment in the longitudinal direction. The diffractogram shows characteristic (hkl) diffraction rings of aluminium and copper. Copper paste was used as the reference material on the sample surface to account for variation in energy of the incident (X-ray) radiation, and surface roughness and distortion of the sample. Based on the reference material, the shift of the Al(311) Bragg reflection was identified and the strain in the longitudinal and transverse direction was calculated with equation (6.4), by permutation of the lattice spacing d^{hkl} with the diffraction angle θ^{hkl} (both are proportional to each other). Stress-free d_0 measurements were performed for each token separately at a point close to the plate border on the measurement line across the weld (Figure 6.19). It was assumed that the RS converges to zero at sufficient distance from the thermal affected zone of the weld as a result of stress equilibrium conditions [153]. The limited beamtime did not allow the measurement of the variation in d_0 of wire cut comb samples from different positions across the thermally affected zone of the weld. As shown in the past [154], the lattice spacing may vary in this zone, for example because of dissolved precipitates. However, the aim of this measurement was to investigate the effect of the iterative laser straightening on the RS state of a friction stir weld. Therefore, potential inaccuracies or errors originating from this assumption were offset through the RS comparison of welded plates before and after the iterative laser straightening. The coordinates of this RS measurement across the weld are shown in Figure 6.19.

Figure 6.20(a)-(c) shows a comparison of the dominant longitudinal RS distribution of a successfully laser straightened FSW plate (red) and one after FSW (black). Because of the thin samples, the RS was calculated under the assumption that there is no out-of-plane component to the stress tensor (biaxial stress state) [134] using

$$\sigma_L = \frac{E}{1-\nu^2}(\varepsilon_L + \nu\varepsilon_T) \tag{6.7}$$

with $E = 73GPa$ and $\nu = 0.33$. Both plates in Figure 6.20(a)-(c) were joined using the same welding parameters, as shown in the table of each Figure and Table 7.7. The scattering of the synchrotron measurement was caused on the one hand by the high resolution of measurement points across the weld ($\Delta x = 1mm$) and on the other hand by the large grains of AA2024-T3 ($\geq 50\mu m$). The strong texture of the samples is seen in the pattern of the (hkl) diffraction rings in the diffractogram of Figure 6.18. To prevent the scattering and increase the statistic, the sample should have been oscillated during the measurement.

The comparison in Figure 6.20 (a)-(c) shows that the ILS significantly reduced the characteristic longitudinal RS peak in the centre of the weld, whose magnitude and width varies, because of the different welding parameters and thus process temperature applied. However, compared with the broad initial longitudinal RS peak after FSW, they are lower in magnitude and, in particular, the tensile RS in the weld seam was reduced for all three plates, joined with different welding parameters. Therefore, the iterative laser straightening not only geometrically flattened the FSW samples, but also significantly reduced the characteristic longitudinal RS peak. A further discussion of those results and the laser forming details applied during the straightening process is presented in section 7.4 and section 7.6.

6.6 Conclusion

The qualitative comparison of a high resolution transverse residual strain measurement through thickness of the thin AISI1010 and AA2024-T3 samples with the analytical-numerical laser forming model, proposed previously [77], showed that it predicts the transverse strain qualitatively in a simplified way. Through assumptions made in the model, it did not match the residual strain distribution in the heat-affected plastified zone. However, the model was extremely useful to understand the relation between bend angle and thermally induced transverse strain and residual strain in laser forming. It showed qualitatively the effect of the two laser forming mechanisms, namely TGM and SM, on the transverse residual strain and therefore contributed to a deeper physical understanding of the laser forming process. In addition, regions such as the thermally plastified HAZ were identified, where superposition of complex thermomechanical processes would necessitate FE-analysis for more accurate residual strain prediction.

6.7 Figures

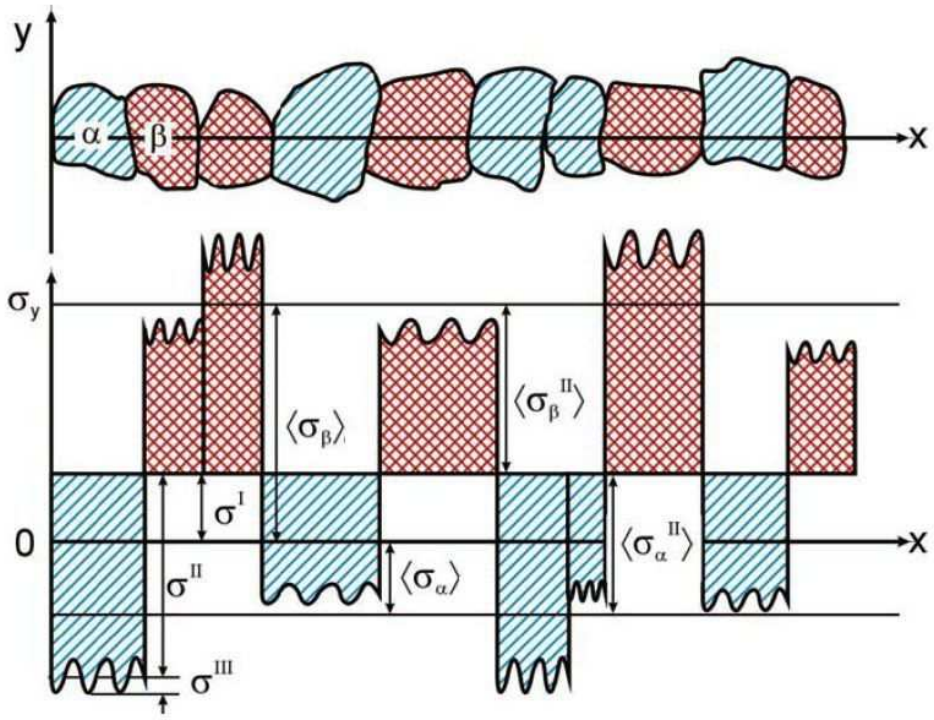

Figure 6.1: Definition of residual macrostresses (σ^I) and microstresses ($\sigma^{II}, \sigma^{III}$) in a multiphase system [155].

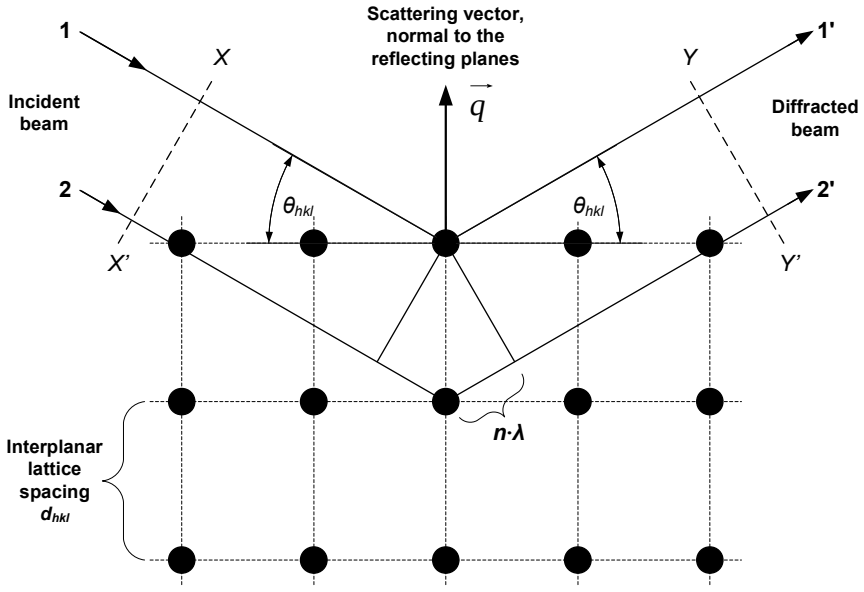

Figure 6.2: Schematic illustration of the reflection of X-rays or neutrons at lattice planes (hkl) after Bragg's law, equation (6.1).

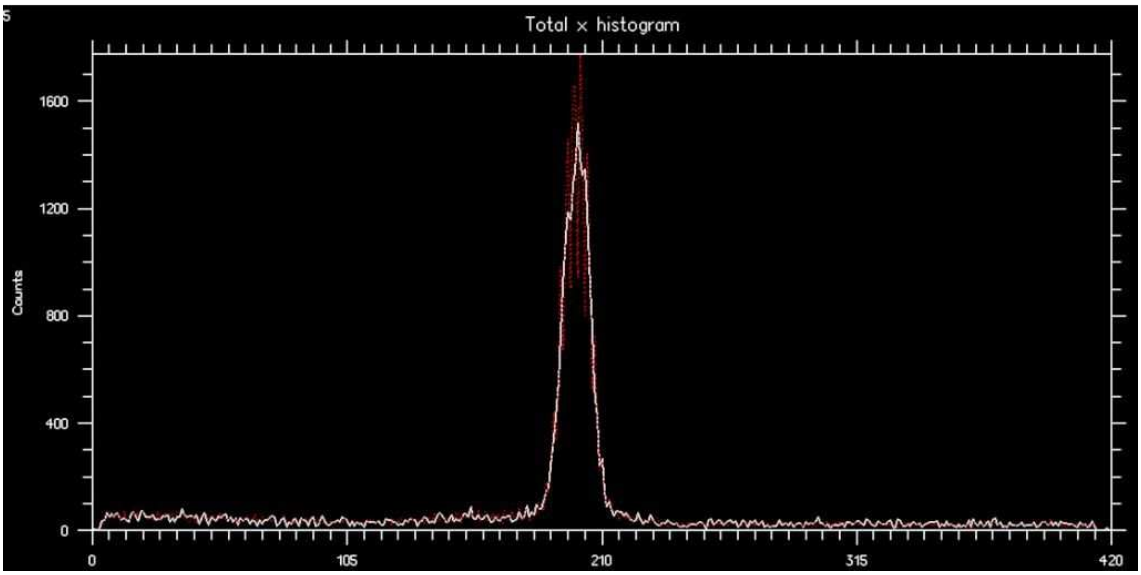

Figure 6.3: Diffraction peak of the Fe(211) Bragg reflection, measured with a monochromatic thermal neutron beam of $\lambda = 1.66\text{Å}$ at the Australian research reactor OPAL.

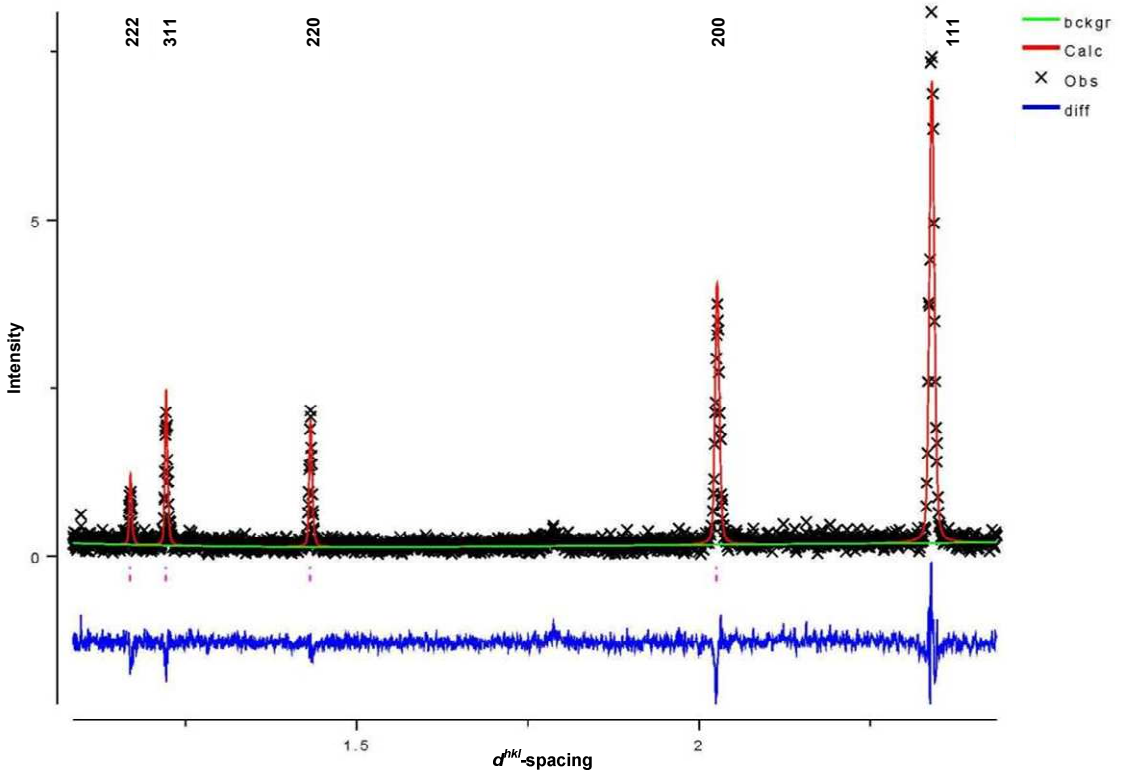

Figure 6.4: Typical time of flight (TOF) diffraction spectrum of an aluminium-copper alloy (AA2024-T3) token with several (hkl) diffraction peaks, measured at the ENGIN-X instrument, ISIS, UK.

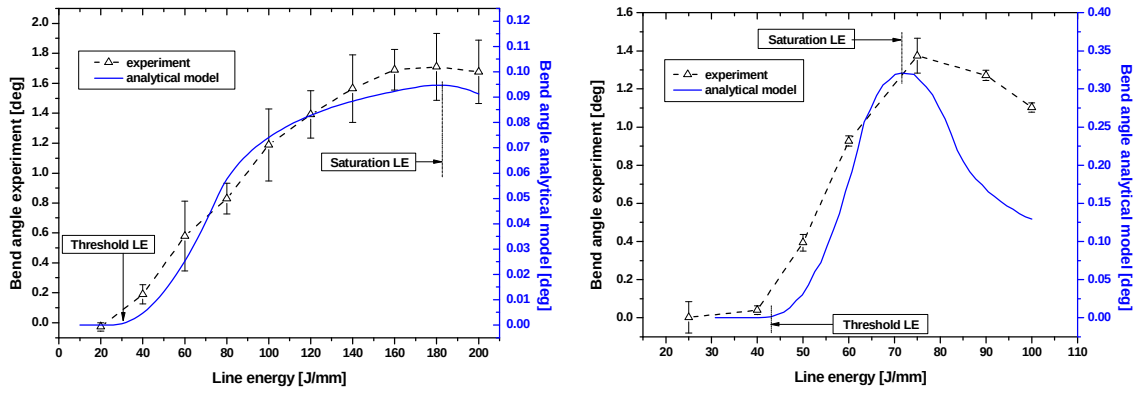

(a) (b)

Figure 6.5: Comparison of the bend angle evolution with LE between the analytical-numerical model [77] and experiment, repeating the calibration data from Figure 2.24(b) and (d) respectively; (a) Low carbon steel (AISI1010), 2.8mm thick; (b) Aluminium-copper alloy (AA2024-T3), 3.2mm thick.

For modelling the following material parameters were chosen:

Low carbon steel (AISI1010) [138]: Thermal diffusivity $D = 8.11 \cdot 10^{-6}\, m^2 s^{-1}$, coefficient of thermal expansion $\alpha_{th} = 11.6 \cdot 10^{-6}\, K^{-1}$, thermal conductivity $k = 41.5\, W(Km)^{-1}$, melting temperature $T_s = 1515.85$ ℃, yield stress $\sigma_f = 305\, MPa$, Young's modulus $E = 207\, GPa$.

Aluminium-copper alloy (AA2024-T3) [144]: Thermal diffusivity $D = 49.7 \cdot 10^{-6}\, m^2 s^{-1}$, coefficient of thermal expansion $\alpha_{th} = 24.7 \cdot 10^{-6}\, K^{-1}$, thermal conductivity $k = 120\, W(Km)^{-1}$, melting temperature $T_s = 638$ ℃, yield stress $\sigma_f = 290\, MPa$, Young's modulus $E = 72.4\, GPa$; Room temperature $T_0 = 20$ ℃. Please note that thermophysical properties were chosen to represent both materials at elevated temperature.

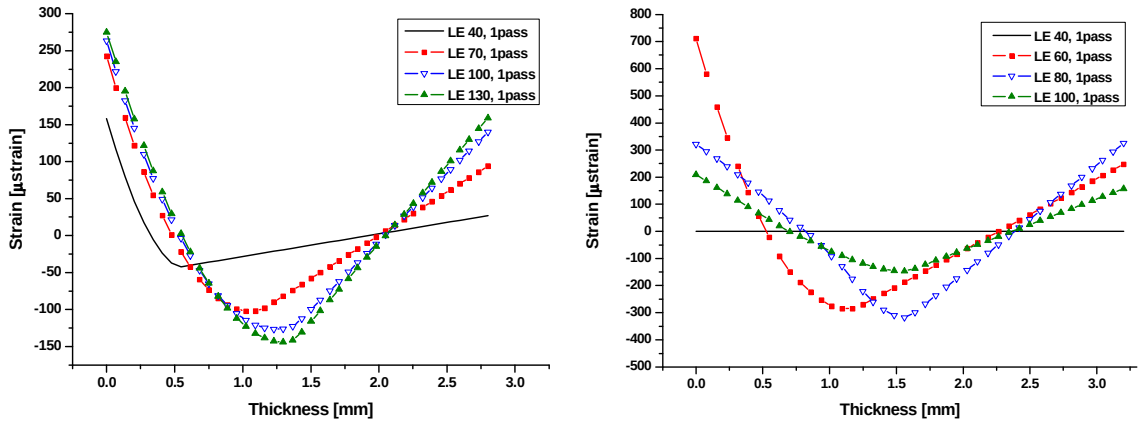

(a) (b)

Figure 6.6: Transverse residual strain through thickness caused by a Gaussian heat source predicted by the analytical-numerical laser forming model [77]; (a) AISI1010, 2.8mm thick; (b) AA2024-T3, 3.2mm thick.

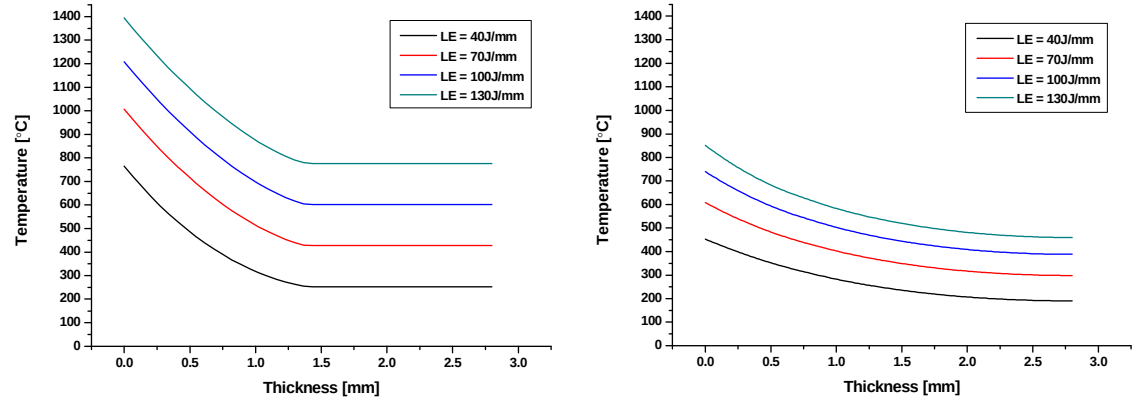

(a) (b)

Figure 6.7: Through thickness temperature calculated for low carbon steel (2.8mm thick); (a) With the analytical-numerical model [78] using equation (2.21) and (2.22); (b) with the thermal FE-analysis (section 4.5) in Comsol®.

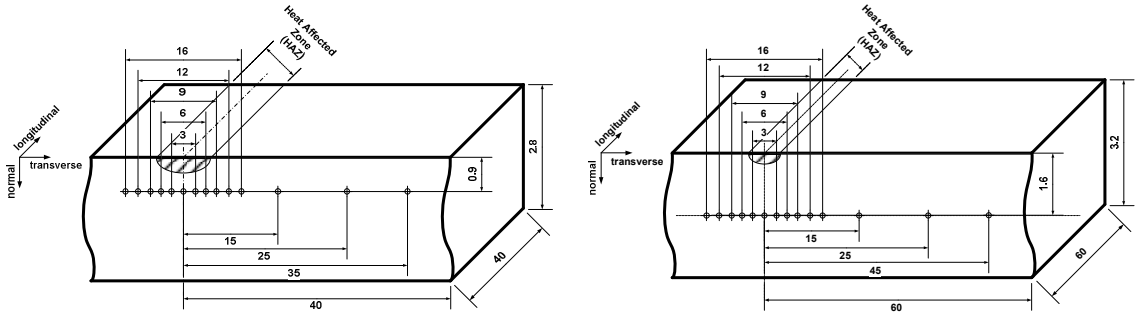

(a) (b)

Figure 6.8: Coordinates of the residual stress measurement across the HAZ; (a) AISI1010; (b) AA2024-T3.

Line Energy [J/mm]	**No. of passes**	**Bend angle [˚]**	**Measurement facility**	***d*-spacing [Å]**			
				in-plane	**error**	**normal**	**error**
0	-------	-------	ANSTO	1.1706	1.4388E-05	1.1705	6.5091E-07
0	-------	-------	ISIS	1.1705	6E-05	1.1705	5E-05
40	1	0.24	ANSTO	1.1706	4.9507E-06	1.1706	6.5071E-06
40	3	0.72	ANSTO	-------	-------	-------	-------
70	1	0.66	ISIS / ANSTO	-------	-------	-------	-------
70	3	1.77	ANSTO	-------	-------	-------	-------
100	1	0.94	ISIS / ANSTO	-------	-------	-------	-------
100	3	2.48	ISIS	-------	-------	-------	-------
130	1	1.43	ANSTO	1.1705	7.3798E-06	1.1705	9.1886E-06
130	1	1.43	ISIS	-------	-------	-------	-------
130	3	3.22	ANSTO	-------	-------	-------	-------

Table 6.1: Sample conditions, measurement facility and variation in d-spacing of 'stress-free' d_0 cubes, AISI1010.

Line Energy [J/mm]	No. of passes	Bend angle [˚]	Measurement facility	*d*-spacing [Å]			
				in-plane	error	normal	error
0	-------	-------	ISIS	1.6535	6.3687E-05	1.6536	7.1035E-05
40	1	0.07	ISIS	1.6535	5.4705E-05	1.6535	5.9196E-05
60	1	0.98	ISIS	1.6536	6.6647E-05	1.6536	6.9300E-05
80	1	1.27	ISIS	1.6537	7.1035E-05	1.6537	7.3485E-05
100	1	1.02	ISIS	1.6536	7.7159E-05	1.6540	7.3485E-05

Table 6.2: Sample conditions, measurement facility and variation in d-spacing of 'stress-free' d_0 cubes, AA2024-T3.

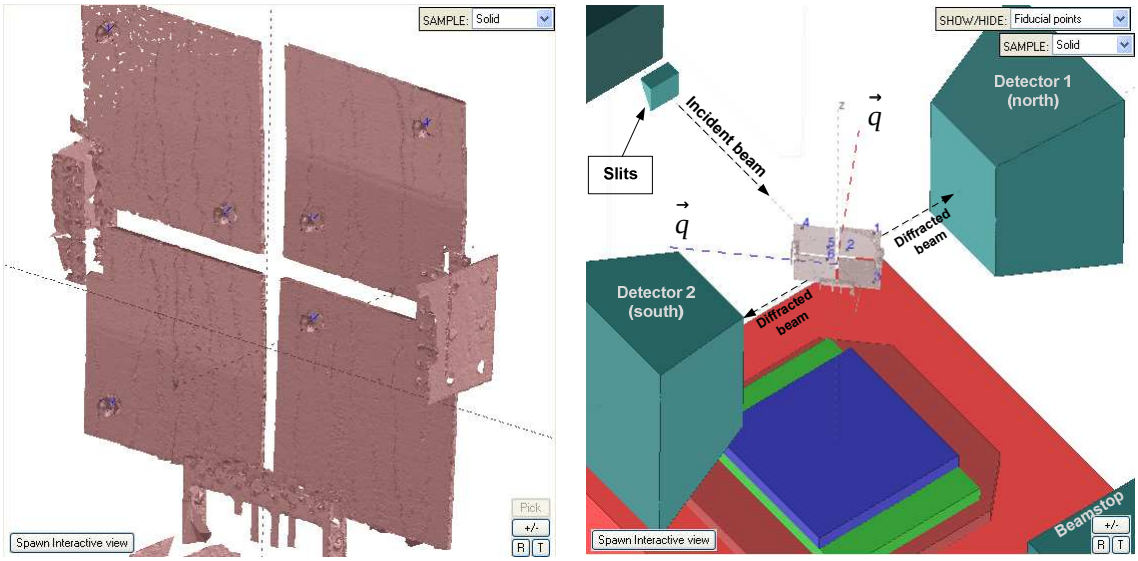

(a) (b)

Figure 6.9: Sample alignment using the software SScanSS [149]; (a) On the specimen holder with Fiducial points; (b) Simulation of specified measurement coordinates in the 'virtual' experimental hutch.

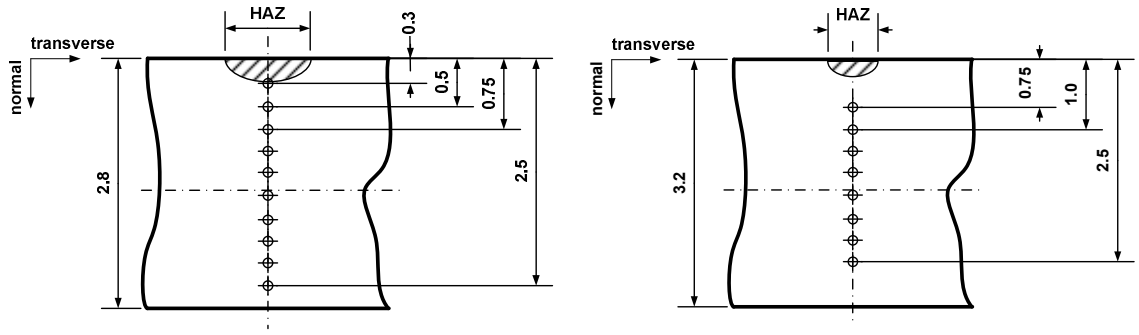

(a) (b)

Figure 6.10: Measurement points of the transverse residual strain through thickness (cross section perpendicular to the laser scan line in the plate centre of the token); (a) AISI1010, measured at ANSTO; (b) AA2024-T3, measured at ISIS.

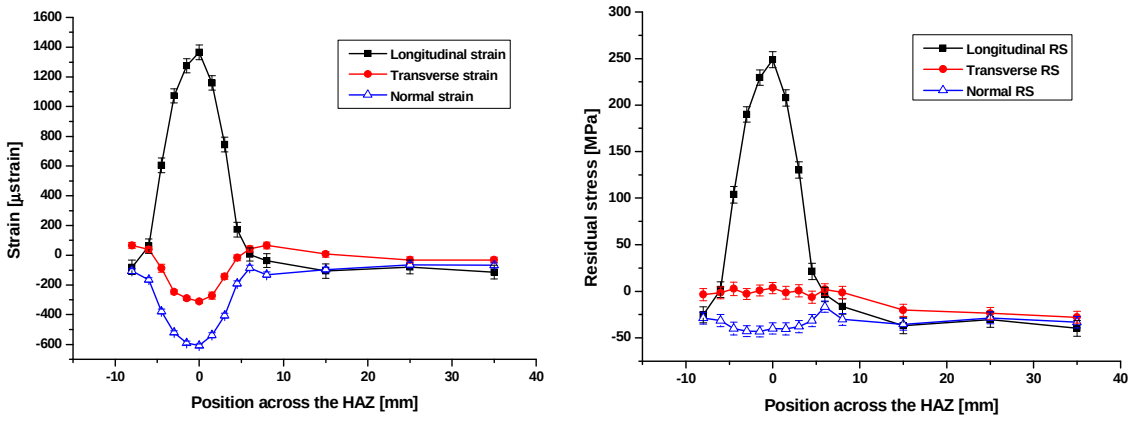

(a) (b)

Figure 6.11: (a) Residual strain across the HAZ; (b) Residual stress across the HAZ; LE = 70J/mm, 1pass; (sample: AISI1010, measured at ISIS).

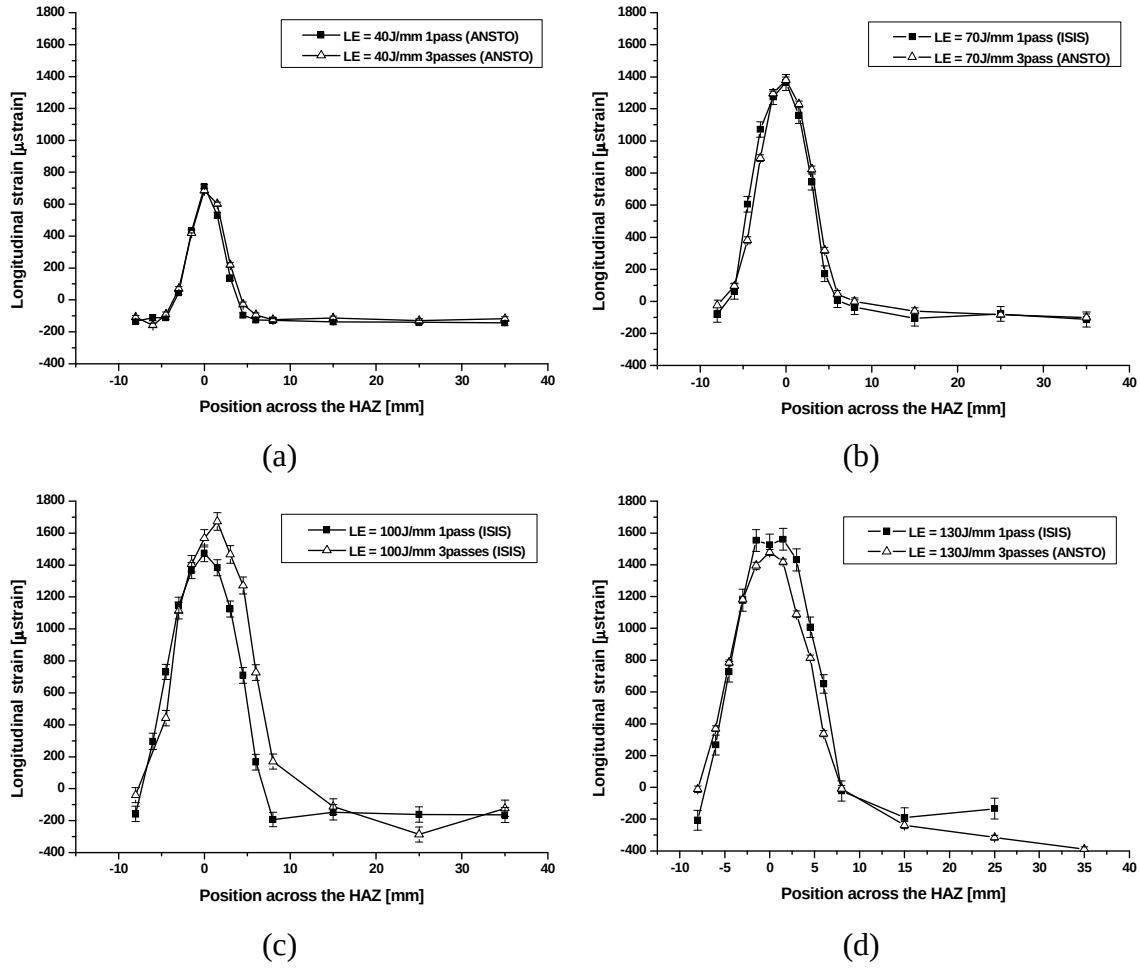

Figure 6.12: Longitudinal strain across the HAZ, one and three passes; (a) LE = 40J/mm; (b) LE = 70J/mm; (c) LE = 100J/mm; (d) LE = 130J/mm; (samples: AISI1010).

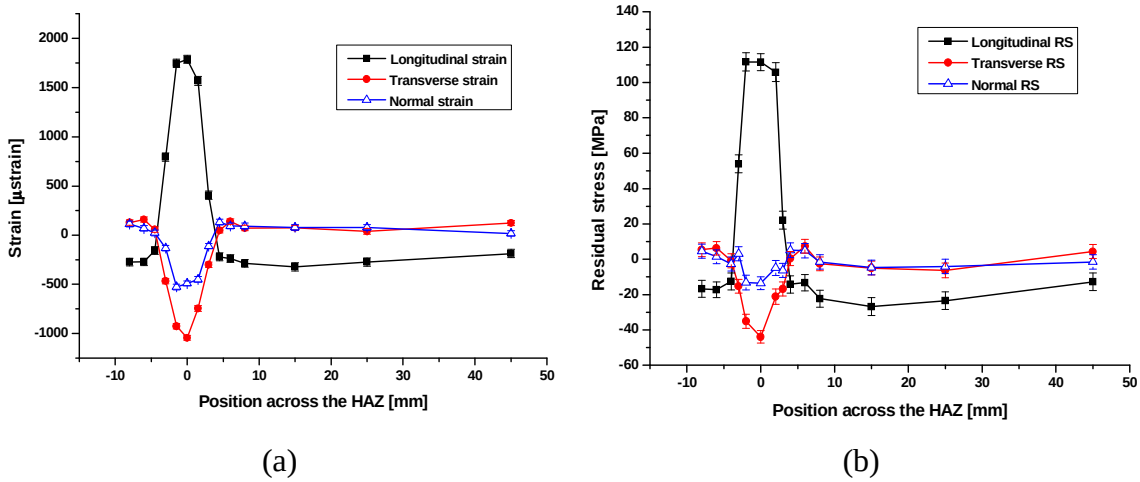

Figure 6.13: (a) Residual strain across the HAZ; (b) Residual stress across the HAZ; LE = 80J/mm, 1pass; (sample: AA2024T3, measured at ISIS).

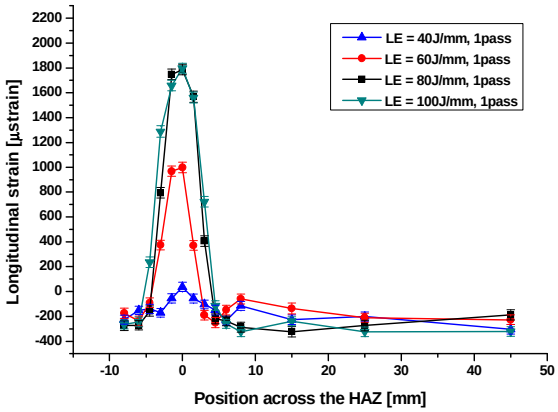

Figure 6.14: Longitudinal strain across the HAZ, 1pass; (samples: AA2024-T3).

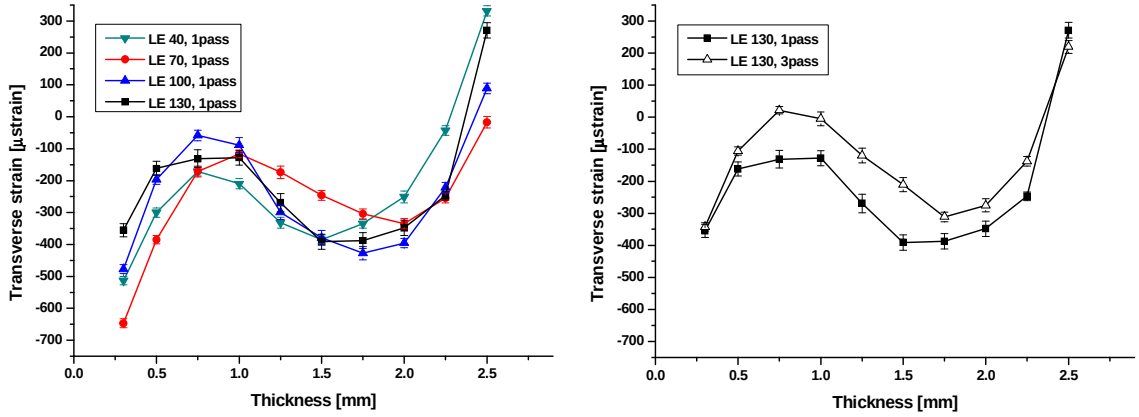

(a) (b)

Figure 6.15: Transverse strain through thickness. (a) Single pass with different LE; (b) One and three passes, LE = 130J/mm; (samples: AISI1010, measured at ANSTO).

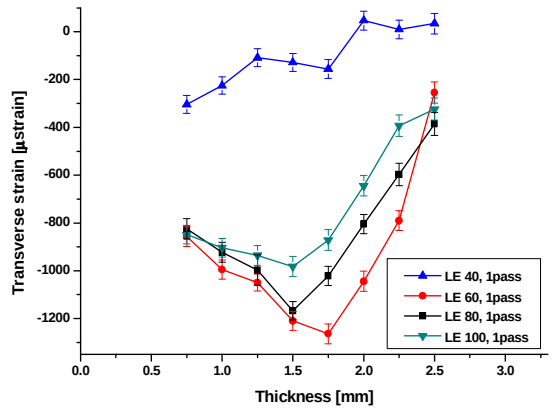

Figure 6.16: Transverse strain through thickness, single pass with different LE; (samples: AA2024-T3, measured at ISIS).

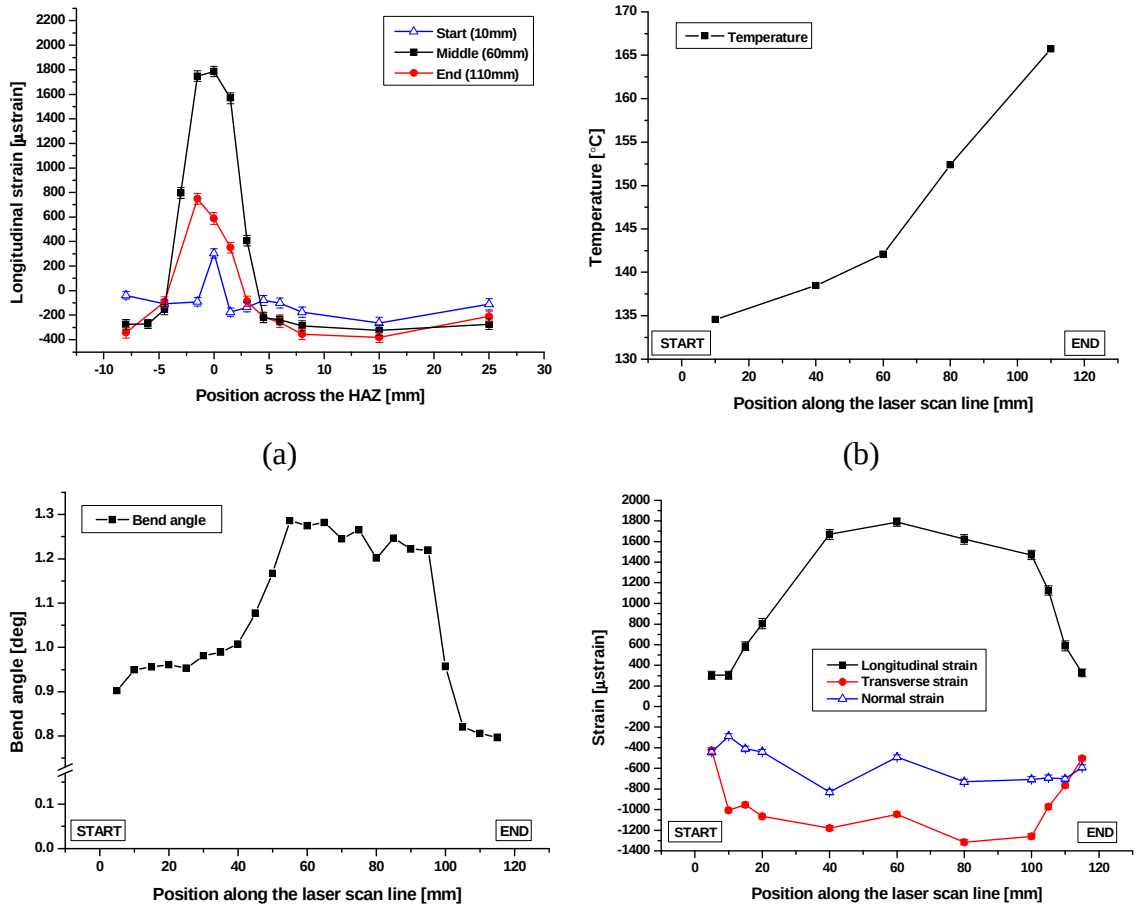

Figure 6.17: (a) Longitudinal strain across the HAZ at start (10mm), middle (60mm) and end (110mm) of the laser scan; (b) Temperature along the laser scan line at 1.6mm depth; (c) Bend angle along the laser scan line; (d) Residual strain along the laser scan line; (sample: LE = 80J/mm, 1pass, AA2024-T3, measured at ISIS); Temperature (b) and bend angle (c) are the average of two independent measurements.

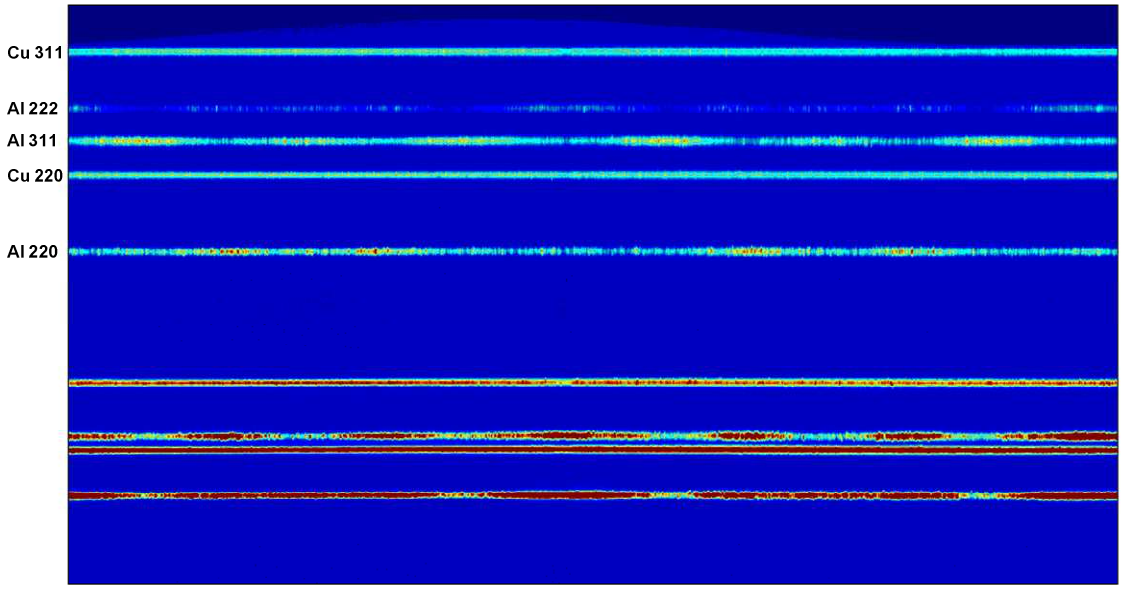

Figure 6.18: Typical diffraction image of AA2024-T3 measured with synchrotron radiation. The image is a 10° segment of the whole diffraction ring recorded (in the longitudinal direction). The intensity pattern, represented by the colour change in the diffraction lines indicates the texture of the material.

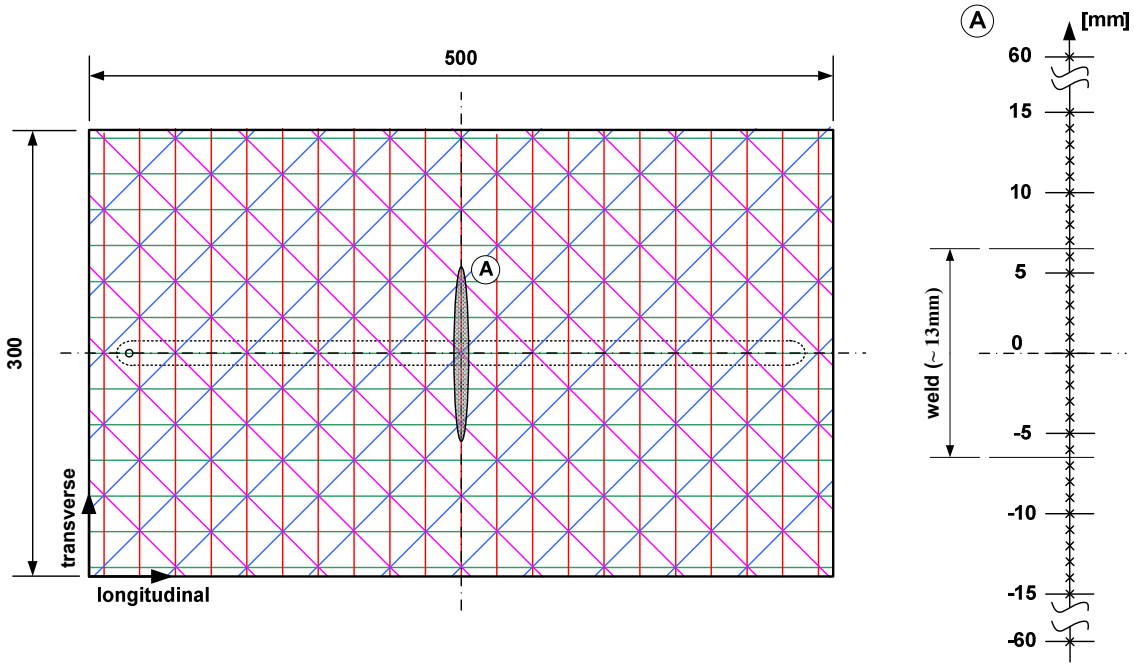

Figure 6.19: Schematic drawing of the laser straightened friction stir welded AA2024-T3 sample with scan lattice applied (scan path distance 24mm) and residual stress measurement points across the weld (points were in the middle of the 2mm thick tokens).

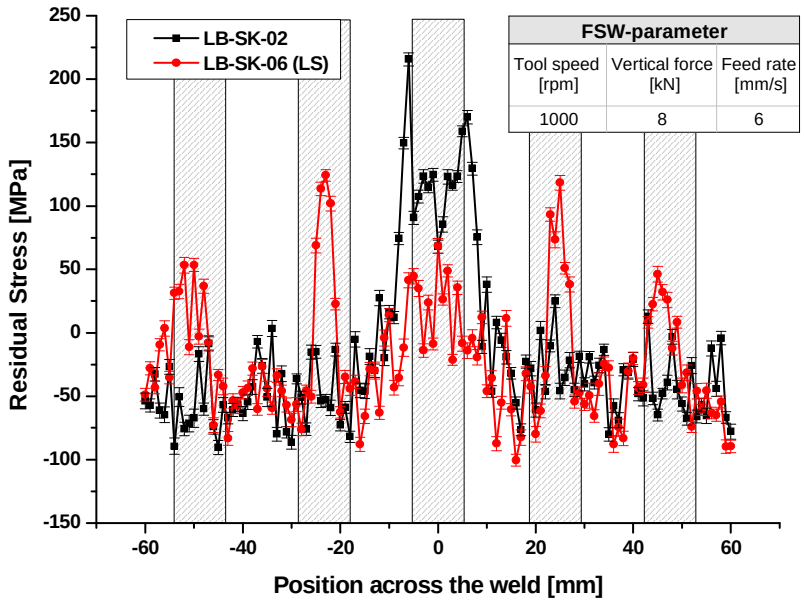
LB-SK-02
LB-SK-06 (LS)
FSW-parameter
Tool speed [rpm]
Vertical force [kN]
Feed rate [mm/s]
1000
8
6
Residual Stress [MPa]
Position across the weld [mm]

(a)

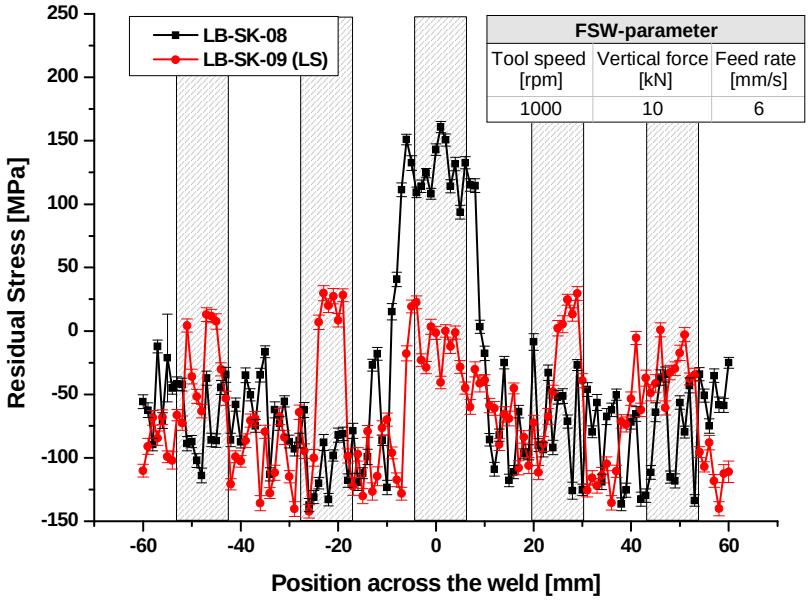
LB-SK-08
LB-SK-09 (LS)
FSW-parameter
Tool speed [rpm]
Vertical force [kN]
Feed rate [mm/s]
1000
10
6
Residual Stress [MPa]
Position across the weld [mm]

(b)

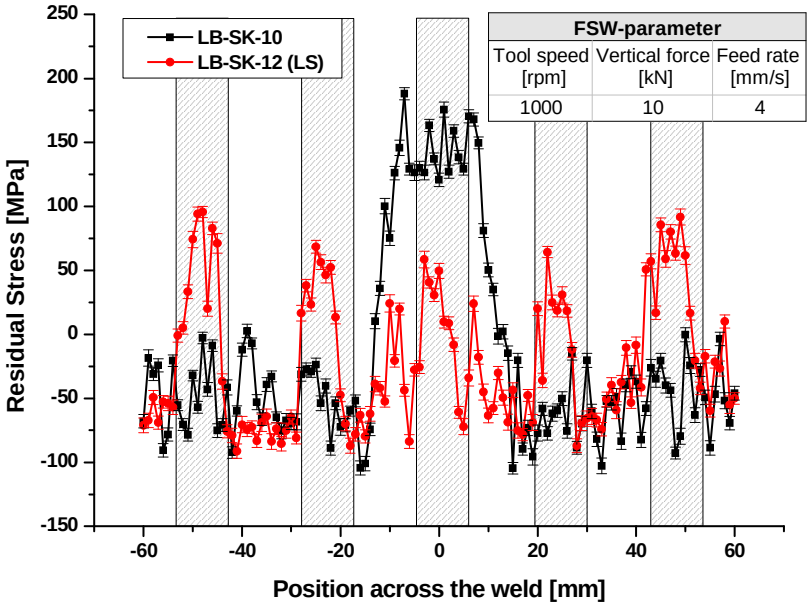

(c)

Figure 6.20: Dominant longitudinal residual stress (RS) of friction stir welded (FSW) AA2024-T3 samples (black), and iterative laser straightened FSW samples (LS, red), both welded with identical parameters; (a)-(c) Shows the longitudinal RS for three different welding parameters, indicated in the table; The shaded columns in the Figures indicate the scan lines in the fixed scan lattice, applied during the iterative laser straightening. They coincide with the positions of the tensile RS peaks; (the RS was measured at HASYLAB/DESY, Germany).

Chapter 7

Iterative laser forming applications

In this chapter, the results are presented, where laser forming was applied to remove welding induced distortion of mild steel and AA2024-T3 tokens. As shown, the ILF process, described in section 2.5.3, was adjusted and successfully applied to straighten butt welds, plates with welded stringers, i.e. with varying thickness, and friction stir welds, based on previous investigations presented. The experimental setup and modifications made in the mechanical FE-analysis for the in-plane strain computation are described first. Then, the results of straightened butt and fillet welded mild steel sample plates are shown, together with a mechanical and metallurgical study of the samples after iterative laser straightening (ILS). A similar procedure was done for straightened friction stir welded (FSW) AA2024-T3 plates.

7.1 Experimental procedure

The experimental setup, procedure and laser forming process parameters for the ILS were kept the same as described in section 3.2. Factors η_κ and η_ε, which determine the fraction of required curvature and shrinkage applied, and the scan path distance in the fixed scan lattice, are given separately for each straightening section. During the ILS, bending scans were applied on the top surface followed by shrinkage scans on the bottom surface. This scan strategy was chosen because of the large, initial sample deformation/distortion compared with the plate thickness and was kept consistent for all straightening applications throughout this study.

The welded tokens were modelled in Comsol®, as shown at the example of a fillet weld in Figure 7.1 (first principal strain). For the strain field computation of laser straightened tokens with the mechanical FE-analysis (section 3.1.1), a uniform plate thickness of 9mm was used, irrespective of their actual thickness. For a purely elastic material behaviour, which was one assumption made in the FE-analysis, the in-plane strain is constant through thickness and is therefore independent of the plate thickness, equation (2.16) [53,54]. The reason for this choice was that FE-simulations showed a better and faster convergence for thicker plates with the tetrahedral or hexahedral mesh elements used. For example, the computation time of a 500x500mm^2 sample was 6 seconds (28617dof) with 9mm thickness, and 30 seconds with the actual plate thickness of 4mm (138570dof) on a 2.6GHz processor with 3GB memory. The strain field

extracted was ± half the actual plate thickness s_0 (reference was the neutral axis at $s_0/2$). In the practical implementation, no strain correction was necessary for the laser straightening, because the required strain field was already compressive everywhere, as it was the 'reverse' deformation compared with that for forming pillow and saddle shape. The material parameters used in the mechanical FE-analysis for mild steel and for AA2024-T3 were the same as in section 3.1.1. All welded sample plates were degreased with acetone, and hand sprayed with graphite coating prior to ILS as described in section 3.2.

After laser straightening, samples for tensile tests, hardness tests and optical microscopy were cut from the corresponding specimen, following the procedure, described in section 5.2. Hereafter, the results of successfully iterative laser straightened distorted welded plates are presented.

7.2 Straightening of butt welded DH36 plates

In order to prove the capability of a potential application of the ILS in the shipbuilding industry where component distortion after welding is still a major problem, welded specimens were supplied by the BAE shipyard in Govan. The DH36 specimens were butt welded with the weld seam along the specimen centre line. Their size was 500x500x4mm^3 and the chemical composition of DH36 is shown in Table 7.1. For the ILS, a calibration database was established, following the procedure described in section 2.5.3. Figure 7.2 shows the experimental calibration graph of DH36 shipbuilding steel, relating bend angle and in-plane strain to LE. The vertical lines in the Figure are representative of the minimum and maximum threshold LE applied in the ILS. The maximum LE was chosen with respect to metallurgical investigations in Chapter 5, where it was shown that a LE of 100J/mm was acceptable for 2.8mm thick low carbon steel. This LE was then scaled to the thickness of 4mm, taking into account the factor $\eta_{LE} = 0.8$ (section 3.2). The minimum LE was chosen above forming threshold and approximately in the near-linear working region.

During the ILS process, the scan path distance in the fixed scan lattice was 40mm, which was a reasonable compromise to achieve enough accuracy on the one hand and on the other hand not to extend the duration of the iterations needlessly (which was ~ half an hour for the settings chosen). The influence of the scan path distance on the ILS process is discussed in section 7.6. Bending and shrinkage scans were applied alternately on top and bottom surfaces respectively, and the dilution factors were chosen

to be $\eta_\kappa = 0.7$ and $\eta_\varepsilon = 0.07$. Those two factors remained the same for all straightening applications of mild steel specimens in this study. The surface, referred to as top surface, was coincident with the top surface for welding the plates together.

The results of the most accurate straightened sample are shown in Figure 7.3 and the accuracy is shown in Table 7.2. After four iterations, the initial *rms* error of 2.61mm (max. total deflection ~ 11.9mm) decreased to an *rms* error of 0.23mm (max. total deflection ~ 1.0mm) of the final shape (Table 7.2 [LFI92]).

Following laser straightening, sections were cut from the sample LFI91 (Table 7.2) and prepared for mechanical and metallurgical investigation. Their location on the plate and the corresponding test performed are shown in Figure 7.4. Positions of laser affected material were chosen to include a maximum number of laser scans per iteration, i.e. points of four crossing laser scan lines in the pattern. The heat input applied, during the four iterations of the ILS is shown for position 1-5 (Figure 7.4) in Table 7.3.

An optical micrograph, taken adjacent to the top surface at position 1 (Figure 7.5[a]) showed no effect on the microstructure compared with parent material (Figure 7.5[b]). As is visible, white pearlite and black ferrite grains are evenly distributed in both micrographs. At position 2 (on the bottom surface) which was scanned amongst others three times at an exaggerated LE of 280J/mm (the result of an error in the laser control) (Table 7.3), the microstructure was visibly affected, as shown in the macrograph of the HAZ in Figure 7.6(a). The micrographs in Figure 7.6(b)-(d) were taken with increasing distance to the laser scanned bottom surface in the HAZ of Figure 7.6(a). The near-surface region (Figure 7.6[b]) shows a characteristic microstructure of a HAZ I in the form of upper and lower bainite with potential martensite formation. The bottom part of the HAZ I (Figure 7.6[c]) comprises lower bainite, and further in the material (Figure 7.6[d]), initiated carbon dissolution, characteristic of a HAZ II, merges into the parent microstructure. It should be noted that the top surface of position 2 did not show any visible effect on the microstructure, despite the erroneous laser power applied on the bottom surface.

Tensile test (sample from position 5) and chrapy test (samples from position 3 and 4) did not show degrading material performance as a result of the ILS applied (Table 7.4). The microhardness through thickness (Table 7.4) measured at position 2 increased from ~ 200 Hv0.2 at parent material to ~ 260 Hv0.2 at the laser scanned (bottom) surface, owing to the formation of bainitic/martensitic microstructure, as shown in the micrograph of Figure 7.6(b).

Clearly, an affected microstructure, as found at position 2, owing to an erroneous laser power, would not be desirable after ILS. In any further industrial straightening application, laser parameters should be chosen to induce sufficient heat for effective laser forming, and should be chosen so that the microstructure is not altered and material performance not degraded. The non-affected properties of all other positions on the straightened sample plate proved the feasibility of those requirements and correct choice of the laser parameter range.

7.3 Straightening of fillet welded mild steel plates

Figure 7.7 and Table 7.5 show the results of a DH36 sample, supplied by the BAE shipyard in Govan, with a fillet welded stringer. The initial *rms* error of 1.11mm (max. total deflection ~ 4.0mm) after welding was successfully reduced in 4 iterations to a final *rms* error of 0.15mm (max. total deflection ~ 0.86mm), applying the settings and procedure described in section 7.2. For the bottom shrinkage scans, the standoff distance of the laser nozzle was increased, so that the CNC table with the 500x500x4mm^3 sample plate (the height of the stringer was ~ 9mm) could move under the laser beam. Therefore the laser beam diameter during bottom shrinkage scans increased to ~ 10mm, which had no adverse effect on the accuracy of the forming result, and was accommodated through the iterative process design.

Fillet welded mild steel sample plates of varying quality with the dimensions 300x500x2mm^3 were supplied by the Welding Engineering Research Centre at Cranfield University to prove the capability of the ILS process on thinner specimens, which should be more sensitive to the process parameters chosen. The experimental database was obtained through linear interpolating between that of 1.5mm and 2.8mm thick AISI1010 (Figure 3.3) because the steel type of the specimens was not specifically known and no excess material was available to perform separate calibration experiments. The minimum and maximum threshold LE was again chosen, based on the metallurgical investigations (Chapter 5), as described in section 7.2.
For the laser straightening, the original vertical stringer height of ~ 160mm was reduced to ~ 85mm for the ILS (Figure 7.8), so that the CNC table could move under the laser beam without altering the standoff distance of 9mm, used in previous experiments. Trials with the original vertical height and increased standoff distance of ~ 170mm

failed because of an unavoidable increase in beam diameter to ~ 17mm, reducing area energy/power density below the forming threshold.

Figure 7.9 and Table 7.6 show the results of a sample which was straightened in 8 iterations from an initial *rms* error of ~ 2.48mm (max. total deflection of ~ 13.2mm) to a final *rms* error of ~ 0.57mm (max. total deflection of ~ 2.9mm). The scan path distance of the most accurate straightening experiment of the fillet welded mild steel samples was 40mm (LFI98, [Table 7.6]). Previous trials with 20mm scan path distance increased the iteration time (~ 20min for 40mm and ~ 40min for 20mm scan path distance) and led to 'overshooting' of the target shape, rather than increased accuracy. As shown in Table 7.6, the sample LFI101 was straightened in 6 iterations with a scan path distance of 30mm. Clearly, through the higher total heat input applied on the plate surface, fewer iterations were needed, despite the initial deflection being significantly larger at the sample LFI101 than that of sample LFI98. Therefore, further investigation into a most effective scan path distance and scan path strategy could be conducted.

7.4 Straightening of friction stir welded (FSW) AA2024-T3 plates

Although FSW [156] is a solid state joining process and involves relatively low process temperature, distortion and residual stresses after welding are still present, as a result of inhomogeneous temperature distribution and impeded shrinkage. The following results presented are from experiments aimed at applying the ILS process on thin 300x500x2mm^3 AA2024-T3 samples after FSW, joined with three different welding parameters (Table 7.7), which induced different amounts of distortion and residual stress (RS). Furthermore, the effect of the ILS on mechanical properties and microstructure of the friction stir weld was investigated. As shown in section 6.5, the study included a comparison of the residual stress state between FSW tokens and laser straightened FSW tokens. The results of this comparison and the effect of the ILS on the RS state are further discussed in section 7.6.

Figure 7.10 shows an example of a straightened FSW plate (LB-SK-12), and Table 7.8 shows the accuracy of all three 2mm thick straightened FSW samples. The scan path distance applied was 24mm and the relation between LE to bending and shrinkage induced was obtained in a similar way (through a linear interpolation) as for uniformly varying thickness plates (Figure 3.3). Minimum and maximum LE applied were again chosen with respect to metallurgical investigations in Chapter 5, where it was shown that a LE of 80J/mm is acceptable for 3.2mm thick AA2024-T3. This LE was then

scaled to the sample thickness, and the maximum LE was chosen accordingly. The minimum LE was chosen above forming threshold and approximately in the near-linear working region.

Generally, the results (Table 7.6) are less accurate than other straightening results presented, owing to the plate thickness and rigidity of the material, which lead to three main observations made during the ILS. First, the plates were likely to buckle or to suddenly flip into a 'reverse' equilibrium state. If this happened, the iteration was stopped, the sample realigned and the iteration continued. Second, the straightening was very sensitive to the minimum and maximum LE chosen and the scan path distance. And third, the unwanted longitudinal distortion of scan paths applied along the weld was significant. An example of this unwanted longitudinal distortion is shown in Figure 7.11, where an iteration was applied on the bottom surface of the initial shape (Figure 7.11[a]), which aimed to reduce the curvature around the y-axis (κ_y). As it can be seen from the shape after the iteration (Figure 7.11[b]), κ_y was reduced as expected, but in addition to that the curvature around the x-axis (κ_x) increased significantly. This unwanted distortion in longitudinal direction is caused by 'edge' and 'size' effects, and is increased even more through residual stresses caused by FSW (Figure 6.20). Therefore, iterations applying preferential scans along the weld (here bottom shrinkage scans) were diluted through $\eta_\varepsilon = 0.05$ and through lowering the minimum threshold LE in the range applied. The decrease of only 4J/mm in the minimum LE shows how sensitive the ILS of those FSW samples was to process parameters chosen.

Macrographs of a sample comparing the friction stir weld before and after ILS are shown in Figure 7.12(a) and Figure 7.12(b) respectively. They are representative for samples, welded with other parameters in this study. From the macrographs, no effect of the laser straightening on the microstructure can be seen. More detailed images, for example through scanning or transmission electron microscopy would be necessary to investigate dissolution and precipitates in the friction stir weld.

The hardness profiles in Figure 7.12(c)-(e) show the hardness across the friction stir weld before and after ILS. It can be seen that the ILS had no effect on the hardness profile. However, the effect of the different friction stir welding parameters applied on the process temperature is visible in the form of a more pronounced softening in the friction zones of the rotating tool shoulder, as seen at sample LB-SK-10 and LB-SK-12 (Figure 7.12[e]). It should be noted that the process temperature in FSW is highest if the vertical force F_v is large and the feed rate v is small (for constant tool rotation speed).

Two other FSW specimens were laser straightened to show that the increased *rms* error was owing to the thickness of the plate and not caused by the friction stir weld. The results of a 375x250x3.2mm^3 sample, supplied by BAE-systems, are shown in Figure 7.13 and Table 7.9. The results of another test plate, 300x500x4mm^3 in size and supplied by GKSS, are shown in Figure 7.14 and Table 7.10. It can be seen that those samples were straightened with fewer iterations and to a higher accuracy (lower *rms* error), compared with that of 2mm thick FSW samples (Table 7.8). The thicker, more rigid and less flexible plates were more insensitive to the ILS process parameters chosen and to unknown process parameters, for example variations in laser light absorption or inaccuracies as part of the iterative process design itself, such as out-of-plane deformation applied at a shrinkage scan. To summarize, even though the 2mm thick AA2024-T3 FSW tokens were successfully straightened, the ILS process was shown to be very sensitive when used on thin plates.

7.5 Straightening of a plate with enclosed area

Through the straightening of different welds, presented in previous sections, the potential of the ILS process was shown. It was also applied to a large 1200x700x4mm^3 DH36 plate with an enclosed area (~ 740x600mm^2) of welded 20mm thick stringers on the sample surface (Figure 7.15[c]), which was supplied by the BAE shipyard in Govan. Those structures are typically integrated in ship decks to increase their rigidity and in such a deck structure one box section follows the other. Therefore, the focus of the ILS was, to reduce the distortion in the enclosed area. Thus, ignoring the edges is valid in this case. The enclosed area is indicated in the surface plots of Figure 7.15(a)-(b) in the form of a black rectangle. Figure 7.15(a) shows the initial shape after welding with an *rms* error of ~ 5.1mm (max. deflection at the plate centre of ~ 14.5mm with respect to zero) and Figure 7.15(b) shows the token after 9 iterations with an *rms* error of ~ 2.8mm (max. deflection at the plate centre of ~ 6.1mm with respect to zero). The laser parameters applied in the ILS were the same as in section 7.2 for DH36 steel. Even though the deflection at the plate centre was reduced by more than 50%, the constraint through the thick stringers was very large and restricted the bending deformation. Therefore the straightening in the enclosed area was reliant on the in-plane shrinkage induced, which was in the order of 0 to 4µm per scan path (Figure 7.2), and clearly not enough to reduce the distortion there effectively, even though several scan paths were applied in the most distorted centre area of this plate. As a result, the *rms* error and both curvature in x- (κ_x) and y-direction (κ_y) remained unchanged from iteration 7 despite

the laser heat applied, like it is shown in Figure 7.15(d). Further straightening, in particular in the enclosed area, would have been possible with a significantly larger number of iterations, which would have been inconveniently slow and not feasible to do.

7.6 Discussion

The choice of the scan path distance in the fixed scan lattice of the ILS process was found to be of importance, in particular during the straightening of thin FSW AA2024-T3 plates. It was shown that, if the two parallel scan lines were too close to each other, 'overshooting' of the target shape occurred rather than more accuracy being achieved in the final shape formed. Furthermore, the iteration time would be extended unnecessarily, which would be unwanted in any further industrial application. Finding the optimum in scan path distance to achieve the required accuracy and to prevent 'overshooting' (if spacing is too close) was done in this study in experimental trials. In their study Cheng *et al*. [95] proposed for butt welding induced distortion correction a rule of thumb for the scan path distance, which was derived from equation (2.20), with

$$d_{paths} = \frac{s_{laser} \cdot d_l}{s_{required}} \tag{7.1}$$

where d_{paths} is the spacing between two adjacent scan paths, s_{laser} is the average transverse stress generated by laser forming, d_l is the laser spot diameter and $s_{required}$ is the welding induced longitudinal residual stress. As is visible from equation (7.1), extensive FE-analysis and knowledge of the welding induced RS prior to laser forming would be required to determine the scan path distance. Clearly, this approach would be time consuming to implement in an iterative process design, whose main advantage is to accommodate those unknown residual stresses, as shown in this study. Therefore, further investigation is necessary to reduce experimental trials for finding a suitable material and geometry-specific scan path distance in the fixed scan lattice applied.

In section 6.5 the longitudinal residual stress (RS) of the 2mm thick FSW samples was compared before and after the ILS. It was shown that the ILS not only geometrically straightened the FSW samples, but also significantly reduced the characteristic tensile longitudinal RS peak in the weld seam.

The total heat input applied during the 10 iterations of the ILS at laser crosses on the line of the RS measurement across the weld is shown in Table 7.11 for all three straightened FSW tokens. If this heat input, the dominant longitudinal RS across the

weld (Figure 6.20) and the final *rms* error (Table 7.8) of the laser straightened plates are considered, some correlations are observed. First, the higher the longitudinal RS after FSW, the higher the heat input applied during the ILS in the weld seam (pos. 0mm [Table 7.11]) and in total (Σ) on the line considered in the RS measurement across the weld (± 60mm from the weld seam). Second, the sample with the largest initial longitudinal RS (LB-SK-12, Figure 6.20[c]) after FSW (and prior to ILS) was straightened most accurately (Table 7.8). Through the high RS, this sample was more constrained and less likely to reverse its distorted shape suddenly during straightening. Clearly, if high residual stresses are already present in the sample prior to laser forming, material plastification is reached at the somewhat lower heat induced. On the other hand, as seen at the sample LB-SK-12 (Table 7.8), the high RS induced distorted the sample to a greater extent. Therefore samples with larger distortion required a greater heat input and were straightened more accurately than those samples with less distortion, as shown in this comparison. However, it must be considered that these relationships established are representative of the line, measured across the weld (±60mm from the weld seam), even though the RS further away from the weld seam in the bulk material converges to zero [153].

7.7 Conclusion

It was shown that the ILS has considerable potential to straighten butt and fillet welded mild steel, and FSW aluminium-copper alloy samples. The accuracy of the straightening trials was found to be lower for thin FSW AA2024-T3 tokens compared with welded mild steel plates, owing to a higher sensitivity to the process and laser parameters chosen. The straightening of a mild steel sample with an enclosed area was stopped after 9 iterations, because the removal of the distortion in the constraint area was found to be solely reliant on the in-plane shrinkage. Therefore further straightening would have been inconveniently slow and not feasible to do. To remove the welding induced distortion, laser parameters were chosen, based on the investigations presented in previous Chapters, so that in a mechanical and metallurgical investigation after the ILS no adverse effects on material properties were found.

Furthermore, it was shown that the initial dominant longitudinal RS of FSW samples after welding was significantly reduced through the ILS in the geometrically straightened samples, which is promising, because large RS gradients inside a sample can superimpose with in-service stresses and are thus undesirable in any component.

7.8 Figures

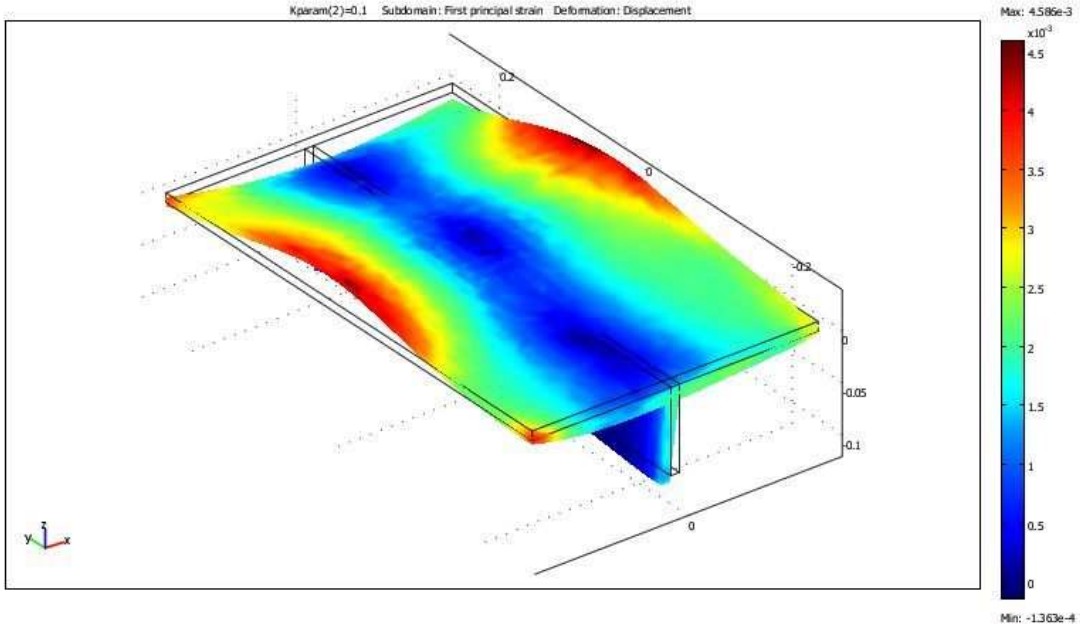

Figure 7.1: First principal strain of a filled welded mild steel plate in the mechanical FE-analysis.

Steel	**%C**	**%Si**	**%S**	**%P**	**%Mn**	**%Ni**	**%Cr**	**%Mo**	**%Nb**	**%Al**	**%N_2**
DH36	0.13	0.42	0.006	0.013	1.35	0.021	0.01	0.003	0.025	0.035	0.005

Table 7.1: Chemical composition of DH36-steel [157]

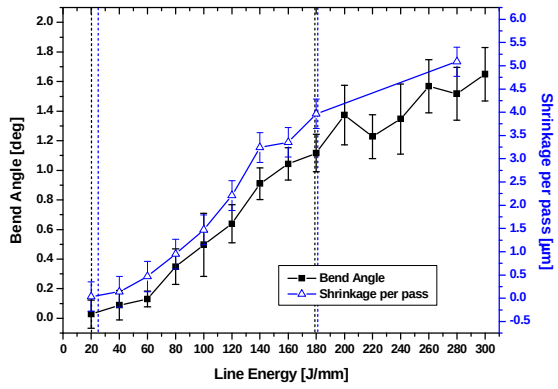

Figure 7.2: Experimental calibration database of DH36 steel, relating bend angle and shrinkage to LE; Vertical lines show minimum and maximum threshold LE applied for iterative laser straightening.

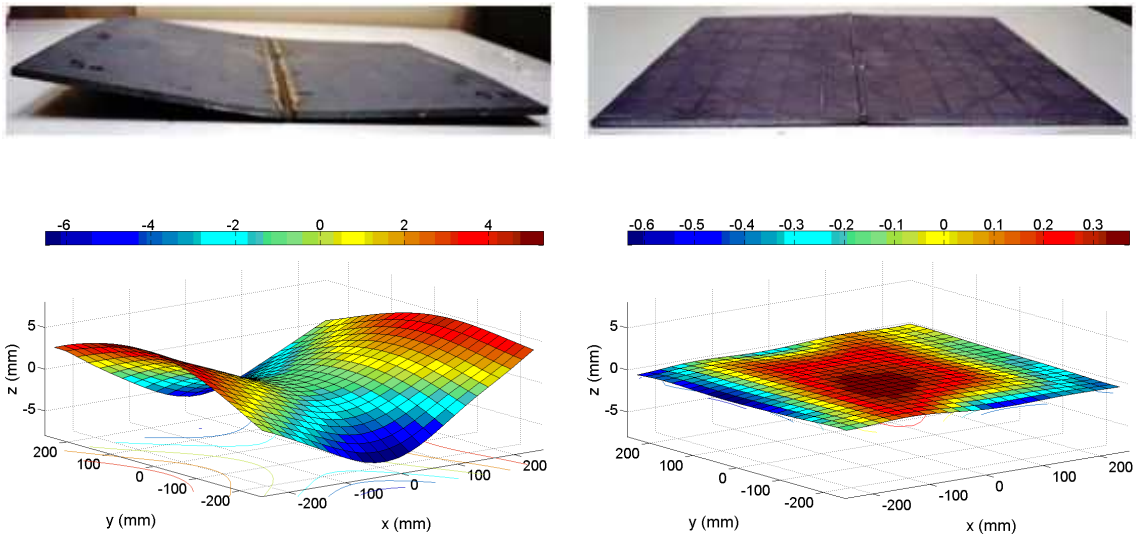

(a) (b)

Figure 7.3: Iterative laser straightened (ILS) DH36 butt welded plate; (a) Distorted shape after welding; (b) Final shape after ILS; (sample: LFI92, supplied by the BAE-shipyard in Govan). The colour scale of the vertical *z*-deflection is in [mm].

Sample	**Number of iterations**	**Scan path distance [mm]**	**Initial**		**Final**	
			Deflection [mm]	***rms* error [mm]**	**Deflection [mm]**	***rms* error [mm]**
LFI92 (BAE)	4	40	11.9	2.61	1.0	0.23
LFI91 (BAE)	4	40	12.1	2.52	1.3	0.27

Table 7.2: Initial and finial *rms* error and deflection of laser straightened butt welded DH36 samples (supplied by the BAE-shipyard in Govan).

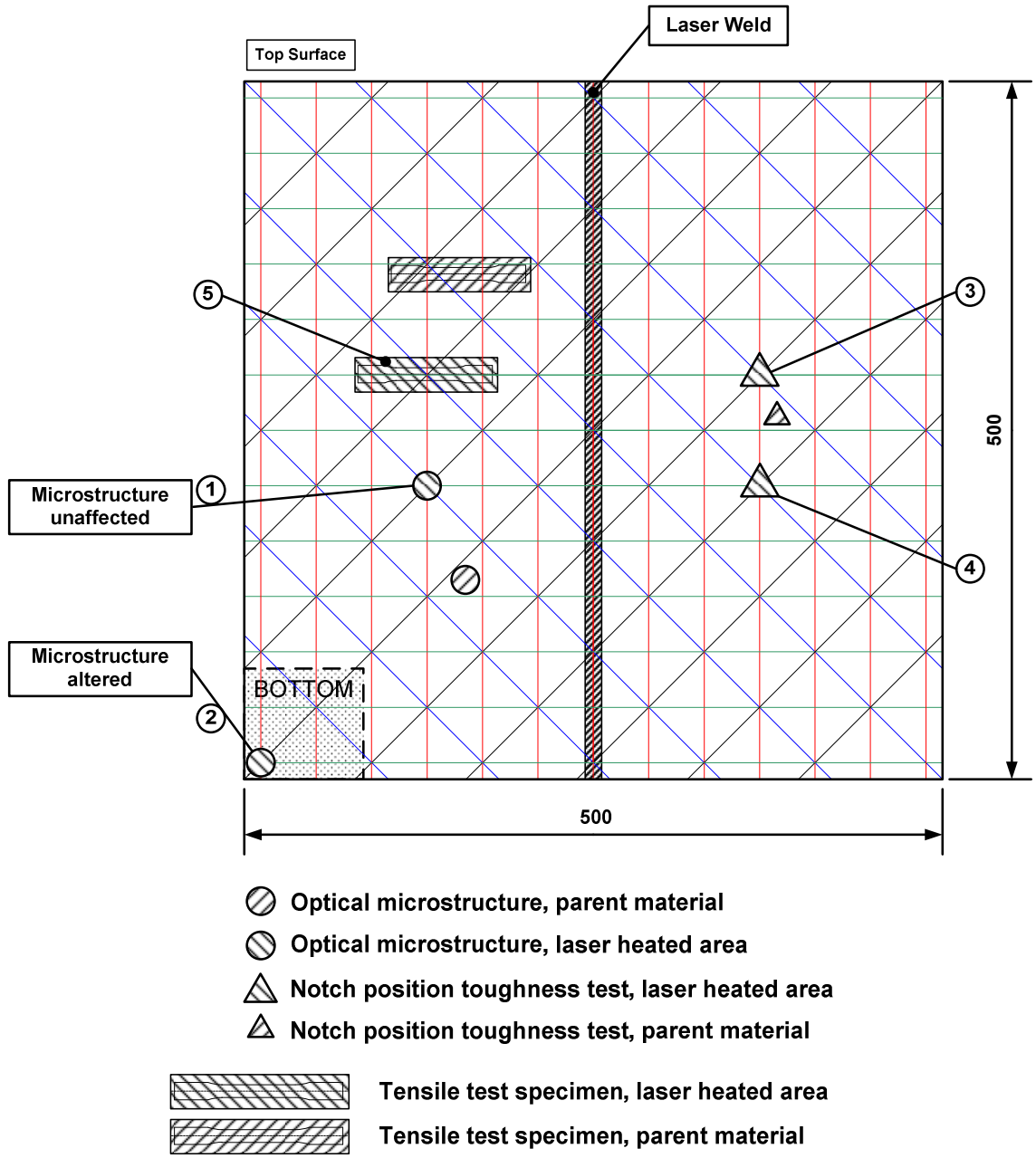

Figure 7.4: Schematic drawing of the laser straightened plate LFI91 with scan lattice applied (scan path distance 40mm), including locations where samples for mechanical and metallurgical tests were extracted.

Iteration	Scan line orientation	**Position on the sample plate** (Figure 7.4)				
		1	**2**	**3**	**4**	**5**
		Heat input in LE [J/mm]				
1 (TOP)	horizontal 0°	42	41	47	59	41
	vertical 90°	0	0	24	32	0
	45°	23	0	26	37	24
	135°	0	0	66	71	0
2 (BOTTOM)	horizontal 0°	22	0	0	0	22
	vertical 90°	88	280	71	62	90
	45°	22	280	44	37	22
	135°	42	280	43	30	30
3 (TOP)	horizontal 0°	37	73	47	46	38
	vertical 90°	35	35	31	29	31
	45°	50	42	35	41	46
	135°	40	48	43	32	36
4 (BOTTOM)	horizontal 0°	0	0	0	0	0
	vertical 90°	0	79	0	0	0
	45°	0	70	0	0	0
	135°	0	38	0	0	0

Table 7.3: Heating condition for position 1-5 (Figure 7.4) where test specimens were extracted; (Iteration 1: TOP bending; Iteration 2: BOTTOM shrinkage; Iteration 3: TOP bending; Iteration 4: BOTTOM shrinkage).

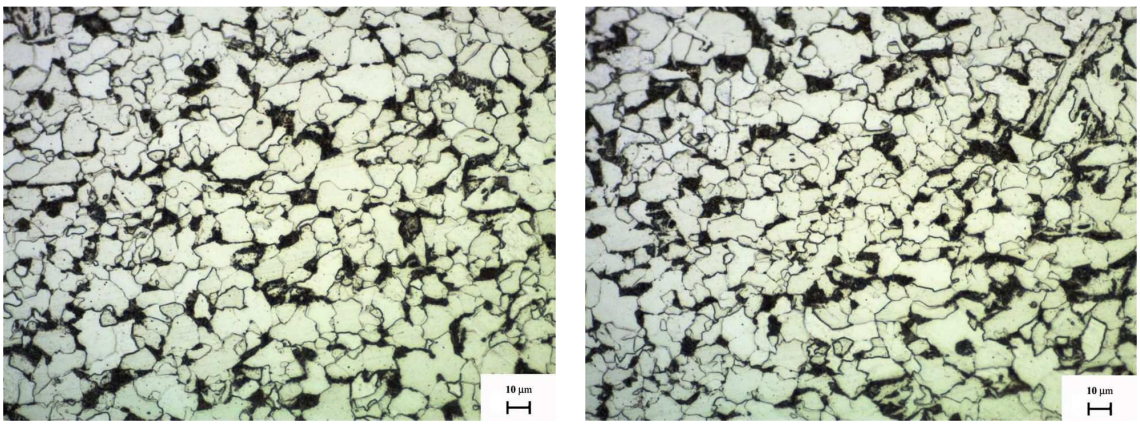

(a) (b)

Figure 7.5: Optical micrograph (mag. x500) of DH36; (a) Adjacent to the top surface at position 1 (Figure 7.4); (b) Parent material.

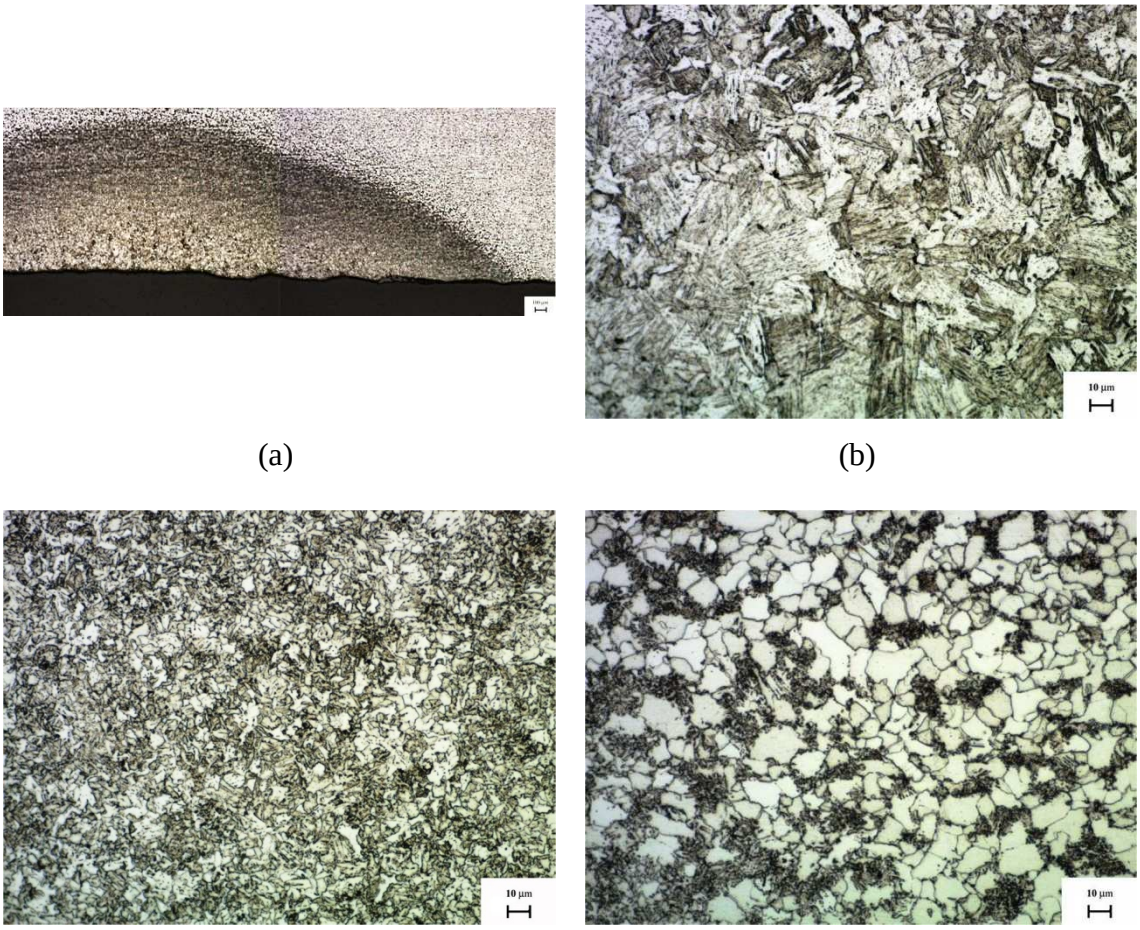

(a) (b)

(c) (d)

Figure 7.6: Effect on the microstructure of exaggerated laser power applied erroneously, at position 2 (Figure 7.4) on the bottom surface; (a) Optical macrograph (mag. x50). Optical micrographs (mag. x500): (b) HAZ I grain growth, upper and lower bainite with potential martensite formation; (c) HAZ I lower bainite; (d) HAZ II initiated carbon dissolution merging into parent microstructure (at the very top of the image).

Tensile test

	Yield tensile strength [MPa]	Ultimate tensile strength [MPa]	Elongation [%]	Hardness [Hv0.2]
Parent material	424	527	28	~ 200-210
Laser cross (pos. 5)	422	528	28	----------
Laser cross (pos. 2)	----------	----------	----------	260
Charpy test				
		Energy absorbed [Joule]		
Parent material		23		
Laser cross (pos. 3)		23		
Laser cross (pos. 4)		22		

Table 7.4: Mechanical properties from samples of positions 5 and 2 (tensile test), and position 3 and 4 (charpy test) in Figure 7.4.

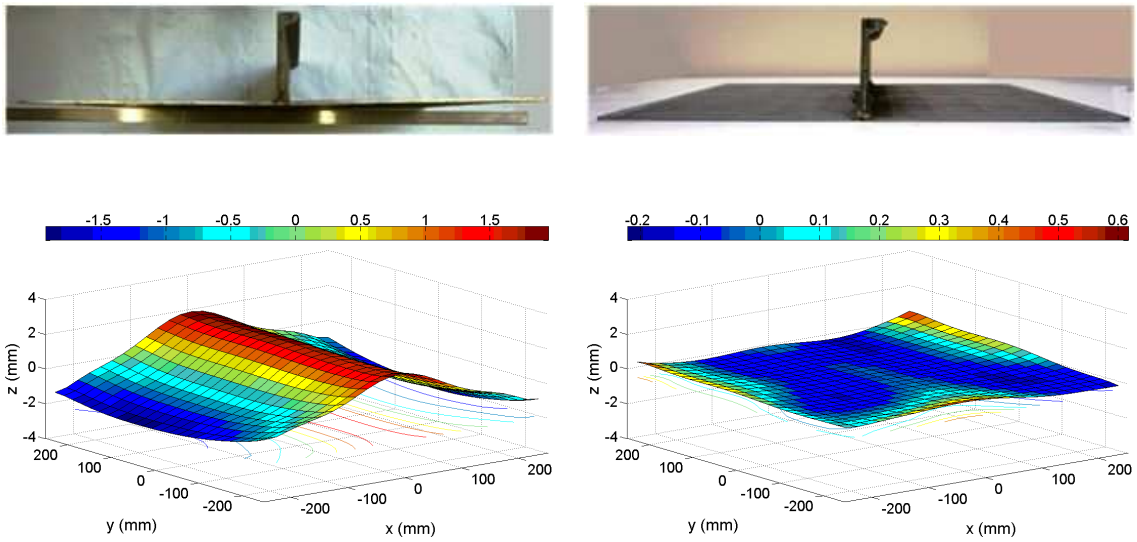

(a) (b)

Figure 7.7: Iterative laser straightened DH36 plate with fillet welded stringer; (a) Distorted shape after welding; (b) Final shape after 4 iterations; (supplied by the BAE-shipyard in Govan). The colour scale of the vertical *z*-deflection is in [mm].

Sample	**Number of iterations**	**Scan path distance [mm]**	**Initial**		**Final**	
			Deflection [mm]	***rms* error [mm]**	**Deflection [mm]**	***rms* error [mm]**
DH36 plate with welded stringer (BAE)	4	40	4.0	1.11	0.8	0.15

Table 7.5: Initial and finial *rms* error and deflection of laser straightened fillet welded DH36 sample with stringer (supplied by the BAE-shipyard in Govan).

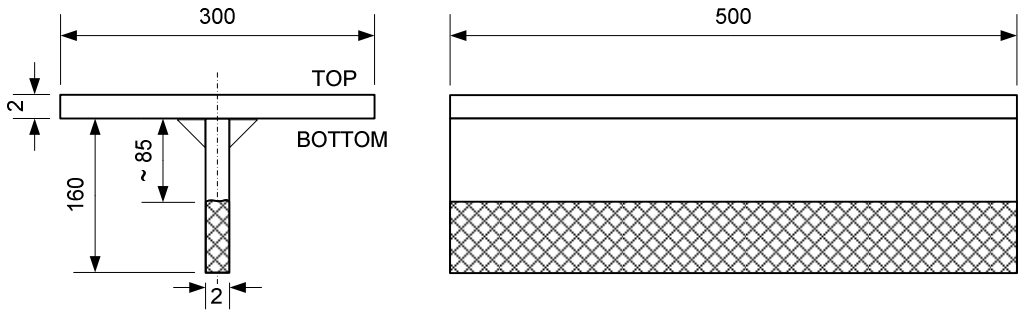

Figure 7.8: Sample dimensions and reduction of the vertical stringer height of fillet welded mild steel specimens (supplied by the Welding Engineering Research Centre at Cranfield University).

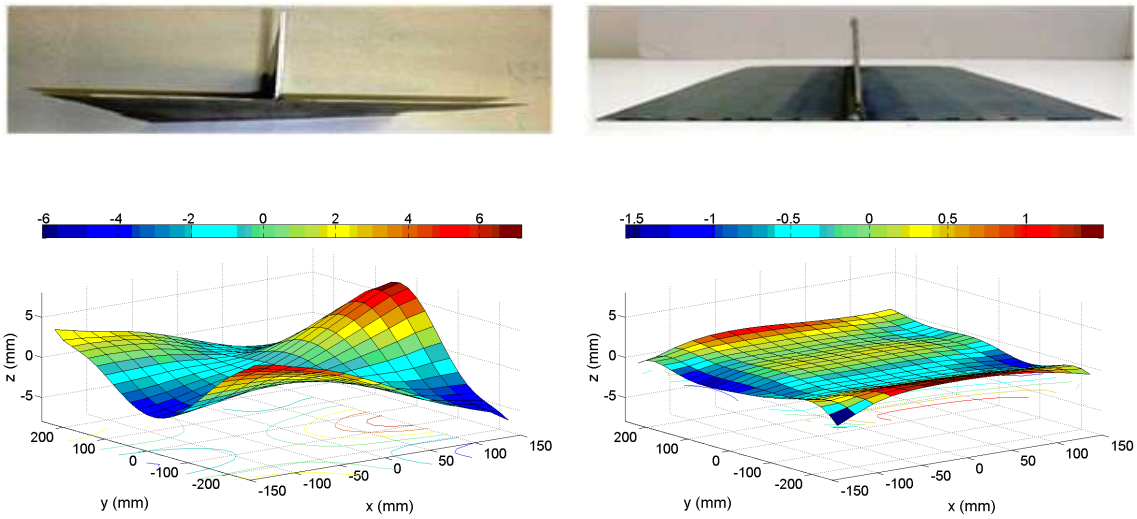

(a) (b)

Figure 7.9: Iterative laser straightened fillet welded mild steel plate; (a) Distorted shape after welding; (b) Final shape after 8 iterations; Minimum threshold LE applied: $LE_\kappa = 22J/mm$, $LE_\varepsilon = 19J/mm$; Maximum threshold LE applied: $LE_\kappa = 80J/mm$, $LE_\varepsilon = 94J/mm$; $\eta_\kappa = 0.7$, $\eta_\varepsilon = 0.07$; (sample: LFI98, supplied by the Welding Engineering Research Centre at Cranfield University). The colour scale of the vertical z-deflection is in [mm].

Sample	**Number of iterations**	**Scan path distance [mm]**	**Initial**		**Final**	
			Deflection [mm]	***rms* error [mm]**	**Deflection [mm]**	***rms* error [mm]**
Fillet welded plate, LFI98 (Cranfield University)	8	40	13.2	2.48	2.9	0.57
Fillet welded plate, LFI101 (Cranfield University)	6	30	21.2	6.27	3.2	0.82

Table 7.6: Initial and finial *rms* error and deflection of laser straightened fillet welded plates (samples supplied by the Welding Engineering Research Centre at Cranfield University).

Sample	FSW parameter		
	Tool speed [RPM]	**Feed rate [mm/s]**	**Vertical force [kN]**
LB-SK-02 LB-SK-06 (LS)	1000	6	8
LB-SK-08 LB-SK-09 (LS)	1000	6	10
LB-SK-10 LB-SK-12 (LS)	1000	4	10

Table 7.7: Friction stir welding (FSW) parameter of the laser straightened (LS) samples; The FSW process was load-controlled, with a tool shoulder diameter of 13mm and a pin length of 1.7mm.

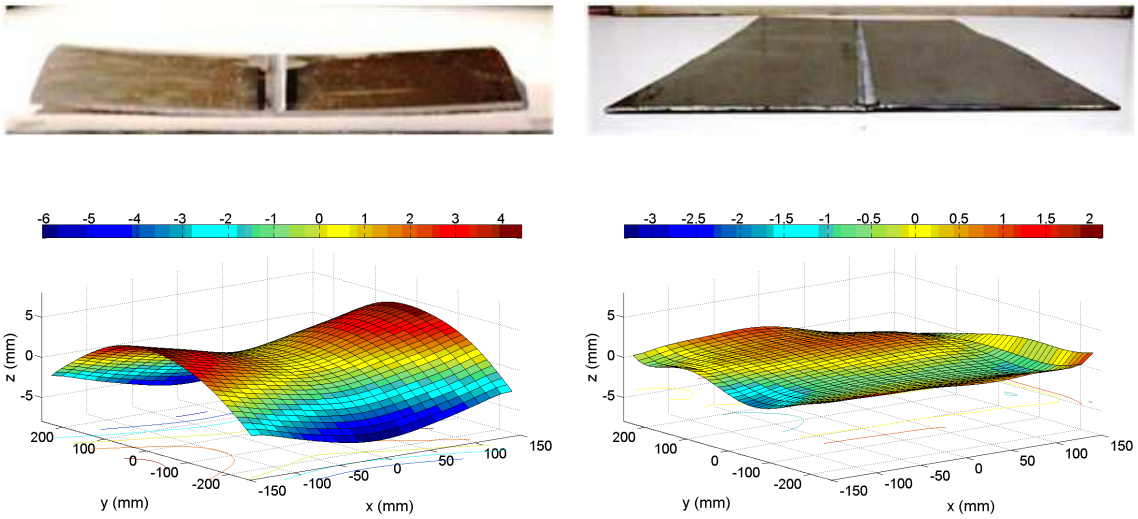

(a) (b)

Figure 7.10: Iterative laser straightened 2mm thick AA2024-T3 FSW plate (LB-SK-12); (a) Distorted shape after FSW; (b) Final shape after 10 iterations; Minimum threshold LE applied: $LE_\kappa = 25J/mm$, $LE_\varepsilon = 21J/mm$; Maximum threshold LE applied: $LE_\kappa = 48J/mm$, $LE_\varepsilon = 52J/mm$; $\eta_\kappa = 0.5$, $\eta_\varepsilon = 0.05$; Please note that the top surface as referred to in the text is as shown in the images (FSW sample supplied by GKSS, Hamburg, Germany). The colour scale of the vertical z-deflection is in [mm].

Sample	**Number of iterations**	**Scan path distance [mm]**	**Initial**		**Final**	
			Deflection [mm]	***rms* error [mm]**	**Deflection [mm]**	***rms* error [mm]**
LB-SK-06 (GKSS)	10	24	8.6	1.81	5.9	1.24
LB-SK-09 (GKSS)	10	24	9.3	1.97	7.1	1.13
LB-SK-12 (GKSS)	10	24	11.0	2.54	4.6	0.72

Table 7.8: Initial and finial *rms* error and deflection of laser straightened 2mm thick FSW AA2024-T3 plates (FSW samples were supplied by GKSS, Hamburg, Germany).

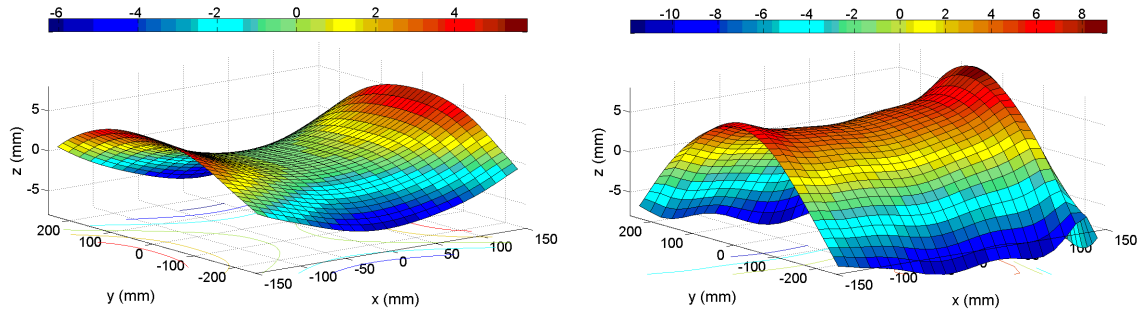

(a) (b)

Figure 7.11: Bending induced along the scan paths (around the x-axis) during an iteration on the bottom surface, which aimed to reduce the deformation around the y-axis; The shape scan was applied on the top surface; (a) Shape before the iteration; (b) Shape after the iteration which was applied on the bottom surface. The colour scale of the vertical z-deflection is in [mm].

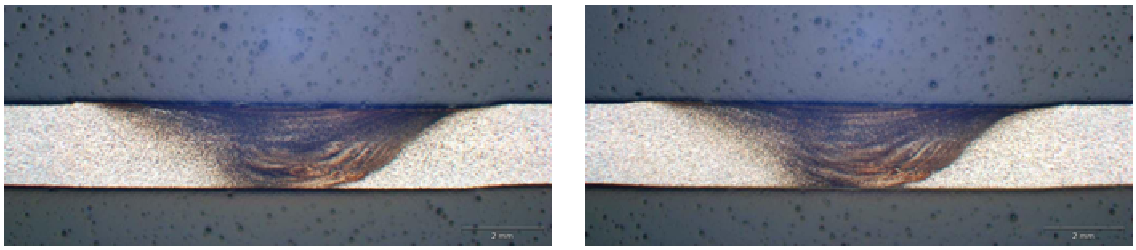

(a) (b)

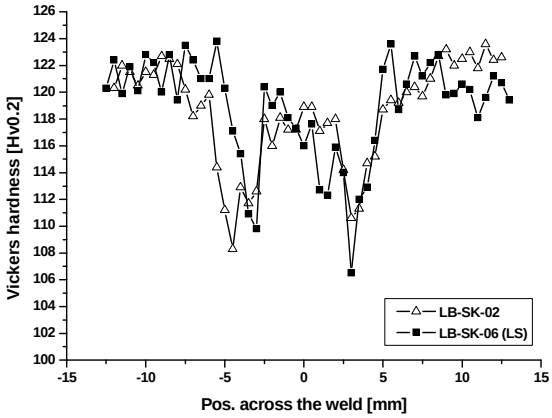

(c)

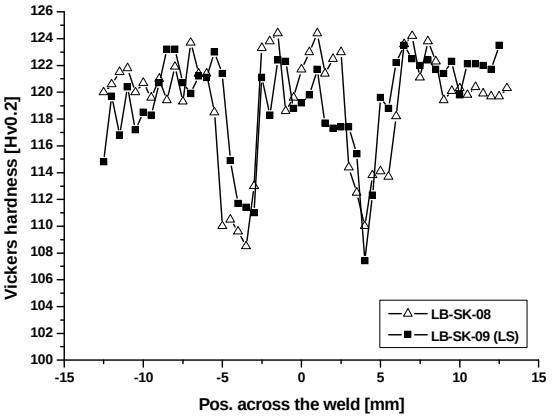

(d)

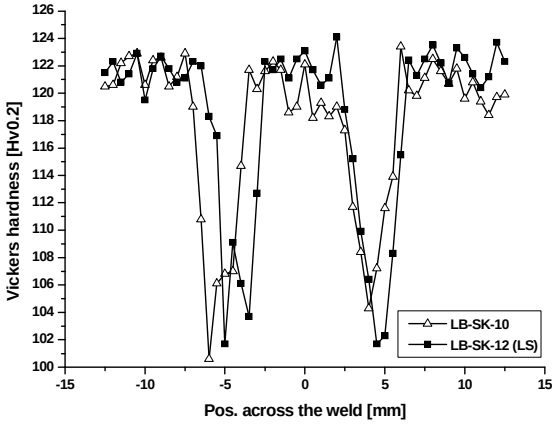

(e)

Figure 7.12: Representative macrographs of friction stir welds; (a) LB-SK-02 after FSW; (b) LB-SK-06 after FSW and ILS.

Hardness profiles across the weld after FSW and ILS (LS); (c) LB-SK-02 and LB-SK-06; (d) LB-SK-08 and LB-SK-09; (e) LB-SK-10 and LB-SK-12.

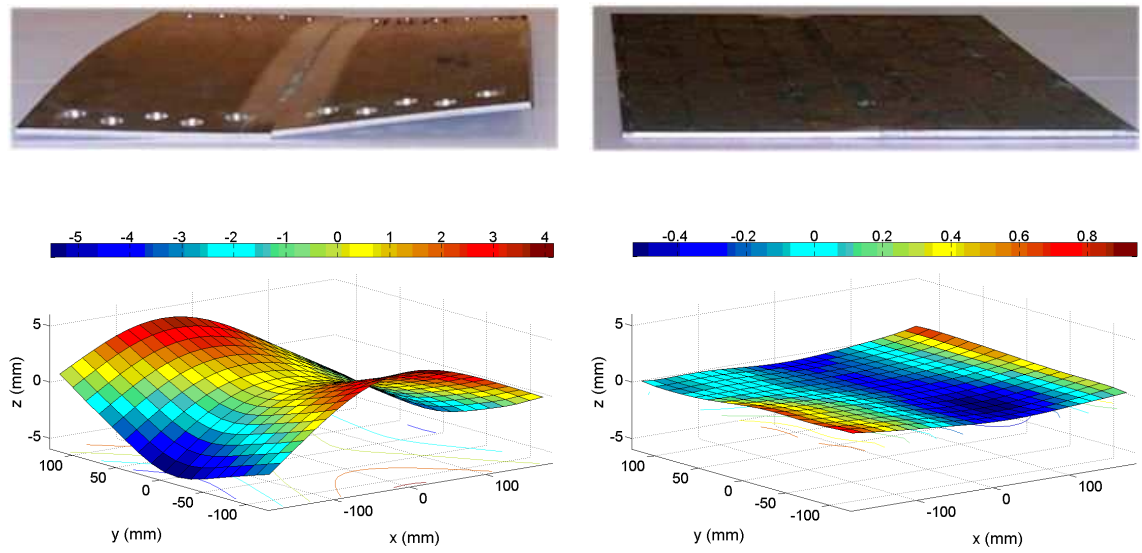

(a) (b)

Figure 7.13: Iterative laser straightened 3mm thick AA2024-T3 FSW plate; (a) Distorted shape after FSW; (b) Final shape after 6 iterations; Minimum threshold LE applied: $LE_\kappa = 38J/mm$, $LE_\varepsilon = 40J/mm$; Maximum threshold LE applied: $LE_\kappa = 75J/mm$, $LE_\varepsilon = 75J/mm$; $\eta_\kappa = 0.6$, $\eta_\varepsilon = 0.6$; (FSW sample was supplied by BAE-systems). The colour scale of the vertical z-deflection is in [mm].

Sample	**Number of iterations**	**Scan path distance [mm]**	**Initial**		**Final**	
			Deflection [mm]	***rms* error [mm]**	**Deflection [mm]**	***rms* error [mm]**
3mm thick FSW plate (BAE)	6	30	9.8	2.20	1.5	0.30

Table 7.9: Initial and finial *rms* error and deflection of 3mm thick laser straightened FSW AA2024-T3 plate (FSW sample was supplied by BAE-systems).

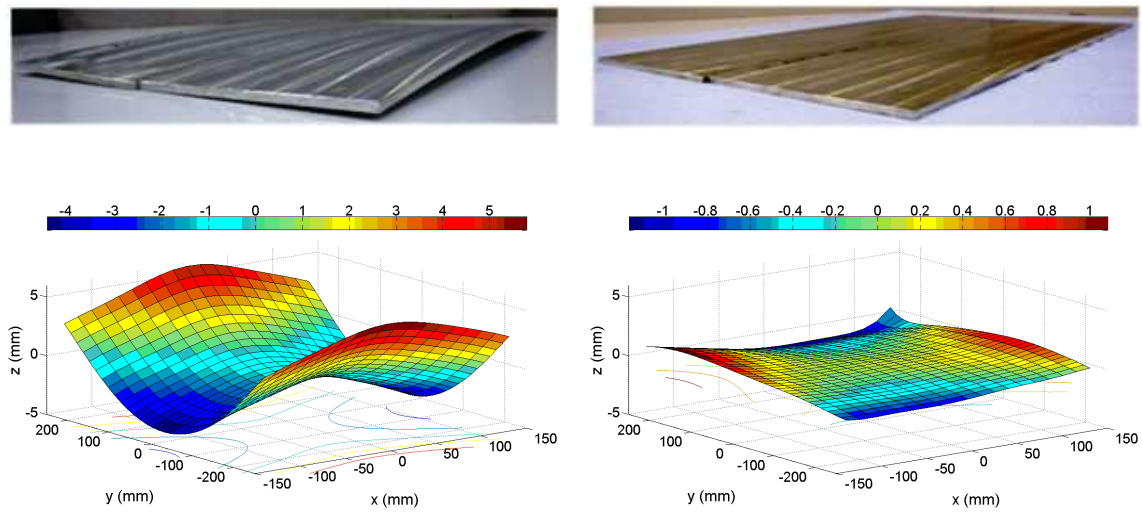

(a) (b)

Figure 7.14: Iterative laser straightened 4mm thick AA2024-T3 FSW plate; (a) Distorted shape after FSW (please note that the shape scan was done on the bottom surface with respect to the weld); (b) Final shape after 8 iterations; Minimum threshold LE applied: $LE_\kappa = 52J/mm$, $LE_\varepsilon = 52J/mm$; Maximum threshold LE applied: $LE_\kappa = 100J/mm$, $LE_\varepsilon = 100J/mm$; $\eta_\kappa = 0.6$, $\eta_\varepsilon = 0.6$; (FSW sample was supplied by GKSS, Hamburg, Germany). The colour scale of the vertical z-deflection is in [mm].

Sample	**Number of iterations**	**Scan path distance [mm]**	**Initial**		**Final**	
			Deflection [mm]	***rms* error [mm]**	**Deflection [mm]**	***rms* error [mm]**
4mm thick FSW plate (GKSS)	8	30	10.2	2.52	2.3	0.48

Table 7.10: Initial and finial *rms* error and deflection of 4mm thick laser straightened FSW AA2024-T3 plate (FSW sample was supplied by GKSS, Hamburg, Germany).

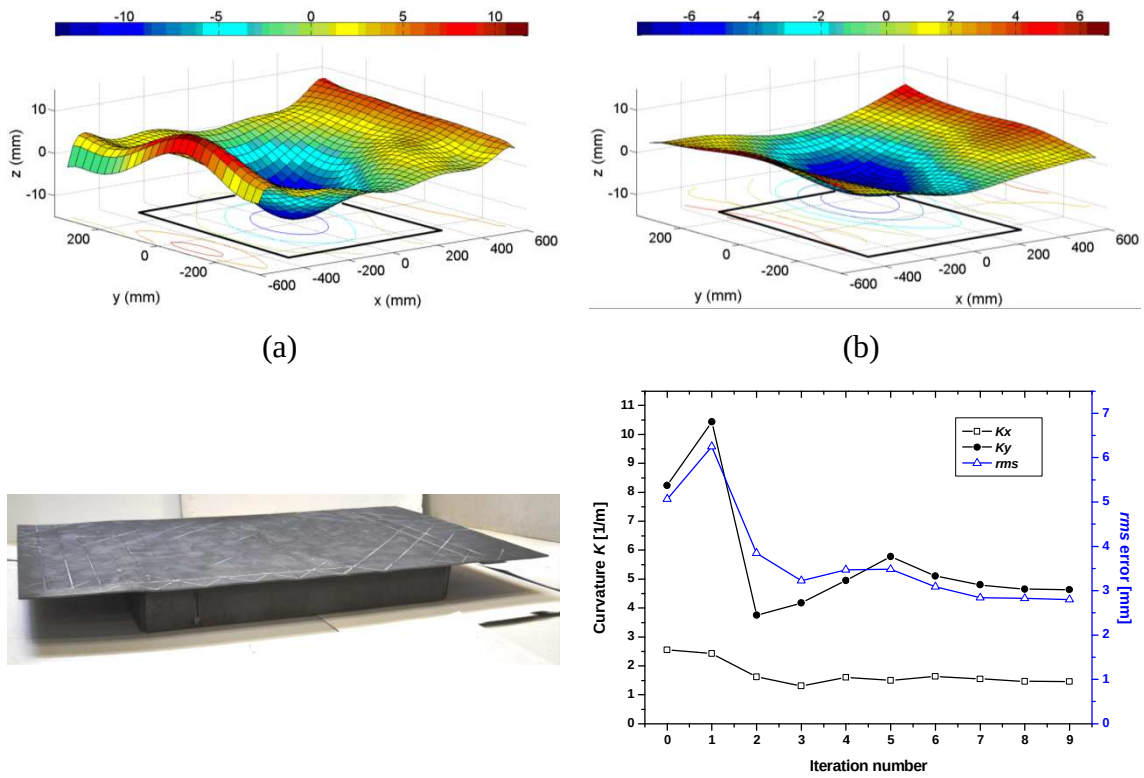

(a) (b)

(c) (d)

Figure 7.15: Plate with enclosed area supplied by the BAE shipyard in Govan; (a) Initial shape; (b) Final shape after iterative laser straightening (9 iterations, scan path distance 60mm); The black rectangle indicates the enclosed area. (c) Picture of the plate after iterative laser straightening; (d) Evolution of the curvature κ_x and κ_y, and *rms* with number of iterations; Top surface is as shown in the image (c). The colour scale of the vertical z-deflection is in [mm].

Pos. of laser crosses on line of RS measurement (Figure 6.19) **[mm]**	**Sample**		
	LB-SK-06	**LB-SK-09**	**LB-SK-12**
	Total heat input applied [J/mm]		
-48	243	250	418
-24	198	174	177
0	275	297	350
24	150	150	177
48	318	319	418
Total heat input (Σ)	1184	1190	1540

Table 7.11: Heat input applied on laser crosses on the line of the RS measurement in the ILS of 2mm thick AA2024-T3 friction stir welded samples.

Chapter 8

Conclusions and future work

This chapter first briefly summarizes the main conclusions of this study. Then, an outlook on future work is given, which is split in two sections: one addresses suggestions for further investigations in the laser forming process; the other highlights fields in industry and discusses the feasibility for laser forming to be applied there. Each section starts with a set of key points, which are then amplified later.

8.1 Conclusions

- Iterative laser forming was further developed to form pillow and saddle shapes on plates of varying thickness.
- The predominant laser forming mechanism was found to change with plate thickness, i.e. in thinner sections in-plane shrinkage is favoured and in thicker sections bending is predominant.
- Temperature ranges where the material properties can be maintained were identified, based on the through thickness peak temperature, independently of system parameters.
- The transverse residual strain profile, measured through the plate thickness was predicted by the analytical-numerical model qualitatively in a simplified way.
- Butt and fillet welded mild steel plates and friction stir welded AA2024-T3 plates were successfully laser straightened.
- The iterative laser straightening process was found to be sensitive to thin, flexible plates and the straightening of a constrained, enclosed area was stopped, because it was inconveniently slow.

Iterative laser forming was further developed to form pillow and saddle shapes on varying thickness plates. To achieve this, a mechanical FE-analysis for the in-plane strain computation was incorporated in the ILF process and validated through 3D forming trials on uniform thickness plates. Then, pillow and saddle shapes on varying thickness plates were successfully formed. These forming experiments showed that the *rms* error for pillow and saddle shapes on uniform thickness plates was approximately in the same order. For varying thickness plates, the saddle shapes were formed least accurately, in particular for the wedged plates, owing to the increased scan path distance

and the change in the pre-dominant forming mechanism with varying thickness. It was found that successful forming of tokens with uniformly varying thickness requires annealing prior to laser forming, to release the residual stress from machining, in particular in the thin section of the wedge shape. To prevent annealing, the sample thickness and thus the rigidity of the plate would have to be increased.
Based on the surface temperature measured with a pyrometer, an ILF approach was sought which would choose the LE required without knowledge of the specific plate thickness. Furthermore, this supplementary control parameter would enable the adjustment of the LE to any other surface temperature fluctuations, such as an approaching plate boundary or non-uniform laser light absorption, which would increase the forming accuracy achieved.

A metallurgical study was conducted on representative low carbon steel (AISI1010) and aluminium-copper alloy (AA2024-T3). Regions within the HAZ were identified from the through thickness hardness distributions and related to the peak temperature reached at corresponding depths. Specifically, for low carbon steel, the depth of HAZ I was determined by the position of the recrystallization temperature range (peak temperatures of approximately 480℃ to 520℃). Similarly for the aluminium alloy, HAZ I was characterised by the 'reduced hardness' temperature range (peak temperatures of approximately 200℃ to 380℃). If HAZ I was a significant fraction of the material section, the material performance was found to degrade unacceptably. Ultimately, minimum service values of failure strain for low carbon steel and ultimate tensile strength for aluminium alloy were not maintained. It is concluded that, for both materials the extent of HAZ I can be restricted to an acceptable depth for the geometry under consideration by controlling the peak through thickness temperature. The use of temperature enables processing regimes to be defined independently of system parameters, such as laser wavelength and surface preparation.

The qualitative comparison of a high resolution transverse residual strain measurement through thickness of the thin AISI1010 and AA2024-T3 samples with the analytical-numerical laser forming model showed that it predicts the transverse strain in a simplified way, and thus has broad validity. It showed qualitatively the effect of the two laser forming mechanisms, namely temperature gradient mechanism and shortening mechanism on the transverse residual strain, and therefore contributed to a deeper physical understanding of the laser forming process. Through the assumptions made in

the model, it did not match the residual strain distribution in the heat affected plastified zone, where complex thermomechanical processes would necessitate extensive FE-analysis for more accurate residual strain prediction.
The RS, measured across the HAZ of low carbon steel (AISI1010) and aluminium-copper alloy (AA2024-T3) tokens, showed that in the centre of the HAZ longitudinal stresses are tensile and dominant, normal stresses are compressive and transverse stresses are predominantly tensile for AISI1010 and compressive for AA2024-T3. The dominant longitudinal residual strain was found to increase with the heat input, associated with higher LE and/or multiple passes, until a threshold was reached. For low carbon steel, this threshold was the result of material yielding in tension and for aluminium-copper alloy, caused by only a minor temperature difference at the measurement depth, indicating that conditions, favouring the shortening, mechanism were reached at the two highest line energies chosen.

Finally, it was shown that the ILF process has the potential to straighten industrial specimens such as butt welds, plates with welded stringers, i.e. varying thickness and friction stir welds. It was found that the ILS process is sensitive to thin, flexible plates, and the straightening of a sample with constrained enclosed area was stopped, because it was solely reliant on the in-plane shrinkage and therefore inconveniently slow.
A comparison of the dominant longitudinal RS of FSW samples before and after straightening showed, that the ILS process not only geometrically flattened the samples, but also significantly reduced the longitudinal RS in the weld seam. The following section delineates fields of future investigation in the laser forming process, and discusses the potential of iterative laser forming to be applied in an industrial process.

8.2 Future work

The potential of the ILF process was shown in the various forming and straightening trials presented in this study. However, there are limitations to the process, e.g.

- For the iterative laser straightening and forming of non-developable surfaces comprising of curvatures with opposite sign, laser scans passes on the top and bottom surface are necessary.
- Prior to the ILF, material and geometry specific calibration experiments are necessary relating bend angle and in-plane shrinkage to system parameters, such as laser line energy.

These limitations are addressed in a number of recommendations for future investigation in the next section and clearly affect the potential of the iterative laser forming process to be applied in an industrial process (section 8.2.2).

8.2.1 Laser forming process

First, the experimental database relating LE to bend angle and in-plane strain of low carbon steel and aluminium-copper alloy tokens with different thickness could be used to validate full thermomechanical models of laser forming, which already exist as shown in the literature. Supplementary experimental data, such as mechanical properties, metallurgy or residual stress after laser forming, presented in this study, could feed into a more profound validation of those models. Such a validated model could then be used, for example, to enhance the understanding of the relation between thermally induced out-of-plane and in-plane strain during a laser scan; or it could be applied prior to the ILF process to replace calibration experiments, so that experimental work would be minimised to few validation trials on the specific token thickness and material. A modified version of the current analytical-numerical model could also be used for those database computations. Furthermore, approaches could then be conducted to develop a simplified version of this full thermomechanical model, which would run quickly enough to be implemented in the ILF process. This implementation would enable to accommodate e.g. the change in bend angle with number of passes, or the bending induced during a shrinkage scan (and the other way round), and therefore enhance process accuracy.

For all forming results presented in this study, the scan paths during an iteration were fixed in a pre-defined scan lattice, and the scan path distance in the lattice was determined through experimental trials. This scan path distance was found to be crucial for the final forming result obtained. Even though the fixed scan lattice approach simplifies strain history and line geometry between subsequent iterations, it is clearly not ideal, because it does not minimise the heat input to the specimen. Therefore, different, more optimized approaches could be sought, which would minimise the thermally induced stress distribution to produce a given shape. Generally, such an optimized scan strategy would reduce processing time per iteration and overall heating of the component, and still give the required shape accuracy. This investigation would involve a more advanced FE-analysis, where a simplified thermomechanical model

could be helpful to reduce extensive computation time caused by the number of scan paths applied in an iteration.

One limitation to the ILF process is that laser scans on both sample surfaces are required. Therefore, future work could investigate convex laser forming (bending away from the laser beam), so that laser treatment on only one side of the sample would be necessary to form or straighten a component. However, conditions for convex forming are difficult to establish, especially for thicker (> 1mm) plates, and a mechanical (contact) load, for example a force controlled roller which vertically pushes the plate down in a certain offset with respect to the laser beam, could be required.

As proposed in Chapter 3, an in-process surface temperature control could be implemented in the ILF process for 3D laser forming. The potential, in the form of a higher forming accuracy, has already been shown for 2D laser scans. This system could then be applied and tested further on plates of varying thickness or monolithic structures, without *a priori* knowledge of detailed specimen thickness. Moreover, this approach would enable the accommodation of process non-uniformities, such as 'edge effects' or variations in laser light absorption.

Further investigation on mechanical and metallurgical properties after laser forming could build on the approach described in Chapter 5, where the extent of HAZ I was determined, based on through thickness hardness and peak temperature. The identification of similar temperature ranges could be extended to different materials, different laser forming parameters (e.g. varying laser power or laser beam diameter) or different token geometries (e.g. thicker tokens). Then, it could be checked if those temperature zones result in similar transferable characteristic mechanical and microstructural changes. These investigations would further validate the approach to use the peak through thickness temperature to identify processing regimes independently of system parameters such as laser wavelength and surface preparation.

The potential of laser forming to shape or straighten metallic components was shown in this study. However, there is still no commercially available, easy-to-handle laser forming system which could be used in an industrial process. Therefore, the production and development of such a user friendly system, which would satisfy the demand of the corresponding industry sector where it would be applied, is still necessary.

8.2.2 Laser forming applications

One of the main industry sectors with a huge demand for straightening applications is the shipbuilding industry, where currently flame and induction straightening are well established. Nevertheless, the older straightening process of flame bending is restricted to materials with low thermal conductivity. Because of the nature of the flame, the heat flux to the work piece is dependent on its surface temperature and thus restricts the type of forming that can be achieved. Moreover, this technique involves apparent health risks - amongst others toxic fumes to the worker. To counteract these apparent risks to health, induction straightening was implemented in shipyards and led to a major step change in man hours of rectification rework per tonne, as shown in Figure 8.1. The rapid heating during induction straightening induces almost pure in-plane strain (shrinkage) which is required to straighten structures with enclosed or constrained areas, such as those used for ship decks. Compared with laser straightening, these current techniques are well established, more formulaic through the use of standard patterns and are field-tested to the rough environment of a shipyard. In addition to that, induction heating induces efficiently in-plane strain on large areas, whereas the laser induced in-plane strain is focused on the small area of the laser spot, which is inefficient in any large scale application and more suitable for smaller, more precise forming applications.

However, induction heating is limited to steel sheets with thickness $s_0 \geq 4mm$ because it requires a certain inductive reactance/resistance for the eddy-current to develop a magnetic field. Furthermore, it is restricted to constrained, fixed areas [158] and cannot be applied to free plats as is the case for laser forming. Currently, the trend in shipyards goes to thinner plates: for example 4mm thick sheets are presently used in projects such as the Type 45 Destroyer programme (BAE-systems); also, it has been reported that German shipyards have already started to use higher strength steel with 3.5mm thickness. Moreover, the use of non-ferrous materials such as high strength aluminium alloys limits the applicability of both induction and flame straightening techniques. Therefore, the potential application of the ILS in shipbuilding industry could become more realistic in future.

Presently, the general attitude in the shipbuilding industry is to accept distortion to a greater or lesser extent, because it is known that welding induced distortion cannot be prevented completely. Although post-process straightening is an option to decrease the amount of work required to remove weld-distortion (Figure 8.1) attention is also being paid to optimise the welding process for minimum distortion. Under consideration of all

facts mentioned in this paragraph, the application of laser straightening in shipbuilding industry is not currently necessary.

Another field where the ILF process could be applied is to correct the shape of components such as compressor [88] or turbine blades [89], or cast ship propellers. The performance characteristic of those parts depends strongly on the curvature variations along their surface, and the modifications required during production or later maintenance necessitate expensive, large-scale machining capability and costly, material-specific tools. This would be an area of further investigation, where laser forming could be applied as a reconditioning and modification tool.

The iterative laser forming could also be applied as a direct manufacturing tool, as shown in the forming of 3D shapes in Chapter 3, or as was investigated in the EcoShape project [90,91] for the aerospace sector (section 2.5.4). Even though composite materials, for example aluminium glass fibre laminates, are advancing fast and being more and more used in aircraft industry, ~70% of an aircraft (such as the Airbus A380) are still made of high-strength aluminium and titanium alloys. Moreover, it was recently reported (source: EADS) that the trend in aircraft industry is turning back to pure high strength aluminium alloy structures again, because of their weldability (e.g. through FSW) and better in-service performance, such as their properties regarding vibration. An example for this turn is the effort made in the COINS (COst effective INtegral metallic Structure) project, which is EU-supported with both industrial partners (e.g. Airbus, BAE-systems) and universities (e.g. Cranfield University). The work presented in sections 7.4 and 7.6 on the straightening of FSW samples, supplied by GKSS, was supported and funded from this project, to investigate tools for post-process distortion control to be applied in future, for example to straighten/shape complex fuselage aluminium panels after a FSW process.

In conclusion, laser forming is most likely to be applied in an industrial process as a correction tool, rather than a primary forming tool. When considering the trends described above, the aircraft industry could show demand for laser forming in future, in the form of straightening/shaping structures after FSW and/or the reconditioning/aligning of turbine blades. However, the potential of this technique was shown, but further process development is needed for laser forming to be applied in such an industrial process.

8.3 Figures

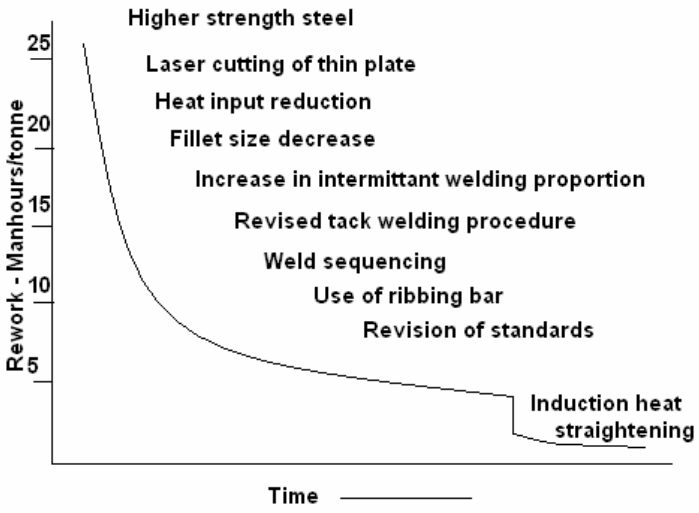

Figure 8.1: Effectiveness of different rectification processes on the rework required in man hours per tonne, representative for the shipbuilding industry [158].

Appendix

A 1 Transformation of principal curvature/strain on the scan grid

The normal strain at an angle θ is given by the equation of transformation of strains [81]:

$$\varepsilon_n = \frac{1}{2}(1+\cos(2\theta))\varepsilon_x + \frac{1}{2}(1-\cos(2\theta))\varepsilon_y + \frac{1}{2}(\sin(2\theta))\gamma_{xy}$$

The required transformation $(\varepsilon_{px}, \varepsilon_{py}, \gamma_{pxy}) \rightarrow \varepsilon_1, \varepsilon_2, \varepsilon_3, \varepsilon_4$ is calculated by determining the inverse of the transfer matrix *M*

$$\begin{pmatrix} \varepsilon_{px} \\ \varepsilon_{py} \\ \gamma_{pxy} \end{pmatrix} = M \begin{pmatrix} \varepsilon_1 \\ \varepsilon_2 \\ \varepsilon_3 \\ \varepsilon_4 \end{pmatrix}$$

With M defined as follows:

$$M = \begin{bmatrix} \frac{1}{2}(1+\cos(-2\theta)) & \frac{1}{2}\left(1+\cos\left(\frac{\pi}{2}-2\theta\right)\right) & \frac{1}{2}(1+\cos(\pi-2\theta)) & \frac{1}{2}\left(1+\cos\left(\frac{3\pi}{2}-2\theta\right)\right) \\ \frac{1}{2}(1-\cos(-2\theta)) & \frac{1}{2}\left(1-\cos\left(\frac{\pi}{2}-2\theta\right)\right) & \frac{1}{2}(1-\cos(\pi-2\theta)) & \frac{1}{2}\left(1-\cos\left(\frac{3\pi}{2}-2\theta\right)\right) \\ \frac{1}{2}\sin(-2\theta) & \frac{1}{2}\sin\left(\frac{\pi}{2}-2\theta\right) & \frac{1}{2}\sin(\pi-2\theta) & \frac{1}{2}\sin\left(\frac{3\pi}{2}-2\theta\right) \end{bmatrix}$$

A 2 Energy dispersive X-ray (EDX) measurement of an AA2024-T3 sample

Sample scanned at LE = 100J/mm, 5 passes:

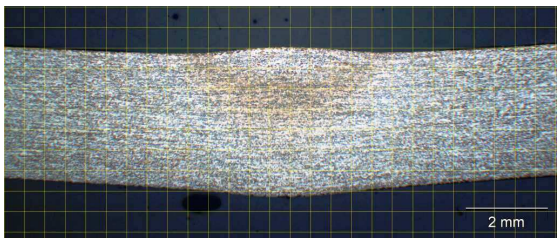

Macrograph of the sample scanned at LE = 100J/mm, 5 passes, showing the discolouration in the HAZ.

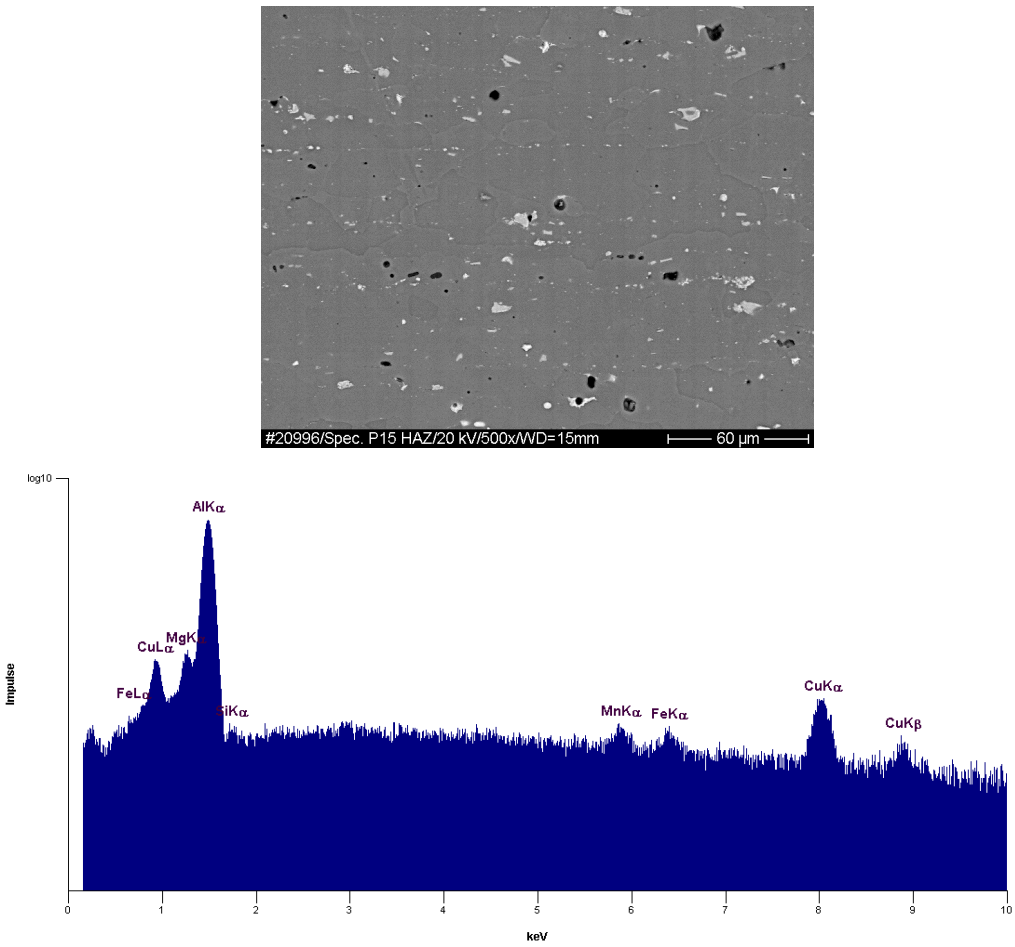

EDX-spectrum taken from a micro area of the HAZ (under a scattering angle of 35°).

Resultant material composition obtained:

Element	Atom-%	Equation	Mass-%	error(±)	Norm%
Mg	1.21	Mg	1.05	0.04	1.05
Al	96.03	Al	92.80	0.19	92.80
Mn	0.22	Mn	0.43	0.09	0.43
Fe	0.24	Fe	0.49	0.10	0.49
Cu	2.30	Cu	5.23	0.27	5.23
<Total>	100.00		100.00		100.00

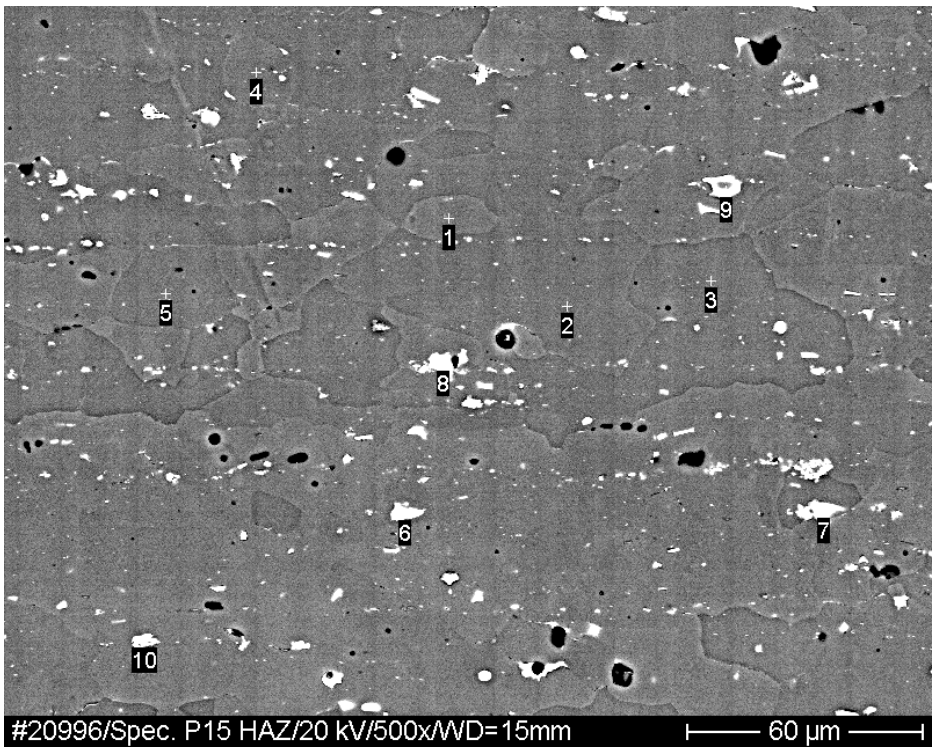

Image showing the particles analyzed in the point analysis.

Chemical composition of the particles analyzed:

Idx	Mg	Al	Si	Mn	Fe	Cu
1	0,90	93,80	0,00	0,49	0,00	4,80
2	0,86	92,48	0,00	0,77	0,49	5,40
3	0,79	94,08	0,00	0,50	0,00	4,62
4	1,08	92,69	0,00	0,57	0,37	5,28
5	0,88	94,10	0,00	0,42	0,00	4,60
6	0,75	69,66	0,34	1,66	5,80	21,79
7	0,72	89,13	0,48	1,46	2,19	6,01
8	0,75	75,66	0,53	1,77	5,11	16,18
9	0,00	55,83	3,73	7,80	19,16	13,48
10	0,88	93,22	0,00	0,72	0,00	5,18

Parent material:

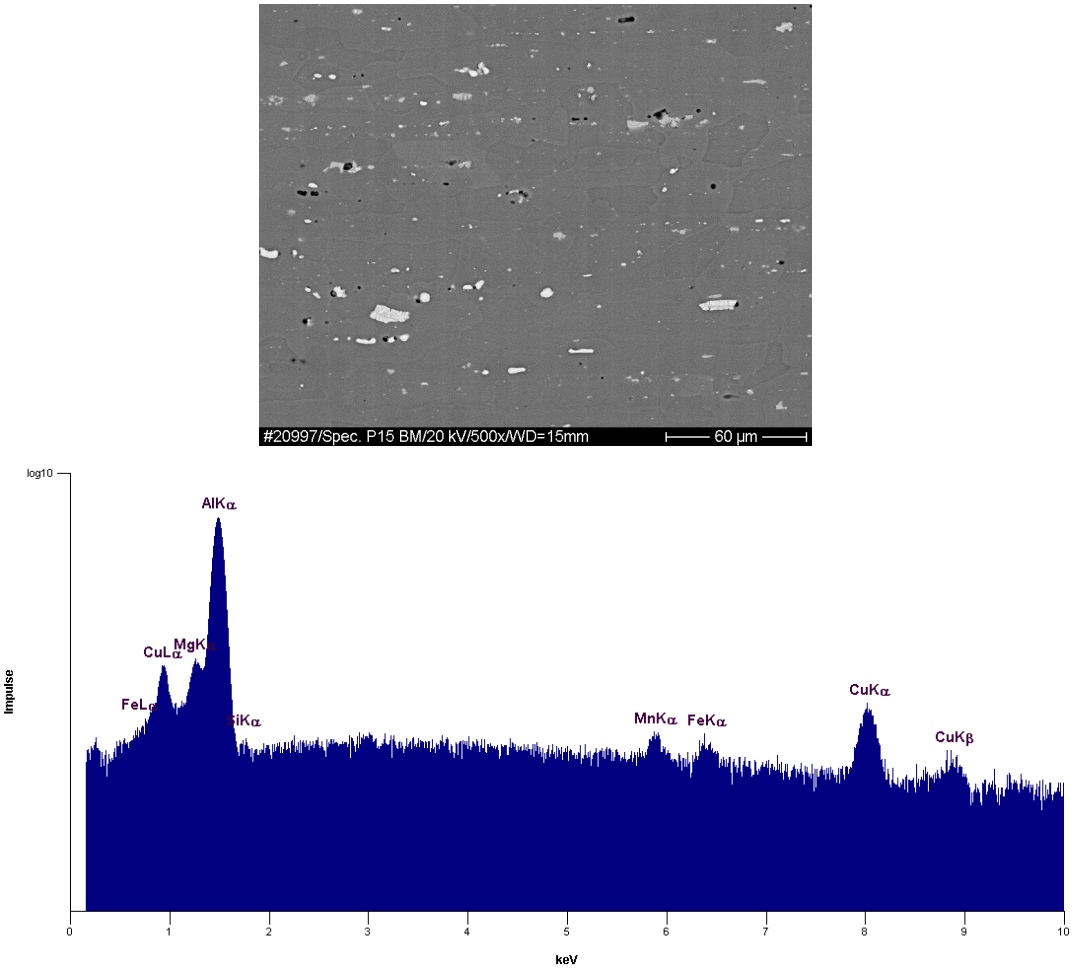

EDX-spectrum taken from a micro area of parent material (under a scattering angle of 35°).

Resultant material composition obtained:

Element	Atom-%	Equation	Mass-%	error(±)	Norm%
Mg	1.06	Mg	0.92	0.04	0.92
Al	95.79	Al	92.13	0.19	92.13
Mn	0.38	Mn	0.74	0.09	0.74
Fe	0.27	Fe	0.53	0.10	0.53
Cu	2.51	Cu	5.68	0.27	5.68
<Total>	100.00		100.00		100.00

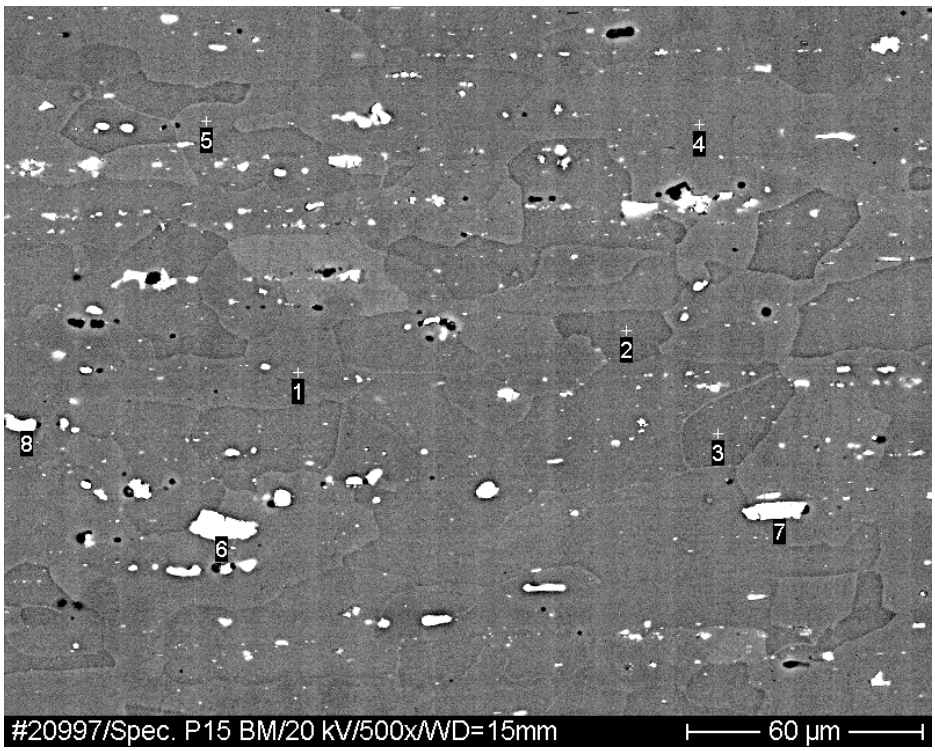

Image showing the particles analyzed in the point analysis.

Chemical composition of the particles analyzed:

Idx	Mg	Al	Si	Mn	Fe	Cu
1	0,77	94,14	0,00	0,62	0,00	4,47
2	0,86	93,11	0,00	0,40	0,25	5,38
3	0,97	94,36	0,00	0,56	0,00	4,12
4	0,95	93,98	0,00	0,42	0,00	4,65
5	0,96	93,69	0,00	0,38	0,00	4,97
6	0,00	40,83	0,42	3,94	13,70	41,11
7	0,00	42,69	0,27	2,47	13,71	40,85
8	0,85	85,01	0,00	0,35	0,00	13,79

References

[1] F. Vollertsen, Forming, Sintering and Rapid Prototyping, Handbook of the Eurolaser Academy, Vol.2. Schuöcker, D (Editor), pp. 357-453 (1998).

[2] W. Li, Y.L. Yao, Numerical and Experimental Investigation of Convex Laser Forming Process, SME J. of Manuf. Proc. Vol. 3, pp. 73-81 (2001).

[3] G. Dearden, S.P. Edwardson, Laser Assisted Forming for Shipbuilding, in Proc. of the SAIL Conference, Williamsburg, VA, USA (2003).

[4] J. Bao, Y.L. Yao, Analysis and Prediction of Edge Effects in Laser Bending, J. Manuf. Sci. Eng. Vol. 123, pp. 53-61 (2001).

[5] Y. Shi, Z. Yao, H. Shen, Research on the mechanisms of laser forming for metal plate, Int. J. of Mach. Tool. Manu. 46, pp. 1689-1697 (2006).

[6] S.P. Edwardson, A study into 2D and 3D laser forming of metallic components PhD thesis, University of Liverpool (2004).

[7] Y. Shi, H. Shen, Z. Yao, J. Hu, Temperature gradient mechanism in laser forming of thin plates, Opt. Laser Eng 39, pp. 858-863 (2007).

[8] F. Vollertsen, An analytical model for laser bending, Lasers Eng. 2, pp. 261-276 (1994).

[9] F. Vollertsen, Mechanisms and models for Laser Forming, Proc. of LANE'94, pp. 345-359 (1994).

[10] F. Vollertsen, Laser Forming Mechanisms, Models, Applications, in LFT Erlangen monograph (1995).

[11] Z. Mucha, J. Hoffman. W. Kalita and S. Mucha, Laser Forming of Thick Free Plates, Proc. of the LANE'97 Vol. 2, pp. 383-392 (1997).

[12] C. L. Yau, K. C. Chan, W. B. Lee, A New Analytical Model for Laser Bending, Proc. of LANE'97 Vol. 2, pp. 357-366 (1997).

[13] H. Arnet, F. Vollertsen, Extending Laser Bending for Generation of Convex Shapes, J. Eng. Manuf. 209, pp. 433-442 (1995).

[14] S.M. Knupfer, A.J. Moore, The effects of laser forming on the mechanical and metallurgical properties of low carbon steel and aluminium alloy samples, Mat. Sci. Eng. A 527, Issue 16-17, pp. 4347-4359 (2010).

[15] F. Vollertsen, I. Komel, and R. Kals, The laser bending of steel foils for microparts by the buckling mechanism – A model, Model. Simul. Mater. Sci. Eng. 3, 107-119 (1995).

[16] J. Magee, Laser Forming of Aerospace Alloys, PhD Thesis, University of Liverpool (1999).

[17] S.P. Edwardson, E. Abed, C. Carey, K.R. Edwards, G. Dearden, K.G. Watkins, Factors influencing the bend per pass in multi-pass laser forming, Proc. of the LANE'07, pp. 557-568 (2007).

[18] F. Vollertsen, M. Rödle, Model for the temperature gradient mechanism, Proc. of LANE'94, pp. 371-378 (1994).

[19] W. W. Duley, Laser Processing and Analysis of Materials, New York Plenum Press, pp. 476 (1983).

[20] Z. Mucha, Analytical Modelling of Laser plates Bending by use of the Temperature Gradient and the Buckling Mechanism and their experimental verification, Proc. of the LANE'07, pp. 619-630 (1997).

[21] S.P. Timoshenko, J.N. Goodier, Theory of elasticity, Third Edition, Engineering Societies Monograph, McGRAW-HILL BOOK COMPANY (1970).

[22] J. Krauss, Basic process in laser bending of extrusions using the Upsetting Mechanism, Proc. of the LANE'97, Vol. 2, pp. 431-438 (1997).

[23] M. Geiger, J. Kraus, T. Pohl, P. Hoffmann, F. Vollertsen, Analytisches Modell fuer das Laserstrahlbiegen von Profilen, Laser Magazin 10, pp. 18-25 (1994).

[24] A.K. Kyrsanidi, T.B. Kermanidis, S.G. Pantelakis, An analytical model for the prediction of distortions caused by laser forming process, J. Mater. Process. Technol 104, pp. 94-102 (2000).

[25] P.J. Chen, S.C. Lin, An analytical model to estimate angle formed by laser, J. Mater. Process. Technol. 108, pp. 314-319 (2001).

[26] H. Shen, y. Shi, Z. Yao, J. Hu, An analytical model for estimating deformation in laser forming, Comp. Mater. Sci. 37, pp. 593-598 (2006).

[27] Y. Shi, Y. Liu, Z.Q. Yao, H. Shen, A study on bending direction of sheet metal in laser forming, J. appl. Physics, 103, 053101 (2008).

[28] P.J. Cheng, S.C. Lin, An analytical model for the temperature field in the laser forming of sheet metal, J. Mat. Proc. Technol. 101, pp. 260-267 (2000).

[29] H. Shen, F. Vollertsen, Modelling of laser forming - An review, Com. Mat. Sci. 46, pp. 834-840 (2009).

[30] F. Vollertsen, M. Geiger, W. M. Li, FDM- and FEM- simulation of laser forming: a comparative study, Adv. Technol. of Plasticity, edited by Z.R. Wang, Y. He, III, 1793-1798 (1993).

[31] M. Geiger, S. Holzer, F. Vollertsen, Laserstrahlbiegen - Simulation eines 3-dimensionalen, thermomechanischen Prozesses, in Metal Forming Process Simulation in Industry, edited by B. Kropli and, E. Luckey, Monchengladbach, Germany, pp. 335-352 (1994).

[32] Y. Shi, H. Shen, Z. Yao, J. Hu, Numerical investigation of straight-line laser forming under the temperature gradient mechanism, Acta Metall. Sin. 19, pp. 144-150 (2006).

[33] W. Li, Y.L. Yao, Numerical and Experimental Study of Strain Rate Effects in Laser Forming, J. Manuf. Sci. Eng. Vol. 122, pp. 445-451 (2000).

[34] J. Chen, Y.L. Yao, Cooling Effects in Multiscan Laser Forming, J. Maunf. Proc. Vol. 3, pp. 60-72 (2001).

[35] W. Li, Y.L. Yao, Laser Forming with Constant Line Energy, Int. J. of Adv. Manuf. Tech. Vol. 17, pp. 196-203 (2001).

[36] W. Li, Y.L. Yao, Laser Bending of Tubes: Mechanism, Analysis and Prediction, ASME J. Manuf. Sci. Eng. Vol. 123, pp. 674-681 (2001).

[37] J. Cheng, Y.L. Yao, Microstructure Integrated Modeling of Multiscan Laser Forming, J. Manuf. Sci. Eng. Vol. 124, pp. 379-388 (2002).

[38] P. Cheng, Y.L. Yao, The Influence of Sheet Metal Anisotropy on Laser Forming Process, J. Manuf. Sci. Eng. Vol. 127, pp. 572-582 (2005).

[39] A.J. Birnbaum, P. Cheng and Y.L. Yao, Effects of Clamping on the Laser Forming Process, J. Manuf. Sci. Eng., pp. 1-41 (2005).

[40] P. Cheng, Y.L. Yao, C. Liu, D. Pratt, Y. Fan, Analysis and Prediction of Size Effect on Laser Forming of Sheet Metal, J. Manuf. Proc., pp. 28-41 (2005).

[41] Y. Fan, Z. Yang, P. Cheng, K. Egland, Y.L. Yao, Numerical and Experimental Investigation of Microstructure Evolution and Mechanical Behaviour of Steel in Laser Forming, ASME Trans. J. Manuf. Eng., pp.1-24 (2005).

[42] Y. Fan, Z. Yang, P. Cheng, K. Egland, Y.L.Yao, Investigation of Effect of Phase Transformations on Mechanical Behaviour of AISI 1010 Steel in Laser Forming, J. Manuf. Sci. Eng. Vol. 129, pp. 110-116 (2007).

[43] G. Yu, K. Masubuchi, T. Maekawa, N.M. Patrikalakis, J. Manuf. Sci. Eng, Trans. ASME 123, pp. 405-410 (2001).

[44] G. Yu, K. Masbuchi, T. Maekawa, N.M. Patrikalakis, FEM Simulation of Laser Forming of Metal Plates, J. Manuf. Sci. Eng. Vol. 123, pp. 405-410 (2001).

[45] L. Zhang, E.W. Reutzel, P. Michaelis, Finite element modelling discretization requirements for the laser forming process, Int. J. Mech. Sci. 46, pp. 623-637 (2004).

[46] Y. Namba, Laser Forming in Space. Proc. of the Int. Conf. on Lasers'85, edited by C.P. Wang (STS Press, McLean 1986), pp.403-407 (1986).

[47] K. Scully, Laser line Heating, J. Ship Prod. Vol. 3, No. 4, pp. 237-246 (1987).

[48] K. Masubuchi, Studies at MIT related to Applications of Laser Technologies to Metal Fabrication, in Proc. of Laser Advanced Materials Processing (LAMP'92), pp. 939-946 (1992).

[49] J. Magee, K.G. Watkins, W. M. Steen, Edge effects in laser forming, Proc. of the LANE'97, pp. 399-406 (1997).

[50] S.P. Edwardson, E. Abed, K. Bartkowiak, K.G. Watkins, Geometrical influences in multi-pass laser forming, J. Appl. Phys. D-Appl. Phys. Vol. 39, Issue 2, pp. 382-389 (2006).

[51] S.P. Edwardson, E. Abed, C. Carey, K.R. Edwards, G. Dearden, K.G. Watkins, Factors influencing the bend per pass in multi-pass laser forming, Proc. of the LANE'07, pp. 557-568 (2007).

[52] A. Sprenger, F. Vollertsen, W.M. Steen, K.Watkins, Influence of Strain Hardening on Laser Bending, Proc. of the LANE'94 Vol. 1, pp. 361-370 (1994).

[53] D. McFarland, B.L. Smith, W.D. Bernhart, Analysis of plates, Spartan Books New York (1972).

[54] S.P. Timoshenko, S. Woinowsky-Krieger, Theory of Plates and Shells, McGraw-Hill Int. 2nd Edition, pp. 416-417 (1959).

[55] M.E. Mortenson, Geometric Modelling, John Wiley & Sons, Inc., New York (1985).

[56] P. Carlone, G.S. Palazzo, R. Pasquino, Inverse analysis of the laser forming process by computational modelling and methods, Comp. & Math. with Appl. Vol. 55, Issue 9, pp. 2018-2032 (2008).

[57] K. Ueda, H. Murakawa, A.M. Rashwan, Y. Okumoto, R. Kamichika, Development of computer-aided process planning system for plate bending by line heating (report I) – relation between final form of the plate and inherent strain, J. Ship Prod. Vol. 10, No. 1, pp. 59-67 (1994).

[58] K. Ueda, H. Murakawa, A.M. Rashwan, Y. Okumoto, R. Kamichika, Development of computer-aided process planning system for plate bending by line heating (report II) - Practice for Plate Bending in Shipyard Viewed from Aspect of Inherent Strain, J. Ship Prod. Vol. 10, No. 1, pp. 59-67 (1994).

[59] K. Ueda, H. Murakawa, A.M. Rashwan, Y. Okumoto, R. Kamichika, Development of computer-aided process planning system for plate bending by line heating (report III) –Relation Between Heating Condition and Deformation, J. Ship Prod. Vol. 10, No. 1, pp. 59-67 (1994).

[60] J. Chen, Y. Yao, Process Design of Laser Forming for Three-Dimensional Thin Plates, J. Manuf. Sci. Eng. Vol. 126, pp. 217-225 (2004).

[61] C. Liu, L. Yao, V. Srinivasen, Optimal Process Planning for Laser Forming of Doubly Curved Shapes, J. Manuf. Sci. Eng. Vol. 126, pp. 1-9 (2004).

[62] H. Hagenah, R. Plettke, M. Geiger, Algorithms for Planning and Control of Laser Forming Applications, Proc. of the IWOTE'08, pp. 191-203 (2008).

[63] J. Kim, S.J. Na, 3D laser-forming strategies for sheet metal by geometric information, Opt. & Laser Technol. 41, pp. 843-852 (2009).

[64] B.K. Hinds, J. McCartney, G. Woods, Pattern development for 3D surfaces, Computer-Aided Design 23, pp. 583–92 (1991).

[65] J. Cheng, Y.L. Yao, Process Synthesis of Laser Forming by Genetic Algorithm, Int. J. Mach. Tool. Manuf. 44, pp. 1619-1628 (2004).

[66] J.G. Shin, J.H. Lee, S.K. Park, A Numerical Thermoplastic Analysis of Line Heating Processes for Saddle-type Shells with the Application of Artificial Neural Network, J. Ship Prod. Vol. 15, No. 1, pp. 10-20 (1999).

[67] P.J. Cheng, S.C. Lin, Using neural networks to predict bending angle of sheet metal formed by laser, Int. J. Mach. Tools & Manuf. Vol. 40, Issue 8, pp. 1185-1197 (2000).

[68] S. Guarino, N. Ucciardello, V. Tagliaferri, An application of neural network solutions to Modelling of diode laser assisted forming process of AA6082 thin sheets, ShetMet 2007 Vol. 344, pp. 325-332 (2007).

[69] T. Hennige, Development of irradiation strategies for 3D-laser forming, J. Mat. Proc. Techn. Vol. 103, pp. 102-108 (2000).

[70] T. Hennige, Laser Forming of Spatially Curved Parts, Proc. of LANE'97 Vol. 2 (1997).

[71] E.W. Reutzel, R.P. Martukanitz, P. Michaleris, L. Zhang, A.J. Savitz, J.P. Magnusen, J.U. Aburdene & K.J. Gombotz, Development of a System for the Laser Assisted Forming of Plate, Proc. of ICALEO 2001.

[72] E.W. Reutzel, J.U. Aburdene, K.J. Gombotz, J. P. Magnusen, R.P., Martukanitz, P. Michaleris, L. Zhang, Continuing Development of a Laser Line Forming System, Proc. of ICALEO 2002.

[73] E.W. Reutzel, K.J. Gombotz, R.P. Martukanitz, P Michaleris, Path Planning Strategies for Laser Line Forming, Proc. of ICALEO 2003, Paper 106.

[74] M. Reeves, A.J. Moore, D.P. Hand, J.D.C. Jones, J.R. Cho, R.C. Reed, S.P. Edwardson, G. Dearden, P. French, K.G. Watkins, Dynamic distortion measurements during laser forming of Ti-6Al-4V and their comparison with a finite element model, J. Eng. Manuf. Vol. 213, pp. 1685-1696 (2003).

[75] S.P. Edwardson, A.J. Moore, E. Abed, R. McBride, P. French, D.P. Hand, G. Dearden, J.D.C. Jones, K.G. Watkins, Iterative Laser Forming of Continuous Surfaces, Proc. of ICALEO 2004.

[76] S.P. Edwardson, E. Abed, P. French, G. Dearden, K.G. Watkins, R. McBride, D.P. Hand, J.D.C. Jones, A.J. Moore, " Development towards controlled three-dimensional laser forming of continuous surfaces", J. of Laser Appl. Vol. 17, No. 4, pp. 247-255 (2004).

[77] R. McBride, F. Bardin, M. Gross, D.P. Hand, J.D.C. Jones, A.J. Moore, Modelling and calibration of bending strains for iterative laser forming, J. Phys. D: Appl. Phys. 38, pp. 4027-4036 (2005).

[78] R. McBride, M. Gross, A.J. Moore, D.P. Hand, J.D.C. Jones, Calibration of bending and membrane strains for Iterative Laser Forming of non-developable surfaces, Proc. of ICALEO 2004.

[79] R. McBride, F. Bardin, M. Gross, D.P. Hand, J.D.C. Jones, A.J. Moore, Iterative laser forming of non-developable surfaces, School of Engineering and Physical Sciences, Heriot-Watt University, Edinburgh, EH14 4AS, not published yet.

[80] P.S. Mohanty, J. Mazumder, Handbook of laser materials processing, Orlando, FL: Laser Institute of America, pp. 191, Chapter 5 (2001).

[81] P.P. Benham, R.J. Crawford, C.G. Armstrong, Mechanics of Engineering Materials, Harlow, United Kingdom: Longman Group Ltd. (1996).

[82] W. Zhang, J. Marte, D. Mika, M. Graham, B. Farell, M. Jones, Laser Forming: Industrial Applications, Proc. of ICALEO 2004 Section D, pp. 27-35.

[83] P. Petrina, H.D. Conway, Deflection and Moment Data for Rectangular Plates with Uniform, Linear and Quadratic Thickness Variations, Trans. ASME J. Appl. Mech. 39, pp 814-815 (1972).

[84] H.D. Conway, Closed Form Solutions for Plates of Variable Thickness, Trans. ASME J. Appl. Mech. 20, pp.564-565 (1953).

[85] A.M. Zekonur, An Exact Solution for the bending of Thin Rectangular Plates with Uniform, Linear and Quadratic Thickness Variations, Int. J. Mech. Sci.,45, pp. 295-315 (2003).

[86] P. Cheng, Y. Fan, J. Zhang, Y. Yao, Laser Forming of Varying Thickness - Part I: Process Analysis, J. Manuf. Sci. Eng. Vol. 128, pp. 634-641 (2006).

[87] P. Cheng, Y. Fan, J. Zhang, Y. Yao, Laser Forming of Varying Thickness - Part II: Process Synthesis, J. Manuf. Sci. Eng. Vol. 128, pp. 642-650 (2006).

[88] P. Cheng, A.J. Birnbaum, Y.L. Yao, Laser Forming of Complex Structures, Proc. of IWOTE'05, pp. 221-238 (2005).

[89] I. Summerside, R. Kuntz, R. van der Meij, Advanced reconditioning technologies for turbine blading at ALSTOM, in Proc. of the ASME Turbo Expo 2008 Vol. 1, pp. 437-447.

[90] T. Hornfleck, J. Silvanus, M.F. Zaeh, A. Schoberth, EcoShape – A robust Laser Beam Forming Process of Aluminium Alloys for Aerospace Applications, Proc. of IWOTE'05, pp.139-148 (2005).

[91] M. F. Zaeh, T.Hornfeck, Development of a robust laser beam bending process for aluminium fuselage structures, Prod. Eng. Res. Devel. Vol. 2, pp. 149-155 (2008).

[92] D.G. Richards, P.B. Prangnell, S.W. Williams, P.J. Withers, Global mechanical tensioning for the management of residual stresses in welds, Mat. Sci. Eng. A 489, pp. 351-362 (2008).

[93] S. Williams, S. Morgan, A. Wescott, M. Poad, S. Wen. Stress Engineering – Control of Residual Stresses and Distortion in Welding, Proc. of IWOTE'08, pp. 229-240 (2008).

[94] T. Nagy, S. Williams, P. Colegrove, C. Ikeagu, I. Fafiolu, Distortion Mitigation in Welded Ship Panels, Proc. of IWOTE'08, pp. 265-275 (2008).

[95] P. Cheng, A.J. Birnbaum, Y.L. Yao, Correction of Butt-Welding induced Distortion by Laser Forming, SME J. Manuf. Process, submitted (2005).

[96] T. Ueda, E. Sentoku, Y. Wakimura, A. Hosokawa, Flattening of sheet metal by laser forming, Opt. Laser Eng. Vol. 47, pp. 1097-1102 (2009).

[97] J. A. Ramos, J. Magee and K. G. Watkins, J. Laser Appl. 13(1) 32-40 (2001).

[98] M. Merklein, T. Hennige and M. Geiger, J. Mater. Process. Tech. 115, pp. 159-165 (2001).

[99] J.G. Cheng, J. Zhang, C.C. Chu, J. Zhe, Experimental study and computer simulation of fracture toughness of sheet metal after laser forming, Int. J. Adv. Manuf. Technol. 26, pp. 1222-1230 (2005).

[100] G.Thomson, M. Pridham, J. Mater. Process. Tech. 118, pp. 40-44 (2001).

[101] H. Shen, Z. Yao, Opt. Laser Eng., pp. 111-117 (2009).

[102] P.J. McGrath, C.J. Hughes, Experimental fatigue performance of laser formed components, Opt. Laser Eng. 45, pp. 423-430 (2007).

[103] J. Zhang, D. Pirzada, Fatigue Life Prediction After Laser Forming, J. Manuf. Sci. Eng. Vol. 127, pp.157-164 (2005).

[104] P. Cheng, Y. L. Yao, The Influence of Sheet Metal Anisotropy on Laser Forming Process, Proc. of ICALEO 2003**,** Paper 101.

[105] Z. Liu, C. Guzman, H. Liu A. Anacleto, I. Francisco, M. Abdoalshafie, L. Ma, O. Abodunrin, P. Skeldon, Corrosion performance and restoration of laser-formed metallic alloy sheets, J. Laser Appl. Vol. 21, Issue 2, pp. 76-81 (2009).

[106] Z. Liu, Phenomena and Mechanisms of Corrosion in Laser-Formed Metallic Alloy Sheets, Proc. of LANE'07 Vol. 1, pp. 545-555 (2007).

[107] R.W.K. Honeycombe, Plastic Deformation of Metals, New York, St. Martin's Press (1968).

[108] M. Topić, R. Bucher, W. Vorster, S.Y. Zhang, P. McGrath, A.M. Korunsky, Mat. Sci. Forum Vols. 524-525, pp. 299-304 (2006).

[109] M.N. Topić, P. McGrath, W.J.J. Vorster, S.Y. Zhang, R. Bucher, A. Venter, A.M. Korunsky, J. Strain Anal. Eng. Vol. 42, pp. 497-504 (2007).

[110] A.M. Venter, M.W. van der Watt, R.C.Wimpory, R. Schneider, P.J. McGrath, M. Topic, Mater. Sci. Forum, Vols. 571-572, pp.63-68. (2008).

[111] http://en.wikipedia.org/wiki/File:Gaussian_curvature

[112] S. Rouquette, F. Bardin, S. Knupfer, D. P. Hand, J. D. C. Jones, A. J. Moore, Iterative Laser Straightening of Weld-Distorted Plates, Proc. of the LANE'07, pp. 581-588 (2007).

[113] S. Knupfer, S. Rouquette and A. J. Moore, Straightening of Distorted Welded Plates by Iterative Laser Forming, Proc. of the IWOTE'08, pp. 205-213 (2008).

[114] Smith, F. William, Hashemi, Javad, Foundations of Materials Science and Engineering (4th edition), McGraw-Hill, ISBN 0-07-295358-6 (2005).

[115] G. Totten, M. Howes and T. Inoue, Handbook of Residual Stress and Deformation of Steel, ASME, Materials Park, Ohio, pp. 152 (2002).

[116] B. Scholtes, Residual Stresses Introduced by Machining, Advances in Surface Treatments, Vol. 4, A. Niku-Lari, Pergamon Press, Oxford, pp. 59-71 (1987).

[117] H.O. Pierson, Handbook of Carbon, Graphite, Diamond and Fulleners – Properties, Processing and Applications, Consultant and Sandia National Laboratories Albuquerque, New Mexico, pp. 56-57 (1993).

[118] K. Wissenbach, A. Gillner, F. Dausinger, Transformation hardening by CO_2 Laser Radiation, Laser and Optoelectronic, AT-Fachverlach Stuttgart (1985).

[119] R. Halliday, R. Resnick, K.S. Krane, Physics 4^{th} edition, John Wiley & Sons Inc., Vol. 2 (1992).

[120] Wolfe, Zissis, The Infrared Handbook, Washington, DC, Office of Naval Research, Department of the Navy (1978).

[121] http://support.fluke.com/rayteksales/Download/Asset/IR_THEORY 55514_ENG_REVB_LR.PDF.

[122] http://www.mellesgriot.com/products/optics/mp_3_5.htm, in Melles Griot Optical Guide (2007).

[123] http://www.westyorkssteel.com/Heat_Treatment/htchart.htm

[124] http://www.coleparmer.com/techinfo/techinfo.asp?htmlfile=Emissivity.htm&ID=254#anchor64.

[125] J.A. Goldak, A. Chakravarti, M. Bibby, A new finite element model for welding heat source, Metall. Trans. B, Vol. 15, pp. 299-305 (1984).

[126] F. Gabriel, D. Ayrault, A. Fontes, J.L. Roatta, M. Raynaud, Global method for estimation of the heat source parameters dedicated to narrow GTA welding, Mathematical modelling of weld phenomena 8, Ed. by H. Cerjak, H. Bhadeshia, E. Kozeschik, 2007 TU Graz.

[127] Massard, Aide-Mémoire du thermicien (Broché), Collection : Elsevier Livres (language: French), ISBN 290607795X, 1997 édition.

[128] H.J. Bargel and G. Schulze, Werkstoffkunde, Springer Verlag Berlin Heidelberg (2005).

[129] J.E. Hatch, Aluminium - Properties and Physical Metallurgy, American Society for Metals (1984).

[130] R.W.K. Honeycombe and R.W. Pethen, J. Less, Dynamic Recrystallization, Common Metals 28, pp. 201-212 (1972).

[131] DIN_50125, Testing of metallic materials - Tensile test pieces, Beuth Verlag (2004).

[132] G. Petzow, Metallographisches Ätzen, Gebrueder Borntraeger 6th edition Berlin Stuttgart (1994).

[133] American Society for Testing and Materials, American Society for Metals: Friction and wear testing: source book of selected references from ASTM standards and ASM handbooks, Materials Park, OH, ASM (1997).

[134] W. Reimers, Neutrons and Synchrotron Radiation in Engineering Materials Science, WILEY-VCH Verlag Weinheim, pp. 44 and pp. 24 (2008).

[135] E.J. Pavlina and C.J Van Tyne, J. Mater. Eng. Perform. Vol. 17 (Dec. 2008).

[136] J.R. Cahoon, W.H. Broughton and A.R. Kuzak, Metall. Trans. Vol. 2, pp. 1979-1983 (1971).

[137] J.R. Cahoon, Metall. Trans. Vol. 3, pp. 3040 (1972).

[138] Metals Handbook 9th Edition Vol. 1, Properties and selection: irons and steels, American Society for Metals, Metals Park, Ohio 44073 (1978).

[139] Metals Handbook: Aluminium and Aluminium Alloys, ASM Specialty Handbook, ASM International, Materials Park OH (1993).

[140] P.J. Withers, H.D.K.H. Badeshia, Mater. Sci. Technol. 17, pp. 355-365 (2001).

[141] H. Behnken: Some basic relations to the stress analysis using diffraction methods, in: V. Hauk (eds.), Structural and Residual Stress Analysis by Nondestructive Methods, Elsevier, Amsterdam, pp. 39-65 (1997).

[142] E. Macherauch, H. Wohlfart, U. Wolfsteig, Haeterei Technische Mitteilungen (HTM) 28, pp. 201-211 (1973).

[143] W. Bragg, The Reflection of X-rays by Crystals, Proc. Roy. Soc. 88a, pp. 428-438 (1913).

[144] Properties & selection: Nonferreous Alloys and pure Metals, Materials Handbook-9th edition Vol. 2, pp. 77 (1979).

[145] M. Marya, G.R. Edwards, J. Mater Process. Tech. 108, pp. 376-383 (2001).

[146] IS0/TTA3, Polycrystalline materials – Determination of residual stresses by neutron diffraction, in: Technology trends assess, ISO (2001).

[147] D. C. I. T. 21432, Non-destructive testing: British Standards Institute (2005).

[148] A.C. Larson, R.B. Von Dreele, General structure analysis system (GSAS), Los Alamos National Laboratory Report LAUR (2000).

[149] J.A. James, J.R. Santisteban, L. Edwards, M.R. Daymond, Physica B, Cond. Matter 350, pp. 743-746 (2004).

[150] A. Steuwer, M. Dumont, M. Peel, M. Preuss, P.J. Withers, Acta Mater 55, pp. 4111-4120 (2007).

[151] M. T. Hutchings, P. J. Withers, T. M. Holden, T. Lorentzen, Introduction to the characterization of residual stress by neutron diffraction, Taylor and Francis, Boca Raton, FL, USA, pp. 204 (2005).

[152] J.R. Taylor, An Introduction into Error Analysis, 2nd edition, Sausalito (1997).

[153] G.Totten, M.Howes and T. Inoue, Handbook of Residual Stress and Deformation of Steel, pp. 142-145, pp. 392-396, ASME, Materials Park, Ohio.

[154] J. Altenkirch, A. Stuewer, M. Peel, D.G. Richards, P.J. Withers, Mat. Sci. Eng. A 488, pp. 16-24 (2008).

[155] D. Dantz, Eigenspannungen in mikrowellengesinterten Ni8Y-ZrO_2 und NiCr8020/8YZrO_2 Gradientenwerkstoffen, Thesis TU Berlin (2000).

[156] W.M. Thomas, E.D. Nocholas, J.C. Needam, M.G. Murch, P. Templesmith, C.J. Dawes, GB Patent Application No. 9125978.8, December 1991 and US Patent No. 5460317 (Oct. 1995).

[157] N.A. McPherson, H. Samson, T.N. Baker, N. Suarez-Fernandez, Steel microstructures in autogenous laser welds, J. Laser Appl. Vol. 15, No. 4, pp. 200-210 (2003).

[158] N.A. McPherson, A. Coyle, M. Wells, Induction heat straightening - A distortion rework reduction tool for thin plate, Welding and Cutting Vol. 7, No.3, pp. 162-166 (2008).